

THÈSE

En vue de l'obtention du

DOCTORAT DE L'UNIVERSITÉ DE TOULOUSE

Délivré par :

Institut National Polytechnique de Toulouse (Toulouse INP)

Discipline ou spécialité :

Science et Génie des Matériaux

Présentée et soutenue par :

M. VENKAT SUNIL KUMAR CHANNAM

le jeudi 14 septembre 2017

Titre :

Synthèse des oxydes fortement corrélés et recherche de leurs propriétés électroniques et optiques

---

École doctorale :

Science de la Matière (SDM)

Unité de recherche :

Centre Inter-universitaire de Recherche et d'Ingénierie des Matériaux (CIRIMAT)

Directeur(s) de Thèse :

M. FRANCIS MAURY

M. NAOUFAL BAHLAWANE

Rapporteurs :

MME ELISABETH BLANQUET, SIMAP GRENOBLE

MME AUSRINE BARTASYTE, FEMTO-ST

Membre(s) du jury :

M. CHRISTOPHE DETAVERNIER, GHENT UNIVERSITY, Président

M. FRANCIS MAURY, TOULOUSE INP, Membre

M. NAOUFAL BAHLAWANE, LUXEMBOURG INSTITUTE OF SCIENCE AND TECHNOLOGY, Membre

MME BRIGITTE CAUSSAT, TOULOUSE INP, Membre

Preface

This PhD thesis is dedicated to the physical chemistry of VO_2 and V_2O_5 thin films and their synthesis through chemical vapour deposition. The research effort shed light at the aspects of VO_2 as a metamaterial and study the interplay of electric and optical properties occurring in this metamaterial region and proposing several innovative applications and proof of concepts. In addition, we report for the first time ever, the nature of thermochromic phenomenon occurring in V_2O_5, its mechanism and the cause of this behaviour. The work described in this thesis has been carried out at the materials research department in Luxembourg institute of Technology (LIST) with academic support from CIRIMAT lab at INP-Toulouse.

This thesis is a cumulative article based; the results and discussion are presented as articles that have been published in international peer-reviewed journals. Detailed introduction, literature review and a summary of the experimental work for both VO_2 and V_2O_5 are presented. An extended abstract is provided in French as an annexe. With this work, I hope to highlight these amazingly responsive systems in a new and unconventional way, and that the outcomes of this research will be useful for future investigation.

C V Sunil Kumar

Luxembourg, August 2017

Acknowledgement

Firstly, I would like to sincerely thank my PhD supervisor Dr. Naoufal Bahlawane. I consider myself to be very fortunate to have worked under his excellent guidance. This thesis could have not materialised without his support and encouragement. He has been an impeccable teacher, a wise mentor and above all a great source of knowledge and inspiration. He has taught me to be scientifically curious and methodical in working. Above all he has inspired me each day with his own example of kindness and extraordinary hard work.

I am also very grateful to Prof. Francis Maury, my scientific advisor from INP-Toulouse, for his ever-encouraging comments and scientific discussions. He has been the guiding hand and the father figure to me in all aspects concerning my PhD. His kindness and great belief in me was very humbling and motivated me to approach my research topics with much enthusiasm.

I also thank the Director of the materials research department at LIST Prof. Jens Krisel and the deputy director of the materials group Dr. Damien Lenoble in believing me and for funding my work; without which none of this work produced here would have been possible.

Special thanks to all the amazing co-workers, especially Serena, David, Dheeraj, Alex, Nohora, Vincent, Hameeda and supporting staff that I had the opportunity to work alongside. Life at LIST and Luxembourg in general has been an absolute joy and I got to meet several people and bond many new friendships.

Finally, and most importantly I would like to thank my Science teachers from the school days Dr. Kameswari and Late Sudha Akka as well as my parents back in India to have given me the strength, confidence and instilled in me the scientific vigour, and supported me whole heartedly to follow my dreams.

List of publications issued in this work.

1. **Synthesis of vanadium oxide films with controlled morphologies: Impact on the metal–insulator transition behavior.**
   S Kumar, D Lenoble, F Maury and N Bahlawane. Phys. Status Solidi A, 212: 1582–1587 (2015).

2. **Electrical switching in Semiconductor-Metal self-assembled VO_2 disordered metamaterial coatings.**
   S Kumar, F Maury and N Bahlawane. Scientific Reports, Article number: 37699 (2016)

3. **Light modulation in smart Cermet based on phase change disordered metamaterial.**
   S Kumar, F Maury and N Bahlawane. (Just submitted) (2017)

4. ***An infrared blackboard based on the disordered metamaterial state of Vanadium oxide.***
   S Kumar, F Maury and N Bahlawane. (In preparation) (2017)

5. ***Visible thermochromism in Vanadium pentaoxide coatings.***
   S Kumar, A Qadir, F Maury and N Bahlawane. ACS Applied Materials and Interfaces 9 (25), pp 21447–21456 (2017).

6. ***Tunable thermochromic properties of V_2O_5 coatings.***
   S Kumar, F Maury and N Bahlawane. Materials today physics (2) pp 1-5; (2017).

7. ***Optical and morphological properties of thermochromic V_2O_5 coatings.***
   S Kumar, F Maury and N Bahlawane. Data in brief (14), pp 348-353 (2017)

Table of Contents

1. Introduction 8

1.2 Vanadium Di Oxide (VO_2) 9

1.3 SMT in Vanadium Oxides 12

1.4 VO_2 as a naturally disordered metamaterial 17

1.5 Chromic properties of Vanadium Oxides 20

2. Synthesis of Vanadium Oxide films 25

2.1 Sol-Gel Technique. 26

2.2 Sputtering 27

2.3 Pulsed Laser Deposition (PLD) 28

2.4 Atomic layer Deposition 29

2.5 Chemical vapour deposition CVD 30

2.5.1 Precursor selection 30

2.5.1.1 Inorganic Vanadium Compounds 30

2.5.1.2 Vanadium Beta-diketonates Compounds 31

2.5.1.3 Vanadium Alkoxide Compounds 31

3. Experimental 33

3.1 Film Deposition techniques 33

3.1.1 Chemical Vapour Deposition. (CVD) 33

3.1.2 Atomic Layer Deposition (ALD) 44

3.1.3 Synthesis of VO_2 films 45

3.1.4 Synthesis of V_2O_5 films 47

3.1.5 Atomic layer deposition of Al_2O_3 on V_2O_5 coatings 47

3.2 Thin film characterisation techniques 48

3.2.1 Scanning electron microscopy (SEM) 48

3.2.2 Profilometer. 53

3.2.3 X-Ray Diffraction (XRD) 55

3.2.4 Electrical resistivity measurements. 61

3.2.5 Raman Scattering. 63

3.2.6 Optical Spectroscopy 70

3.2.7 Thermal imaging using a Near Infrared camera. 76

References 82

4. Results and Discussions 96

4.1 Synthesis of Vanadium oxide films with controlled morphologies: Impact on the metal insulator transition behaviour 96

4.2 Electrical switching in semiconductor-metal self-assembled vo_2 disordered metamaterial coatings. 110

4.3 Light Modulation in Smart Cermet Based on Phase Change Disordered Metamaterial 137

4.4 An infrared blackboard based on the disordered metamaterial state of Vanadium oxide. 151

4.5 Visible thermochromism in Vanadium pentoxide coatings 165

4.6 Tunable thermochromic properties of V_2O_5 coatings 191

4.7 Optical and morphological properties of thermochromic V_2O_5 coatings 208

5. Conclusions and Future Work 214

Références 237

1. Introduction

In strongly correlated electron systems, observed electronic and structural behaviours result from the complex interplay between multiple, sometimes competing degrees-of freedom. As a result, these [1,2] materials exhibit a variety of unusual behaviours, such as high-temperature superconductivity, colossal magneto resistance, exotic magnetic, charge and orbital ordering, and insulator-to-metal transitions. [1,2] Oxides of vanadium are typical strongly-correlated materials that have been widely-studied by theoretical and experimental condensed-matter and materials community for more than half a century. Among all the oxides of Vanadium, Vanadium di oxide (VO_2) and Vanadium pentoxide (V_2O_5) are of particular interest and they enjoy a cult following in the research community and for good reasons. VO_2 and V_2O_5 have been the materials of choice to understand fundamental exciting physics and were implemented for the cutting edge industrially relevant applications. [3–9]

Chapter 1 of the thesis deals with the basic structures, properties and background of VO_2 and V_2O_5 followed by a brief review on some novel and unique functionalities of these materials. The naturally disordered metamaterial nature of VO_2 and its impact on the near infrared thermochromic behaviour combined with the concept of rewritable patterns is introduced. In case of V_2O_5, the study is mainly focused on the optical properties and visible thermochromism. The tunability aspect of this property is investigated by different metal ion doping and through selective oxygen deficiency control.

Chapter 2 reviews the synthesis of VO_2 and V_2O_5 by both wet chemical as well as physical vapour deposition, however special focus is given to the Chemical vapour deposition (CVD) synthesis of vanadium oxide through gas phase evaporation of metal organic precursors.

In depth details about the experimental aspects pertaining to this thesis are provided in **chapter 3**, whereas results and discussion are detailed systematically as journal publications in **chapter 4**.

The goal of this thesis is to draw the reader's attention away from the traditional and more often discussed aspects of VO_2 and V_2O_5 and re-introduce these highly responsive and remarkable materials with a completely new perspective and outlook. The results of this research, many of which believed to be reported for the first time, further strengthen the fact that there is still a lot of untapped potential regarding these two materials.

1.2 Vanadium Di Oxide (VO_2)

VO_2 belongs to the class of — smart material, [10] which generally responds to external temperature, electric or magnetic fields and/or pressure stimuli. Therefore it has the capabilities of sensing, actuating, and switching, relying on an intrinsic property of the material. These external stimuli bring upon a phase transition in VO_2, resulting in large variation of electrical and optical properties. This phase transition is at the heart of VO_2 properties. Thin films and nanoparticles of VO_2 tend to survive the stress generated during repeated cycles of phase transition better than bulk crystals and are therefore suited for many device applications. [11,12]

As far as VO_2 is concerned, several crystalline temperature phases have been reported namely M1, T, M2 and R. The understanding of VO_2 and the metal-insulator transition is even more complicated due to the presence of these additional phases. They appear on application of uniaxial stress or on doping of VO_2 with small amounts of Cr, Fe, Al, or Ga of the order of few percent. A comprehensive phase diagram of Cr doped VO_2 is given by Pouget et al. [13–15] According to the authors, Cr-doped VO_2 on cooling from a high temperature R phase, enters the monoclinic M2 phase in a first order metal-insulator transition. On further lowering of the temperature, transition proceeds to a triclinic T phase and finally followed by a first order transition to the monoclinic M1 phase. It is worth noting that the Cr concentration in the films was very low at 0.015%.

Later on, Pouget et al [16] demonstrated that both the M2 and T phases could be likewise stabilized by applying uniaxial stress. It was pointed out that the critical uniaxial stress needed for appearance of the M2 phase is very low, indicating

that the difference in free energies of the M1 and M2 phases in pure VO_2 are extremely small. Therefore, M2 and the T phases must be interpreted as alternative phases of pure VO_2 whose free energies are only slightly higher than that of the M1 phase of the pure material. As a consequence, the M2 phase was regarded as a metastable modification of the M1 phase. In contrast, the T phase appears as a transitional state, which displays characteristics of both monoclinic phases.

M1 phase has been the most attractive owing its unique near room temperature insulator-to-metal phase transition and technological applicability. VO_2 M1 undergoes a metal-insulator transition to the rutile phase (VO_2 R) that occurred at 340 K and ambient pressure. [17] This transition is accompanied by an abrupt change in the resistivity over several orders of magnitude. To better understand this transition, several models have been proposed ranging from Peierls to Mott-Hubbard-type scenarios. All these models point out the role of lattice instabilities, electron-phonon interaction and electron-electron correlations. Yet, all these models are not enough to explain all the phenomena occurring in vanadium dioxide.

The large change in electrical resistivity and transmittance/reflectivity and optical properties during the semiconductor-to-metal (SMT) transition for VO_2 occurs closer to room temperature than any other commonly-known compound and can also be conveniently depressed to about room temperature by doping. [18] The SMT in VO_2 has triggered numerous suggestions and their subsequent realizations for technological applications. These include thermally activated VO_2 thin films and nanoparticles for optical switching, [19] resistive switching, [20] thermal relays and energy management for solar cells and glazing [21] ; and sensors and actuators. [22–25] VO_2 has also been proposed as the channel layer in field-effect transistors to produce Mott transistors. [26,27] VO_2 thin films also have potential applications in the millimetre-wave and microwave portions of the electromagnetic spectrum, [28] and have an even greater range of potential applications that are only beginning to be explored. VO_2 single-crystalline nanobeams have lately opened a whole new possibility of using switching

nanowires with enhanced mechanical strength and stress-resistance. [29] A gas sensor application utilizing the SMT in VO_2 has also been realized recently. [30]

In a much recent development it was discovered that Metallic VO_2 contradicts the Wiedemann-Franz Law [31] that holds that the ratio of the electronic contribution of the thermal conductivity (κ) to the electrical conductivity (σ) of a metal is proportional to the temperature. The thermal conductivity that could be attributed to electron movement was 10% of the amount predicted by the Wiedemann-Franz Law. The reason for this appears to be the fluidic way that the electrons move through the material, reducing the typical random electron motion. [32]

1.3 Vanadium pentaoxide (V_2O_5)

V_2O_5 is the saturated (highest oxidation state) oxide, and therefore the most stable one, in the V–O system. It crystallizes with an orthorhombic [33] unit cell structure belonging to the Pmnm space group with lattice parameters a=11.510 Å, b=3.563 Å, and c=4.369 Å. It has a layer-like structure and it is composed of distorted trigonal bipyramidal coordination polyhedra of O ions around V ions. The polyhedra share edges to form $(V_2O_4)_n$ zigzag double chains along the (001) direction and are cross linked along (100) through shared edges and vertices as shown in figure 1 The distorted polyhedra have a short (1.58 Å) vanadyl bond, $[VO]^{2+,}$ and four O ions located in the basal plane at distances ranging from 1.78 to 2.02 Å. The sixth O ion in the coordination polyhedron lies along the vertical axis opposite to the V–O bond at a distance of 2.79 Å.

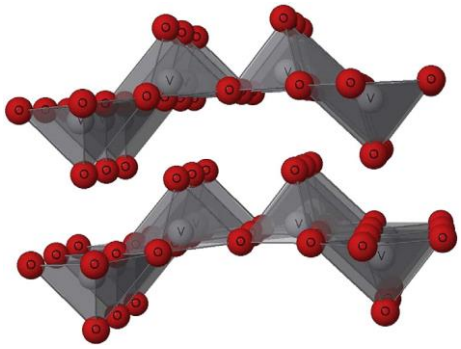

Figure 1: Perspective view of two layers of V_2O_5. V ions are represented as grey balls, O ions as red balls.

From a chemical point of view, V_2O_5 is an excellent catalyst [34] due to its rich and diverse chemistry that is based on two factors: the variety of vanadium oxidation states, ranging from 2+ to 5+, and the variability of oxygen coordination geometries. It is a brown/yellow solid, although when freshly precipitated from aqueous solution, its colour is deep orange. Due to its high oxidation state, it is both an amphoteric oxide and an oxidizing agent. This structural richness is related to the existence of differently coordinated oxygen ions which provide an important ingredient for controlling physical and chemical surface properties.

From the industrial perspective, it is the most important compound of vanadium, being principal precursor to alloys of vanadium and is a widely used industrial catalyst. [35] Another important use of vanadium (V) oxide is in the manufacture of sulphuric acid, an important industrial chemical with an annual worldwide production of 165 million metric tons in 2001, with an approximate value of US $8 billion. Vanadium (V) oxide serves the crucial purpose of catalysing the mildly exothermic oxidation of sulphur dioxide to sulphur trioxide by air in the contact process. [36]

Due to its layered structure, V_2O_5 is a promising material for energy storage systems and has a high ionic storage capacity. V_2O_5 has drawn significant interest in the past decades for its use in several industrially important applications such as electro chromic devices, [37] Gas sensors, [38] and reversible cathode materials for Li^+ ion batteries. [39] Due to its high temperature coefficient of resistance (TCR), vanadium (V) oxide finds use as a detector material in bolometers and micro bolometer arrays for thermal imaging. [40]

1.3 SMT in Vanadium Oxides

Many vanadium oxides show SMT/MIT characteristics. These include VO_2, V_2O_3 and most of the magneli phases. [41,42] Figure 2 shows the electrical resistivity versus temperature for several oxides of vanadium, including VO_2 and V_2O_3. While V_2O_3 exhibits the highest order of change in resistivity, the low temperatures at which the SMT takes place make it a non-preferred choice for most of the real world applications. Therefore, VO_2 is the most appealing oxide of

vanadium that can be exploited in real world conditions, because its SMT occurs closest to room temperature.

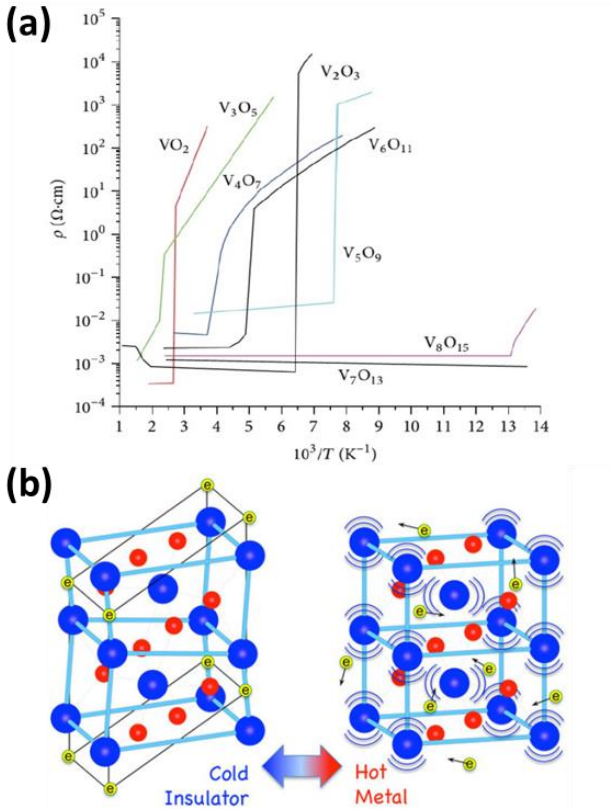

Figure 2 : (a) Electrical resistivity across the SMT in various vanadium oxide phases [41] and (b) Changes in the crystal structure and electronic properties of vanadium dioxide (VO_2) occur during its SMT (V blue; O red). Above 67°C (right), large-amplitude, nonlinear lattice vibrations (phonons) lead to a tetragonal crystal structure with mobile electrons (yellow) indicating that the VO_2 is a metal. At lower temperatures (left), the electrons are localized in the atomic bonds in the distorted monoclinic crystal structure indicating that the VO_2 is an insulator.

In single crystals, the resistivity change reaches a factor of 10^5 over a temperature range of 0.1 K [43]. Hysteresis associated with this transition is of about 2 K. The conductivity jump and the narrowness of the hysteresis loop are very good indications of how close the stoichiometry is to VO_2. Small deviations destroy the sharpness of the transition and increase the hysteresis width. The crystalline state of the material has an influence too: polycrystalline material will have a broader transition than single crystals. The transition temperature also

depends on the crystalline state and oxygen non-stoichiometry. As a rule, the SMT in VO_2 is to a certain degree suppressed in thin films as compared to single crystals.

Despite the many efforts made towards obtaining an understanding of their electronic behaviour, the vanadium oxides still pose many open questions. This fully applies to VO_2 as far as the nature of transition is concerned. Some authors related its phase transition to a Mott-Hubbard scenario, whereas others attributed it to electron-phonon coupling (a Peierls mechanism) on the basis of the crystal symmetry change. There are others who also state that the metal insulator transition in VO_2 has a combined nature, having the features of both Mott and Peierls transitions. The debate seems to be still unresolved.

Peierls transition [44–46] **:** it is a metal insulator transition occuring by a quasi-one dimensional metal when it reaches the Peirls temperature T_p. By quasi-one dimensional one must understand that there is a three dimensional metal where the atoms form chains in one direction that are responsible for the electric conductivity. · Above T_p, the atoms are equally spaced with the lattice constant "a". Below T_p, there is a distortion and as a result, the periodicity of the lattice doubles to 2a because of electron-phonon interactions in the conduction band. This process is called dimerization and happens spontaneously when the metal is cooled down.

In the case of a metal, the bands are only half filled. When the periodicity of the lattice doubles, the brillouin zone boundary also doubles, moving in to the point where the last filled state is $\frac{\pi}{2a}$. The filled states go to a lower energy and the empty ones to a higher. That process causes a gap in the dispersion relation at the Fermi energy using the perturbation theory. By undergoing that transition, the system gains electronic energy when atoms pair, but it has also a cost of elastic energy to perform the transition. Thus, it only takes place when there is more energy gained that it costs. When we go from rutile to monoclinic we observe a strong splitting of the $dx_2{-}y_2$ band into two narrow sub bands at the lower and upper edge of the t_{2g} group of bands. This is a consequence of the metal-metal

dimerization. In addition to that, the V $3dxz$ and dyz bands are upshift because of the zigzag-like anti ferroelectric displacement of the vanadium atoms.

So, in the low-temperature M1 structure of VO_2 metal-metal dimerization split the $dx_2{-}y_2$ band into bonding and antibonding branches, whereas other states shift to higher energy due to reduced V-O distances. As a result, insulating state is interpreted as due to a Peierls-like instability of the $dx_2{-}y_2$ band in an embedding reservoir of electrons. This Peierls instability allows to explain both the destabilization of the rutile structure in terms of increased metal-metal bonding and the SMT. Even if the strong dimerization, as well as the non-magnetism suggest that VO_2 might be a typical case of Peierls insulator, several experimental works showed that minute amounts of Cr-substitutions, uniaxial stress applied to pure VO_2 lead to a new phase M2 in which only half of the V-atoms dimerize, while the others are contained in chains of equally spaced atoms that behave like spin ½ Heisenberg chains. The fact that this phase is also an insulating one suggests that VO_2 can be described also as a Mott-Hubbard insulator.

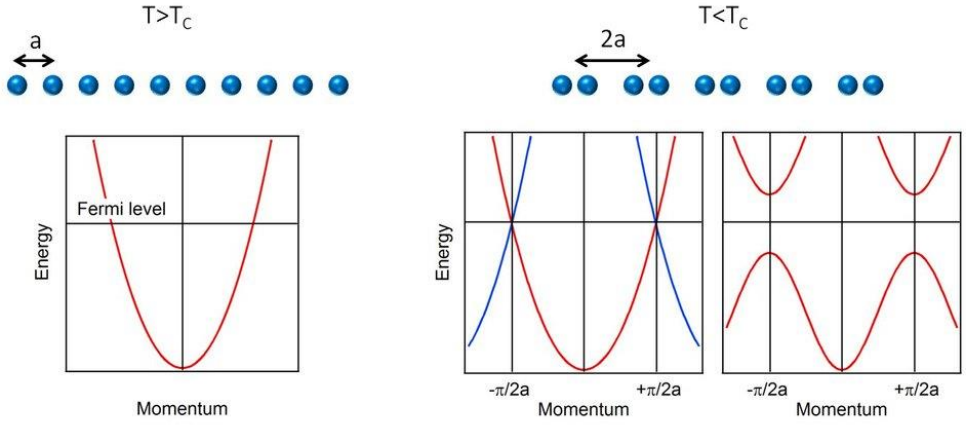

Figure 3: Peierls transition in a one-dimensional half-filled chain of atoms. Left: Crystal structure and corresponding band structure for temperatures higher than the critical temperature T_C. Right: At low temperatures $T < T_C$ a periodic lattice distortion doubles the size of the unit cell (Brillouin zone).

Mott-Hubbard transition: [47–50]

In this theory, the SMT is caused by the strong electron-electron correlation effects. At low temperatures the majority of electrons are localized in the crystal because of the strong electrostatic interaction that prevents them from moving. Electron delocalization is not energetically favoured in Mott insulators compared to a state where electrons are localized in their own atomic states. The competition between the two states determines a critical value above which the crystal is metallic and insulating below. Hubbard introduced a model which gives a meaningful description to the two competing forces presented by Mott. The electron hopping process (which is the kinetic energy term) tends to delocalize the electrons into Bloch states and thus giving a metallic behaviour to the crystal. By contrast, the correlated electron-electron interaction tends to localize the electrons into their own atomic states thus making the crystal an insulator.

A critical question, so far unanswered, is whether the structural and electronic phase transitions in VO_2 occur congruently. For non-equilibrium phase transformations in thin VO_2 films, induced by ultra-short laser pulses, it was reported that the electronic SMT leads the Structural phase transition (SPT), [51] and that the SPT presents a kinetic bottleneck for the transition. It was also observed that for the shortest attainable excitation pulses, a coherent phonon associated with a breathing mode of the VO_2 lattice appears simultaneously with the SMT. [52] Ultrafast electron diffraction measurements on single-crystal VO_2 excited by femtosecond near-IR laser pulses demonstrated the existence of transitional structural states with lifetimes up to hundreds of picoseconds. [53] On the other hand, in the case of adiabatic, thermally induced phase transitions, Qazilbash et al. [54] have recently reported an intermediate electronic state characterized by strongly correlated metallic nano puddles with properties distinct from those of the high temperature tetragonal metal. A recent study by Okimura et al [55] of temperature-dependent XRD on thin VO_2 films on sapphire (0001) substrates suggests the possibility that the M2 structure may be an intermediate state during phase transition. Micro-X-ray diffraction studies of epitaxial VO_2 on (1010) sapphire substrate evidence the existence of a monoclinic metallic phase.

Taken together, these observations indicate the possibility of local energy minima other than the M1 and R phases in the region of strong correlation.

1.4 VO_2 as a naturally disordered metamaterial

A metamaterial by definition is a material engineered to have a property that is not found in nature. They are made from assemblies of multiple elements fashioned from composite materials such as metals or plastics. The materials are usually arranged in repeating patterns, at scales that are smaller than the wavelengths of the phenomena they influence. Metamaterials derive their properties not from the properties of the base materials, but from their newly designed structures. Their precise shape, geometry, size, orientation and arrangement gives them their unique properties capable of manipulating electromagnetic waves: by blocking, absorbing, enhancing, or bending waves, to achieve benefits that go beyond what is possible with conventional materials.

Appropriately designed metamaterials can affect waves of electromagnetic radiation or sound in a manner not observed in bulk materials. [56] Those that exhibit a negative index of refraction for particular wavelengths have attracted significant research. [57] [58] Potential applications of metamaterials are diverse and include optical filters, medical devices, remote aerospace applications, sensor for electromagnetic detection and, smart solar power management. [59,60]

The phase changing nature of VO_2 has certainly drawn the interest of many research groups to investigate VO_2's electrical and optical transitions to couple with existing metamaterial concepts to enhance and tune the exotic properties. However, it was not until recently that VO_2 by itself was recognised as a naturally disordered metamaterial. [61–63]

In a narrow range of temperature, between the fully semiconducting and fully metallic phase, there exist third intermediate states of VO_2, where both semiconducting and metallic phases co-exist. This intermediate region was termed as an Inhomogeneous composite medium composed of metallic and insulating domains. Using a "composite medium model" the author [53] described the formation and clustering of the metallic domains. When temperature (T)

exceeds the transition temperature (Tc) the conducting clusters become larger and form conducting path throughout the film as shown in figure 4.

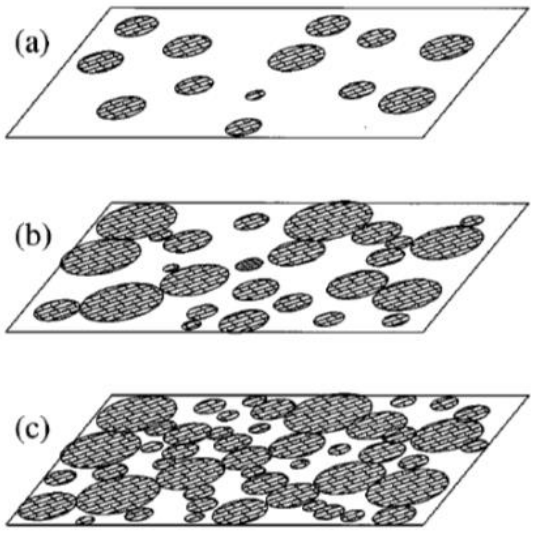

Figure 4: Schematic diagram of the SMT in VO_2 film. The metallic domains start to form nucleation droplets in the film surface sporadically (a), as T approaches T_C (b), the domains grow larger and start to form clusters as T increases further. Above T_C, the metallic domains form an infinite cluster (c) [64]

Later the same region of phase co-existence is also been referred to as monoclinic and correlated metal (MCM) by Kim et al. [65] and strongly co-related metal by M. M. Qazilbash et al. [66] The shaded region in figure 5 represents this state in VO_2 over a finite temperature range in the transition region.

Mikhail A. Kats et al. [62] coins the term “naturally disordered metamaterial” and stated thatin this transitional state, the film comprises nanoscale structures of metallic- and insulating VO_2, and the resulting effective medium behaves as a tuneable disordered metamaterial.

Nanoscale inclusions of the metallic phase emerge in the surrounding insulating-phase VO_2, which grow and connect in a percolation process, eventually leading to a fully metallic state at the end of the transition. These metallic inclusions are much smaller than the scale of the wavelength at infrared frequencies (> 800

nm), and thus VO_2 can be viewed as a natural, reconfigurable, disordered metamaterial with variable effective optical properties across the phase transition.

This metal-dielectric phase co-existence within the phase transition results in widely tuneable optical properties; in fact, the naturally occurring nanoscale structures in the SMT region can be viewed as a reconfigurable disordered metamaterial. The SMT has been utilized for optical switching.

The metamaterial region or the region of phase co-existence opens new opportunities to investigate VO_2 in a new perspective. The plethora of interesting physics that VO_2 offers makes it an ideal system for more exotic applications that have not been fully explored yet. **This thesis aims to shed light at the aspects of VO_2 as a metamaterial and study the interplay of properties occurring in this metamaterial region** like thermally triggered electrical switching and the ability to tune the hysteresis amplitude by selective temperature inputs within the hysteric region ultimately leading to control and stabilise the system at highly insulating or conducting phase at the same temperature by employing restrictive temperature modulation.

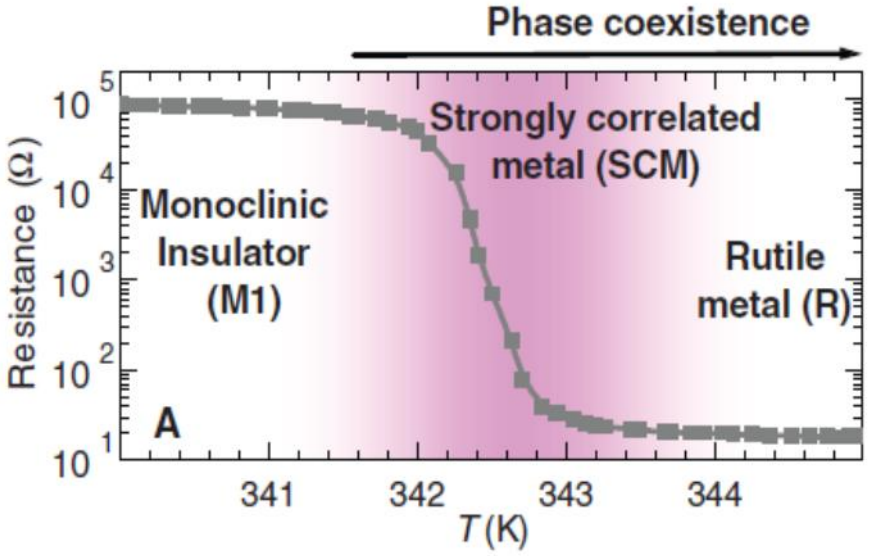

Figure 5: The phase diagram of VO_2 and the resistance-temperature curve showing SMT. The shaded area highlights the region of the phase diagram in which the strongly correlated metal (SCM) [67] **or what we refer to as the metamaterial region.**

1.5 Chromic properties of Vanadium Oxides

Vanadium oxides are popular not just for the host of exciting structural and electrical properties that they offer, but also due to the numerous changes occurring in the optical properties. Interaction of light with vanadium oxides has sparked immense interest in the research community for both VO_2 and V_2O_5.

VO_2 is famous for its property of undergoing thermochromic transition to significantly reflect NIR radiation upon heating beyond its phase transition temperature. In the semiconducting state, it allows transmission of IR radiation and in the metallic state it switches to IR reflective state. This property has sparked a great deal of research in developing VO_2 as smart window coatings for energy efficient buildings and IR reflective devices, thermal cameras, optical modulators etc. All these applications take in to account the phase change occurring from semiconducting to metallic phase.

Probing the physics of this intermediate state is still at an early stage because the material quality of VO_2 films has only recently been improved to the point where a complex region such as the intermediate state of the phase transition can be explored with reproducibility. The SMT in this material has been known for over 50 years; careful thermal profiles and composition control are required to obtain reversible transition properties. Studies on thin film VO_2 with reproducible phase-transition properties can be considered an emerging field, and within that, the intermediate state (i.e., a mixture of metallic and insulating states) is now being recognized as an opportunity, especially given recent interest in metamaterials that often require composite structures comprising domains of sub wavelength dimensions with vastly different optical properties.

Some pioneering work has been done in this regard by M. Kats [68] who demonstrated a perfect absorber at wavelength of 11.6 μm comprising an ultra-thin film of VO_2 on a sapphire substrate. The coatings can be tuned into the perfect absorption state by varying the temperature near the SMT. In this transitional state, the film comprises nanoscale structures of metallic and insulating VO_2, and the resulting effective medium behaves as a tunable disordered metamaterial with large optical absorption at infrared frequencies

(figure 6 a). The interaction of light with VO_2 and the underlying sapphire substrate results in essentially complete absorption of the incident light because of critical coupling.

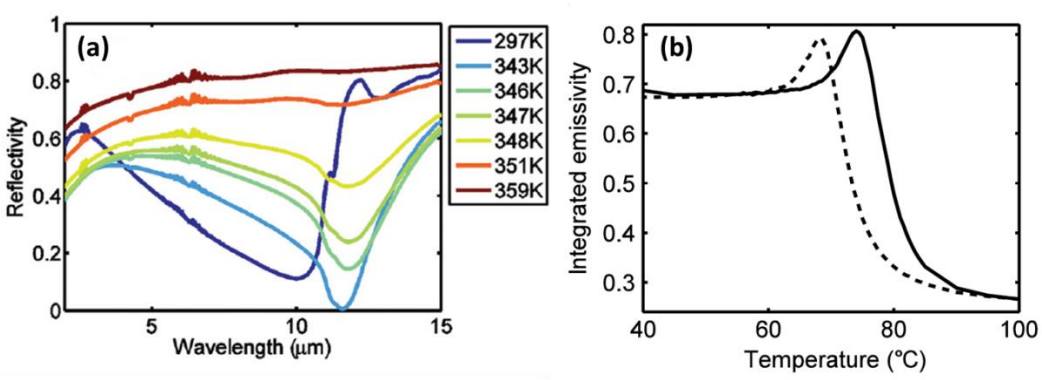

Figure 6: (a) reflectivity spectrum at temperatures from 297K to 360 K. At 343 K, the reflectivity drops to 0.0025 at 11.6 um. (b) The integrated emissivity of the VO_2-sapphire sample over the 8 to 14 um wavelength range. [69] **The continuous and dotted lines in (b) represent the heating and cooling stages of the cycle respectively.**

Using the same principle of changing the temperature of VO_2 in the vicinity of SMT, it was observed that there exists a certain region where the metallic inclusions form a specific order through which VO_2 undergoes perfect thermal emission and large broadband negative differential thermal emittance. [70] Geometries incorporating VO_2 with optical resonances in the infrared is promising for a wide array of applications calling for tunable infrared emissivity, narrow-band perfect blackbody like emission (figure 6b), negative differential thermal emittance, emissivity hysteresis, or some combination thereof. By controlling the temperature inputs, tunable emissivity coatings can be produced that can change their thermal emissivity to any value between 0 and 1 instantaneously for extended periods, this kind of precise control in emissivity is incredibly useful for solar selectivity and thermal management in space applications.

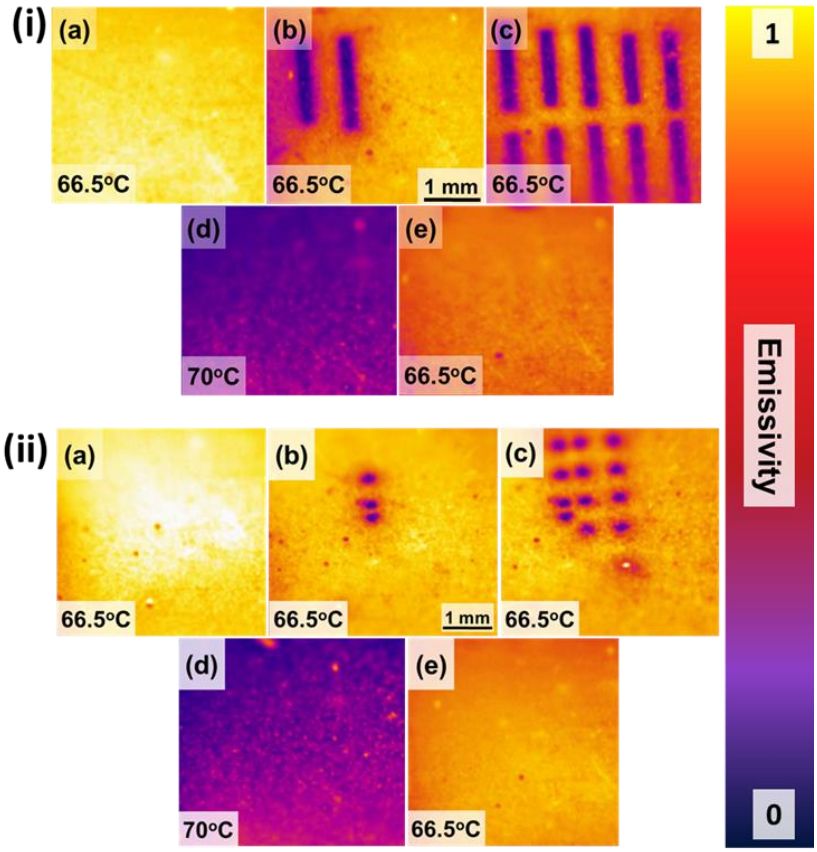

Figure 7: Infrared images from a thermal camera shows reversible patterning on a VO_2 surface using a laser to draw (i) lines and (ii) dots. (a) VO_2 film is maintained at a steady state temperature of 66.5°C, upon laser irradiation the temperature is instantaneously increased for about 4-5 °C causing localised phase change from a high emissive state to low emissivity state (b)(c). Due to the intrinsic hysteretic behaviour of VO_2, the patterns remain without any degradation. Increasing the temperature of the whole film and bringing back to the steady state (d) & (e) erases and resets the VO_2 film.

As another example from the work as part of this thesis shown in figure 7, the controllable emittance can be utilized to make a rewritable infrared ‘‘blackboard’’ by keeping the entire sample at the phase-transition temperature and using a cold or hot probe (such as a laser beam or soldering iron) to ‘‘write’’ patterns by thermally induced localized change of emissivity. These persistent patterns could be viewed with a thermal camera but would otherwise be invisible. A digital version of this device can be used as a rewritable infrared identification tag.

These patterns or images show in figure 7 “written” on VO_2 also act as dynamic conducting pathways in a highly resistive semiconducting matrix. This opens up a whole new way of utilizing reversible patterning and also in designing variable Meta structures and their investigations for exotic applications that are only limited to one’s imagination.

V_2O_5 on the other hand also exhibit interesting chromogenic properties like electrochromism and photochromism. Electrochromism [71,72] is the phenomenon displayed by some materials of reversibly changing colour by using bursts of charge to cause electrochemical redox reactions in electrochromic materials. Due the layered structure, V_2O_5 easily accommodates guest ions with a consequent perceptible colour change from Yellow to Blue. This is reversed by applying voltage in the reverse polarity. The process however is not instantaneous.

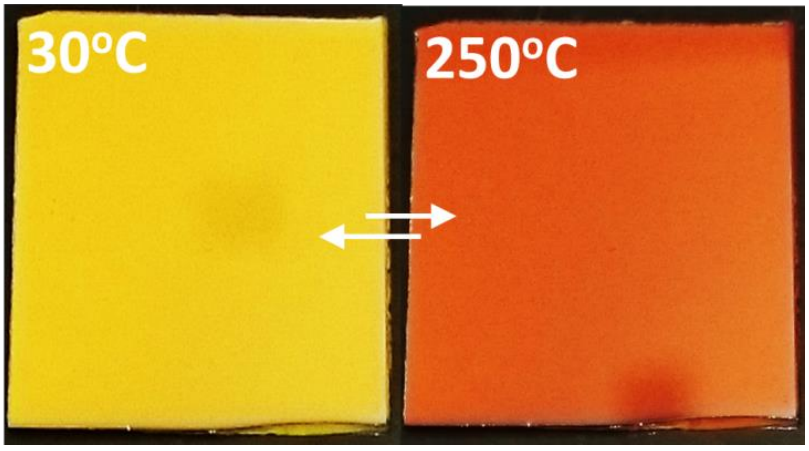

Figure 8: Thermochromic transition of yellow to orange colour in V_2O_5 coatings [73]

Photochromism is a phenomenon of colour change occurring on the surface of the films or material upon exposure of electromagnetic radiation. Shigeru Nishio et al [74] reported the first evidence of reversible visible light photochromism in V_2O_5. The authors used visible laser light (514.5 nm) to irradiate the oxide, which turns blue-black upon irradiation due to photo reduction of V^{5+}, and this effect is confirmed to be irradiation-induced and not heat-induced. However, the irradiation time is around 10 min and to retrieve the initial conditions the oxide must be annealed at 400°C in air.

Thermochromism, the property of changing the colour due to the variation in temperature is quite sought after for its various industrially relevant applications. While many metal oxides exhibit thermochromism, the exact mechanism of this reversible transition was not understood completely. V_2O_5 was also never mentioned as thermochromic material until now. **In this thesis, we report the nature of thermochromic transition occurring in V_2O_5, its mechanism and the cause of this behaviour.** Therefore, tuning of thermochromic nature was achieved for V_2O_5 coatings. Through understanding the fundamentals of thermochromism in V_2O_5 we believe, the same can be applied to all thermochromic binary oxide systems in general.

2. Synthesis of Vanadium Oxide films

In this section, we concentrate on the different techniques and chemistries used to grow both V_2O_5 and VO_2 films. V_2O_5 is thermodynamically the most stable oxide among all other vanadium oxides and is quite straight forward to synthesize. Hence its growth conditions are widely reported and can be generally described as oxidation of VOx films in oxygen atmosphere or ambient air. However, V_2O_5 films are much sought after for wide variety of application as previously mentioned. Therefore, much of the research on V_2O_5 is devoted to obtaining specific film properties like crystallinity, morphology and microstructure for its intended applications.

Contrary to V_2O_5, VO_2 needs special mentions for being quite challenging to grow as device grade films or coatings which offers excellent and reliable performance without degrading over time and oxidizing into other oxides or form a mixed oxide phase. The narrow window of thermodynamically favourable conditions that are required for VO_2 films imply a strict control over the process conditions.

A brief literature review of the most common fabrication techniques for VO_x synthesis is provided in this section. Precise control over the purity and the phase of the film is difficult as vanadium oxide forms several stable oxides such as VO, V_6O_{13}, V_3O_5, V_4O_7 etc. The phase diagram (figure 9) of vanadium oxide system shows the possible occurrence of nearly twenty stable vanadium oxide phases. The existence of these competing oxide phases offers particular challenge to the growth of both bulk and thin films of VO_2. Due to the multi valence state characteristics of the vanadium ions, oxygen stoichiometry has been also observed to significantly influence phase formation and the properties of the resulting vanadium oxides. With different fabrication conditions, different phases of vanadium oxides including V_2O_3, [V_nO_{2n-1} (Magneli phase)], VO_2, [V_nO_{2n+1} (Wadsley phase)] and V_2O_5 phases may co-exist in the thin film.

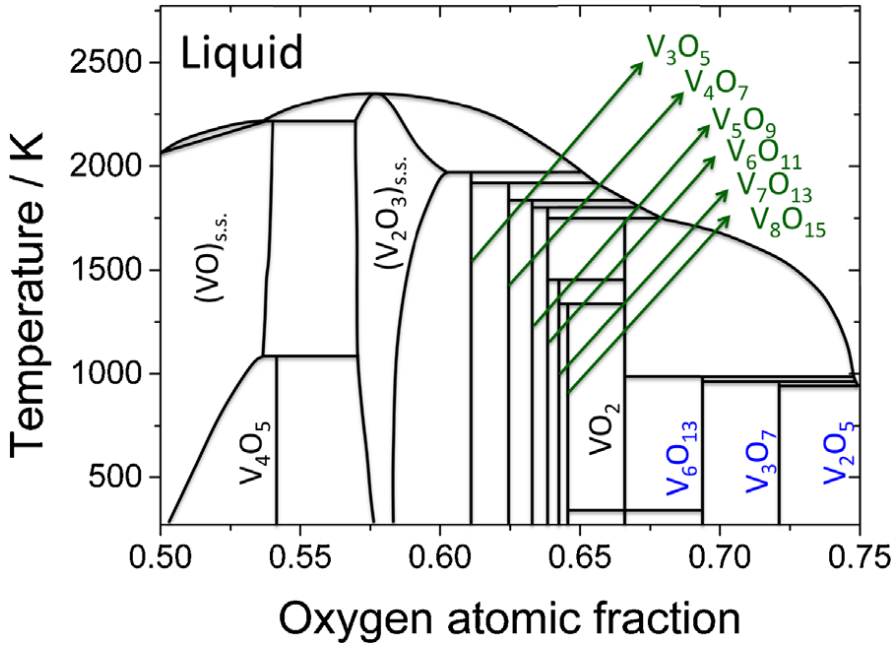

Figure 9: Schematic V-O phase diagram showing, Magnéli series, V_nO_{2n+1}, highlighted in blue, while the Wadsley series, V_nO_{2n-1}, is highlighted in green.

2.1 Sol-Gel Technique.

The sol-gel method has been widely employed for depositing VO_2 films because of its many advantages, such as low cost, large area deposition, and the ease of metal-doping. The sol-gel process is a wet-chemical technique for the fabrication of materials (typically a metal oxide) starting from a chemical solution containing colloidal precursors (sol). Typical precursors are metal alkoxides and metal chlorides, which undergo hydrolysis and polycondensation reactions to form a colloid, a system composed of solid particles (size ranging from 1 nm to 1 μm) immersed in a solvent. [75–77] The sol then evolves towards the formation of an inorganic network containing a liquid phase (gel). Formation of a metal oxide involves connecting the metal centers with oxo (M-O-M) or hydroxo (M-OH-M) bridges, thereby generating metal-oxo or metal-hydroxo polymers in solution, which is then deposited on a substrate or cast in a specific container or used to synthesize powders. The sol-gel approach is an inherently low temperature technique that allows for the fine control on the product‘s chemical composition, as even small quantities of dopants, can be introduced in the sol directly, which

gets transferred on the films upon subsequent coating method. [78–82] The precursor sol in case of VO_2 is generally deposited on the desired substrate to form a film (*e.g*. by dip-coating or spin-coating with a solution of vanadium isopropoxide, $VO(OC_3H_7)_3$ diluted in an alcohol, (e.g., ethanol or isopropanol), and then a subsequent annealing process in a reducing atmosphere. A drying process serves to remove the liquid phase from the gel thus forming a porous material, and then a thermal treatment (annealing) may be performed in order to favour further crystallization and densification. The precursor sol in case of VO_2 is generally deposited on the desired substrate to form a film (*e.g*. by dip-coating or spin-coating). The inorganic sol-gel method using V_2O_5 as the precursor was demonstrated by Dachuan et al. [83] According to Livage et al [84] vanadium oxide gels can be synthesized either via the acidification of aqueous solutions of vanadates, for e.g. $NaVO_3$ or via the hydrolysis of vanadium oxo-alkoxides, $VO(OR)_3$. Application oriented VO_2 films have been made using sol-gel process by several groups. [85–87] C.B. Greenberg introduced this process for making VO_2 as the gelation-hydrolysis method. [88] It has since been found that using the equivalent n-propoxide vanadium compound gives VO_2 also, and it is likely that a wide variety of organometallics and solvents can be used, since the final oxidation state of the vanadium ion depends on the pyrolysis conditions in air rather than the starting material.

2.2 Sputtering

Sputtering, in its many forms, is the most common physical vapor deposition process [89] for growing vanadium dioxide thin films. Vanadium dioxide thin films were first grown by reactive sputtering in 1967 by Fuls, Hensler and Ross of the Bell Telephone Laboratories. [90] They made their films by reactive ion-beam sputtering of a vanadium target in an argon-oxygen atmosphere. Other enhanced sputtering methods used to facilitate the deposition process include RF and DC sputtering and magnetron sputtering. The advantages of sputtering processes are film uniformity, scalability to larger substrate sizes and efficiency of deposition compared to the other methods. The simplest form of sputtering involves a diode sputtering by energetic ions (usually argon ions) from gas-discharge plasma

bombarding a target that forms the cathode for the discharge. Target atoms bombard the substrate (the anode), forming a coating. These sources feature a magnetically assisted discharge, in which a permanent magnet defines lines of magnetic flux perpendicular to the applied electric field from the DC or RF source, and is thus parallel to the surface of the target. The magnetic field concentrates and intensifies the plasma, in the space immediately above the target, by trapping of electrons near the target surface. This magnetron effect results in enhanced ion bombardment by the Ar ions, and thus much higher sputtering rates for both DC and RF discharges. After the first experiments in VO_2 deposition by reactive sputtering, and further analysis of those samples by Rozgonyi and Hensler, [91] both RF and DC reactive sputtering were studied by Duchene et al. [92] Similar results were obtained in both cases, but since RF sputtering was more suitable for depositing insulating oxides and had the abovementioned advantages over DC sputtering, it became the preferred method for VO_2 deposition. To standardize the fabrication of VO_2 thin films by sputter deposition, numerous studies have detailed the influence of sputter deposition parameters, like temperature, oxygen partial pressure, plasma emission ratio of oxygen and vanadium, etc. on the structure, optical and electrical properties of the deposited VO_2.

2.3 Pulsed Laser Deposition (PLD)

Pulsed Laser Deposition (PLD), another physical vapor deposition technique, is a comparatively recent inclusion in the world of thin film depositions, and is extensively used in oxide growth. In PLD a high power pulsed laser beam is focused on a target of the desired composition inside a ultra-high vacuum (UHV) chamber. Material vaporized from the target is deposited as a thin film on a substrate, for example Si wafer, facing the target. This process can occur in ultra-high vacuum or in the presence of a background gas, such as oxygen which is commonly used when depositing oxides.

Pulsed laser ablation as a deposition technique was realized in the late 1980s, and it was first used for VO_2 deposition by Singh *et al* in 1993 [93]. They used a KrF pulsed excimer laser (248 nm) to ablate a metallic vanadium target in UHV

deposition chamber with Ar and O_2 (10:1) atmosphere, and a substrate temperature of about 500^oC. The partial oxygen pressure was found to be critical for the preparation of the pure VO_2 phase, for as many as thirteen different phases ranging from V_4O to V_2O_5 could exist in the system. The as-deposited samples were annealed for about an hour at the same temperature and pressure to obtain the VO_2 that feature sharp SMT. Soon after, Kim and Kwok [94] reported that they were successful in depositing high quality VO_2 films on sapphire by PLD at high temperature without post-annealing. Maaza et al, [95] was the first to claim room temperature growth of VO_2 by PLD, and the as-deposited films showed rather sharp phase transitions at around 70^oC, though it has not yet been reproduced by any other group. PLD of VO_2 thin films has been done on variety of substrates, including silicon, glass, sapphire, fused silica and quartz. [96] In 2004, Suh et al [51] described the effect of nucleation and growth of VO_2 nanoparticles and thin films on the SMT, where the films and nanoparticles were grown by PLD. They showed that the width and shape of the hysteresis is determined by the competing effects of crystallinity and grain size. Recently, in-situ studies of the initial growth phase of vanadium dioxide films using synchrotron-based X-ray diffraction were reported in detail by Pauli *et al*. [97] They showed that films grown at room temperature are basically amorphous and only crystallize into the VO_2 phase upon thermal annealing at 420^oC in a background of O_2, with the nano-sized islands sometimes having a preferential orientation depending on the match with the substrate crystallography. This leads us to the discussion of hetero-epitaxial growth of VO_2 on substrates which have good lattice match with that of VO_2 thin films.

2.4 Atomic layer Deposition

Atomic layer deposition involves self-limited surface reactions for the growth of metal oxide by sequentially exposing the surface to metal and oxygen sources one after the other. ALD of vanadium oxides was first studied for catalytic applications and for Li-ion batteries. In these cases, V_2O_5 was the phase of interest. [98,99] V_2O_5 reported starting from vanadyl-tri(isopropoxide) precursor. Furthermore, post-deposition annealing of other vanadium oxide phases in air is

expected to result in V_2O_5. In case of VO_2 the controlled reduction of the ALD grown V_2O_5 yields good quality films but the reduction conditions are often governed by very narrow operating conditions which makes VO_2 synthesis by ALD difficult. Nevertheless, considerable amount of research has been performed by the group of Detavernier at Ghent university and significant advances were reported [100–103] for the growth of high quality VO_2 films by ALD using relatively new kind of precursors such as tetrakis(ethylmethylamino) vanadium [TEMAV], tetrakis(dimethylamino)vanadium, [TDMAV], and tetrakis(diethylamino)-vanadium [TDEAV]. [104,105]

2.5 Chemical vapour deposition CVD

Chemical vapor deposition (CVD) is a common industrial process for depositing high quality and high-performance thin films. In a typical CVD process, the wafer (substrate) is exposed to one or more volatile precursors, which react and/or decompose on the surface to produce the desired deposit. Volatile by products are removed by gas flow through the reaction chamber.

2.5.1 Precursor selection

Precursor choice is a main factor in determining the chemistry of the films obtained by CVD and given below are a non-exhaustive list of commonly used precursors and process conditions used by various authors to grow vanadium oxide films.

2.5.1.1 Inorganic Vanadium Compounds

Manning et al. [106] reported the growth of V_2O_5 at 450–520°C, while VO_2 grew above 500°C. With respect to organometallic vanadium precursors, VCl_4 was found to yield vanadium oxide thin films that showed improved surface smoothness and very acceptable thermochromic properties. Vanadium oxynitrate, $VO(NO_3)_3$, was also implemented as a highly volatile single-source precursor to grow pure V_2O_5 at 350–500°C. Polycrystalline V_2O_5 coatings without preferred orientation were reported at 550–600°C in both cases. Field and Parkin [107] have reported on the CVD of vanadium oxide, under atmospheric

pressure, starting from chlorinated vanadium precursors, $VOCl_3$ and VCl_4. The authors noticed that the thermolysis of $VOCl_3$ or VCl_4 does not allow the production of coatings up to 600°C. The reaction of water vapour with VCl_4 yields coatings starting at 450°C, while $VOCl_3$ allows the growth in the entire investigated temperature range. A focus has been given to the $VOCl_3$/water system under atmospheric pressure by Manning and Parkin [108]. The reaction of water vapor with $VOCl_3$ already occurs at room temperature to yield amorphous vanadium oxide. The obtained amorphous thin films were converted to crystalline V_2O_5 upon heating above 240°C. [109] The authors reported the dominant formation of VO_2 above 600°C in the case where the reactive gas contains an excess of water vapor, while the V_2O_5 phase prevails in the presence of an excess of $VOCl_3$ and/or at low deposition temperatures. The deposition of VO_2 was also reported starting from the reaction of $VOCl_3$ with water vapor at 650°C.

2.5.1.2 Vanadium Beta-diketonates Compounds

Metal acetylacetonate solutions like $V(acac)_3$ and $VO(acac)_2$, were intensively investigated for CVD processes under atmospheric and reduced pressures. Vernardou et al. [110] noted the formation of VO_2 using $VO(acac)_2$ in methanol at 450°C.The reaction of $VO(acac)_2$ with molecular oxygen under PECVD conditions has allowed the growth of highly oriented V_2O_5 thin films at temperatures as low as 200°C. [111] The use of a vanadyl acetylacetonate precursor, $VO(acac)_2$, with ethanol at growth temperatures from 525 to 530°C results in VO_2. [112,113] The reaction of $VO(acac)_2$ with molecular oxygen at 500°C [114,115] results the formation of crystalline V_2O_5.

2.5.1.3 Vanadium Alkoxide Compounds

Vanadium alkoxides [116,117] have been reported as efficient single-source precursors for the synthesis of vanadium oxide films. Mathur et al. [117] have reported on the grown phases starting from the thermal decomposition of vanadium oxo-tri-isopropoxide ($VO(OiPr)_3$) under reduced pressure. The authors

reported the formation of a single-phase coating of V_2O_5 at 500°C. A single phase of V_7O_{13} was obtained at 600°C, while VO_2 was grown at 700°C.

Louloudakis et al. [116] reported atmospheric pressure (AP)CVD using $VO(OiPr)_3$ as a single-source precursor at 300°C. Films obtained were identified as having V_2O_5 nano-crystals embedded in an amorphous vanadium oxide matrix. Films grown below 150°C were identified as monoclinic VO_2.

Amorphous vanadium oxide, with high performance for lithium batteries, was grown at 105°C using the reaction of $VO(OiPr)_3$ with water vapour. [118] Crociani et al. [119] have investigated $VO(OiPr)_3$ and reported the possibility of growing either VO_2 or V_2O_5 at 550°C by adjusting the water and oxygen ratio as the reactant gas. The CVD of V_2O_5 was reported starting from $VO(OiPr)_3$, [120] and $VO(OC_3H_7)_3$ resulting in the growth of V_2O_5 and V_6O_{13} thin films at 350–400°C. [121]

3. Experimental

The experimental aspects of this research are presented in this section. We discuss the thin film deposition techniques, starting with the basics of chemical vapour deposition and then discuss the Vanadium oxide film synthesis performed on the custom-built reactor nicknamed “sputnik” followed by the industrial scale reactor named MC200 and finally about ALD.

Followed by thin film characterisation techniques used primarily in the analysis of purity, morphology and the SMT behaviour of various vanadium oxide phases obtained. These include X-ray diffraction (XRD), Raman scattering, profilometer, electrical sheet resistance measurements and Scanning electron microscopy (SEM). Followed by the discussion on characterizing the SMT and thermochromic properties of VO_2 and V_2O_5 by optical methods using UV-VIS spectroscopy and Infrared imaging by thermal camera.

3.1 Film Deposition techniques

3.1.1 Chemical Vapour Deposition. (CVD)

Chemical vapor deposition is a synthesis process in which the chemical constituents react in the vapor phase near or on a heated substrate to form a solid deposit. The number of chemical reactions used in CVD is considerable and include thermal decomposition (pyrolysis), reduction, hydrolysis, disproportionation, oxidation, carburization, and nitridation. These reactions can be activated by several methods. The most important are as follows:

Thermal activation: This takes place at high temperatures i.e., 400 -900°C, although the temperature can also be lowered considerably (300-500°C) if metal organic precursors are used (MOCVD).

Plasma activation: That typically takes place at much lower temperatures, i.e., 300–500°C but use plasma to activate the reactant species

Photon activation: Uses shortwave ultraviolet radiation, which can occur by the direct activation of a reactant or by the activation of an intermediate.

A CVD reaction is governed by thermodynamics, that is the driving force which indicates the direction the reaction is going to proceed (if at all), and by kinetics, which defines the transport process and determines the rate-control mechanism, in other words, how fast it is going. Chemical thermodynamics is concerned with the interrelation of various forms of energy and the transfer of energy from one chemical system to another in accordance with the first and second laws of thermodynamics. In the case of CVD, this transfer occurs when the gaseous compounds, introduced in the deposition chamber, react to form the solid deposit and by-products gases.

Growth mechanisms

During deposition, adatoms interact with the substrate surface and/or with others adatoms. The strength of interactions defines the growth mechanism of the films, figure 10 shows a schematic of all the models described below.

Volmer-Weber (Island Model)

Three-dimensional growth occurs when adatoms interact preferentially with each other than with the surface. This results in the formation of adatom clusters or islands leading to the growth of rough films over the substrate surface.

Van Der Merwe (Layer by layer model)

Two-dimensional growth occurs when adatoms attach preferentially to the surface sites resulting to the growth of thin-films via layer by layer mechanism (a homogeneous film is formed prior to the growth of any subsequent layer).

Stransky-Krastanov Mechanism (Mixed Model)

A last growth mode involves both Wolmer-Weber and Van der Merwe mechanisms A two-dimensional growth occurs until a critical layer thickness (depending on the surface energy, the lattice parameters of both substrate and film…) is reached. Then, the three-dimensional growth takes place.

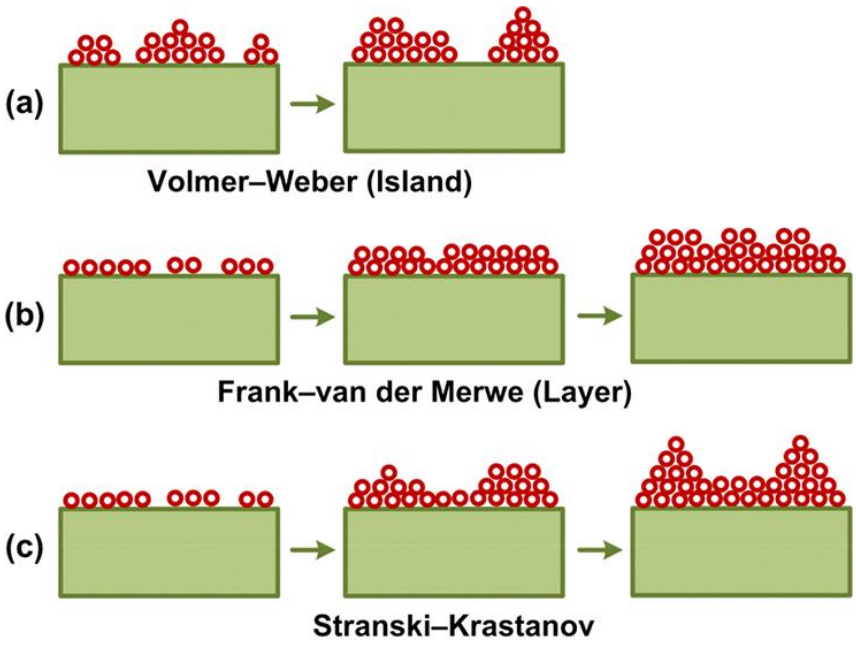

Figure 10: Different thin film growth mechanisms. (a) island growth model, (b) the layer by layer model, and (C) the mixed growth model. [1]

The first step of a theoretical analysis is to ensure that the desired CVD reaction will take place. This will happen if the thermodynamics is favourable, that is if the transfer of energy—the Gibbs free energy change of the reaction (ΔGr) is negative. To calculate ΔGr, it is necessary to know the thermodynamic properties of each component, specifically their free energies of formation (also known as Gibbs free energy), ΔGf. The following equation expresses the relationship:

$$\Delta Gr = \sum \Delta G\ products - \sum \Delta G\ reactants$$

The free energy of formation is not a fixed value but varies as a function of several parameters which include the type of reactants, the molar ratio of these reactants, the process temperature, and the process pressure. The following equation represents this relationship:

$$\Delta G G_r = \Delta G_f + RT \ln K$$

Where ΔG_f is standard free energy of the formation of species, R is the gas constant and T is absolute temperature and K is the equilibrium constant.

As thin films grow, they follow the Gibbs free energy principle. The free energy rule states that the total free energy of a system decreases with increasing size of particles. This leads to the growth pattern described in the figure 11. First, particles nucleate. Next, the individual nuclei grow. As they increase in size, the individual nuclei begin to impinge on each other. The overall system lowers the free energy through coalescence. As growth continues, the remaining area forms channels, leading to a continuous film.

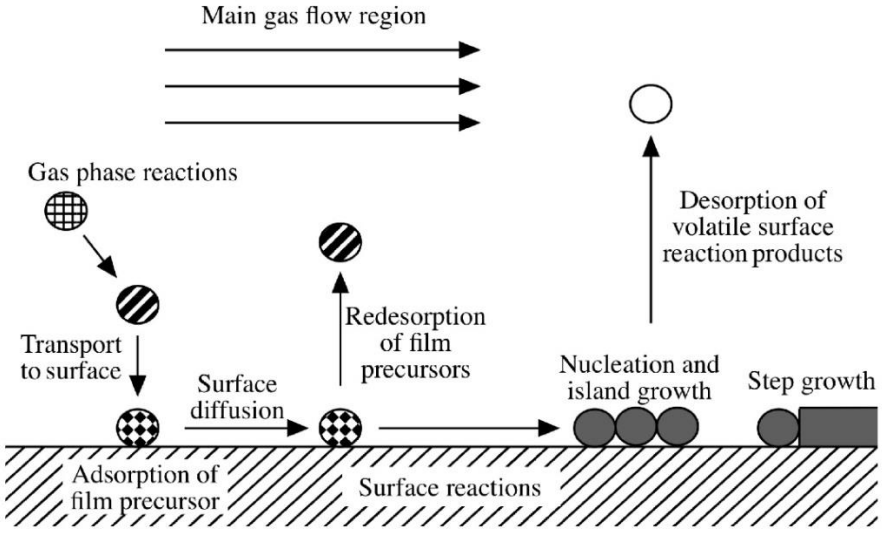

Figure 11 : An overview of the various stages of film growth over the surface in a CVD process.[2]

A normal CVD process involves complex flow dynamics since gases are flowing into the reactor, reacting, and then by-products are exhausted out of the reactor. The sequence of events during a CVD reaction is are as follows:

- Precursor gases input into the chamber by pressurized gas lines.
- Mass transport of precursors from the main flow region to the substrate through the boundary layer
- Adsorption of precursors on the substrate
- Chemical reaction on the surface
- Atoms diffuse on the surface to growth sites.
- Desorption of by-products of the reactions
- Mass transport of by-products to the main flow region

During CVD the growth rate of the film is limited by either surface reaction kinetics, mass transport (diffusion) of precursors to the substrate, or the feed rate of the precursors.

Rate-Limiting Steps: CVD growth is controlled by rate limiting steps. The rate-limiting step is generally determined by either the surface reaction kinetics or by mass transport. A deposition limited by mass transport is controlled by the diffusion of reactants through the boundary layer and diffusion of by-products out of the boundary layer. Mass transport limits reactions when the temperature and pressure are high. These conditions increase the thickness of the boundary layer and make it harder for gases to diffuse through. In addition, decomposition of the reactants is typically quicker since the substrate is at a higher temperature. When mass transport limits the growth, either increasing the gas velocity or rotating the substrate during growth will decrease the boundary layer and increase the growth rate. In the mass transport limited growth regime increases in reactant concentrations will to a point increase the deposition rate. However, at very high reactant concentrations, gas phase nucleation will occur and the growth rate will drop. Slow deposition in a CVD reactor can often be attributed to either gas phase nucleation, precursor depletion due to hot walls, thick boundary layer formation, low temperature, or low precursor vapour pressure.

Precursor flow rate limits the deposition when nearly all the reactant is consumed in the chamber. The flow rate is more important for a hot wall reactor since the heated walls will decompose a large amount of the precursor. Cold wall reactors tend to have higher deposition rates since the reactants are not depleted by the walls.

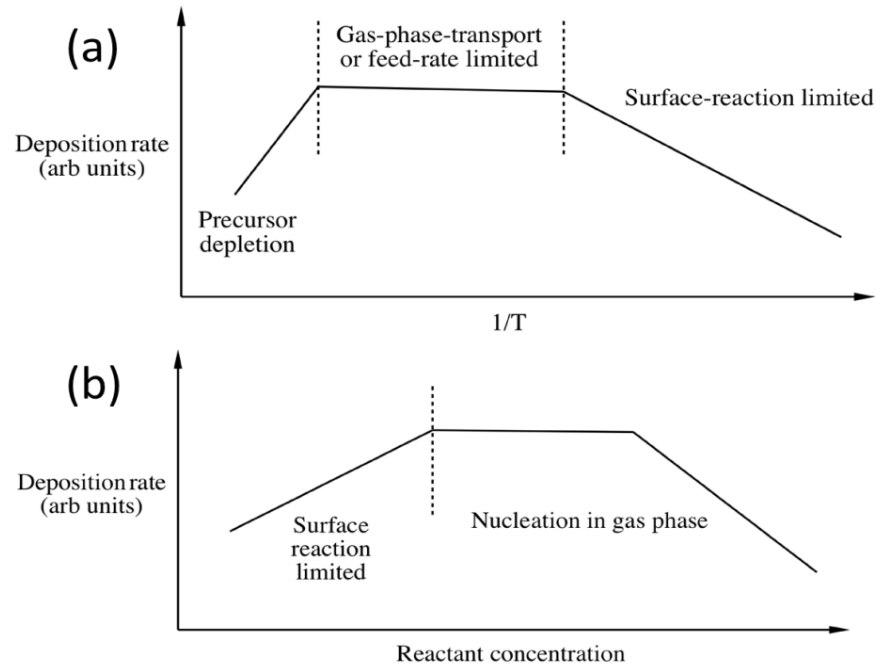

Figure 12: (a) Dependence of CVD deposition rate on temperature and (b) Demonstration of deposition rate on reactant concentration for CVD deposition [3,4]

A plot of growth rate versus temperature, known as an Arrhenius plot, can be used to determine the rate limiting step of a reaction (Figure 12a). Mass transport limits reactions at high temperatures such that growth rate increases with partial pressures of reactants, but is constant with temperature (Figure 12b). Surface reaction kinetics dominates at low temperatures where the growth rate increases with temperature, but is constant with pressures of reactants. Feed rate limited reactions are independent of temperature, since it is the rate of gas delivery that is limiting the reaction. The Arrhenius plot will show where the transition between the mass transport limited and the surface kinetics limited growth occurs in the temperature regime.

In CVD, the reactor configuration also plays a vital role in determining the type of films that one would want to grow. [5] A reactor is a chamber made of a material that does not react with the chemicals being used. It must also withstand high temperatures. This chamber is composed by reactor walls, liner, a susceptor, gas injection units, and temperature and pressure control units. Usually, the reactor walls are made from stainless steel or quartz. Ceramic or special glasses, such

as quartz, are often used as the liner in the reactor chamber between the reactor wall and the susceptor. A substrate sits on a susceptor which is at a controlled temperature.

In a hot-wall CVD, entire chamber is heated as depicted in figure 13 (a). This may be necessary for some gases to be pre-cracked before reaching the wafer surface to enhance their reactivity. Reactors can be constructed either vertically or horizontally and the configuration is decided based on the desired nature of flow. However, reactions usually occur on the walls, and, in most cases, the fraction of the surface area of the reactor covered with deposit can vary and lead to problems when reproducing deposition conditions. In addition, homogeneous gas-phase reactions in the heated gas can occur, which can lead to reduced deposition rates, particle formation and loss of selectivity. For these reasons, hot-wall reactors are used primarily at the laboratory scale to study a given precursor for CVD. They are also used to determine reaction-product distributions because the large heated surface area can consume the precursor completely and provide high yields of the reaction products.

Another type of reactor used to carry out MOCVD is a cold-wall reactor. Where the substrate is supported by a pedestal which acts as a susceptor. The pedestal/susceptor is the primary origin of heat energy in the reaction chamber. Along with the susceptor, the walls of the column are heated to prevent precursor condensation, without impacting the film growth. In contrast the hot wall reactor, the walls of the reaction chamber in a cold-wall reactor are typically made of quartz which is largely transparent to the electromagnetic radiation. The reaction chamber walls in a cold-wall reactor in figure 13 (b), however, may be indirectly heated by heat radiating from the hot pedestal/susceptor, but will remain cooler than the pedestal/susceptor and the substrate the pedestal/susceptor supports.

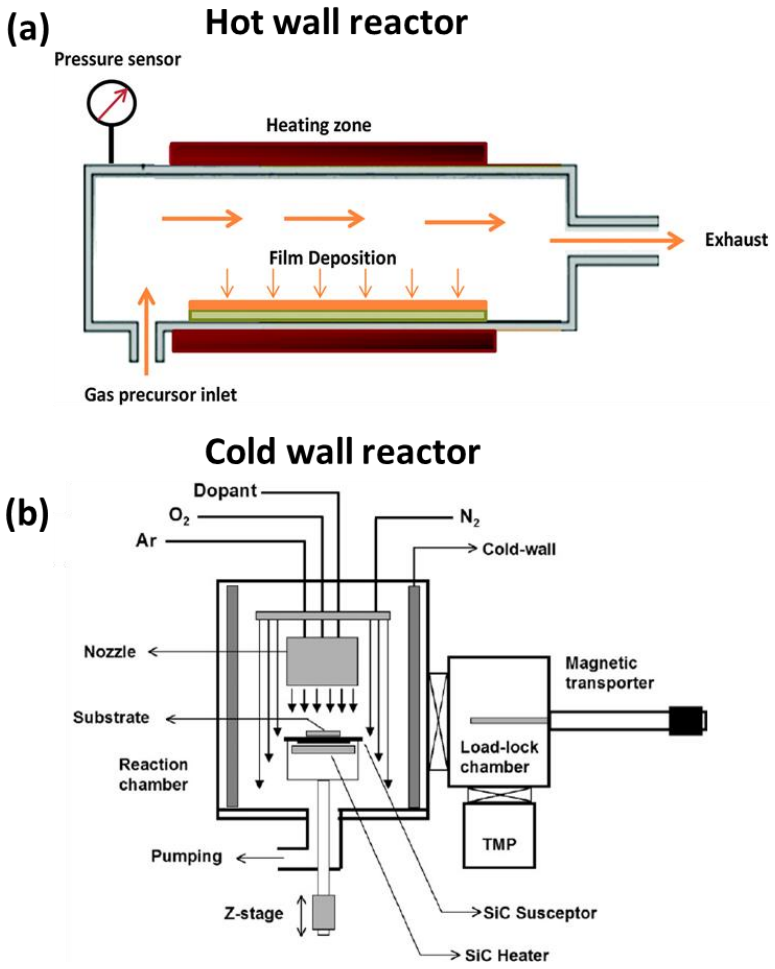

Figure 13: Schematic diagram of (a) hot wall reactor and (b) a cold walled reactor.

The "sputnik" CVD Reactor

For this work, thin films of VO_2 and V_2O_5 were primarily grown using a custom built MOCVD reactor nicknamed the "Sputnik" with direct liquid injection using a programmable injectors for the precursor delivery. The reactor as shown in figure 14 has four input injectors for precursor delivery. Precise precursor delivery is controlled by setting the injection frequencies and opening times. Rapid vaporisation of the liquid precursor is achieved by maintaining the injectors at 200°C. A vertical heated transport column directs the gas phase reactants perpendicularly over the silicon substrate with the help of an inert carrier gas like N_2 or Ar. The silicon substrate lies on top of the heating plate at elevated temperatures. Since the transport column is maintained at 250°C, we can

essentially call this setup as a warm walled reactor as opposed to a cold or a hot walled reactor.

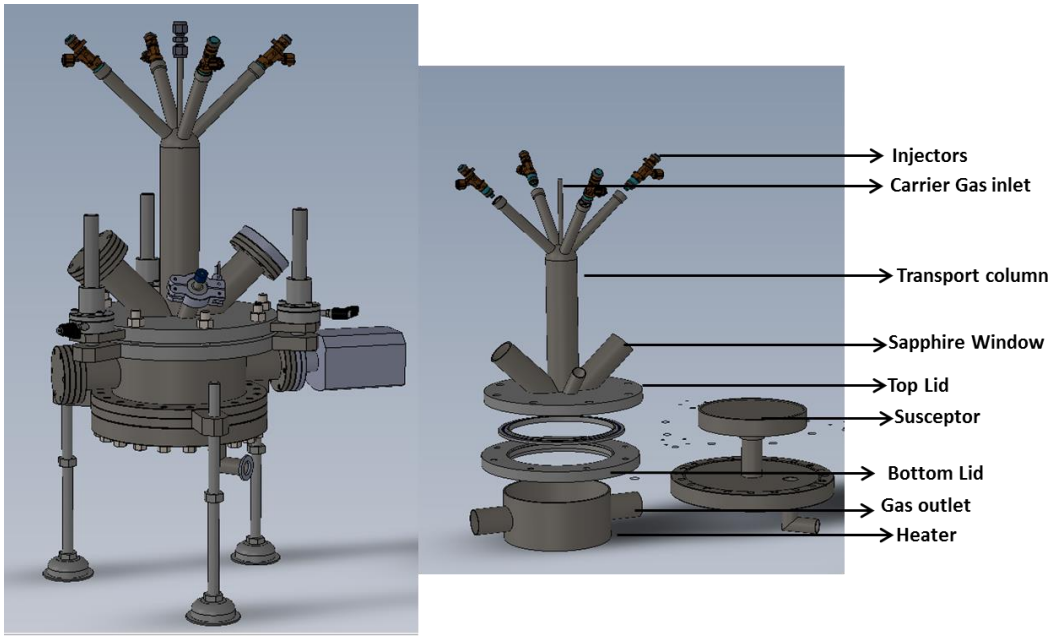

Figure 14: Computer aided drawing of the CVD reactor labelled with each constituent part.

The quantity of liquid or solution injected/delivered per unit time through the injector is only what is required per unit time for the process and this is adjusted based on the required liquid flow rate. The chemical precursor remains at room temperature as long as it is not required to be vaporized for the process which is advantageous for temperature sensitive precursors. Film deposition can be carried out in a wide range of temperatures ranging from 250 to 600°C at an operating base pressure of as low as 1.2 mbar.

DLI vaporizers can handle both liquid and solid ALD and CVD precursors. Solid precursors need to be dissolved in organic solvents. The technology is a particularly well suited method for low vapour pressure and poorly thermally stable liquid or solid ALD and CVD precursors.

Advantages of DLI:

Precise measurement and control of the precursor quantity injected in the vaporizer per unit time and by consequence precise control of the vapour flow that is generated

Fast vapour flow control ON-OFF

Capability to operate under vacuum or at atmospheric pressure

Precursor container remains at room temperature: no precursor thermal decomposition overtime, limited safety issues, easy and quick container refill/replacement

Best approach to generate stable vapours flow when solid precursor is used.

Best approach to vaporize low vapour precursors and thermally sensitive precursor while minimizing precursor thermal decomposition

Sequential injection achieves accurate control of doping levels.

The Annealsys MC200

The MC200 is an industrial grade MOCVD reactor based on DLI technique. It has several additional benefits compared to the small-scale reactor mentioned above. Some key advantages of the MC200 are as follows.

- Large area of deposition, up to 8” wafers.
- Distance from the substrate and the injection can be varied. This helps in optimizing the film characteristics.
- Ability to introduce sample rotation, to aid in better uniformity of the films.
- Can reach significantly lower pressures (10^{-5}mbar)
- Stainless steel thermally controlled chamber
- Rotating Substrate holder with vertical motion and heating substrate holder up to 800°C
- Optional capacitive plasma
- Up to 4 direct liquid injection vaporizers
- Vacuum and pressure control

A schematic of the reactor is show in figure 15, displaying all the vital entities of the MOCVD reactor, a photograph of the reactor in full is show in figure 16.

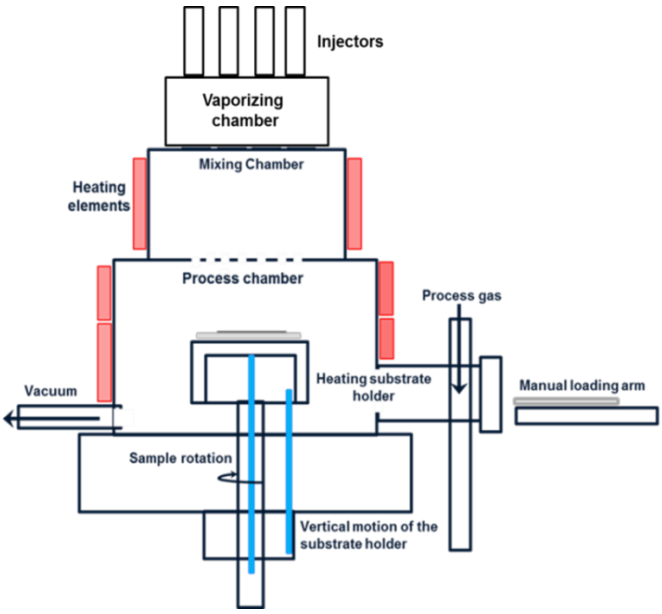

Figure 15 Schematic diagram of the MC200 MOCVD reactor used to grow wafer scale VO_2 films.



Figure 16 Photograph of the Annealsys MC200 MOCVD reactor at LIST.

3.1.2 Atomic Layer Deposition (ALD)

Atomic Layer Deposition (ALD) is a thin film deposition method in which a film is grown on a substrate by exposing its surface to alternate gaseous species (typically referred to as precursors). [122,123] In contrast to chemical vapour deposition, the precursors are never present simultaneously in the reactor, but they are inserted as a series of sequential, non-overlapping pulses as shown in figure 17. In each of these pulses the precursor molecules react with the surface in a self-limiting way, so that the reaction terminates once all the reactive sites on the surface are consumed.

The primary advantages of ALD are all derived from the sequential, self-saturating, gas-surface reaction control of the deposition process. Firstly, the conformity of ALD-deposited films is often the critical factor in choosing ALD over competing deposition techniques such as CVD or sputtering. Conformity of high aspect ratio and three dimensionally-structured materials is made possible by its self-limiting characteristic, which restricts the reaction at the surface to no more than one layer of precursor.

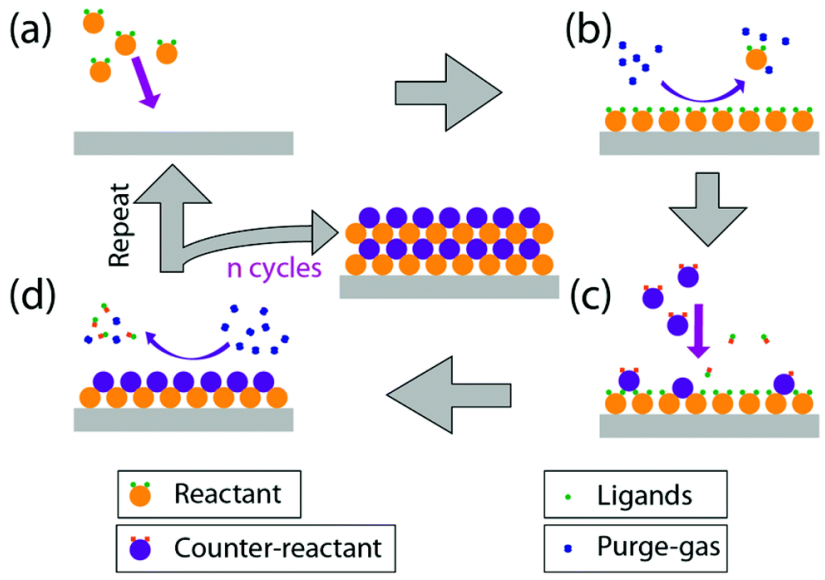

Figure 17 A typical ALD cycle is demonstrated. (a) Reactant is chemisorbed on the substrate till saturation occurs. (b) Excess unreacted reactants are purged away. (c) The, coreactant is pulsed and reacts with surface. (d) Excess coreactant and by-products are purged away with inert purge gas.

With sufficient precursor exposure times, the precursor can reach into deep trenches, allowing for complete reaction with the entire surface. Subsequent cycles allow for uniform growth on high aspect ratio structures, whereas CVD and PVD may suffer from non-uniformity due to faster surface reactions and shadowing effects, respectively.

Process and coating properties

Excellent adhesion: Chemisorption of precursors with the surface provides excellent adhesion.

Saturation: Self–terminating surface reactions enable automatic processing and eliminate the need for over–precise dosing and continuous operator attendance.

Sequential: Digital–like sequential growth provides excellent accuracy without the need for extensive in situ feedback or operator attendance.

Surface–controlled reactions: Surface reactions enable unconditionally conformal coatings, regardless of if the substrate is dense, porous, and tubular, a powder or otherwise complex in shape.

Precise and reliable: Film growth thickness during a single ALD cycle is process specific, but typically about 1 Å (0.1 nm).

Thin, dense, and smooth: ALD enables depositing layers less than one nanometre in thickness.

3.1.3 Synthesis of VO_2 films

Case I (Sputnik)

Thin films of VO_2 were deposited on silicon substrates by DLI–MOCVD in a vertical warm wall stagnation point flow reactor (Sputnik). Low concentration (5 10^{-3} M) ethanol solutions of 99.9% pure Vanadium oxy-tri-isopropoxide ($[VO(O^iPr)_3]$ were used as the precursor. Liquid injection was performed in an evaporation tube maintained at 200 ^oC to secure an instantaneous vaporization of the precursor solution. Substrates were maintained at a constant temperature within the 400–600 ^oC range during deposition. The precursor injection was

maintained at 4 Hz with 2 ms opening time resulting in a liquid flow rate of 2.5 ml min^{-1}. Nitrogen was used as the carrier gas with a flow rate, 40 sccm and the chamber pressure being adjusted in the 3–9 mbar range. Time of deposition was adjusted from 15 to 180 min allowing the growth of different film thicknesses. Substrates were allowed to cool to room temperature in nitrogen atmosphere under vacuum before withdrawing from the chamber and no post deposition annealing was performed. All the samples were handled in air after deposition.

Case II (MC200)

Films of vanadium oxide were deposited on silicon substrates using direct liquid injection MOCVD (MC200 from Anneal Sys), which is a stagnation point-flow warm-walled reactor. Cyclohexane solution containing $5x10^{-3}$ mol/l of vanadium (V) oxy-tri-isopropoxide was used as a single-source precursor, which was maintained under nitrogen atmosphere at room temperature before its injection into the evaporation chamber at a frequency of 2 Hz and an adjusted opening time to reach a feeding rate of 1 g/min. The pressure and temperature of the evaporation chamber were maintained at 0.6 mbar and 200°C during deposition respectively, whereas the walls of the reactor were maintained at 200°C. During the growth, 500 sccm of nitrogen carrier gas was introduced alongside the precursor injection and the total pressure of the reactor was automatically regulated at 0.6 mbar. The substrate is maintained at 600°C during the 2 hours of deposition and the subsequent heat treatments.

Furthermore, an hour-long annealing was performed at 600°C right after the deposition under oxygen partial pressure of $1x10^{-2}$ mbar. The sample is then further subjected to annealing at the same temperature under vacuum (~ 0.6 mbar) acting as a reducing atmosphere for 4 hours, after which the chamber is allowed to cool down. All depositions were carried out on 4-inch silicon wafers without removing the upper native oxide layer that might act as a barrier. Samples were later cut into smaller pieces for analysis purposes. Uniform, high quality VO_2 films were observed throughout the wafers in a homogeneous manner.

3.1.4 Synthesis of V_2O_5 films

V_2O_5 films were synthesized by oxidising the as deposited VO_2 films in presence of O_2 atmosphere or by annealing the VO_2 films above 300^oC in ambient atmosphere. The appearance of yellow colour upon oxidation confirms the presence of V_2O_5. A series of Cr-doped V_2O_5 thin films was also grown by the implementation of mixed precursor feedstock with adjusted Cr/V ratio. Doping V_2O_5 films with Cr was achieved by simply mixing at various dilutions a 5 mm ethanol solution of chromium acetylacetonate, $Cr(acac)_3$, into the vanadium precursor used for the MOCVD deposition.

Post deposition thermal treatment

After VO_x deposition, samples were allowed to cool till room temperature in argon atmosphere at low pressure before withdrawing from the chamber. Further handling of the samples was carried out under ambient atmosphere. Post deposition annealing was performed under ambient air at 300-580^oC. The annealing time was adjusted to allow a complete oxidation from VO_x to V_2O_5. While 10 min were sufficient for oxidation at 550^oC, significantly longer times were required at lower temperatures; this can be explained by simple temperature dependent oxidation kinetics.

3.1.5 Atomic layer deposition of Al_2O_3 on V_2O_5 coatings.

V_2O_5 has a layered structure with a large affinity towards accommodating guest molecules between the interlayer spaces. This property of V_2O_5 has made it an ideal candidate for many applications like gas and humidity sensing, energy storage and catalysis. To prove that thermochromism in V_2O_5 is an intrinsic property, and that it does not depend on the atmospheric conditions, we isolated the coatings from ambient atmosphere. The passivation was performed using the established ALD of Al_2O_3. All the samples were coated with a 20 nm of Al_2O_3 oxide. In addition to encapsulation, Al_2O_3 would also act as a protection layer by making V_2O_5 scratch resistant and prevent from aging via a change of the oxygen deficiency.

ALD of Al_2O_3 was performed using the sequential introduction of Trimethylaluminum (TMA) and water. The pulse times for each reactant were adjusted to 40 ms with a 15-sec purge in between each pulse. The rather large pulse and purge times were chosen to achieve complete conformal coverage over the film. ALD was carried out at 120° C under partial pressure of 2 mbar and Argon was used as the carrier gas at a flow rate of 50 sccm.

3.2 Thin film characterisation techniques

3.2.1 Scanning electron microscopy (SEM).

The scanning electron microscope (SEM) [124,125] uses a focused beam of high-energy electrons to scan the surface. This electron beam is produced at the top of the column, accelerated downward and passed through a combination of lenses and apertures to the sample. The sample is mounted on a stage in the chamber area and, both the column and the chamber are evacuated by a combination of pumps. Figure 18 (a) and (b) shows the schematic and photographic image of a scanning electron microscope.

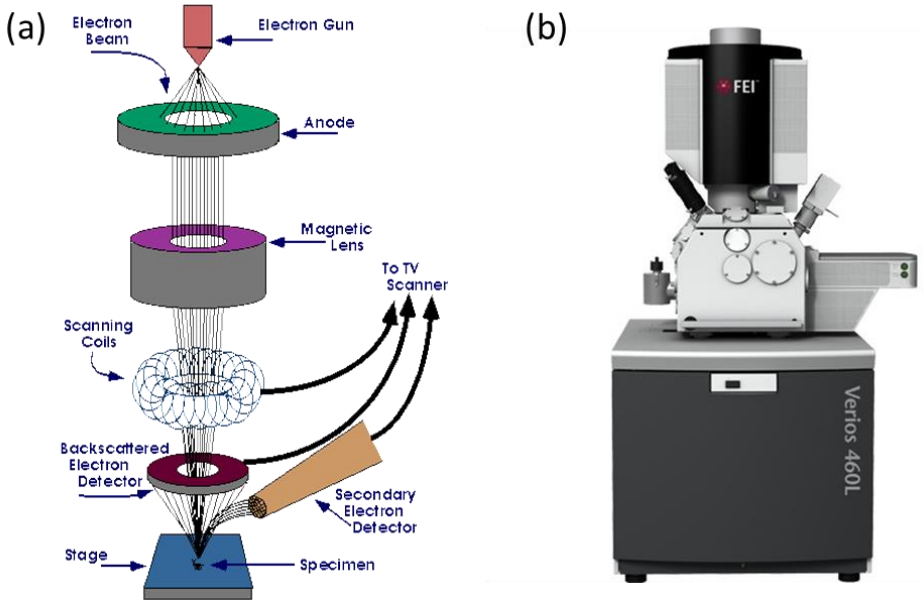

Figure 18 Detailed schematic of the working principle of a scanning electron microscope and (b) a photographic image of the SEM used for analysis in this study.

The signals that derive from beam-sample interactions reveal information about the sample including external morphology (texture), chemical composition, and crystalline structure and orientation of materials making up the sample. In most applications, data are collected over a selected area of the surface of the sample, and a 2-dimensional image is generated that displays spatial variations in these properties. Areas ranging from approximately 1 cm to 5 microns in width can be imaged in a scanning mode using conventional SEM techniques. An example of surface and cross section SEM images are shown in figure 19. Here two different morphologies are observed as a result of growing the films with two distinct precursor concentrations. Such morphological information is crucial in determining the final properties of thin films.

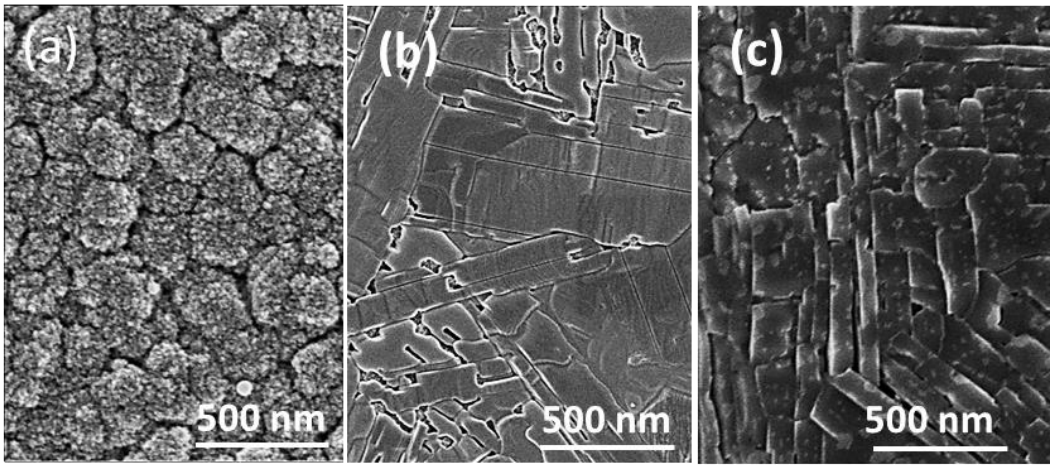

Figure 19: Surface SEM micrographs of the as deposited VO_X film (a) with a nanocrystalline morphology. (b) & (c) show the surface micrographs of V_2O_5 and VO_2 formed after oxidation and reduction treatments respectively.

When the electron beam interacts with a sample in a SEM, multiple events occur as shown in figure 20. In general, different detectors are needed to distinguish secondary electrons, backscattered electrons, or characteristic x-rays. Depending upon the accelerating voltage and sample density, the signals come from different penetration depths. After Auger electrons, the secondary electrons come from the next most shallow penetration depth. A secondary electron detector (SED), is used to produce a topographic SEM image. SED images have high resolution that are independent of the material and are acquired from in-

elastically scattered electrons close to the surface. No material composition information is available. A backscattered electron detector (BSD) detects elastically scattered electrons. As the intensity of backscattering is proportional to the mean atomic number, images developed from them involve information on variations in sample composition.

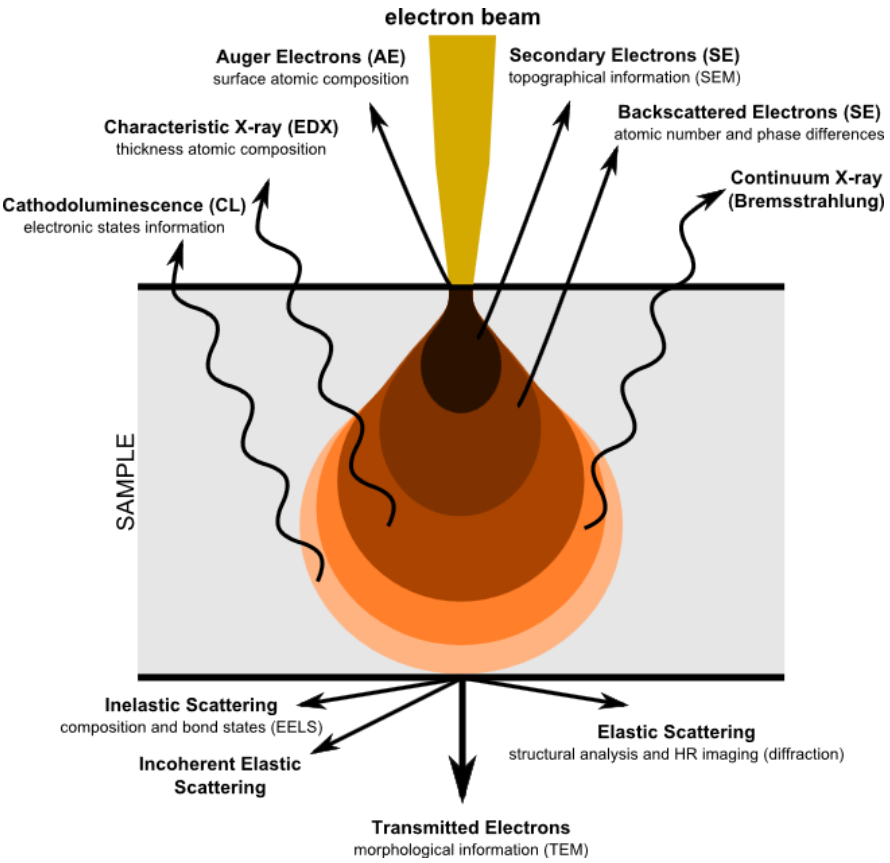

Figure 20: Schematic of various kinds of interactions occurring when electron beam is incident on a sample.

Charging effect [126–128] - When the number of incident electrons is greater than the number of electrons escaping from the specimen, then a negative charge builds up at the point where the beam hits the sample. This phenomenon is called charging and it causes a range of unusual effects such as abnormal contrast and image deformation and shift. Sometimes a sudden discharge of electrons from a charged area may cause a bright flash on the screen. These make it impossible to capture a uniform image of the specimen and may even be

violent enough to cause small specimens to be dislodged from the mounting stub. The level of charge will relate to (1) the energy of the electrons and (2) the number of electrons. The energy of the electrons is related to the kV (i.e. high kV = high energy) so reducing kV can reduce charging. The number of electrons relates to many parameters including, beam current, the emission level of the gun, the spot size, and the apertures between the gun and the specimen. So reducing the current density by adjusting these parameters can also reduce charging.

In scanning electron microscopy, x-rays are emitted when the electron beam displaces an inner shell electron that is replaced by an outer shell electron. [129–131] Because each element has a unique energy difference between outer and inner electron shells, the x-rays that are detected yield elemental identification. The atoms are ionized by the primary electron beam leading to holes generated on the core shells; following ionization the electrons from outer shells fill the holes and cause the emission of X-ray fluorescence lines. The characteristic X-ray lines are named according to the shell in which the initial vacancy occurs and the shell from which an electron drops to fill that vacancy. Electron dispersive spectrum (EDS) data can be obtained at a point, along a line or mapped over an area.

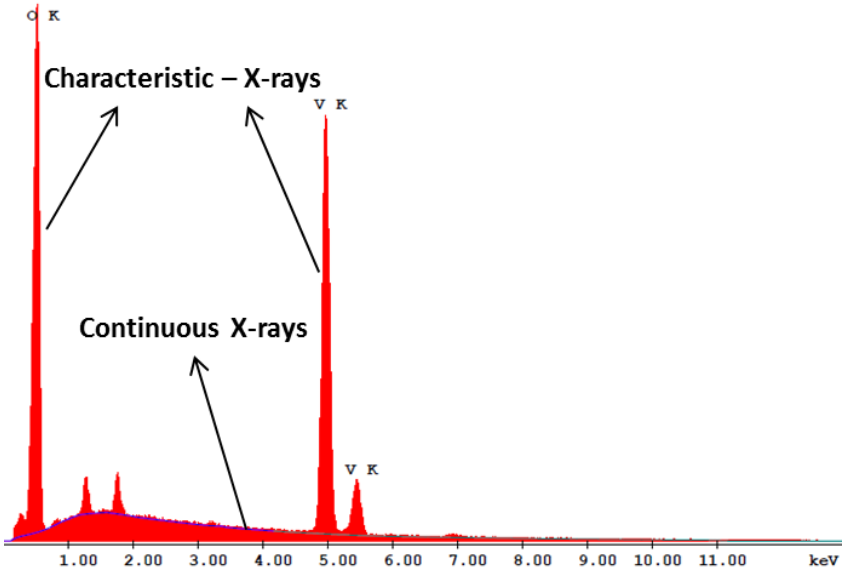

Figure 21: An EDX spectra of VOx films showing both characteristic and continuous X rays.

Electron Back Scatter Diffraction

Electron backscatter diffraction (EBSD) is a microstructural-crystallographic characterisation technique to study any crystalline or polycrystalline material. The technique involves understanding the structure, crystal orientation and phase of materials in the Scanning Electron Microscope (SEM). [132–134] Typically it is used to explore microstructures, revealing texture, defects, grain morphology and deformation. It can be combined with complementary techniques within the SEM for phase discrimination.

EBSD can be used to find the crystal orientation of the material located within the incident electron beam's interaction volume. Scanning the electron beam in a prescribed fashion results in a microstructural maps. These maps can spatially describe the crystal orientation of the material being interrogated and can be used to examine micro texture and sample morphology. The maps give information about grain orientation, grain boundary and diffraction pattern.

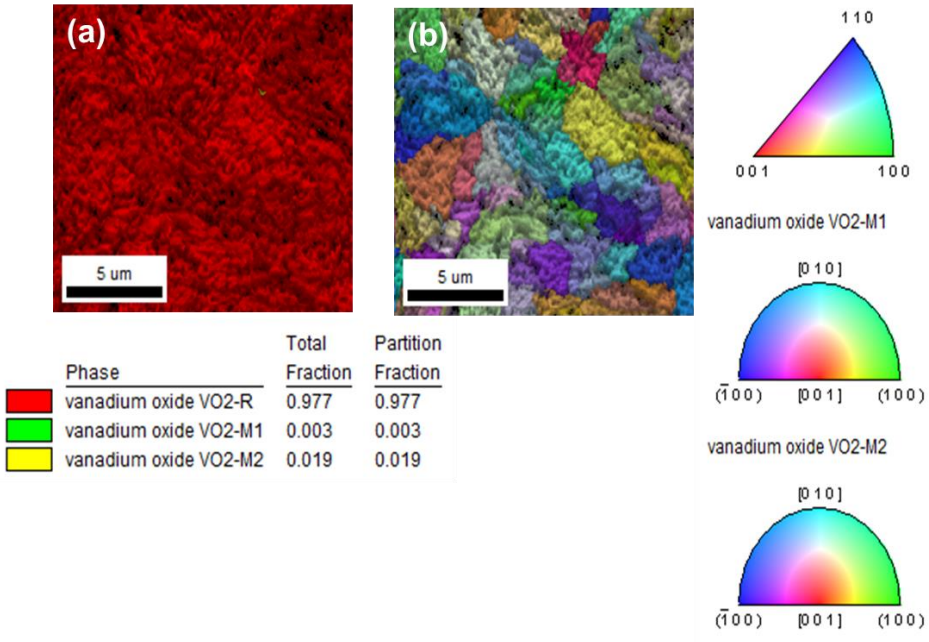

Figure 22: EBSD analysis of VO_2 films showing (a) surface phase map and (b) colour coded crystallographic orientations. It is clearly seen here from (a) that the film is majorly composed of R phase.

VO_2 films were studied by EBSD to map the texture, phase distribution and the crystallographic orientation of the domains. Temperature dependent imaging was also performed in the anticipation to distinguish between the room temperature M1 and high temperature R phase along with the intermediate M2 phase. However, as shown in the figure 22, VO_2 films featured just the “R” phase throughout. This observation could be attributed to the intrusive character of electron beam, which facilitates SMT switches the area under exposure to R phase, thus making the analysis inconclusive.

3.2.2 Profilometer.

Profilometer is used to measure a surface's topography in terms critical dimensions as step, curvature, flatness. A diamond stylus is moved vertically to touch the surface and then moved laterally across the sample for a specified distance. A force feedback enables operating at the specific contact force. While it provides height in Z resolution, a profilometer is sensitive to contamination and might be destructive on soft surfaces.

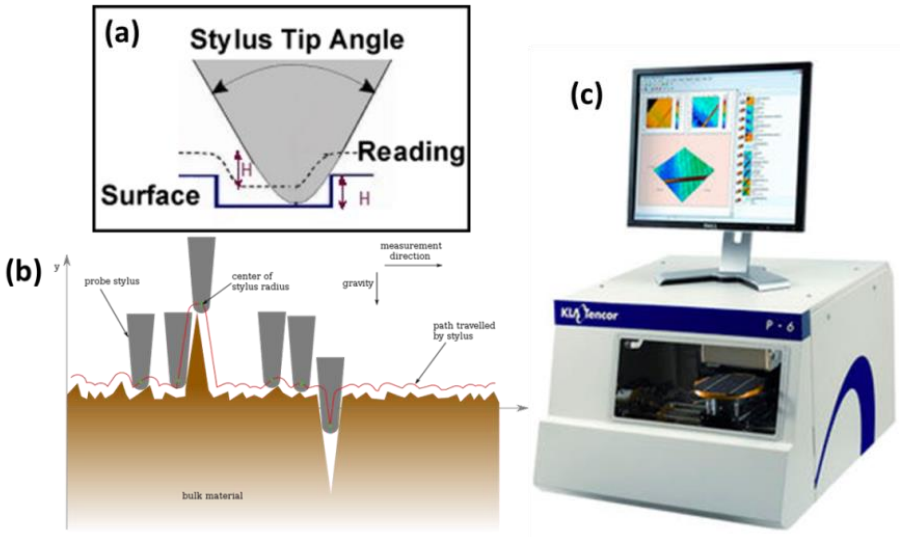

Figure 23: (a) Basic operating principle of a stylus based profilometer, (b) the operation of measuring a surface topography using a contact based stylus profilometer and (c) and photograph of the KLA Tencor table top profilometer used to measure film thickness in this study.

As shown in figure 23, a profilometer measures surface variations in vertical stylus displacement as a function of position. A typical vertical features ranging in height from 10 nanometres to 1 millimetre can be probed. The height position of the diamond stylus generates an analog signal which is converted into a digital signal, stored, analysed, and displayed. The radius of diamond stylus ranges from 20 nanometres to 50 µm, and the horizontal resolution is controlled by the scan speed and data signal sampling rate. The stylus tracking weight can range from less than 1 to 50 milligrams. Profilometer can be used for measuring surface roughness and topography as well as thickness of the film by step height measurement. (figure 24)

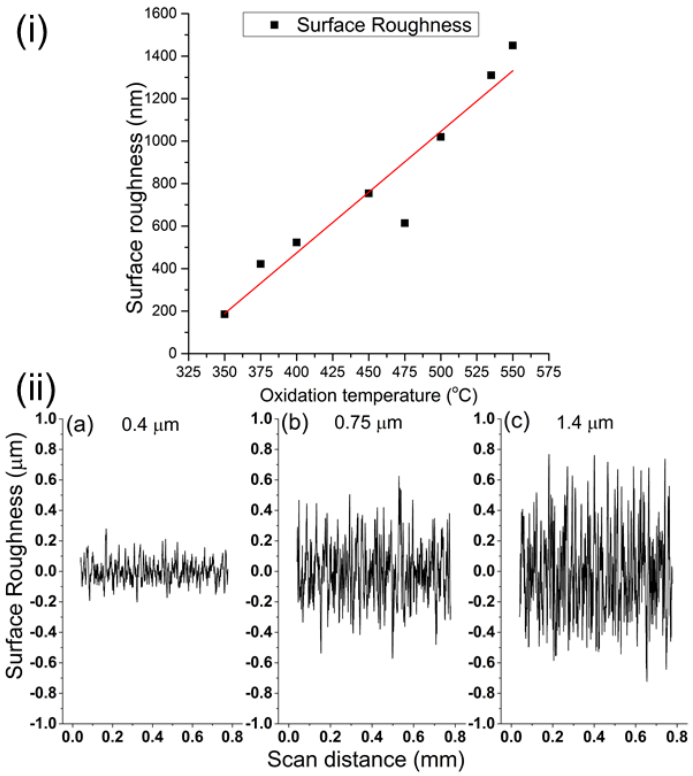

Figure 24: (i) Surface roughness increases linearly with oxidation temperature. (ii) Roughness profile of coatings oxidised at (a) 350°C, (b) 450°C and (c) 550°C measured using a profilometer tip dragging across the surface with a scan distance of 0.8 mm at a force of 10 milli grams. [73]

To measure the thickness of the films, a small scratch is made on the surface of the film and the profile of the film is scanned across the scratch. Since the film is

deposited in Silicon substrates, due the difference in the hardness value in the Moh's hardness scale [135–137] of both silicon (7) and steel razor (5.5), a scratch made by a steel razor would remove the VO_x films but not the underlying silicon surface. Hence the film thickness is calculated by measuring the step height of the scratched surface (figure 25). This offers a very simple way to measure film thickness without the use of complex models that are usually needed for ellipsometry measurements.

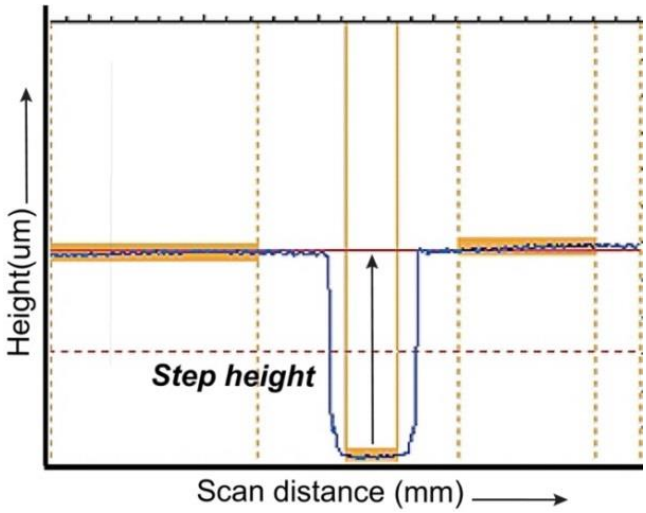

Figure 25: A step height profile over a scratch made by drawing a steel razor across the VO2 film.

3.2.3 X-Ray Diffraction (XRD)

The origin of X rays: In November 1895, Wilhelm Rontgen discovered X-rays while working at the University of Wurzburg, Germany. Rontgen was investigating cathode rays in different types of evacuated glass tubes and trying to determine their range in air. He noticed that while the rays were being produced, a screen coated in fluorescent barium platinocyanide would glow. He was intrigued because the screen was too far from the tube to be affected by the cathode rays.

He assumed unknown rays, X-rays, were being emitted from the walls of the tube while the cathode ray tube was running. To his amazement, Rontgen found that the rays could pass straight through his hand and cast shadows of his bones on

the fluorescent screen. He spent several weeks privately investigating the rays before publishing his results at the end of the year.

Rontgen's paper described many of the properties of X-rays. He showed that they were:

- Very penetrating and were able to pass through materials that are opaque to visible light.
- Invisible to the human eye.
- Would cause many types of material to fluoresce and could be recorded on photographic paper.

They were named 'rays' because they moved in straight lines like visible light.

Using X-rays as an analytical tool: The Bragg father and son duo explained that an X-ray which reflects from the surface of a substance has travelled less distance than an X-ray which reflects from a plane of atoms inside the crystal. The penetrating X-ray travels down to the internal layer, reflects, and travels back over the same distance before being back at the surface. The distance travelled depends on the separation of the layers and the angle at which the X-ray entered the material. For this wave to be in phase with the wave which reflected from the surface it needs to have travelled a whole number of wavelengths while inside the material. Bragg expressed this in an equation now known as Bragg's Law: [138,139]

$$n\lambda = 2\mathrm{d}\sin\theta$$

When λ is the wavelength of the X-ray, n is an integer (1, 2, 3 etc.) The reflected waves from different layers are perfectly in phase with each other and produce a bright point on a piece of photographic film. d is the interatomic distance and the angle of diffraction is θ. A visual representation of Bragg's law is shown in figure 26. The x-ray diffraction pattern of a pure substance is, therefore, like a fingerprint of the substance. The powder diffraction method is thus ideally suited for characterization and identification of polycrystalline phases.

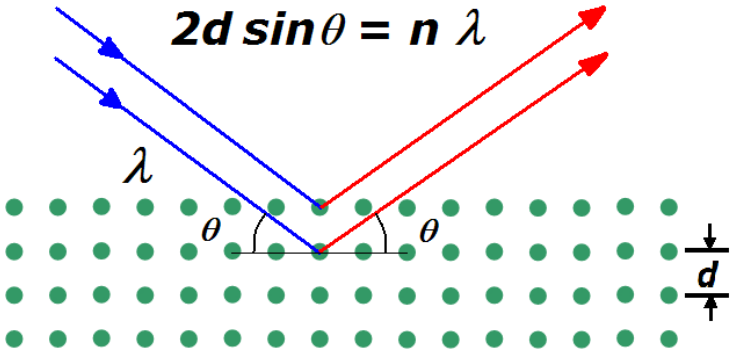

Figure 26: A schematic representation of Bragg's law.

X-ray diffractometers consist of three basic elements: an X-ray tube, a sample holder, and an X-ray detector. In a typical X-ray diffraction instrument, X-rays are generated in a cathode ray tube by heating a filament to produce electrons, accelerating the electrons toward a target by applying a voltage, and bombarding the target material with electrons. When electrons have sufficient energy to dislodge inner shell electrons of the target material, characteristic X-ray spectra are produced. These spectra consist of several components, the most common being Kα and Kβ. Kα consists, in part, of Kα1 and Kα2. Kα1 has a slightly shorter wavelength and twice the intensity as Kα2. The specific wavelengths are characteristic of the target material (Cu, Fe, Mo, Cr). Filtering, by foils or crystal monochrometers, is required to produce monochromatic X-rays needed for diffraction. Kα1and Kα2 are sufficiently close in wavelength such that a weighted average of the two is often used. Copper is the most common target material for single-crystal diffraction, with CuKα radiation = 1.5418Å. These X-rays are collimated and directed onto the sample. As the sample and detector are rotated, the intensity of the reflected X-rays is recorded. When the geometry of the incident X-rays impinging the sample satisfies the Bragg Equation, constructive interference occurs and a peak in intensity occurs. A detector records and processes this X-ray signal and converts the signal to a count rate which is then output to a device.

The geometry of an X-ray diffractometer as shown in figure 27 a is such that the sample rotates in the path of the collimated X-ray beam at an angle θ while the

X-ray detector is mounted on an arm to collect the diffracted X-rays and rotates at an angle of 2θ. The instrument used to maintain the angle and rotate the sample is termed a goniometer. Within the scope of the current study of Vanadium oxide films XRD technique plays a vital role in determining whether the as grown films feature a pure, or mixed phase oxides.

Measurements can also be performed at controlled temperatures using a specially designed temperature cell, which allows for programmable temperature profiles. Figure 27 b shows the temperature cell used in this study.

Temperature dependent XRD of VO_2 films give information regarding the structural phase transition of VO_2 and the reversible nature of the transition. Figure 28 shows an excellent example of how XRD can be used to characterize the phase transition in VO_2. Here we follow the position of (010) peak in both heating and cooling cycle under ambient air conditions. Notice the difference in temperature at which an abrupt shift occurs in both cycles. This difference in temperature is a direct consequence of the hysteretic behaviour of VO_2 phase transition.

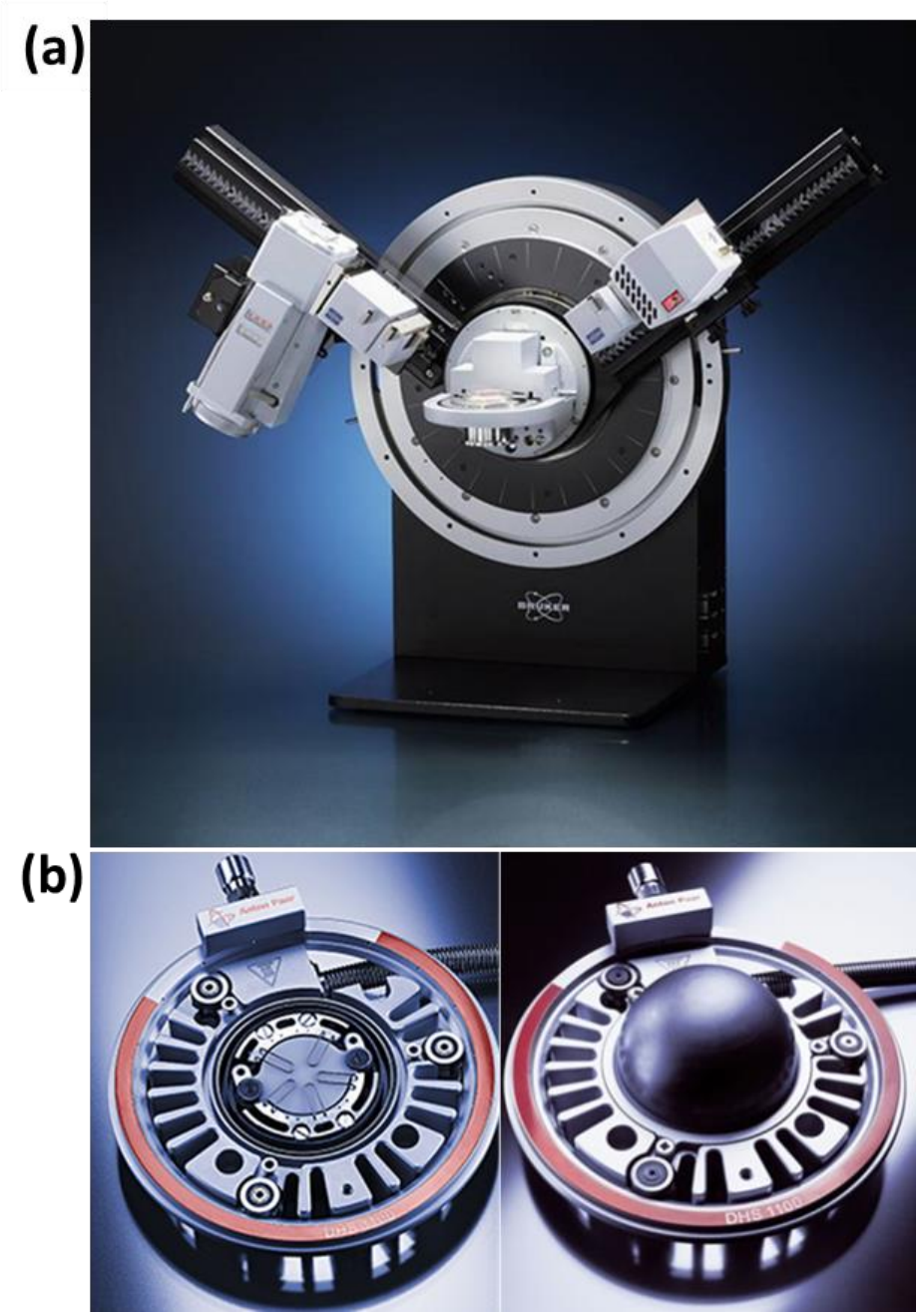

Figure 27 : (a) A bruker D8 diffractometer in the goniometer configuration and (b) temperature control stage with and without the graphite dome that is used to provide inert gas atmosphere.

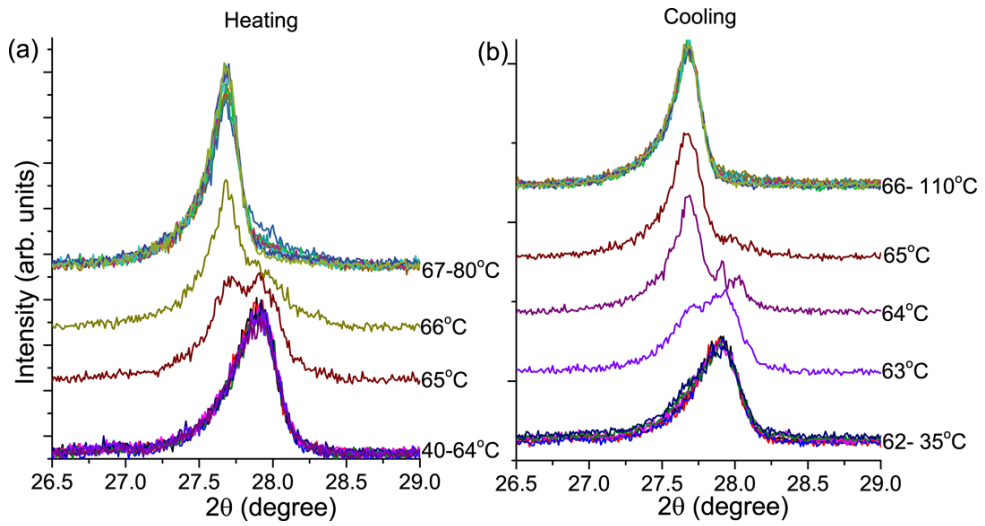

Figure 28: Tracking the structural phase transition in VO_2 in (a) heating and (b) cooling cycles [20]

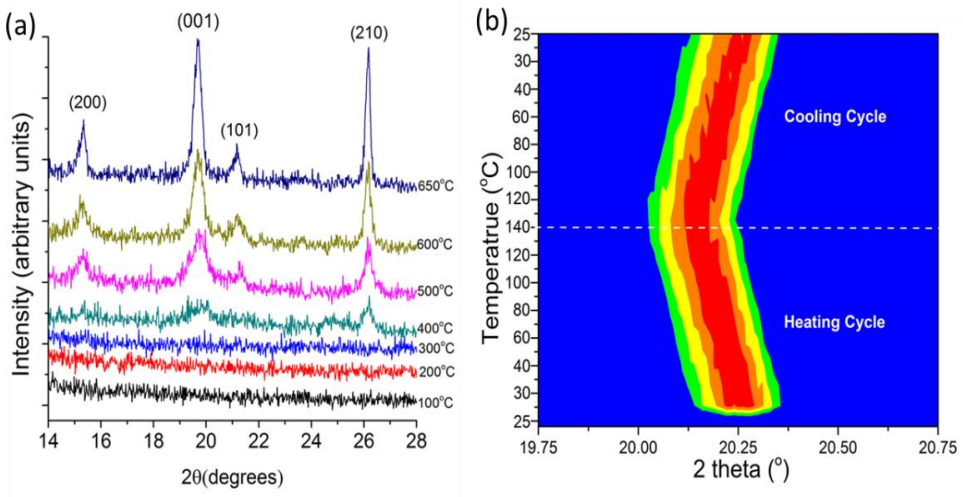

Figure 29: (a) Oxidation of as deposited VOx films as a function of temperature to find out the precise window at which V_2O_5 starts forming. (b) Contour plot of the peak (001) showing reversible nature of the thermochromic transition during heating and cooling from RT to 150°C. [73]

Oxidation of VO_x films to V_2O_5 was also tracked by analysing the phase transformation by heating the samples from RT to 650°C (figure 29 a) to determine the temperature at which the film transforms to pure V_2O_5. Figure 29 b shows reversible shift in the peak corresponding to (001) orientation.

3.2.4 Electrical resistivity measurements.

One of the most common methods of measuring a material's surface resistivity is by using either the two- or four-point probe method. This method use probes aligned either linearly or in a square pattern that contact the surface of the test material. [8] Measuring surface resistivity with four probes dates to 1916 where Wenner [140,141] discussed using the technique to measure the earth's resistivity. Both two and four probe methods are the most popular methods for measuring resistivity.

Most surface resistivity measurements are made on semiconductor wafers or thin films on a small surface area substrate. Since the measurements are made on finite sized areas, correction factors have to be used based on the sample geometry. This correction factor depends on the sample thickness, edge effects, thickness effects, and the location of the probe on the sample. Many studies have been performed on correction factors, with tables outlining the necessary adjustments. Other considerations that need to be considered for accurate four-point probe measurements are the spacing of the probes, and temperature effects. Small spacing differences in probe spacing can cause the resistivity values to vary widely across a sample surface. A high quality four-point head is necessary to get repeatable and reliable resistivity values

In the two point probe method,(figure 30b) two voltage probes are at a fixed spacing distance and are moved together along the material surface. Current is sent through one probe and exits through the second probe. The voltage between the two probes is measured be either a potentiometer or a voltmeter. By combining both the voltage (V) and current (I) measurements into the two surface probes, it is possible to calculate material surface resistance (R) between the two probes as

$$R = \frac{V}{I}$$

Four point probe based instrument as shown in figure 31(b) use a long established technique to measure the average resistance of a thin layer or sheet by passing current I through the outside two points of the probe and measuring

the voltage V across the inside two points. If the spacing between the probe points is constant, and the conducting film thickness is less than 40% of the spacing, and the edges of the film are more than 4 times the spacing distance from the measurement point, the average resistance of the film or the sheet resistance (ρ) is given by:

$$\rho = \frac{\pi}{\ln(2)} \frac{V}{I}$$

where:

$$\frac{\pi}{\ln(2)} = 4.53$$

Therefore:

$$\rho = 4.53 \frac{V}{I}$$

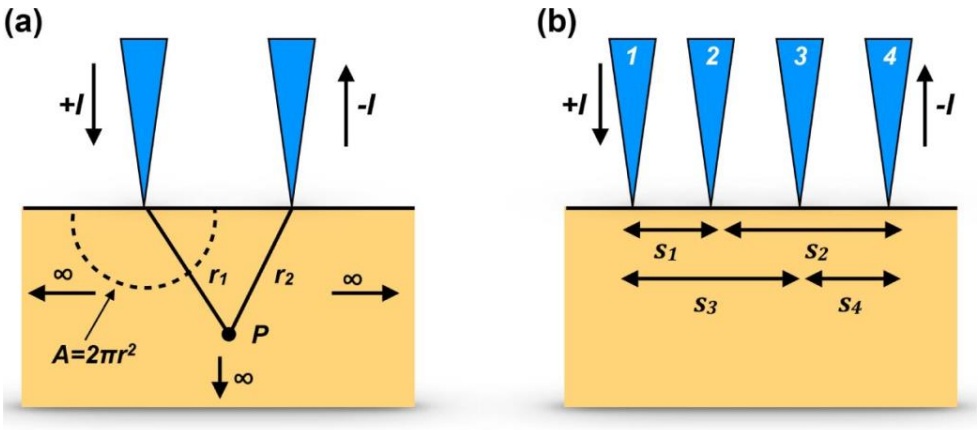

Figure 30: A schematic of two point and four point probe setup to measure resistivity of thin films. [142]

While simple in principle, there are experimental issues to take into account when using a four-point probe. In particular, the application of a metal to a semiconductor forms a schottky diode rather than an ohmic contact. Very high or very low resistivity samples require adjustment of the drive current to obtain a reliable reading.

VO_2 undergoes SMT around 68°C, therefore temperature dependent electrical resistivity measurements take the centre stage to characterize the SMT and compare the electrical characteristics among films grown with different process conditions. Temperature dependent sheet resistance and resistivity of VO_2 and V_2O_5 films was measured by placing the samples on a hot plate and systematically cycling the temperature with an adjust rate of heating.

Figure 32 shows such resistivity vs temperature dependent measurement of a 500 nm VO_2 film. An abrupt and a massive electrical resistivity drop of more than 3 orders of magnitude are noticed when heating VO_2 films above 67°C. Temperature dependent resistivity is measured by a four point probe while placing the sample on a heater and cycling the temperature from 30 to 80°C.

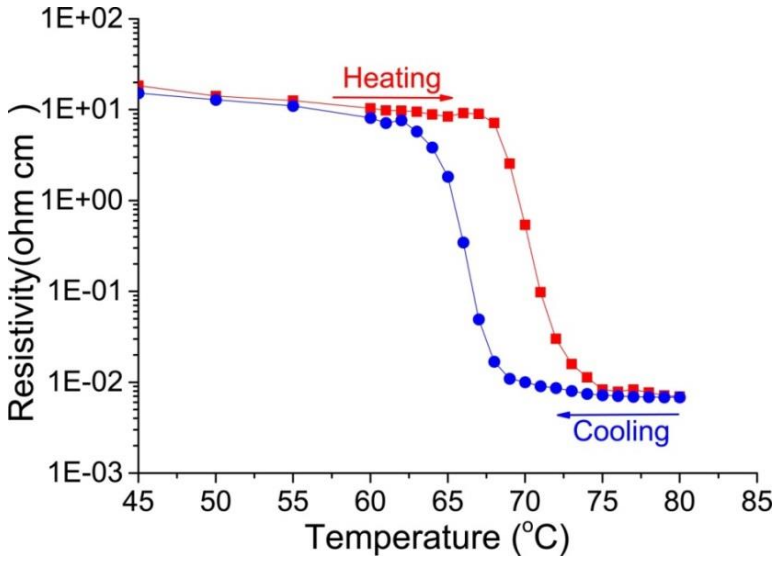

Figure 31: Change in electrical resistivity of VO_2 film with temperature in heating and cooling cycles.[13]

3.2.5 Raman Scattering.

When a beam of light is impinged upon a molecule, photons are absorbed by the material and scattered. The vast majority of these scattered photons have exactly the same wavelength as the incident photons and are known as Rayleigh scatter. In the scattering process, the incident photon excites an electron into a higher "virtual" energy level (or virtual state) and then the electron decays back to a

lower level, emitting a scattered photon. In Rayleigh scattering the electron decays back to the same level from which it started and thus Rayleigh scattering is often referred to as a form of elastic scattering. Figure 32 (a) and (b) show the illustrations of the Raman scattering process.

The Raman Effect arises when a photon is incident on a molecule and interacts with the electric dipole of the molecule. It is a form of electronic spectroscopy, although the spectrum contains vibrational frequencies. In classical terms, the interaction can be viewed as a perturbation of the molecule's electric field. [143–145]In quantum mechanical terms the scattering can be described as an excitation to a virtual state lower in energy than a real electronic transition with nearly coincident de-excitation and a change in vibrational energy. In the Raman Effect the electron excited in the scattering process decays to a different level than that where it started and is termed inelastic scattering.

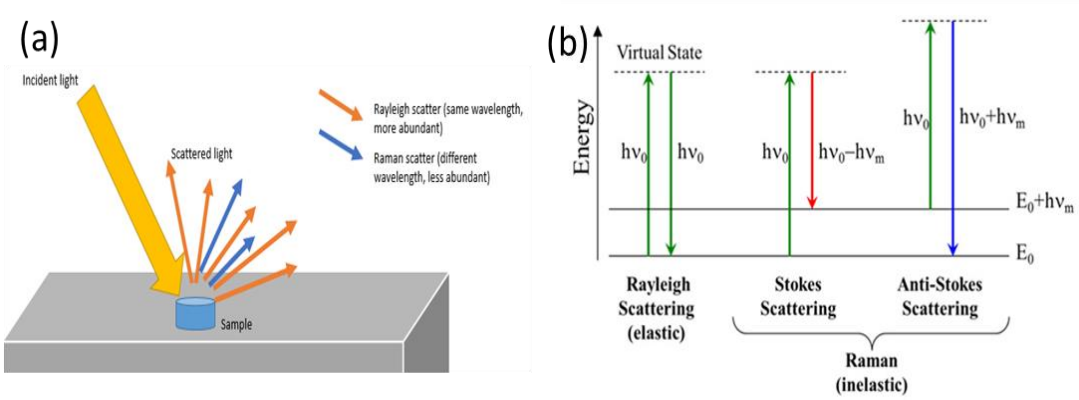

Figure 32: (a) Illustration of a Raman scattering process and (b) Schematic of Rayleigh (elastic) and Raman (inelastic) scattering of light on its interaction with matter [15]

The energy of a vibrational mode depends on molecular structure and environment. Atomic mass, bond order, molecular substituents, molecular geometry and hydrogen bonding all effect the vibrational force constant which, in turn dictates the vibrational energy. Much effort has been devoted to estimation or measurement of force constants. For small molecules, and even for some extended structures such as peptides, reasonably accurate calculations of vibrational frequencies are possible with commercially available software.



Figure 33: Photograph of the Renishaw in via Raman spectrometer.

Vibrational Raman spectroscopy is not limited to intramolecular vibrations. Crystal lattice vibrations and other motions of extended solids are Raman-active. Their spectra are important in such fields as polymers and semiconductors. In the gas phase, rotational structure is resolvable on vibrational transitions. The resulting vibration/rotation spectra are widely used to study combustion and gas phase reactions generally. Vibrational Raman spectroscopy in this broad sense is an extraordinarily versatile probe into a wide range of phenomena ranging across disciplines from physical biochemistry to materials science.

Advantages of Raman Spectroscopy

Raman spectroscopy is useful for chemical analysis for several reasons:

Specificity: Because Raman detects fundamental vibrations, Raman bands have a good signal-to-noise ratio and are non-overlapping. This allows a Raman spectrum to be used for everything from “fingerprinting” of samples to constructing complex chemical models of reaction processes.

- Analysis of aqueous systems: The IR spectrum of water is strong and relatively complex, making IR inadequate for analysis of aqueous solutions due to heavy interference by the water bands. However, the Raman spectrum

of water is weak and unobtrusive, allowing good spectra to be acquired of species in aqueous solution.

- Analysis of organic and inorganic chemistries: If a covalent chemical bond exists between chemical species then a unique Raman signature may be produced.
- Wide concentration range: The measured intensity of a Raman species is directly proportional to the concentration. This allows a Raman analysis to measure a species concentration from a fraction of 1% to 100% without sample dilution.
- No sample preparation: Unlike most other chemical analysis techniques, Raman requires no special preparation of the sample. In fact, no contact with the sample is needed, because Raman involves only illuminating a sample with a laser and collecting the scattered photons.
- Non-destructive Analysis: Raman involves only illuminating a sample, often through a window, with a laser and collecting the scattered photons this makes Raman spectroscopy non-destructive.
- Compatible with Common Windows: Can utilize standard sampling containers and windows manufactured of glass, sapphire, transparent polymers, and diamond to measure samples in situ.
- Quantitative Raman: Because the intensity of a Raman band is directly proportional to the number of molecules giving rise to the band, then the Raman band can be used to provide a measure of the concentration of a molecule.
- Short measurement times: A Raman spectrum can, typically, be acquired on a timescale from a fraction of a seconds to several minutes, thus Raman can be used to monitor chemical reactions in “real time.”

A Raman system is conceptually simple and includes the following main components:

- A laser excitation source
- Excitation delivery optics
- A sample

- Collection optics
- A wavelength separation device
- Detector and associated electronics
- A recording device.

Figure 34 shows a picture of a Raman system. In practice because the Raman effect is weak, the efficiency of and optimization of each of the instrumental components into an integrated system is critically important. Only an optimized system can be capable of producing the greatest measurement potential, over the widest range of same types, and able to measure the lowest concentration of species in the shortest amount of time possible.

Temperature dependent measurements were carried out with the help of a programmable heating stage from Linkam as shown in figure 35. The Linkam heating stage allows for computer controlled temperature increments as small as 0.1 ^{o}C with an operating limit of temperatures from -170°C till 600°C. Upon heating above 67°C VO_2 undergoes an abrupt transition from a monoclinic semiconducting phase to a rutile metallic phase. (figure 35)



Figure 34: Photograph of a linkam stage with a glass opening for the laser to shine on the substrate.

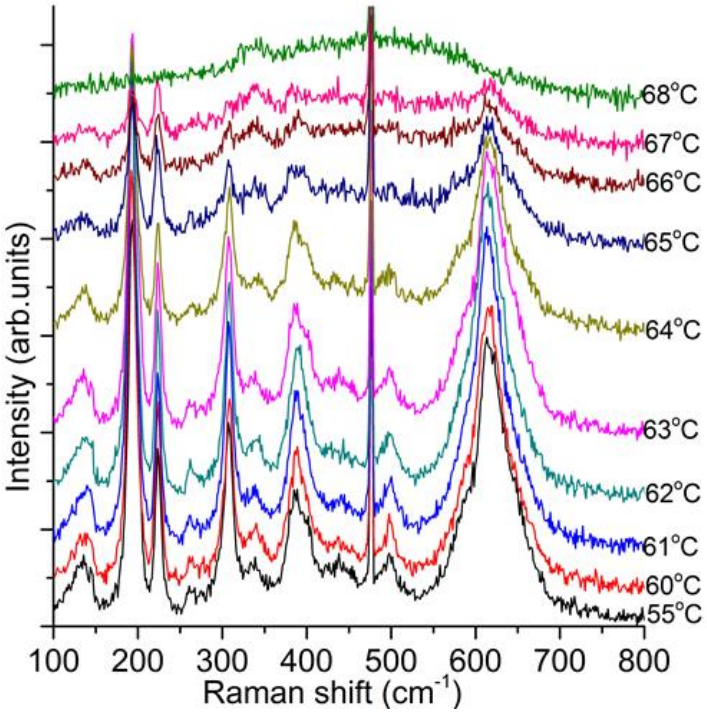

Figure 35: Temperature dependent Raman spectra of VO_2 film showing loss of signal at SMT during heating cycle. [20]

Raman scattering proved to be an indispensable technique in tracking temperature dependent phase transitions and is an effective way to characterize the films in a non-destructive and non-invasively.

Raman spectral imaging or mapping is a method for generating detailed chemical images based on a sample's Raman spectrum. A complete spectrum is acquired at each and every pixel of the image or selected area of interest, and then treated to obtain an image based on material composition. A typical experiment uses sequential sample movement and spectrum acquisition, repeated hundreds, thousands or even millions of times, to collect data from the user defined image area. Raman imaging has been successfully used for label-free investigations at cellular and subcellular level. Cell compartments, cell responses to drugs and different stages of the cell cycle from the stem cell to the completely differentiated cell were successfully distinguished. This technique is also able to differentiate between healthy and cancer cells, indicating great potential for replacing conventional cancer detection tools with Raman detection in the future. [146,147]

In our specific case Raman maps were studied to investigate the metamaterial state of VO_2, and to resolve the spatial distribution of the M1, M2 and R phase of VO_2 at a steady state temperature of 66.5^{o}C. VO_2 sample was maintained at the set temperature and Raman spectra were collected for each pixel over the area of 100 μm^2. The total measurement time exceeded over 100hrs and finally a spatial map of various phases is presented which was constructed on the basis of the difference in the Raman signature corresponding to each phase.

Raman map shown in figure 36, constructed by measuring Raman scattering over an area to investigate the spatial distribution of various phases of VO_2 namely M1, M2 and R at that temperature. Each uniquely coloured dot corresponds to a different phase of VO_2 that is clearly distinguished by the spectra in (b)

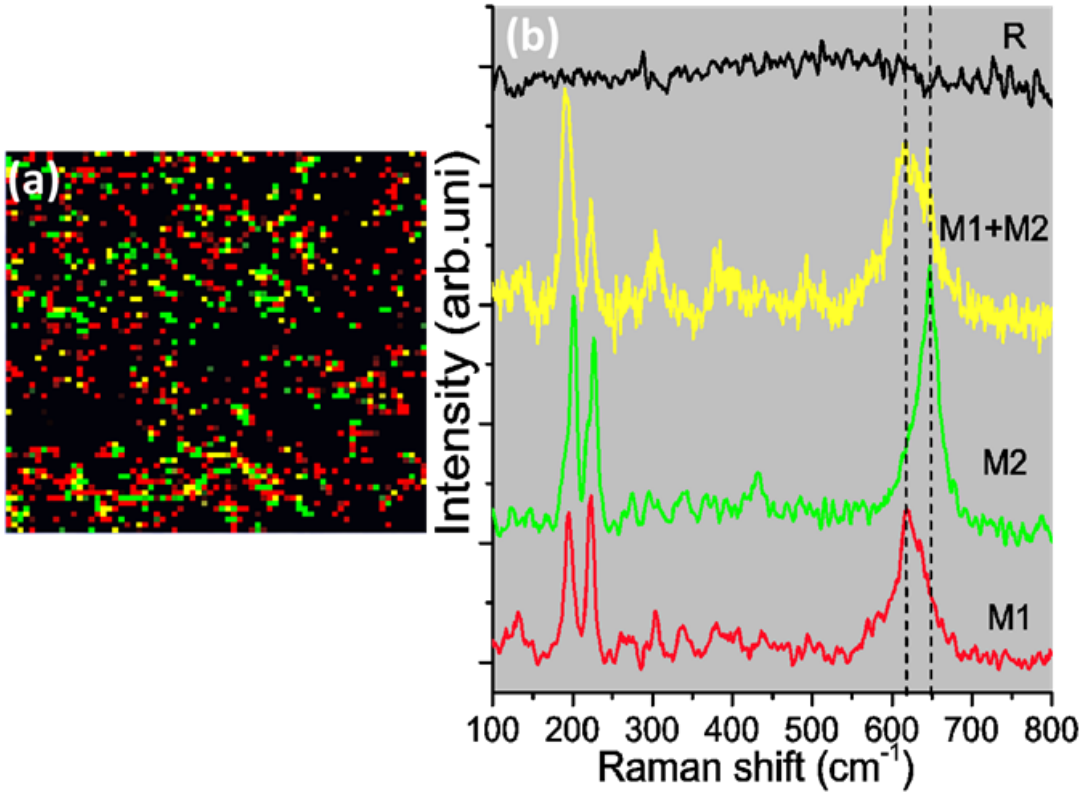

Figure 36: (a) Raman surface mapping of the M1, M2, M1+M2 and R phases as measured at 67.5^{o}C (each dot correspond to 1x1 μm2 analysis area) and (b) Raman spectra corresponding to the colour-coded used in the mapping. [20]

3.2.6 Optical Spectroscopy.

Upon interaction of electromagnetic radiation with a sample surface, depending on the characteristic of the surface and its environment; the light may undergo, transmission, absorption, or reflection (internal, and specular and diffuse reflection) as shown in figure 37. In practice, all three types of reflections can occur at the same time, although with different contributions.

Photons are absorbed in materials by several processes. The variety of absorption processes and their wavelength dependence allows us to derive information about the chemistry of a surface from its reflected light. The human eye is a crude reflectance spectrometer: we can look at a surface and see colour. Our eyes and brain are processing the wavelength-dependent scattering of visible-light photons to reveal something about what we are observing, like the red colour of hematite or the green colour of olivine. A modern spectrometer, however, can measure finer details over a broader wavelength range and with greater precision. Thus, a spectrometer can measure absorptions due to more processes than what can be seen with the eye.

UV-Vis-NIR spectrophotometers are used in a wide variety of fields for applications such as quantitative analysis, colorimetry, or transmittance or reflectance measurements of optical elements, in addition to measuring the thickness of thin films or coatings. [148–150]

When using UV-Vis-NIR spectroscopy, various measurement techniques are available to suit a given sample's physical characteristics. For example, if a film is on an opaque substrate, such as a wafer, reflection measurement is used to measure its thickness. If the film is on a transparent substrate, or if only the film itself is subjected to analysis, transmission measurement can be used to measure its thickness. A typical line diagram of a spectrometer is depicted in figure 38.

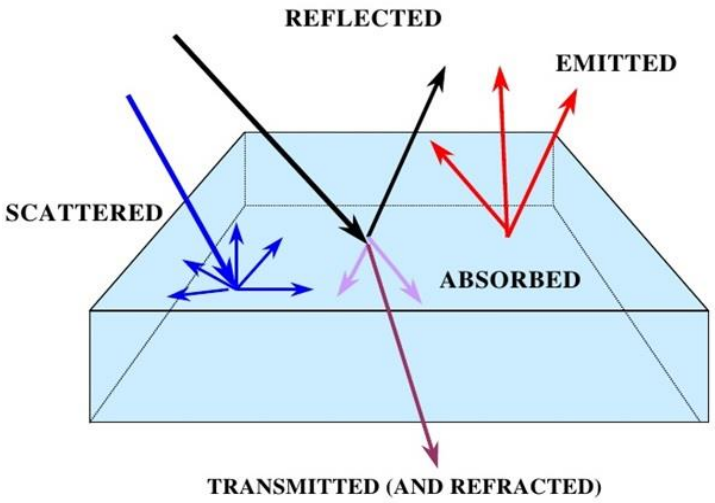

Figure 37: A schematic of the various phenomena occurring when light is incident on a substrate.

Transmission measurements involve shining light on a sample and measuring the light transmitted through the sample. The characteristics of the measurements and the points to be aware of differ according to the type of transmitted light measured. This method is generally used on thin transparent film or glass not exceeding approximately 3 mm thickness. Transmission measurements are also used to confirm the almost 100% transmittance found in samples with anti-reflection coatings applied to suppress reflection.

While many methods are available to measure the thickness of a film, UV-Vis spectroscopy permits easy, non-destructive thickness measurements of many types of film. When light is directed on a thin film, a portion of the light can be reflected from the front and rear surfaces of the film. Depending on the thickness of the film, reflected light from both surfaces of the film can interact to form a thickness dependent interference pattern.

Integrating spheres (figure 39) collect reflected light from samples over a full hemisphere. The sphere, by nature of its internal diffuse reflection and integration of the energy, is insensitive to directional reflectance features coming from the sample, and therefore, gives a very repeatable “integrate” response to the reflectance of the sample placed in the beam at the sphere port. Sample placement and incidence beam/collection alignment are less critical to the

measurement results because the integrating sphere looks at representative integrated energy from all angles at the same time.

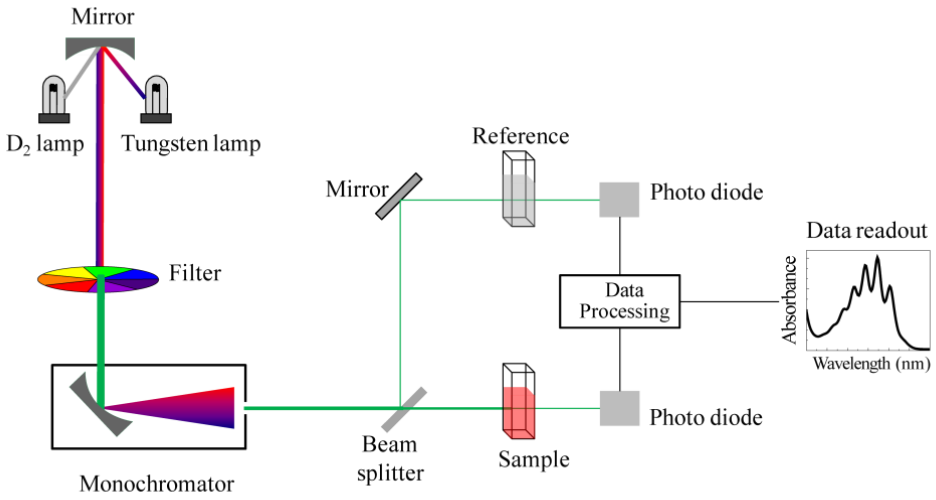

Figure 38: A schematic of a spectrophotometer with various components.

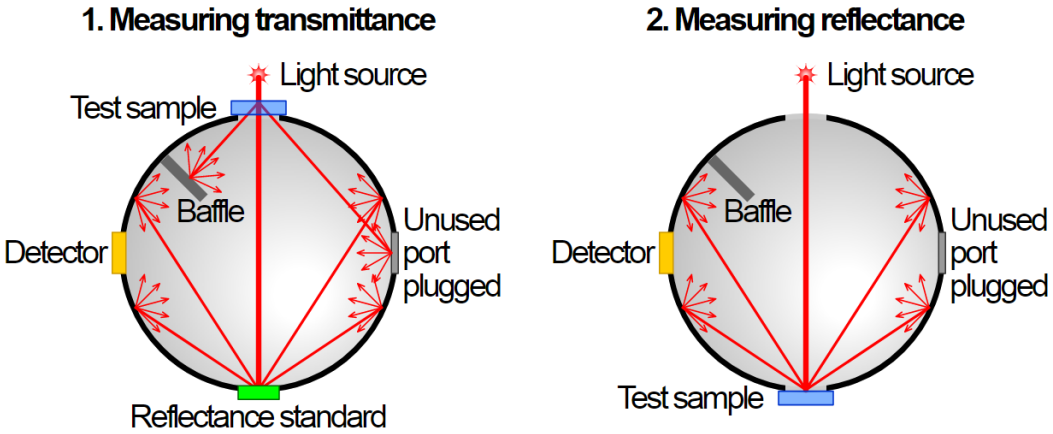

Figure 39: Working of an integration sphere in transmittance and reflectance modes of measurements respectively [17]

The single largest application for integrating spheres is the measurement of the reflectance and transmittance of diffuse or scattering materials. The measurements are routinely performed as a function of the wavelength.

In the ultraviolet, diffuse transmittance is used to determine the UV resistance of pharmaceutical containers, sun protective clothing, and automotive paints. In the

visible spectrum, the colour of materials is quantified and controlled in industries such as paints, textiles and the graphic arts. In the infrared, the total hemispherical reflectance determines surface emissivities applied to radiant heat transfer analysis of thermal control coatings and foils used in spacecraft design.

A transmittance measurement places a material sample at the entrance port to the sphere and the angle of incidence is set at 0° (Figure 39-1). In reflectance measurements, the sample is placed at a port opening opposite the entrance port and the angle of incidence is usually slightly off normal up to 10°. The specular component can be excluded from the measurement by using normal (0°) incidence or by fitting another port in the specular path and using a black absorbing light trap to extinguish the specular flux. Reflectance measurements at larger or variable incident angles are performed by placing the sample at the centre of the sphere and rotating it about a fixed input beam. Baffles are placed to prevent the photo detector on the sphere from directly viewing the irradiated sample in either measurement. In the reflectance geometry, a baffle is usually placed between the portions of the sphere wall that receives the specular component as well (Figure 39-2). It is best to use a photo detector with a hemispherical field-of-view to reduce any sensitivity to the scatter distribution function of the sample. Figure 40 shows a picture of the UV/Vis/NIR spectrophotometer with a 150 mm integration sphere.



Figure 40: Photograph of the spectrophotometer by Perkin Elmer with a 150 mm integration sphere.

Optical reflectivity measurements were performed as a function of temperature to track the SMT and infrared reflectivity in VO_2 and to investigate the thermochromism in the visible region for V_2O_5 films. Custom made ceramic based resistive heaters were used in conjunction with a temperature controller shown in figure 41. The Si substrate is made to come in intimate contact with the heater and a K type thermocouple is placed on the surface, such that the temperature is regulated precisely.



Figure 41: Resistive heater from Bach ceramics (left) and the temperature controller from Horst used to regulate the temperature. (Right)

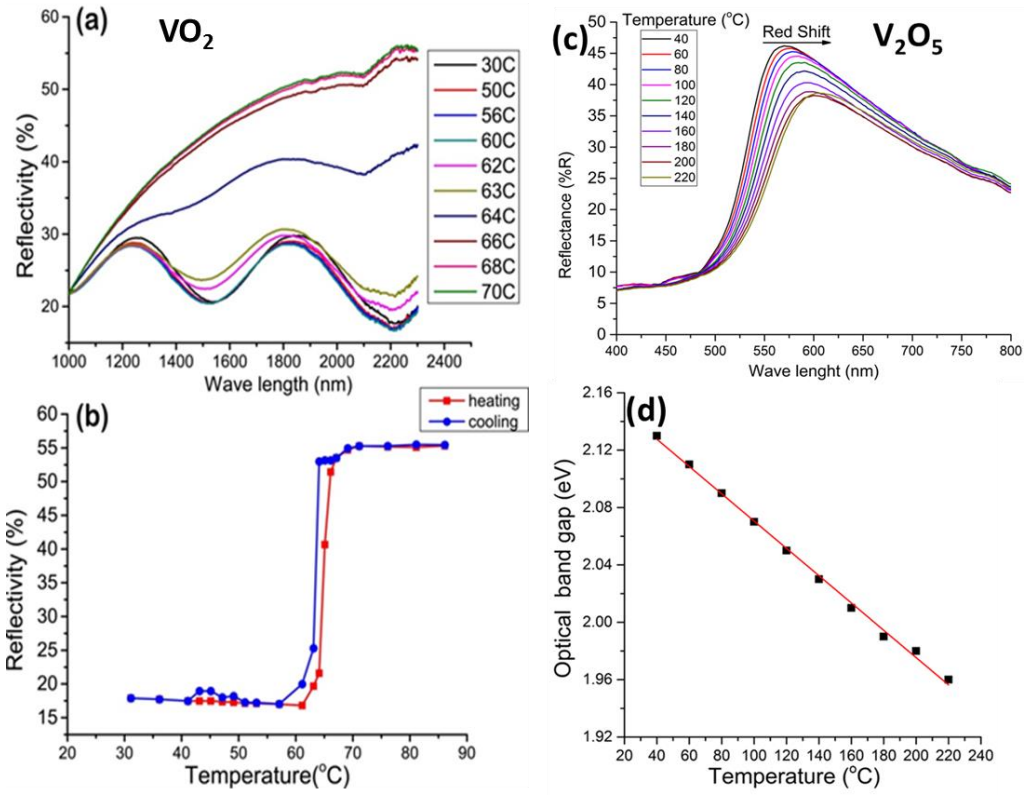

Figure 42: (a) Temperature-dependent infrared reflectivity in the NIR region: Reflection spectra in the NIR upon heating (b) and the variation in reflection across the transition temperature displayed for the arbitrary selected wavelength λ=2300 nm. (c) Reflectance spectra showing thermochromic red shift of V_2O_5 in the visible region and (d) the variation of optical energy band gap calculated form the raw data of the corresponding spectra at each temperature.[10,13]

SMT induced, Infrared reflectivity for VO_2 films is shown in figure 42a. Temperature dependent reflectance spectroscopy in the NIR region reveals an abrupt change in the IR reflectivity of VO_2 films form 18% in semiconducting monoclinic state to 55% in the rutile state (Figure 42b). By setting the incident radiation at 2300 nm and performing the temperature cycling, we observe an abrupt nature of the optical transition which is very similar to the profile of electrical resistivity change as a function of temperature. Therefore, reflectance spectra for VO_2 can be used as an effective way to characterise the SMT behaviour in VO_2 films.

For V_2O_5 coatings, temperature dependent reflectivity measurements in the visible spectrum reveal an apparent red shift (figure 42c). An important distinction to be made here in between VO_2 and V_2O_5 in the spectral range of interest, VO_2 is investigated in NIR region (1000-2300 nm) whereas for V_2O_5 its performed in the visible range of spectrum (400-800 nm).

The optical band gap E_g was calculated as function of temperature using the temperature-dependent reflectance spectra, by Tauc's equation[151,152],

$$\alpha h\nu = B(h\nu - E_g)^r$$

and α is absorption coefficient that is calculated as

$$\alpha = \frac{1}{d}\ln\frac{(100 - R^2)}{T}$$

Where E_g = the optical energy gap of the film, B = a constant, hv = the incident photon energy d is the thickness of the film, T is the transmittance, R is the reflectance and r is a numeric value equal to 1/2 for allowed direct transitions and 2 for allowed indirect transitions. The optical energy gap is estimated by plotting $(\alpha h\nu)^{1/r}$ versus (hv), then interpolating the straight line to the photon energy axis at the value $(\alpha h\nu)^{1/r} = 0$. The obtained data for vanadium pentaoxide films were found to give a better fit for the exponent r = 1/2 confirming the direct allowed nature of the involved transition. Figure 42 d shows the temperature dependence of optical band gap for thermochromic V_2O_5 films.

3.2.7 Thermal imaging using a Near Infrared camera.

The thermal behaviour of materials (solids, liquids, or gases) is constantly affected by their surroundings. The natural drive towards thermal equilibrium promotes heat is exchange between objects via three mechanisms: conduction, convection, and radiation. Conduction is defined as heat transfer between two solid bodies that are in physical contact with each other. Convection is heat transfer, usually between a solid material and a liquid or gas. Conduction and convection are dependent on physical contact between materials. Radiation is a process of heat transfer, characteristic of all matter (at temperatures above

absolute zero). Radiation passes through a vacuum, and can also pass through gases, liquids and even solids.

When radiative power is incident on an object, a fraction of the power will be reflected (r), another portion will be absorbed (a), and the final portion will be transmitted (t) through the object. The total Power Law describes all of this:

$$r + a + t = 1$$

The ability of an object to absorb radiation is also related to its ability to emit radiation. This is identified as Kirchhoff's law [153,154] $\mathrm{a} = \in$ where: a = absorbance and $\in$ = emissivity.

Therefore, when the thermal imager observes the thermal radiation from real objects, part of what is detected by the thermal imager is reflected from the surface of the object, part is emitted by the object, and part may be transmitted through the object.

All objects with temperature T> 0 K emit infrared (thermal) radiation. The intensity of the radiation depends on the temperature and nature of the material's surface. At lower temperatures, the majority of this thermal radiation is at longer wavelengths. As the object becomes hotter, the radiation intensity rapidly increases and the peak of the radiation shifts towards shorter wavelengths. The relationship between total radiation intensity (all wavelengths) and temperature is defined by the Stefan Boltzmann law [155,156]

$$Q = e\, s\, T^4$$

Where Q = radiation intensity, e = emissivity of material, s = Stefan-Boltzmann constant and T = absolute temperature.

Emissivity is the measure of an object's ability to emit infrared energy. Emitted energy indicates the temperature of the object. Ideally emissivity can have a value from 0 (perfect absorber) to 1.0 (perfect blackbody). At a given temperature, the maximum radiation is achieved when the object has an emissivity of 1, and the object is qualified as perfect radiator. However, in our real world, there are no true blackbodies, that is, no perfect radiators. For this reason,

infrared imaging and temperature calculation is calibrated using an object whose real temperature is known across all the wavelengths of measurements.

Most thermal-imaging devices scan at a rate of 30 frames per second. They can sense temperatures ranging from -20°C to 2000°C, and can normally detect changes in temperature of about 0.2^{o} K

There are two common types of thermal-imaging devices:

Un-cooled - This is the most common type of thermal-imaging device. The infrared-detector elements are contained in a unit that operates at room temperature. This type of system is completely quiet, activates immediately and has the battery built right in. [157,158]

Cryogenically cooled – These are expensive and more susceptible to damage from rugged use, these systems have the elements sealed inside a container that cools them to below 0°C. The advantage of such a system is the incredible resolution and sensitivity that result from cooling the elements. Cryogenically-cooled systems can detect a difference as small as 0.1 K. [159,160]

IR camera construction is similar to a digital video camera. The main components are a lens that focuses IR onto a detector, plus electronics and software for processing and displaying the signals and images. Instead of a charge coupled device that video and digital still cameras use, the IR camera detector is a focal plane array (FPA) of micrometre size pixels made of various materials sensitive to IR wavelengths. FPA resolution can range from about 160 × 120 pixels up to 1024 × 1024 pixels. Certain IR cameras have built-in software that allows the user to focus on specific areas of the FPA and calculate the temperature. Other systems utilized a computer or data system with specialized software that provides temperature analysis. Both methods can supply temperature analysis with better than ±1°C precision. FPA detector technologies are broken down into two categories: thermal detectors and quantum detectors. A common type of thermal detector is an uncooled micro bolometer made of a metal or semiconductor material. These typically have lower cost and a broader IR spectral response than quantum detectors. Still, micro bolometers react to

incident radiant energy and are much slower and less sensitive than quantum detectors.

The operation of a quantum detector is based on the change of state of electrons in a crystal structure reacting to incident photons. These detectors are generally faster and more sensitive than thermal detectors. Quantum detectors are made from materials such as InSb, InGaAs, PtSi, HgCdTe (MCT), and layered GaAs/AlGaAs for QWIP (Quantum Well Infrared Photon) detectors. However, they require cooling, sometimes down to cryogenic temperatures using liquid nitrogen or a small Stirling cycle refrigerator unit.

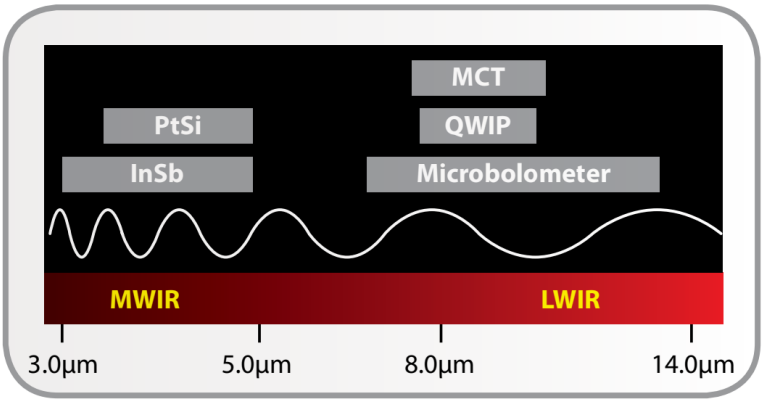

Figure 43 : Examples of detector materials and their spectral responses. [161,162]

Typically, IR cameras are designed and calibrated for a specific range of the IR spectrum. This means that the optics and detector materials must be selected for the desired range. Figure 43 illustrates the spectral response regions for various detector materials. Because IR has the same properties as visible light regarding reflection, refraction, and transmission, the optics for thermal cameras are designed in a fashion similar to those of a visual wavelength camera. However, the types of glass used in optics for visible light cameras cannot be used for optics in an infrared camera, as they do not transmit IR wavelengths well enough. Conversely, materials that are transparent to IR are often opaque to visible light. IR camera lenses typically use Si and Ge materials. Normally Si is used for MWIR (medium wavelength IR) camera systems, whereas Ge is used in LW (long wavelength) cameras. Si and Ge have good mechanical properties, i.e., they do not break easily, they are non-hygroscopic, and they can be formed into

lenses with modern turning methods. As in visible light cameras, IR camera lenses have antireflective coatings. With proper design, IR camera lenses can transmit close to 100% of incident radiation.



Figure 44: Photograph of the FLIR X6580 thermal camera.

The thermal camera used in this study (figure 44) is the FLIR X6580sc high resolution research grade model, operating in the spectral range of 1.5 – 5.1 µm. The X6580sc is equipped with a cooled Indium Antimonide (InSb) detector that's sensitive enough to distinguish temperature differences less than 25 mK (20 mK typical). The camera produces temperature measurements with an accuracy of +/-1% and a wide temperature range that automatically adjusts to best fit the thermal scene Infra-red imaging, thus provides an excellent way to track changes in the optical properties during SMT of VO_2 films.

In most applications, the emissivity of an object is based on referred values. Although camera software may include an emissivity table, users usually have the capability of inputting emissivity values for an object ranging from 0.1 to 1.0. Many cameras also provide automatic corrections based on user input for reflected ambient temperature, viewing distance, relative humidity, atmospheric transmission, and external optics. As described earlier the temperature calculations are based on radiance measurements and the object's emissivity. However, when the emissivity value is unknown or uncertain, the reverse process can be applied. By measuring the object temperature, emissivity can be addressed. This is usually done when exact emissivity values are needed. There are two common methods of doing this. The first method establishes a known temperature by using an equalization box. This is essentially a tightly controlled

temperature chamber with circulating hot air. The length of time in the box must be sufficient to allow the whole object to be at a uniform temperature. In addition, it is absolutely necessary that the object stabilize at a temperature different from the surroundings where the actual measurements will take place. Usually, the object is heated to a temperature at least 10°C above the surroundings to ensure that the thermodynamics of the measurements are valid. Once the object has reached the set temperature, the lid is drawn off and a thermogram is captured of the object. The camera and/ or software for processing thermograms can be used to get the emissivity value.

The “adjacent spot” method is much simpler, but still gives reasonably exact values of the emissivity. It uses an area of known emissivity. The idea is to determine the temperature of the object with the camera in the usual way. The object is adjusted so that the area with unknown emissivity is very close to an area of known emissivity. The distance separating these areas must be so small that it can be safely assumed they have the same temperature. From this temperature measurement, the unknown emissivity can be calculated.

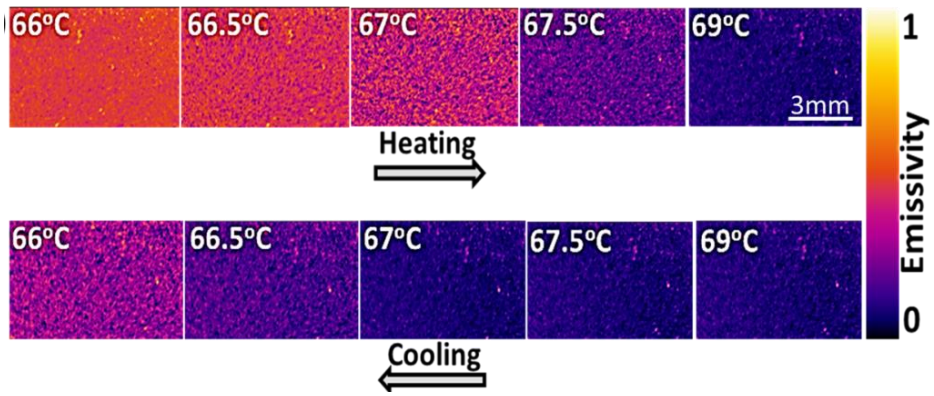

Figure 45: A series of images taken by a thermal camera during temperature cycling of VO_2 films. [20]

Near infrared imaging provides invaluable insights into the dynamics of phase transitions occurring inside the hysteresis loop of VO_2 during the SMT (figure 45). It proved to be an efficient tool to record the reversible patterning and interplay of the emissivity states of the disordered metamaterial states which are otherwise invisible to the naked eye.

References

(1) Morosan, E.; Natelson, D.; Nevidomskyy, A.; Si, Q. Strongly Correlated Materials. *Advanced Materials* **2012**, *24* (36), 4896–4923.

(2) Wei, J.; Natelson, D. Nanostructure Studies Of Strongly Correlated Materials. *Nanoscale* **2011**, *3* (9), 3509.

(3) Benmoussa; Ibnouelghazi; Bennouna; Ameziane, E. L. Structural, Electrical And Optical Properties Of Sputtered Vanadium Pentoxide Thin Films. *Thin Solid Films* **1995**, *265* (1-2), 22–28.

(4) Partlow; Gurkovich; Radford; Denes. Switchable Vanadium Oxide Films By A Sol- Gel Process. *Journal Of Applied Physics* **1991**, *70* (1), 443–452.

(5) Taylor, A.; Parkin, I.; Noor, N.; Tummeltshammer, C.; Brown, M. S.; Papakonstantinou, I. A Bioinspired Solution For Spectrally Selective Thermochromic Vo2 Coated Intelligent Glazing. *Opt Express* **2013**, *21 Suppl 5*, A750–64.

(6) Wu, C.; Feng, F.; Xie, Y. Design Of Vanadium Oxide Structures With Controllable Electrical Properties For Energy Applications. *Chem Soc Rev* **2013**, *42* (12), 5157–83.

(7) Chalker, C. J.; An, H.; Zavala, J.; Parija, A.; Banerjee, S.; Lutkenhaus, J. L.; Batteas, J. D. Fabrication And Electrochemical Performance Of Structured Mesoscale Open Shell V2o5 Networks. *Langmuir* **2017**, *33* (24), 5975–5981.

(8) Tepavcevic, S.; Liu, Y.; Zhou, D.; Lai, B.; Maser, J.; Zuo, X.; Chan, H.; Král, P.; Johnson, C. S.; Stamenkovic, V.; Markovic, N. M.; Rajh, T. Nanostructured Layered Cathode For Rechargeable Mg-Ion Batteries. *Acs Nano* **2015**, *9* (8), 8194–205.

(9) An, H.; Mike, J.; Smith, K. A.; Swank, L.; Lin, Y.-H. H.; L Pesek, S.; Verduzco, R.; Lutkenhaus, J. L. Highly Flexible Self-Assembled V2o5 Cathodes Enabled By Conducting Diblock Copolymers. *Sci Rep* **2015**, *5*, 14166.

(10) Huang, Z.; Chen, S.; Lv, C.; Huang, Y.; Lai, J. Infrared Characteristics Of Vo 2 Thin Films For Smart Window And Laser Protection Applications. *Applied Physics Letters* **2012**, *101* (19), 191905.

(11) Nag, J.; Jr, R. Synthesis Of Vanadium Dioxide Thin Films And Nanoparticles. *J Phys Condens Matter* **2008**, *20* (26), 264016.

(12) Pergament, Al; Stefanovich, Gb; Kuldin, Na; Velichko, Aa. On The Problem Of Metal-Insulator Transitions In Vanadium Oxides. *Isrn Condensed Matter Physics* **2013**, *2013*.

(13) Pouget JP, Launois H. Metal-insulator phase transition in VO2. Le Journal de Physique Colloques. **1976**; 37(C4):C4-49..

(14) Pouget, Jp; Launois, H; D'haenens, Jp; Merenda, P. Electron Localization Induced By Uniaxial Stress In Pure Vo 2. *Physical Review Letters* **1975**.

(15) Pouget, Jp; Launois, H; Rice, Tm; Dernier, P; Gossard, A. Dimerization Of A Linear Heisenberg Chain In The Insulating Phases Of V 1− X Cr X O 2. *Physical Review B* **1974**.

(16) Pouget; Launois; D'haenens; Merenda; Rice. Electron Localization Induced By Uniaxial Stress In Pure VO_2. *Physical Review Letters* **1975**, *35* (13), 873–875.

(17) Guo, H.; Chen, K.; Oh; Wang, K.; Dejoie, C.; Asif, S.; Warren; Shan; Wu; Minor. Mechanics And Dynamics Of The Strain-Induced M1–M2 Structural Phase Transition In Individual Vo 2 Nanowires. *Nano Letters* **2011**, *11* (8), 3207–3213.

(18) Macchesney, J. B.; Guggenheim, H. J. Growth And Electrical Properties Of Vanadium Dioxide Single Crystals Containing Selected Impurity Ions. *Journal Of Physics And Chemistry Of Solids* **1969**, *30* (2), 225–234.

(19) Chen, S.; Ma, H.; Yi, X.; Xiong, T.; Wang, H.; Ke, C. Smart Vo2 Thin Film For Protection Of Sensitive Infrared Detectors From Strong Laser Radiation. *Sensors And Actuators A: Physical* **2004**, *115* (1), 28–31.

(20) Kumar, S.; Maury, F.; Bahlawane, N. Electrical Switching In Semiconductor-Metal Self-Assembled Vo2 Disordered Metamaterial Coatings. *Sci Rep* **2016**, *6*, 37699.

(21) Manning, T.; Parkin, I.; Pemble, M.; Sheel, D.; Vernardou, D. Intelligent Window Coatings: Atmospheric Pressure Chemical Vapor Deposition Of Tungsten-Doped Vanadium Dioxide. *Chemistry Of Materials* **2004**, *16* (4), 744–749.

(22) Hur, M. G.; Masaki, T.; Yoon, D. H. Thermochromic Properties Of Sn, W Co-Doped Vo2 Nanostructured Thin Film Deposited By Pulsed Laser Deposition. *J Nanosci Nanotechnol* **2014**, *14* (12), 8941–5.

(23) Qian, X.; Wang, N.; Li, Y.; Zhang, J.; Xu, Z.; Long, Y. Bioinspired Multifunctional Vanadium Dioxide: Improved Thermochromism And Hydrophobicity. *Langmuir* **2014**, *30* (35), 10766–71.

(24) Zhang, Z.; Gao, Y.; Chen, Z.; Du, J.; Cao, C.; Kang, L.; Luo, H. Thermochromic Vo2 Thin Films: Solution-Based Processing, Improved Optical Properties, And Lowered Phase Transformation Temperature. *Langmuir Acs J Surfaces Colloids* **2010**, *26* (13), 10738–44.

(25) Agrawal; Loverme. Variable Emissivity Coatings And Their Applications. **2010**.

(26) Nakano; Shibuya; Okuyama; Hatano; Ono; Kawasaki; Iwasa; Tokura. Collective Bulk Carrier Delocalization Driven By Electrostatic Surface Charge Accumulation. *Nature* **2012**, *487* (7408), 459–462.

(27) Ruzmetov, D.; Gopalakrishnan, G.; Ko, C.; Narayanamurti, V.; Ramanathan, S. Three-Terminal Field Effect Devices Utilizing Thin Film Vanadium Oxide As The Channel Layer. *Journal Of Applied Physics* **2010**, *107* (11), 114516.

(28) Hood; Denatale. Millimeter- Wave Dielectric Properties Of Epitaxial Vanadium Dioxide Thin Films. *Journal Of Applied Physics* **1991**, *70* (1), 376–381.

(29) Cao; Ertekin; Srinivasan; Fan; Huang; Zheng; Yim, J.; Khanal; Ogletree; Grossman; Wu. Strain Engineering And One-Dimensional Organization Of Metal–Insulator Domains In Single-Crystal Vanadium Dioxide Beams. *Nature Nanotechnology* **2009**, *4* (11), 732–737.

(30) Strelcov, E.; Lilach, Y.; Kolmakov, A. Gas Sensor Based On Metal-Insulator Transition In Vo2 Nanowire Thermistor. *Nano Letters* **2009**, *9* (6), 2322–6.

(31) Franz; Wiedemann. Ueber Die Wärme-Leitungsfähigkeit Der Metalle. *Annalen Der Physik Und Chemie* **1853**, *165* (8), 497–531.

(32) Lee, S.; Hippalgaonkar, K.; Yang, F.; Hong, J.; Ko, C.; Suh, J.; Liu, K.; Wang, K.; Urban, J.; Zhang, X.; Dames, C.; Hartnoll, S.; Delaire, O.; Wu, J.

Anomalously Low Electronic Thermal Conductivity In Metallic Vanadium Dioxide. *Science* **2017**, *355* (6323), 371–374.

(33) Wei, J.; Natelson, D. Nanostructure Studies Of Strongly Correlated Materials. *Nanoscale* **2011**, *3* (9), 3509.

(34) Lee, J.; Song, Y.-H.; Cha, M.; Kim, S. Effects Of Hydrocarbons And Water Vapor On No X Using V 2 O 5 −Wo 3 /Tio 2 Catalyst Reduction In Combination With Nonthermal Plasma. *Industrial & Engineering Chemistry Research* **2007**, *46* (17), 5570–5575.

(35) Bauer, G.; Güther, V.; Hess, H.; Otto, A.; Roidl, O.; Roller, H.; Sattelberger, S. *Ullmann's Encyclopedia Of Industrial Chemistry*; 2000.

(36) Cook, E. Peregrine Phillips, The Inventor Of The Contact Process For Sulphuric Acid. *Nature* **1926**, *117* (2942), 419–421.

(37) Fang; Liu; Wang; Liu; Yao. Orientated Growth Of V 2 O 5 Electrochromic Thin Films On Transparent Conductive Glass By Pulsed Excimer Laser Ablation Technique. *Journal Of Physics D: Applied Physics* **2000**, *33* (23), 3018–3021.

(38) Wang, Y.-T. T.; Whang, W.-T. T.; Chen, C.-H. H. Hollow V_2O_5 Nanoassemblies For High-Performance Room-Temperature Hydrogen Sensors. *Acs Appl Mater Interfaces* **2015**, *7* (16), 8480–7.

(39) Muralidharan, N.; Brock, C. N.; Cohn, A. P.; Schauben, D.; Carter, R. E.; Oakes, L.; Walker, D. G.; Pint, C. L. Tunable Mechanochemistry Of Lithium Battery Electrodes. *Acs Nano* **2017**, *11* (6), 6243–6251.

(40) Fieldhouse, N.; Pursel, S.; Horn, M.; Bharadwaja, S. Electrical Properties Of Vanadium Oxide Thin Films For Bolometer Applications: Processed By Pulse Dc Sputtering. *Journal Of Physics D: Applied Physics* **2009**, *42* (5), 055408.

(41) Pergament; Stefanovich; Kuldin; Velichko. On The Problem Of Metal-Insulator Transitions In Vanadium Oxides. *Isrn Condensed Matter Physics* **2013**, *2013*, 1–6.

(42) Bahlawane, N.; Lenoble, D. Vanadium Oxide Compounds: Structure, Properties, And Growth From The Gas Phase. *Chemical Vapor Deposition* **2014**, *20* (7-8-9), 299–311.

(43) Mansingh, A.; Singh, R.; Krupanidhi, S. B. Electrical Switching In Single Crystal Vo2. *Solid-State Electronics* **1980**, *23* (6), 649–654.

(44) Kagoshima, S. Peierls Phase Transition. *Japanese Journal Of Applied Physics* **1981**, 1617–1634.

(45) Calais, J. Is The Peierls Transition A Transition? *International Journal Of Quantum Chemistry* **1977**, 547–553.

(46) Lépine. Peierls And Spin-Peierls Phase Transitions In Structurally Unstable Quasi-One-Dimensional Solids. *Solid State Communications* **1982**, 375–378.

(47) Gebhard, F. The Mott Metal-Insulator Transition. **2000**.

(48) Montorsi; Rasetti. Mott-Hubbard Metal-Insulator Transition. *Il Nuovo Cimento D* **1994**, 1649–1657.

(49) Fehske; Wellein; Weiße; Göhmann; Büttner; Bishop, A. R. Peierls-Insulator Mott-Insulator Transition In 1d. *Physica B: Condensed Matter* **2002**, 562–563.

(50) Hansmann, P.; Toschi, A.; Sangiovanni, G.; Saha- Dasgupta, T.; Lupi, S.; Marsi, M.; Held, K. Mott–Hubbard Transition In V2o3 Revisited. *Phys Status Solidi B* **2013**, *250* (7), 1251–1264.

(51) Suh; Lopez; Feldman; Haglund. Semiconductor To Metal Phase Transition In The Nucleation And Growth Of Vo2 Nanoparticles And Thin Films. *Journal Of Applied Physics* **2004**, *96* (2), 1209–1213.

(52) Kübler; Ehrke; Huber; Lopez; Halabica; Haglund; Leitenstorfer. Coherent Structural Dynamics And Electronic Correlations During An Ultrafast Insulator-To-Metal Phase Transition In Vo 2. *Physical Review Letters* **2007**, *99* (11).

(53) Tan, Y.; Chen, L.; Wang, D.; Chen, Y.; Akhmadaliev, S.; Zhou, S.; Hong, M.; Chen, F. Tunable Picosecond Laser Pulses Via The Contrast Of Two Reverse Saturable Absorption Phases In A Waveguide Platform. *Sci Rep* **2016**, *6*, 26176.

(54) Qazilbash; Brehm; Chae, B.-G.; Ho, P.-C.; Andreev; Kim, B.-J.; Yun, S.; Balatsky; Maple; Keilmann; Kim, H.-T.; Basov. Mott Transition In Vo2 Revealed By Infrared Spectroscopy And Nano-Imaging. *Science (New York, N.Y.)* **2007**, *318* (5857), 1750–3.

(55) Okimura, K.; Sakai, J.; Ramanathan, S. In Situ X-Ray Diffraction Studies On Epitaxial Vo2 Films Grown On C-Al2o3 During Thermally Induced Insulator-Metal Transition. *Journal Of Applied Physics* **2010**, *107* (6), 063503.

(56) Kshetrimayum, R. S. A Brief Intro To Metamaterials. *Ieee Potentials* **2005**, *23* (5), 44–46.

(57) Shelby. Experimental Verification Of A Negative Index Of Refraction. *Science* **2001**, *292* (5514), 77–79.

(58) Pendry. Negative Refraction. *Contemporary Physics* **2004**, *45* (3), 191–202.

(59) Brun; Guenneau; Movchan. Achieving Control Of In-Plane Elastic Waves. *Applied Physics Letters* **2009**, *94* (6), 061903.

(60) Guenneau, S.; Movchan, A.; Pétursson, G.; Ramakrishna, A. Acoustic Metamaterials For Sound Focusing And Confinement. *New Journal Of Physics* **2007**, *9* (11), 399–399.

(61) Rensberg J, Zhang S, McLeod AS, Schwarz C, Goldflam M, Nawrodt R, Liu M, Kerbusch J, Zhou Y, Ramanathan S, Basov DN. Metasurfaces based on artificially induced phase coexistence in phase-change materials. InNovel Optical Materials and Applications . Optical Society of America **2015**.

(62) Kats, M.; Blanchard, R.; Zhang, S.; Genevet, P.; Ko, C.; Ramanathan, S.; Capasso, F. Vanadium Dioxide As A Natural Disordered Metamaterial: Perfect Thermal Emission And Large Broadband Negative Differential Thermal Emittance. *Physical Review X* **2013**, *3* (4), 041004.

(63) Liu, X.; Padilla, W. J. Thermochromic Infrared Metamaterials. *Adv. Mater. Weinheim* **2016**, *28* (5), 871–5.

(64) Choi; Ahn; Jung; Noh; Kim. Mid-Infrared Properties Of A Vo 2 Film Near The Metal-Insulator Transition. *Physical Review B* **1996**, *54* (7), 4621–4628.

(65) Kim, B.-J.; Lee, Y.; Chae, B.-G.; Yun, S.; Oh, S.-Y.; Lim, Y.-S.; Kim, H.-T. Temperature Dependence Of Mott Transition In Vo_2 And Programmable Critical Temperature Sensor. *Arxiv* **2006**.

(66) Qazilbash, M.; Tripathi, A.; Schafgans, A.; Kim, B.-J.; Kim, H.-T.; Cai, Z.; Holt, M.; Maser, J.; Keilmann, F.; Shpyrko, O.; Basov, D. Nanoscale Imaging Of

The Electronic And Structural Transitions In Vanadium Dioxide. *Arxiv* **2011**, *83* (16).

(67) Kim, H.-T.; Lee, Y.; Kim, B.-J.; Chae, B.-G.; Yun, S.; Kang, K.-Y.; Han, K.-J.; Yee, K.-J.; Lim, Y.-S. Monoclinic And Correlated Metal Phase In Vo 2 As Evidence Of The Mott Transition: Coherent Phonon Analysis. *Physical Review Letters* **2006**, *97* (26).

(68) Kats, M.; Sharma, D.; Lin, J.; Genevet, P.; Blanchard, R.; Yang, Z.; Qazilbash, M.; Basov; Ramanathan, S.; Capasso, F. Ultra-Thin Perfect Absorber Employing A Tunable Phase Change Material. *Applied Physics Letters* **2012**, *101* (22), 221101.

(69) Kats, M.; Blanchard, R.; Zhang, S.; Genevet, P.; Ko, C.; Ramanathan, S.; Capasso, F. Vanadium Dioxide As A Natural Disordered Metamaterial: Perfect Thermal Emission And Large Broadband Negative Differential Thermal Emittance. *Physical Review X* **2013**, *3* (4).

(70) Kats, M.; Blanchard, R.; Zhang, S.; Genevet, P.; Ko, C.; Ramanathan, S.; Capasso, F. Vanadium Dioxide As A Natural Disordered Metamaterial: Perfect Thermal Emission And Large Broadband Negative Differential Thermal Emittance. *Physical Review X* **2013**, *3* (4).

(71) Lu, Y.-R.; Wu, T.-Z.; Chen, C.-L.; Wei, D.-H.; Chen, J.-L.; Chou, W.-C.; Dong, C.-L. Mechanism Of Electrochemical Deposition And Coloration Of Electrochromic V2o5 Nano Thin Films: An In Situ X-Ray Spectroscopy Study. *Nanoscale Research Letters* **2015**, 387.

(72) Liu, Y.; Jia, C.; Wan, Z.; Weng, X.; Xie, J.; Deng, L. Electrochemical And Electrochromic Properties Of Novel Nanoporous Nio/V2o5 Hybrid Film. *Solar Energy Materials And Solar Cells* **2015**, 467–475.

(73) Kumar, S.; Qadir, A.; Maury, F.; Bahlawane, N. Visible Thermochromism In Vanadium Pentoxide Coatings. *Acs Applied Materials & Interfaces* **2017**, *9* (25), 21447–21456.

(74) Nishio, S.; Kakihana, M. Evidence For Visible Light Photochromism Of V2O5. *Cheminform* **2002**, 7–7.

(75) Pierre, A. Introduction To Sol-Gel Processing. **1998**.

(76) Segro, S.; Malik, A. Handbook Of Sample Preparation. **2012**, 419–443.

(77) Grosso, D.; Boissière, C.; Faustini, M. The Sol-Gel Handbook. **2015**, 277–316.

(78) Brinker, J.; Scherer, G. Sol-Gel Science. **1990**, 744–785.

(79) Sladkevich, S.; Mizrahi, S.; Gun, J.; Prikhodchenko, P.; Rizkov, D.; Shelkov, R.; Kyi, N.; Gutkin, V.; Lev, O. Sol-Gel Methods For Materials Processing. **2008**.

(80) Pierre, A. Introduction To Sol-Gel Processing. **1998**.

(81) Hirashima, H.; Sasaki, S.; Gengyou, M. Sol-Gel Processing And Applications. **1994**.

(82) Wheeler, G. Handbook Of Sol-Gel Science And Technology. **2017**.

(83) Dachuan, Y.; Niankan, X.; Jingyu, Z.; Xiulin, Z. Vanadium Dioxide Films With Good Electrical Switching Property. *Journal Of Physics D: Applied Physics* **1996**, *29* (4), 1051–1057.

(84) Livage; Guzman; Beteille; Davidson. Optical Properties Of Sol-Gel Derived Vanadium Oxide Films. *Journal Of Sol-Gel Science And Technology* **1997**, *8* (1-3), 857–865.

(85) Chae, B.-G.; Kim, H.-T.; Yun, S.-J.; Kim, B.-J.; Lee, Y.-W.; Youn, D.-H.; Kang, K.-Y. Highly Oriented Vo[Sub 2] Thin Films Prepared By Sol-Gel Deposition. *Electrochemical And Solid-State Letters* **2006**, *9* (1), C12.

(86) Chen, J.-L. L.; Chang, C.-C. C.; Ho, Y.-K. K.; Chen, C. L.; Hsu, C.-C. C.; Jang, W.-L. L.; Wei, D.-H. H.; Dong, C.-L. L.; Pao, C.-W. W.; Lee, J.-F. F.; Chen, J.-M. M.; Guo, J.; Wu, M.-K. K. Behind The Colour Switching In Gasochromic Vo2. *Phys Chem Chem Phys* **2015**, *17* (5), 3482–9.

(87) Liu, C.; Cao, X.; Kamyshny, A.; Law, J. Y.; Magdassi, S.; Long, Y. Vo/Si-Al Gel Nanocomposite Thermochromic Smart Foils: Largely Enhanced Luminous Transmittance And Solar Modulation. *J Colloid Interface Sci* **2014**, *427*, 49–53.

(88) Greenberg, C. Undoped And Doped Vo2 Films Grown From Vo(Oc3h7)3. *Thin Solid Films* **1983**, *110* (1), 73–82.

(89) Thornton, J. Plasma-Assisted Deposition Processes: Theory, Mechanisms And Applications. *Thin Solid Films* **1983**, *107* (1), 3–19.

(90) Fuls; Hensler; Ross. Reactively Sputtered Vanadium Dioxide Thin Films. *Applied Physics Letters* **1967**, *10* (7), 199–201.

(91) Rozgonyi; Hensler. Structural And Electrical Properties Of Vanadium Dioxide Thin Films. *Journal Of Vacuum Science And Technology* **1968**, *5* (6), 194–199.

(92) Duchene; Terraillon; Pailly. R.F. And D.C. Reactive Sputtering For Crystalline And Amorphous Vo2 Thin Film Deposition. *Thin Solid Films* **1972**, *12* (2), 231–234.

(93) Borek, M.; Qian; Nagabushnam; Singh. Pulsed Laser Deposition Of Oriented Vo2 Thin Films On R- Cut Sapphire Substrates. *Applied Physics Letters* **1993**, 3288–3290.

(94) Kim; Kwok. Pulsed Laser Deposition Of Vo 2 Thin Films. *Applied Physics Letters* **1994**, *65* (25), 3188–3190.

(95) Maaza; Bouziane; Maritz; Mclachlan, D. .; Swanepool; Frigerio, J. .; Every. Direct Production Of Thermochromic Vo2 Thin Film Coatings By Pulsed Laser Ablation. *Optical Materials* **2000**, *15* (1), 41–45.

(96) Sobhan, M. A.; Kivaisi, R. T.; Stjerna; Granqvist, C. G. Thermochromism Of Sputter Deposited Wxv1−Xo2 Films. *Solar Energy Materials And Solar Cells* **1996**, *44* (4), 451–455.

(97) Pauli; Herger; Willmott; Donev; Suh; Haglund. X-Ray Diffraction Studies Of The Growth Of Vanadium Dioxide Nanoparticles. *Journal Of Applied Physics* **2007**, *102* (7), 073527.

(98) Elam, J.; Xiong, G.; Han, C.; Wang, H.; Birrell, J.; Welp, U.; Hryn, J.; Pellin, M.; Baumann, T.; Poco, J.; Satcher, J. Atomic Layer Deposition For The Conformal Coating Of Nanoporous Materials. *Journal Of Nanomaterials* **2006**, *2006*, 1–5.

(99) Musschoot, J.; Deduytsche, D.; Meirhaeghe, R.; Detavernier, C. Ald Of Vanadium Oxide. **2009**, 29–37.

(100) Rampelberg, G.; Schutter, B.; Devulder, W.; Martens, K.; Radu, I.; Detavernier, C. In Situ X-Ray Diffraction Study Of The Controlled Oxidation And Reduction In The V–O System For The Synthesis Of Vo 2 And V 2 O 3 Thin Films. *J. Mater. Chem. C* **2015**, *3* (43), 11357–11365.

(101) Mattelaer, F.; Geryl, K.; Rampelberg, G.; Dendooven, J.; Detavernier, C. Amorphous And Crystalline Vanadium Oxides As High-Energy And High-Power

Cathodes For Three-Dimensional Thin-Film Lithium Ion Batteries. *Acs Appl Mater Interfaces* **2017**, *9* (15), 13121–13131.

(102) Rampelberg, G.; Deduytsche, D.; Schutter, B.; Premkumar, P.; Toeller, M.; Schaekers, M.; Martens, K.; Radu, I.; Detavernier, C. Crystallization And Semiconductor-Metal Switching Behavior Of Thin Vo2 Layers Grown By Atomic Layer Deposition. *Thin Solid Films* **2014**, *550*, 59–64.

(103) Rampelberg, G.; Schutter, B.; Devulder, W.; Martens, K.; Radu, I.; Detavernier, C. In Situ X-Ray Diffraction Study Of The Controlled Oxidation And Reduction In The V–O System For The Synthesis Of Vo 2 And V 2 O 3 Thin Films. *J. Mater. Chem. C* **2015**, *3* (43), 11357–11365.

(104) Peter, A.; Martens, K.; Rampelberg, G.; Toeller, M.; Ablett, J.; Meersschaut, J.; Cuypers, D.; Franquet, A.; Detavernier, C.; Rueff, J.-P.; Schaekers, M.; Elshocht, S.; Jurczak, M.; Adelmann, C.; Radu, I. Metal-Insulator Transition In Ald Vo 2 Ultrathin Films And Nanoparticles: Morphological Control. *Advanced Functional Materials* **2015**, *25* (5), 679–686.

(105) Premkumar; Toeller; Radu; Adelmann; Schaekers; Meersschaut; Conard; Elshocht. Process Study And Characterization Of Vo2 Thin Films Synthesized By Ald Using Temav And O3 Precursors. *Ecs Journal Of Solid State Science And Technology* **2012**, *1* (4), P169–P174.

(106) Manning, T.; Parkin, I.; Clark, R.; Sheel, D.; Pemble, M.; Vernadou, D. Intelligent Window Coatings: Atmospheric Pressure Chemical Vapour Deposition Of Vanadium Oxides. *Journal Of Materials Chemistry* **2002**, 2936–2939.

(107) Field; Parkin. Atmospheric Pressure Chemical Vapour Deposition Of Vanadium(V) Oxide Films On Glass Substrates From Reactions Of Vocl3 And Vcl4 With Water. *Journal Of Materials Chemistry* **2000**, 1863–1866.

(108) Manning, T.; Parkin, I. Vanadium(Iv) Oxide Thin Films On Glass And Silicon From The Atmospheric Pressure Chemical Vapour Deposition Reaction Of Vocl3 And Water. *Polyhedron* **2004**, *23* (18), 3087–3095.

(109) Szörényi; Bali; Hevesi. Structural Characterization Of Amorphous Vanadium Pentoxide Thin Films Prepared By Chemical Vapour Deposition /Cvd/. *Journal Of Non-Crystalline Solids* **1980**, *35*, 1245–1248.

(110) Vernardou; Pemble, M. E.; Sheel, D. W. Tungsten- Doped Vanadium Oxides Prepared By Direct Liquid Injection Mocvd. *Chemical Vapor Deposition* **2007**, *13* (4), 158–162.

(111) Barreca, D.; Armelao, L.; Caccavale, F.; Noto, V.; Gregori, A.; Rizzi, G.; Tondello, E. Highly Oriented V2o5nanocrystalline Thin Films By Plasma-Enhanced Chemical Vapor Deposition. *Chemistry Of Materials* **2000**, 98–103.

(112) Warwick, M.; Ridley, I.; Binions, R. Thermochromic Vanadium Dioxide Thin Films From Electric Field Assisted Aerosol Assisted Chemical Vapour Deposition. *Surface And Coatings Technology* **2013**, 163–167.

(113) Warwick, M.; Binions, R. On The Effects Of Electric Fields In Aerosol Assisted Chemical Vapour Deposition Reactions Of Vanadyl Acetylacetonate Solutions In Ethanol. *Journal Of Nanoscience And Nanotechnology* **2011**, 8126–8131(6).

(114) Yin, H.; Yu, K.; Peng, H.; Zhang, Z.; Huang, R.; Travas-Sejdic, J.; Zhu, Z. Porous V 2 O 5 Micro/Nano-Tubes: Synthesis Via A Cvd Route, Single-Tube-Based Humidity Sensor And Improved Li-Ion Storage Properties. *Journal Of Materials Chemistry* **2012**, 5013–5019.

(115) Wang; Su; Chen; Yu; Han; Wang; Xin; Lan; Liu. Low Temperature Growth Of Vanadium Pentoxide Nanomaterials By Chemical Vapour Deposition Using Vo(Acac)2 As Precursor. *Journal Of Physics D: Applied Physics* **2010**, *43* (18), 185102.

(116) Louloudakis; Vernardou; Spanakis; Katsarakis; Koudoumas. Electrochemical Properties Of Vanadium Oxide Coatings Grown By Apcvd On Glass Substrates. *Surface And Coatings Technology* **2013**, *230*, 186–189.

(117) Mathur, S.; Barth, S. Molecule- Based Chemical Vapor Growth Of Aligned Sno2 Nanowires And Branched Sno2/V2o5 Heterostructures. *Small* **2007**, *3* (12), 2070–2075.

(118) Okuhara; Inumaru; Misono; Matsubayashi. Studies In Surface Science And Catalysis. *Part B* **1993**, 1767–1770.

(119) Crociani, L.; Carta, G.; Natali, M.; Rigato, V.; Rossetto, G. Mocvd Of Vanadium Oxide Films With A Novel Vanadium(Iii) Precursor. *Chemical Vapor Deposition* **2011**, *17* (1- 3), 6–8.

(120) Okuhara; Inumaru; Misono; Matsubayashi. Studies In Surface Science And Catalysis. *Part B* **1993**, 1767–1770.

(121) Mantoux; Groult; Balnois; Doppelt; Gueroudji. Vanadium Oxide Films Synthesized By Cvd And Used As Positive Electrodes In Secondary Lithium Batteries. *Journal Of The Electrochemical Society* **2004**, *151* (3), A368.

(122) Godlewski, M. Atomic Layer Deposition. *Semiconductor Science And Technology* **2012**, 070301.

(123) Kääriäinen, T.; Cameron, D.; Kääriäinen, M.-L.; Sherman, A. Atomic Layer Deposition. **2013**, 243–253.

(124) Witzani; Hörl. Scanning Electron Mirror Microscopy. *Scanning* **1981**, 53–61.

(125) Mcmullan. Scanning Electron Microscopy 1928–1965. *Scanning* **1995**, 175–185.

(126) Ichinokawa, T.; Iiyama, M.; Onoguchi, A.; Kobayashi, T. Charging Effect Of Specimen In Scanning Electron Microscopy. *Japanese Journal Of Applied Physics* **1974**, 1272–1277.

(127) Fischer, E.; Hansen, B.; Nair, V.; Hoyt, F.; Dorward, D. Scanning Electron Microscopy. *Current Protocols In Microbiology* **2012**, Unit 2b.2.

(128) Zhang, H.-B.; Feng, R.-J.; Ura, K. Utilizing The Charging Effect In Scanning Electron Microscopy. *Science Progress* **2004**, 249–68.

(129) Fitting, H.; Kuhr, J.; Goldberg, M.; Becher, B.; Barfels, T. Edx Depths Analysis Of Mis-Structures. *Mikrochimica Acta* **1997**, 235–238.

(130) Loretto, M. H. Medium-Voltage Edx And Eels. *Ultramicroscopy* **1989**, 302–307.

(131) Kinoshita, H.; Tanaka, N.; Jamal, M.; Kumihashi, M.; Okuzono, R.; Tsutsui, K.; Ameno, K. Application Of Energy Dispersive X-Ray Fluorescence Spectrometry (Edx) In A Case Of Methomyl Ingestion. *Forensic Science International* **2012**, 103–105.

(132) Suzuki, S. Electron Backscatter Diffraction Method. *Journal Of The Japan Welding Society* **2016**, 736–739.

(133) Randle, V. Advances In Electron Backscatter Diffraction. *Materials Science And Technology* **2006**, 1261–1261.

(134) Day, A. Electron Backscatter Diffraction In Materials Science. **2009**.

(135) Staples, L. Friedrich Mohs And The Scale Of Hardness. **1964**.

(136) Cu. Hardness Tests. *Nature* **1923**, 242–243.

(137) Gerberich, W.; Ballarini, R.; Hintsala, E.; Mishra, M.; Molinari, J.; Szlufarska, I. Toward Demystifying The Mohs Hardness Scale. *Journal Of The American Ceramic Society* **2015**, 2681–2688.

(138) Hillier. X-Ray Diffraction And The Identification And Analysis Of Clay Minerals. *Clay Minerals* **1999**, 210–211.

(139) Graham, R. X-Ray Diffraction And The Identification And Analysis Of Clay Minerals. *Soil Science* **1999**, 72–73.

(140) Wenner. A Method Of Measuring Earth Resistivity. *Bulletin Of The Bureau Of Standards* **1916**, 469.

(141) Wenner, F. A Method For Measuring Earth Resistivity. *Journal Of The Franklin Institute* **1915**, 373–375.

(142) Schuetze, A.; Lewis, W.; Brown, C.; Geerts, W. A Laboratory On The Four-Point Probe Technique. *American Journal Of Physics* **2004**, 149–153.

(143) Woodward. Raman Spectroscopy. **1970**, 1–31.

(144) Mccubbin, F. Raman Spectroscopy. **2014**, 1–1.

(145) Steger. Raman Spectroscopy. **1970**.

(146) Gordon, K.; Mcgoverin, C. Raman Mapping Of Pharmaceuticals. *International Journal Of Pharmaceutics* **2010**, 151–62.

(147) Ropret, P.; Miliani, C.; Centeno, S. Raman Imaging. **2012**.

(148) Burgess, C. Uv-Vis Spectroscopy. *Trac Trends In Analytical Chemistry* **1993**, X.

(149) Ago, H. Uv/Vis Spectroscopy. *Journal Of The Japan Society Of Colour Material* **2005**, 531–538.

(150) Perkampus, H.-H.; Perkampus, H.-H. Uv-Vis Spectroscopy And Its Applications. **1992**, 10–25.

(151) Tauc, J.; Grigorovici, R.; Vancu, a. Optical Properties and Electronic Structure of Amorphous Germanium. Phys. Status Solidi 1966, 15 (2), 627–637.

(152) Sangiorgi, N.; Aversa, L.; Tatti, R.; Verucchi, R.; Sanson, A. Spectrophotometric Method For Optical Band Gap And Electronic Transitions Determination Of Semiconductor Materials. *Optical Materials* **2017**, 18–25.

(153) Mcmahon. Thermal Radiation From Partially Transparent Reflecting Bodies. *Journal Of The Optical Society Of America* **1950**, 376.

(154) Weinberg. Correction To “Kirchoff”S Third And Fourth Laws’. *Ire Transactions On Circuit Theory* **1958**, 139–139.

(155) Crepeau, J. Josef Stefan: His Life And Legacy In The Thermal Sciences. *Experimental Thermal And Fluid Science* **2007**, 795–803.

(156) Lima, J. De; Santos. Generalized Stefan-Boltzmann Law. *International Journal Of Theoretical Physics* **1995**, 127–134.

(157) Shaham, Y.; Schellhase. High-Performance Ir Cameras. **1996**, 316.

(158) Horn, S.; Lohrmann, D.; Campbell, J.; Perconti, P.; Balcerak, R. Uncooled Ir Technology And Applications. **2001**, 210–221.

(159) Wode, S.-A. Active Spatial Resolution Enhancement For Cooled Ir Cameras. **2017**.

(160) Bae, S.; Kim, Y.-H.; Kim, B.-H.; Lee, H.-J.; Jung, H. Current Status Of Cooled Ir Detectors At I3system. **2014**

(161) Planinsic, G. Infrared Thermal Imaging: Fundamentals, Research And Applications. *European Journal Of Physics* **2011**, 1431.

(162) Reynolds, W. Toward Quantifying Infrared Clutter. **1990**, 232–240.

4. Results and Discussions

4.1 Synthesis of Vanadium oxide films with controlled morphologies: Impact on the metal insulator transition behaviour

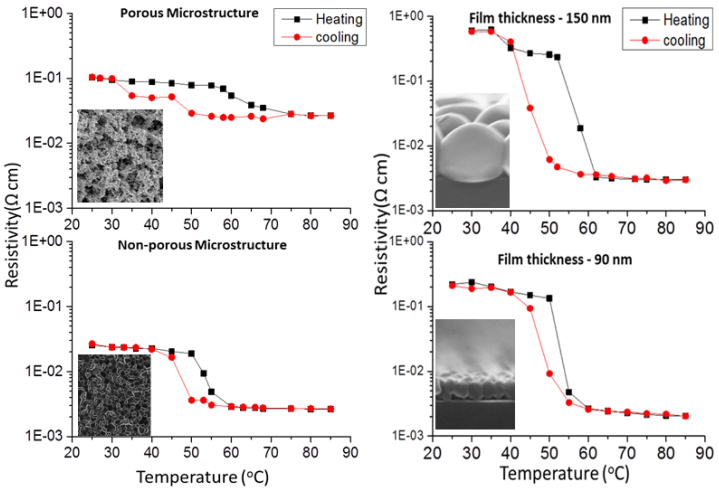

Vanadium oxide films with various morphologies were synthesised by controlling the CVD parameters. SMT behaviour depends greatly on the film porosity and thickness. Temperature of deposition, partial pressure of deposition and precursor concentration play a vital role in determining the morphology of the film which ultimately impacts the SMT.

Published as Kumar S, Lenoble D, Maury F. and Bahlawane N. Synthesis of vanadium oxide films with controlled morphologies: Impact on the metal–insulator transition behaviour. *Phys. Status Solidi A*, 212: 1582–1587 (2015)

Abstract

Precise control over the growth of VO_2 films with different morphologies is achieved by varying the deposition parameters in the DLI-MOCVD process such as temperature, pressure, concentration of precursor and time of deposition. In this study, thin films of VO_2 with wide range of morphologies having Metal to Insulator Transition (MIT) temperature of (t_c) 52^oC were deposited. Adjusting the process parameters has allowed the growth of highly porous nanocrystalline films and dense microcrystalline films with controlled crystallite size up to several hundred nanometres. Vanadium (V) oxy tri-isopropoxide was used in this study as a single source precursor. Porous films lead to a diffuse change in resistivity across the transition temperature while the crystalline films have sharp and high resistivity drop (Δρ). This enabled a qualitative study of the MIT behaviour with respect to the microstructure of the films and correlates the effect of deposition conditions to the obtained morphologies. Fine control over the morphology without additional doping or post deposition process provides the ability to tailor VO_2 thin films for their respective applications.

1 Introduction

Vanadium (IV) oxide (VO_2) undergoes a reversible phase transition from an insulating monoclinic to a conducting rutile structure around the transition temperature (t_c) 68–70^oC [1]. Intrinsic material properties like electrical resistivity, optical transmission and mechanical strain undergo abrupt changes occurring at MIT [2]. This remarkable behaviour of the material has sparked immense interest and has been actively researched for potential applications ranging from ultra-fast nanoelectronic switches, transistors, thermoelectric devices and thermochromic smart windows [3–6].

In most cases, however, the focus is always mainly on reducing the T_c closer to room temperature. Doping with impurities is one way to reduce the T_c but resulted in sacrificing the sharpness of the phase transition [7–10]. Thin undoped nanocrystalline VO_2 films were reported exhibiting the MIT at T_c as low as 55 ^oC.

The growth of single phase VO_2 remains a challenge due to the fact that a number of stable phases of vanadium oxides could form in a narrow range of composition, thus, requiring a strict control on growth conditions for obtaining a single pure phase of VO_2 [11]. Various types of thin film deposition techniques have been employed for VO_2 film synthesis like pulsed laser deposition (PLD) [5, 12], molecular beam epitaxy (MBE) [3], magnetron sputtering [13], chemical vapour deposition (CVD) [14–17], sol–gel processing [18, 19] and atomic layer deposition [20– 22]. In this study, we use direct liquid injection–metal organic chemical vapour deposition (DLI–MOCVD) and a single source precursor to grow VO_2 films of varying thickness and microstructure.

Several authors have reported results correlating the film thickness, grain size and crystallinity with the MIT [23–26] and provided rather conflicting views relating film morphology and MIT behaviour as each case has only one or limited types of morphologies being studied.

Therefore, it is important to properly understand this property with respect to various microstructures and their influence on the grain boundary density and crystallinity. In this study, we grow single phase VO_2 films of various morphologies and crystallinities by varying the deposition parameters to compare the MIT behaviour, hysteresis width (ΔT) and Δp corresponding to each unique microstructure

2 Experimental

2.1 Deposition of VO_2 Thin films of VO_2 were deposited on silicon substrates by DLI–MOCVD in a warm wall vertical stagnation point flow reactor. Low concentration (5 10^3 M) ethanol solutions of 99.9% pure V oxy-tri-isopropoxide ([$VO(O^iPr)_3$] were used as the precursor. Liquid injection was performed in an evaporation tube maintained at 200°C to secure an instantaneous vaporization of the precursor solution. Substrates were maintained at a constant temperature within the 400–600°C range during deposition. The precursor injection was maintained at 4 Hz with 2 ms opening time resulting in a liquid flow rate of 2.5 ml

min^{1}. Nitrogen was used as the carrier gas with a flow rate, 40 sccm and the chamber pressure being adjusted in the 3–9 mbar range.

Time of deposition was adjusted from 15 to 180min allowing the growth of different film thicknesses. Substrates were allowed to cool to room temperature in nitrogen atmosphere under vacuum before withdrawing from the chamber and no post deposition annealing was performed. All the samples were handled in air after deposition.

2.2 Characterization Film thickness was measured using an Alpha step d-500 Profilometer from KLA-Tencor and FEI Helios Nanolab 650^{TM} scanning electron microscope (SEM). Surface and cross-sectional morphologies were characterized by SEM at a working distance of 4mm with 25kV voltage.

X-ray diffraction (XRD) was used to characterize the films using the Bruker D8, with CuK_a as the X-ray source. Data were collected in the Θ–2Θ (locked couple) mode from 2Θ of 20 to 60 ^{o} with a step size of 0.05 ^{o}.

Raman spectroscopy was performed using an InVia Raman spectrometer from Renishaw with a 532 nm laser at low power of 0.2mW to avoid non-controlled surface heating and the resulting phase transition upon laser irradiation. The resistivity of the films was measured using a Hall effect measurement system HMS-3000 in van der Pauw configuration. Temperature-dependent resistivity measurements were performed by placing the sample on a heating stage, while a thermocouple was placed on the sample to measure the surface temperature.

The characterization techniques employed in this study provide complementary insights to understand the interplay between the growth control parameters, film characteristics and the corresponding MIT behaviour.

3 Results and discussion CVD enables a convenient number of parameters of deposition namely (i) temperature of deposition, (ii) chamber pressure, (iii) concentration of the precursor and (iv) time of deposition. The main objective of this study is to obtain different morphologies of VO_2 by varying the growth parameters and to investigate their impact on MIT behaviour.

3.1 Deposition temperature An increase in grain size and crystalline morphology is observed when the temperature of deposition was increased from 450 to 600 ^{o}C. Figure 1 shows SEM micrographs of films deposited at various temperatures. It depicts a transition of morphology from a porous nanocrystalline to a compact microcrystalline to well-formed large crystallites of VO_2. Thickness of the resulting films was measured at 1.4mm, 800 and 200nm for the deposition temperatures of 450, 500 and 600°C, respectively.

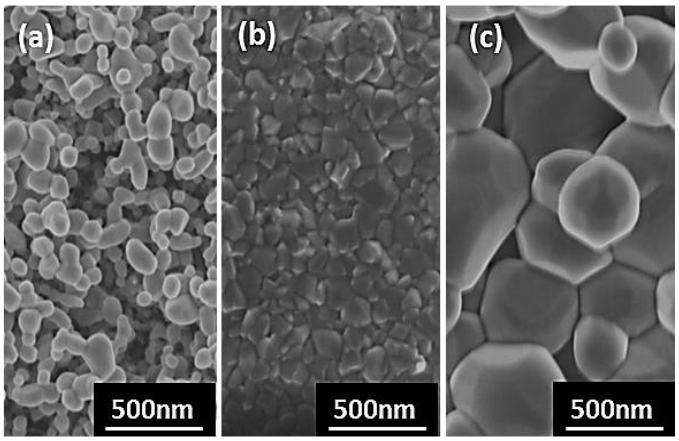

Figure 1 SEM micrographs of VO_2 films (a) (b) and (c) deposited at 450°C, 500°C and 600°C respectively. (Chamber pressure of 6 mbar). The average grain size is (a) 14.8nm, (b) 15nm and (c) 130 nm

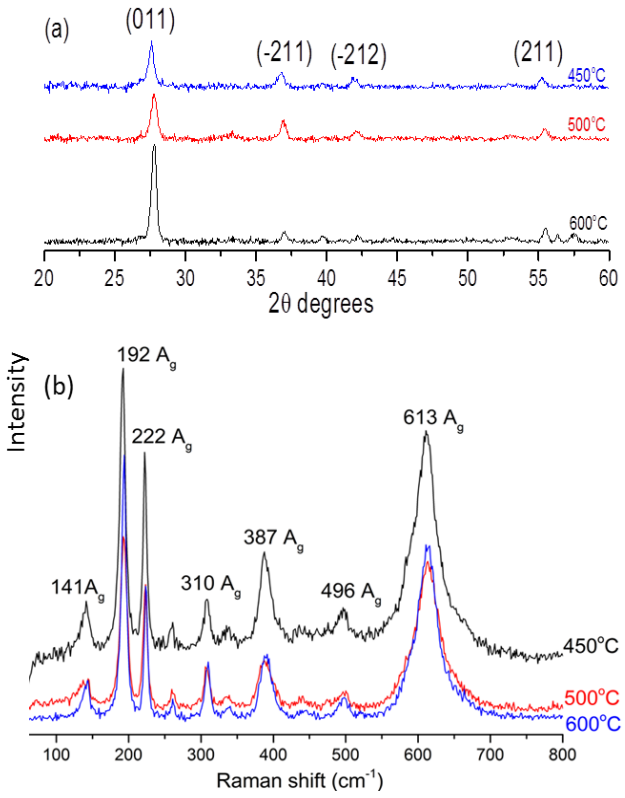

Figure 2 **X-Ray Diffraction (a) and Raman spectra (b) of films deposited at 450°C, 500°C and 600oC respectively. The peaks indicated for XRD correspond to PDF data card no. 00-009-0142 [8,24,27] and Raman peaks observed also indicate the formation of monoclinic VO2. [27–31]**

X-ray diffractograms and Raman spectra, shown in Fig. 2, reveal single phase growth of monoclinic VO_2 in this temperature range, Raman vibrational peaks observed at 141,192, 222, 310, 387, 496 and 613 all correspond to Ag mode VO_2. No significant change was observed in the Raman spectra when the deposition temperature was increased from 450 to 600°C.

3.2 Precursor concentration Film thickness and microstructure depend on precursor concentration for MOCVD process, a 2.5 and 5mM of V oxy tri-isopropoxide in absolute ethanol solution was used as the precursor.

At 500°C, VO_2 films with high porosity and thickness of 2.2mm were grown with a 5mM concentrated precursor solution which contrasts the films grown at 2.5mM featuring a smooth surface comprising individual large crystallites of VO_2 of thickness 190nm forming across the surface as shown in Fig. 3.

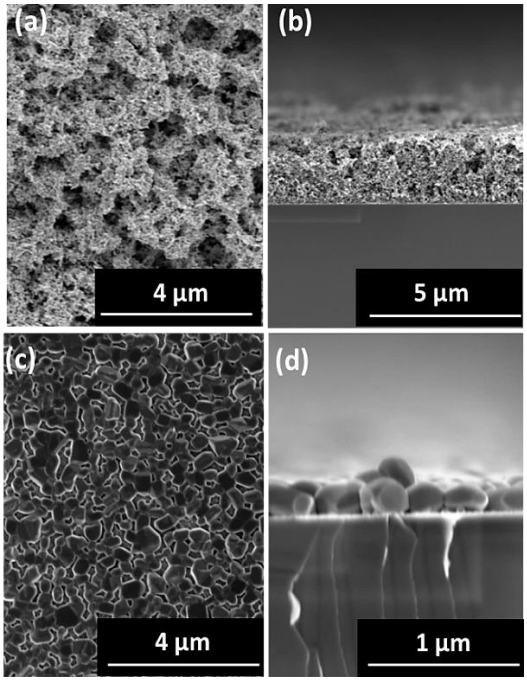

Figure 3 (a, c) Surface & (b, d) cross-section SEM micrographs of VO_2 films grown at 500oC with 5 (a, b) and 2.5mM (c, d) precursor concentration at total pressure 9 mbar)

3.3 Deposition time Highly crystalline well ordered VO_2 films were grown with 2.5mM precursor concentration. Shown in Fig. 4 are cross-section SEM micrographs of films deposited at 575 ^{o}C for 15, 30 and 120min, revealing film thicknesses of 90, 150 and 720nm, respectively. The film thickness at different times corresponds to a constant growth rate (5.6) nm/min without an incubation time.

The crystals grew anisotropically while retaining the single layer morphology. Hence, the increase in the film thickness is due to the growth and the merging of individual grains rather than a formation of multi-layered film composed of several microcrystalline grains. This structure reveals the high surface diffusion of the deposition species.

3.4 Chamber pressure with increasing chamber pressure, the films exhibit an increase in the surface roughness as shown in Fig. 5. The two-dimensional morphology at low pressure is partially replaced by a three-dimensional flaky sheet. Although cross-section inspection shows that early stage of deposition

yields a similar morphology in the 3–9 mbar pressure range. It is evident from Fig. 5e and f that formation of these flakes is favoured at higher chamber pressures, while simultaneously resulting in films with increased porosity and surface roughness. On close inspection of the flakes shown in Fig. 6, it was revealed that they are in fact formed by the aggregation of nanocrystalline grains of VO2 similar to the film shown in Fig. 1a. These small nanocrystalline grains grew upwards at higher pressure and form a microstructure similar to petals in a rose flower. This type of morphology can be very well suited to gas sensing or absorbing applications where high porosity combined with high and accessible surface area play a key role in determining the effectiveness of the device.

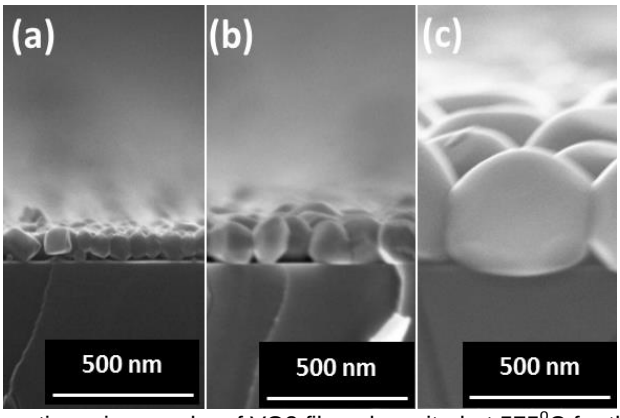

Figure 4 SEM cross-section micrographs of VO2 films deposited at 575°C for the duration of (a) 15, (b) 30 and (c) 120 minutes

3.5 MIT behaviour of different morphologies It is important to note that due to seemingly numerous ways of synthesising VO_2 films exhibiting MIT behaviour and equally varied number if not more ways of measuring this transition, a wide variety of measurement procedures have been reported like resistivity, transmittance, Raman spectra across the тс. To be able to compare the ΔT and тс for different morphologies, we chose a simple four-point probe resistivity measurement system, which sounds as the most prevalent method depicting the quality of films while still obtaining enough information about the films characteristics. Electrical resistivity of the films was measured during heatingandcoolingofthesampleinthe20–90°Ctemperature window.

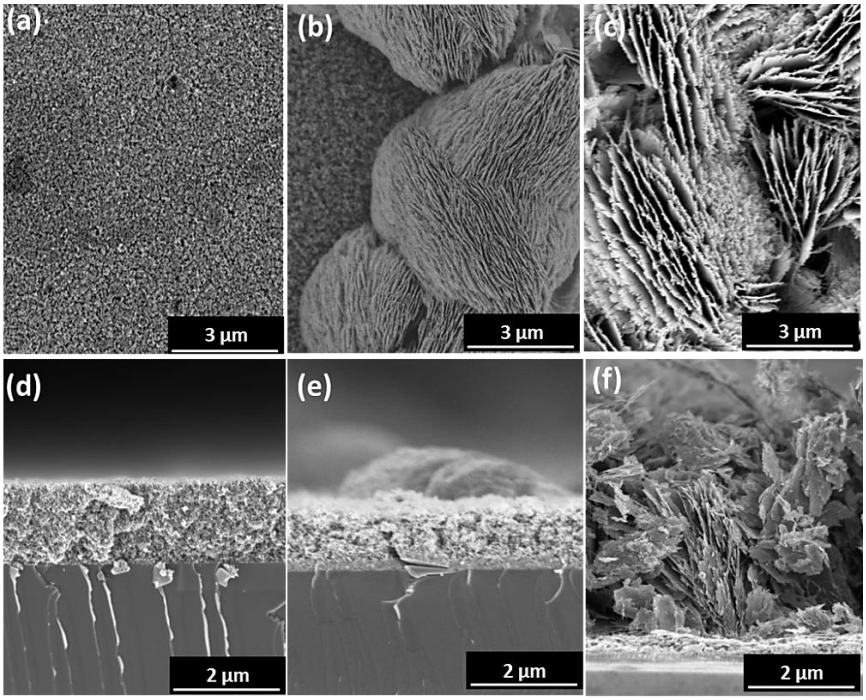

Figure 5 (a) (b) (c) are SEM surface micrographs and (d) (e) (f) are the cross section of VO2 films deposited at chamber pressure 3, 6 and 9 mbar respectively. (Temperature – 450°C, concentration – 2.5mM)

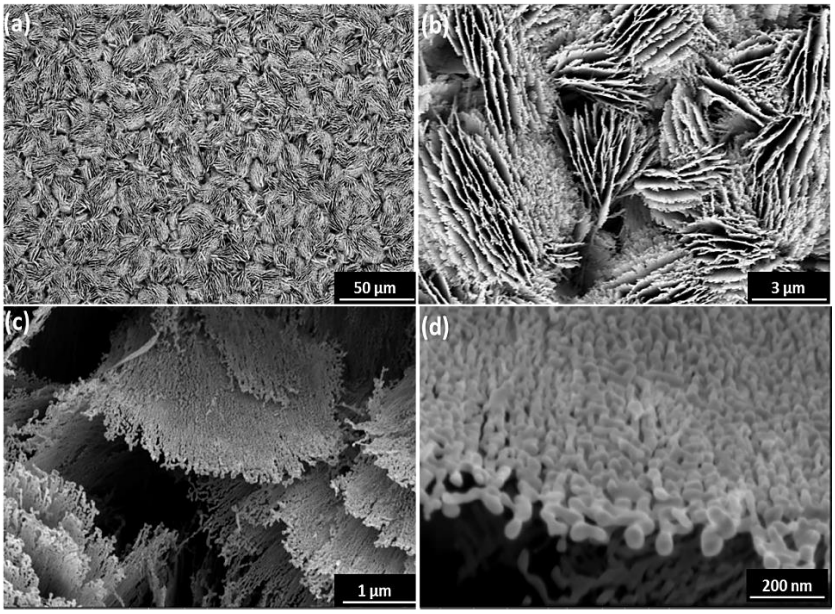

Figure 6 Surface micrographs of VO2 film grown at 9-mbar shown at different magnifications. (Temperature – 450°C, concentration – 2.5mM).The average grain size is ~ 16.45 nm.

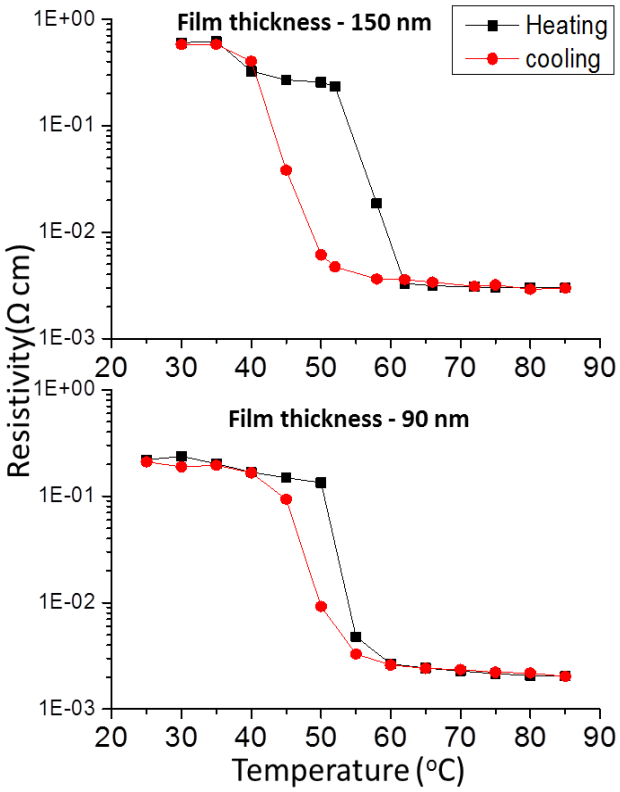

Figure 7 Comparison of the MIT behaviour of VO_2 film of thickness 150 nm and 90 nm for the top and bottom plot respectively.

This offers a convenient way to measure ΔT which does not extend beyond this temperature interval. It is widely reported that τc of VO_2 bulk crystals is between 68–72°C [1] with the ratio of resistivity in insulating (monoclinic) phase to the metallic (rutile) phase of the order of 10^5. Epitaxial films were reported to exhibit similar properties seen in single-bulk crystals [12, 32]. Whereas polycrystalline films have the tendency to have a smaller-resistivity drop and broader-hysteresis curve [5, 33, 34]. The top and bottom hysteresis plots shown in Fig. 7 correspond to the films depicted in Fig. 4a and b, respectively, which have similar morphology. The films are composed of a single layer of well-formed grains. VO2 film in Fig.4 a resembles an epitaxial film in appearance with all grains having the same size and shape resulting in higher resistivity drop (Δp) and a narrow ΔT of 78°C.While the film in Fig. 4b has a larger grain size but lack uniform size distribution as observed in thinner films, resulting in a broader ΔT of 12°C. Films with higher density of grain boundaries and smaller grain size exhibit a diffuse MIT behaviour with a broad **Δ**T. The T_c for both film morphologies is same at

52°C in the heating phase. In Fig. 8, the top and bottom hysteresis curves correspond to the morphologies as shown in Fig. 1a (porous) and b (compact), respectively. Due to the smaller grain size and the porosity of the film in Fig. 1a, **Δρ** is diminished and the **ΔT** is broadened. Films with a compact microstructure, as shown in Fig.1b, exhibit a narrower **ΔT** and sharper **Δρ** compared to a porous film. It is, however, interesting to note that the MIT temperature remains relatively unchanged at 52 ^{o}C during the heating phase irrespective of the microstructure. On comparing the hysteresis curves obtained from the morphologies of Figs. 4a and 1b shown as the bottom curves of Figs. 7 and 8; we observe a higher **Δρ** and lower **Δ**T for films with better crystallinity.

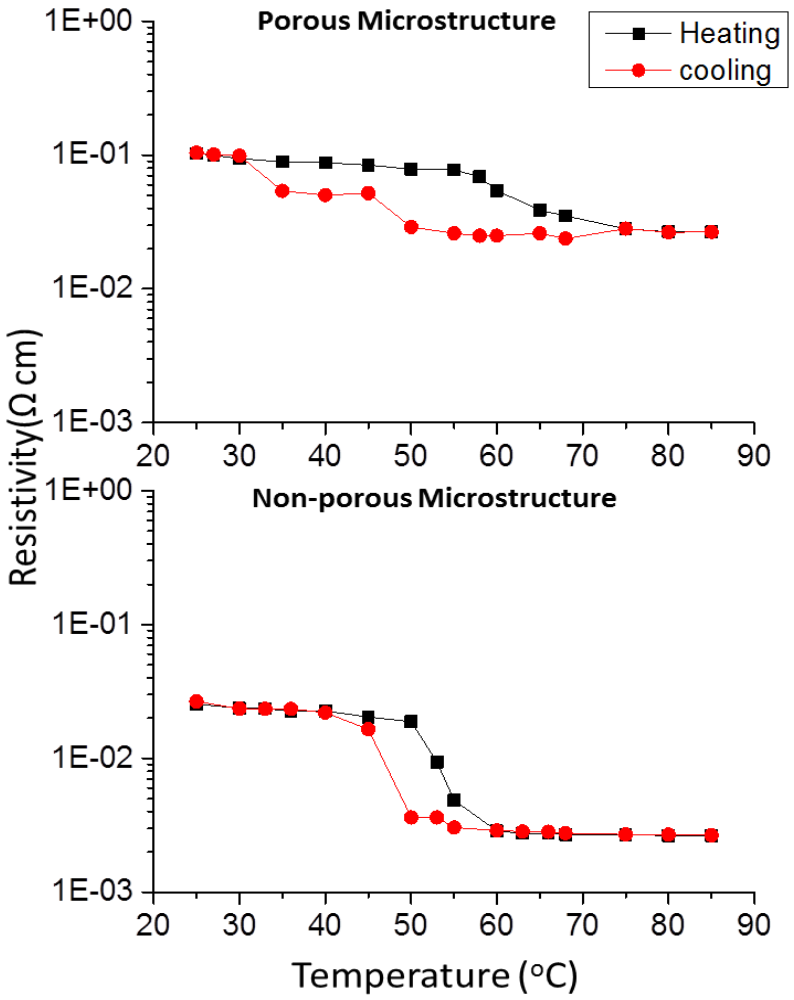

Figure 8 Comparison of the MIT behaviour of VO_2 with porous (top) and compact (bottom) films with the thickness of 1.4 µm each.

4 Conclusions

Thin films of Vanadium dioxide with different microstructures and morphologies were grown by MOCVD starting from [VO(OiPr)3]. This process was used to grow films of thickness ranging from 90 nm to 3 µm with fine control over porosity, crystallinity and grain size. This study reveals that morphology of VO2 plays a pivotal role on the MIT behaviour. Film thickness, grain size, porosity, crystallinity and shape of the crystallites all have an impact on the ΔT, Δρ and Tc. Having achieved a precise control over the growth of the films and the resulting microstructure, we have the freedom and ability to fine tune the film growth and MIT as per the desired application.

References

1. F. J. Morin, Phys. Rev. Lett. 3(1), 34–36 (1959).
2. J. Nag and R. Jr, J. Phys.: Condens. Matter 20, 264016 (2008).
3. Z. Yang, C. Ko, and S. Ramanathan, Annu. Rev. Mater. Res. 41, 337–367 (2011).
4. A. L. Pergament, G. B. Stefanovich, and A. A. Velichko, J. Sel. Top. Nanoelectron. Comput. 24–43 (2013).
5. M. Warwick and R.Binions, J.Mater.Chem.A2,3275–3292 (2013).
6. M. A. Kats, R. Blanchard, S. Zhang, P. Genevet, C. Ko, S. Ramanathan, and F. Capasso, Phys. Rev. X 3(4), 041004 (2013).
7. D. Vernardou, M. E. Pemble, and D. W. Sheel, Chem. Vap. Depos. 13, 158–162 (2007).
8. C. Piccirillo, R. Binions, and I.P. Parkin, Chem. Vap. Depos. 13, 145–151 (2007).
9. T. Manning, I. Parkin, C. Blackman, and U. Qureshi, J. Mater. Chem. 15, 4560–4566 (2005).
10. A. Gentle, A. Maaroof, and G. Smith, Nanotechnology 18, 025202 (2007).
11. N. Bahlawane and D. Lenoble, Chem. Vap. Depos. 20, 299– 311 (2014).

12. K. Martens, N. Aetukuri, J. Jeong, M. G. Samant, and S.S. Parkin, Appl. Phys. Lett. 104(8), 081918 (2014).
13. J. B. Kana, J. M. Ndjaka, G. Vignaud, A. Gibaud, and M. Maaza, Opt. Commun. 284(3), 807–812 (2011).
14. M. Field and I. Parkin, J. Mater. Chem. 10, 1863–1866 (2000).
15. T. Manning and I. Parkin, J. Mater. Chem. 14, 2554–2559 (2004).
16. M.E. Warwick and R. Binions,J.SolidStateChem.214,53– 66 (2014).
17. L. Crociani, G. Carta, M. Natali, V. Rigato, and G. Rossetto, Chem. Vap. Depos. 17,6-8 (2011)
18. J. Livage, G. Guzman, F. Beteille, and P. Davidson, J. Sol-Gel Sci. Technol. 8, 857–865 (1997).
19. J. Livage, Solid State Ion. 86–88, 935–942 (1996).
20. I. Muylaert, J. Musschoot, K. Leus, J. Dendooven, C. Detavernier, and P. Van Der Voort, Eur. J. Inorg. Chem. 2012, 251–260 (2012).
21. J. Musschoot, D. Deduytsche, R. L. Van Meirhaeghe, and C. Detavernier, ECS Trans. 25(4), 29–37 (2009).
22. G. Rampelberg, K. Devloo-Casier, D. Deduytsche, M. Schaekers, N. Blasco, and C. Detavernier, Low temperature plasma-enhanced ALD of vanadium nitride as copper diffusion barrier, in: 13th Int. Conf. on Atomic Layer Deposition (ALD 2013).
23. J. Y. Suh, R. Lopez, L. C. Feldman, and R. F. Haglund, Jr, J. Appl. Phys. 96(2), 1209–1213 (2004).
24. M. Miller and J. Wang, J. Appl. Phys. 117, 034307 (2015).
25. A. P. Peter, K. Martens, G. Rampelberg, M. Toeller, J. M. Ablett, J. Meersschaut, D. Cuypers, A. Franquet, C. Detavernier, J.-P. Rueff, M. Schaekers, S. Van Elshocht, M.Jurczak, C.Adelmann,and I.P.Radu, Adv.Funct.Mater. DOI 10.1002/adfm.201402687 (2014).
26. L. Hongwei, L. Junpeng, Z. Minrui, T.S. Hai, S.C. Haur, Z. Xinhai, K. Lin, Opt. Express 22, 30748–30755 (2014).
27. X. J. Wang, H. D. Li, Y. J. Fei, X. Wang, Y. Y. Xiong, Y. X. Nie, and K. A. Feng, Appl. Surf. Sci. 177(1), 8–14 (2001).

28. C. Wen, L. Mai, J. Peng, Q. Xu, and Q. Zhu, J. Solid State Chem. 177(1), 377–379 (2004).
29. V. S. Vikhnin, I. N. Goncharuk, V. Y. Davydov, F. A. Chudnovskii, and E. B. Shadrin, Phys. Solid State 37, 1971– 1978 (1995).
30. R.G. Maniand S.Ramanathan, Appl.Phys. Lett.91,062104 (2007).
31. P. Schilbe, Physica B 316, 600–602 (2002).
32. T.-H. Yang, J. Mater. Res. 25(3), 422–426 (2010).
33. T. D. Manning and I. P. Parkin, Polyhedron 23(18), 3087– 3095 (2004).
34. N. Nandakumar and E. Seebauer, Thin Solid Films 519, 3663–3668 (2011).

4.2 Electrical switching in semiconductor-metal self-assembled VO_2 disordered metamaterial coatings.

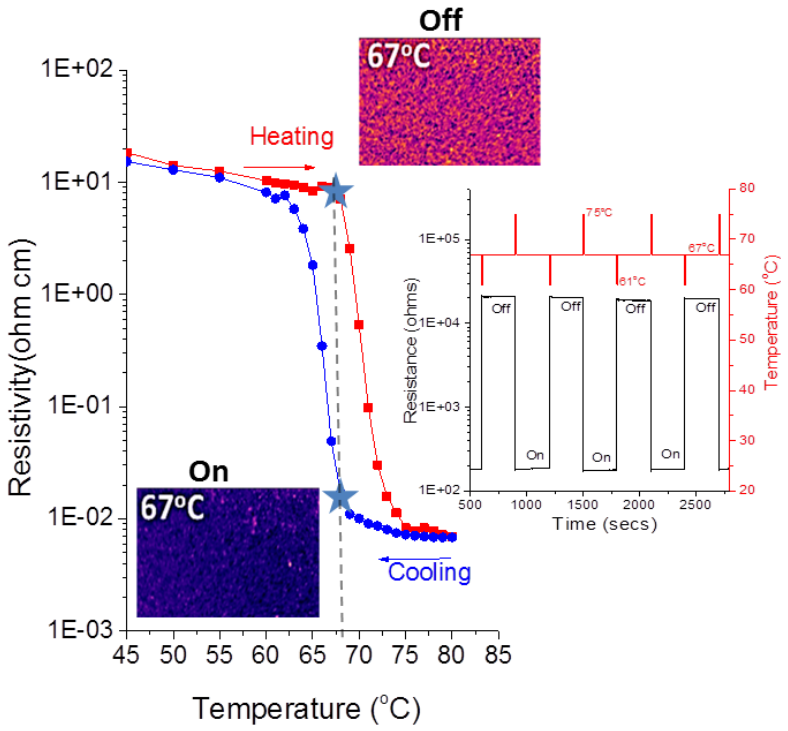

VO_2 coatings were grown by implementing the oxidative sintering technique. The films feature an electrical resistivity change exceeding three orders of magnitude and a narrow hysteresis, 3K. Short heating or cooling pulses are shown to reliably induce the coalescence/confinement of the metallic domains in the metamaterial region. The degree of coalescence was triggered thermally with high precision to provide a reliable electrical switching.

Published as Kumar, S., Maury, F. and Bahlawane, N. Electrical Switching in Semiconductor-Metal Self-Assembled VO_2 Disordered Metamaterial Coatings. *Scientific Reports* 6, Article number: 37699 (2016)

Abstract

As a strongly correlated metal oxide, VO_2 inspires several highly technological applications. The challenging reliable wafer-scale synthesis of high quality polycrystalline VO_2 coatings is demonstrated on 4" Si taking advantage of the oxidative sintering of chemically vapor deposited VO_2 films. The semiconductor-metal transition occurs as expected at 67°C from the pure monoclinic, M1, phase to yield a pure rutile phase. This transition comes with an abrupt electrical resistivity change exceeding three orders of magnitude and a narrow hysteresis, 3K, properties that are comparable to these of epitaxial or single crystal VO_2. Spatially resolved infrared and Raman analyses evidence the self-assembly of VO_2 disordered metamaterial, comprising monoclinic (M1 and M2) and rutile (R) domains, at the transition temperature region. The M2 phase mediates the M1-R transition in restricted areas. Short heating or cooling pulses are shown to reliably induce the coalescence/confinement of the metallic domains within the otherwise stable metamaterial. The degree of coalescence was triggered thermally with high precision to provide a reliable electrical switching with adjustable amplitude and profile.

Introduction

The property of exhibiting phase transitions in strongly correlated metal oxides has opened new application possibilities. Vanadium dioxide (VO2) has seen a particular interest owing to its Semiconductor to Metal Transition (SMT) occurring at a temperature (Tc) of 67°C.[1] VO_2 undergoes a first order phase transition from a highly resistive semiconducting monoclinic (M1) phase to a metallic rutile (R) phase with an effective change of electrical resistivity of 3-4 orders of magnitude within a narrow range of temperature.[2–4] This change in electrical properties is accompanied by a remarkable optical transition, where the material shows thermochromic behaviour in the infrared (IR) region. VO_2 effectively reflects the IR radiation in the high temperature rutile phase while being IR transparent at the

low temperature monoclinic phase.[5,6] Such unique combination of properties marks it as a crucial material of study not only for developing intelligent thermal, resistive, and optical switches,[7–14] but also from the fundamental point of view.

Obtaining high quality VO_2 films, essential for high technological applications, remains a challenge as vanadium forms multiple stable oxides like V_2O_3, V_2O_5 and V_6O_{13}.[15] Hence, it is crucial to control the growth conditions to a high degree of precision to obtain pure single-phase films. Polycrystalline and epitaxial films have been grown by various deposition techniques including Sol gel,[16] Pulsed Laser Deposition (PLD),[4] Molecular Beam Epitaxy (MBE),[17] Atomic Layer Deposition (ALD),[18] Sputtering,[19] and Chemical Vapor Deposition (CVD).[20–22] Epitaxial films grow on pre-treated and appropriately oriented Al_2O_3 or TiO_2 substrates or buffer layers.[23–25] The SMT-relevant indicators of the VO_2 films quality are the amplitude of resistivity change and hysteresis width. Ideally, VO_2 films show 3-4 orders of magnitude resistivity change with a narrow hysteresis width of $\Delta T\sim$ 3-4 K. Bulk single crystal offers slightly higher amplitude of resistivity change but is susceptible to breakdown after few cycles of switching between semiconducting and metallic phases.[26] Although, polycrystalline thin films withstand frequent cycling, they usually feature broad hysteresis and small amplitudes of resistivity change, due to the presence of high density of grain boundaries and grain-boundary defects.[22,27,28] Sintering as-grown VO_2 films to decrease the density of grain boundaries is not conceivable for practical applications due to the high melting point of this phase (1970°C). The depression of the melting point, usually observed in nano-crystalline materials [29] is unlikely to reduce the sintering temperature to a reasonable range. Epitaxial VO_2 films attracted a considerable attention owing to their improved morphological advantages and SMT quality. Nevertheless, cost, process conditions, ease of synthesis, morphological control and industrial integration remain limiting challenges for epitaxial growth of VO_2. Hence, it is worth investigating ways to grow polycrystalline VO_2 films without specific buffer layers, yet still matching the performances of epitaxial or single crystal VO_2.

The synthesis of high quality, electronic grade, wafer-scale VO_2 films by MOCVD is achieved involving an oxidative sintering step. The investigation of the

electrical and optical properties across the SMT reveals the self-assembly of a VO_2–disordered metamaterial in which the coalescence and confinement of metallic domains are highly controllable.

Results and discussion

As-deposited films

The as-grown films using cyclohexane as a liquid carrier (step 1) are XRD-amorphous (**figure 1a**), which contrasts with the crystalline VO_2 films obtained with ethanol at this temperature range.[23] On the other hand, cyclohexane is thermally more stable than ethanol at 600°C.[30] For instance, the pyrolysis of ethanol in the temperature range 576-624°C produces essentially methane, hydrogen and oxygen containing compounds as acetaldehyde and carbon monoxide.[31] In contrast to cyclohexane, ethanol is able to participate into the deposition chemistry as a potential source of oxygen. It is worth mentioning that the as-grown films represent the VO_2 characteristic Raman signature **(figure 1b)** but do not feature any obvious sudden change of electrical resistivity upon heating. It is therefore necessary to apply post-treatments to improve the crystallinity of VO_2 films and decrease the density of the grain boundaries.

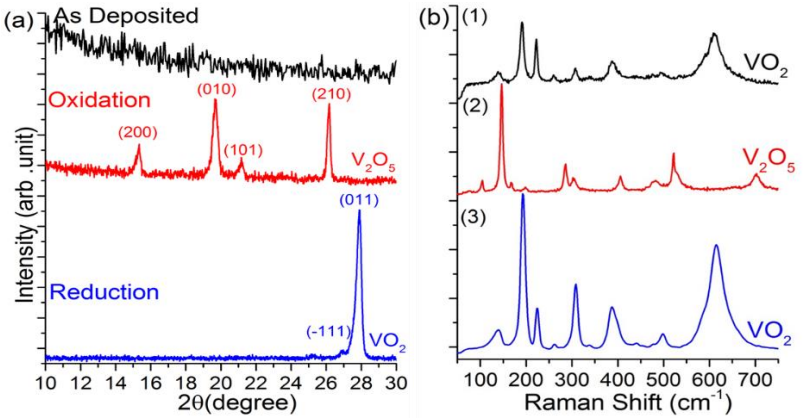

Figure 1. XRD patterns (a) and Raman spectra (b) of (1) as-grown film, (2) pure phase orthorhombic V_2O_5 (PDF no-750457) obtained after oxidation and (3) monoclinic VO_2 M1 phase (PDF no-03-065-2358) obtained upon V_2O_5 annealing under vacuum. The average crystallite size of V_2O_5 and VO_2 is 22 nm and 27 nm respectively.

Post deposition thermal treatment

Two approaches were implemented to induce the sintering of VO_2 films. Annealing under vacuum in the absence of oxygen was performed at 600°C directly in the deposition chamber. As this temperature is far below the melting point (1970°C) of VO_2, no significant sintering took place as shown in **figure 2** (a→d). The second approach involves the conversion of VO_2 to V_2O_5, that exhibits a lower melting point (690°C), prior sintering. This approach proves to be successful as displayed in **figure 2 (a→b)**. The conversion of VO_2 to V_2O_5 was performed under the O_2 partial pressure of 0.01 mbar. The XRD analysis, supplementary information (S1), shows the occurrence of the VO_2 – V_2O_5 conversion already at 400°C. Fixing the temperature at 600°C was essentially implemented to induce an efficient sintering over a short period (1 h) and to simplify this multi-step process by keeping the substrate temperature constant.

The sintered V_2O_5 films undergo reduction to VO_2 at the same temperature in the absence of oxygen as shown in **figure 1, and 2**. The surface micrographs, **figure 2 a-b-c**, display the evolution of the film microstructure at the various steps of the process from porous nano grains to large and well-shaped domains. Upon reduction under vacuum, V_2O_5 releases oxygen without significantly affecting the obtained dense morphology **(Figure 2b-c)**. An extended treatment under these conditions is expected to yield V_2O_3.[32]

XRD and Raman scattering, **figure 1**, indicate the nano-crystalline nature of the as-grown VO_2 films that are XRD-amorphous but feature the characteristic VO_2 Raman peaks. The oxidative sintering step yields an orthorhombic V_2O_5 that converts into crystalline VO_2 (M_1) after further annealing under vacuum. Raman spectrum of the crystalline VO_2 features an enhanced scattering intensity.

Film properties

Temperature programmed X- ray diffraction was carried from room temperature up to 130°C. Contour plots shown in **figure 3** point towards an abrupt change of the diffractogram during heating and cooling cycles. Figure 3(a) shows the phase transition of VO_2 in the 50 – 80°C range whereas figure 3(b) presents a closer

look at the changes taking place near the structural phase transition in the 61-70°C range. The peak at $2\theta = 27.9^{o}$ corresponding to (011), vanishes abruptly at 65-66°C in the heating cycle. Above this temperature a diffraction peak at $2\theta = 27.6^{o}$ is suddenly detected. The reverse transition occurs at 63-64°C upon cooling, which reveals a narrow hysteresis width of ~1-2K. Further detailed X-ray diffraction data can be found in the supplementary section (Figure S2).

The optical reflectivity and thermal imaging were acquired as a function of temperature for 500 nm-thick VO_2 films. The wavelength-dependent total hemispherical reflections in the near infrared region (NIR) are displayed in **figure 4** across the SMT. The thermochromic behavior is clearly shown by an abrupt increase of the reflection from e. g. 18% to 55% at λ=2300 nm by increasing the temperature. Figure 4(b) shows the reflection hysteresis curve at this wavelength. The observed sharp transition and narrow hysteresis, which agree with the XRD results, are relevant assets for energy efficient glazing and static solar control applications. [9,11,33,34]

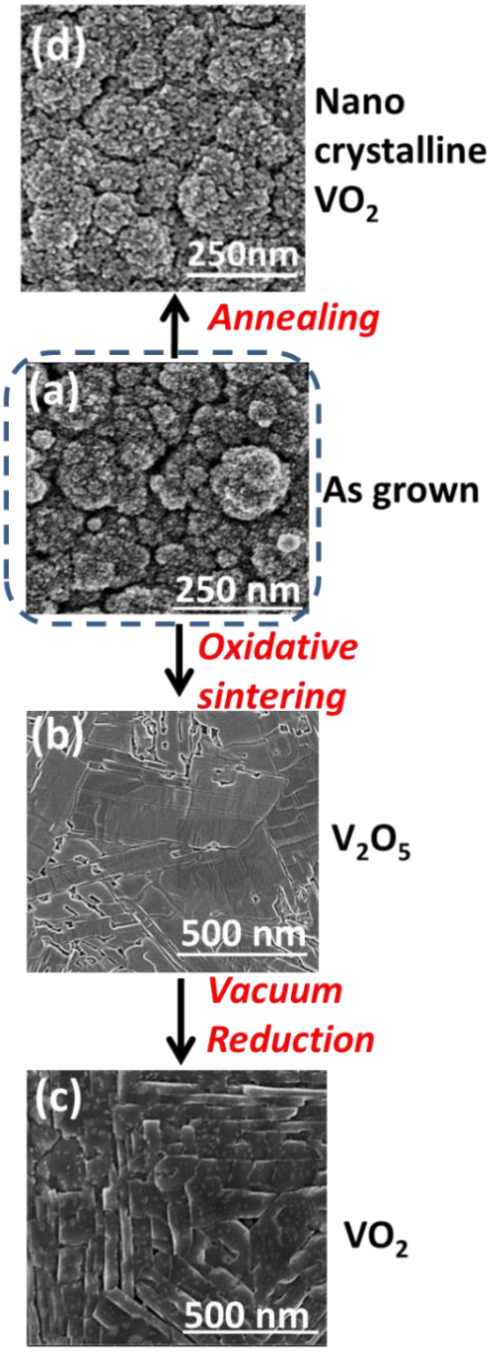

Figure 2. Scanning electron micrographs showing the evolution of film morphology at different stages of film processing from (a) the as-grown amorphous vanadium oxide film, (b) sintered V2O5 film to a (c) sintered VO2 by vacuum reduction. 4 hours annealing of VO2 at 600°C under vacuum induces a marginal morphological impact (d). The film thickness is 500 nm.

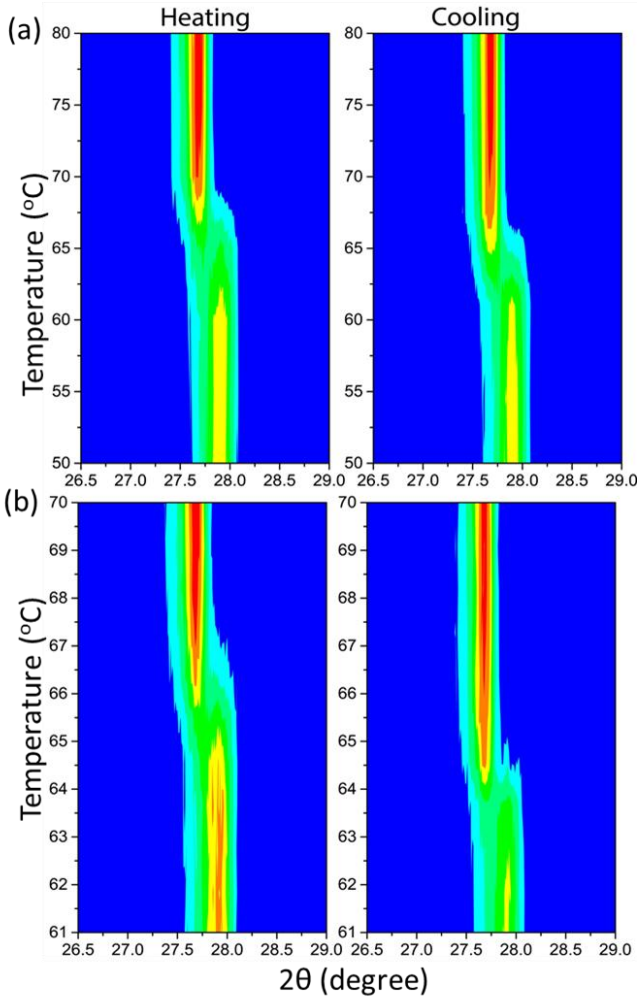

Figure 3. Contour plots of X-ray diffraction during the structural phase transition occurring during heating and cooling stages in the ranges: 50 to 80oC (a) and 61 - 70oC (b).

Based on the spectroscopic measurements it is clear that the monoclinic and rutile phases of VO_2 feature contrasting thermal emissivities. This contrast was represented in the NIR imaging to spatially resolve the phase transition across the SMT. The surface temperature is captured using a neighboring coated silicon with a thick (4-5 µm) carbon nanotube layer which acts as a perfect black body.

NIR images in **figure 5a** display the evolution of the rutile metallic domains (low emissivity) with increasing temperature across the transition. These domains grow rapidly in size with a small increase in temperature until coalescence. Similar to temperature dependent XRD patterns and NIR reflection behavior, we

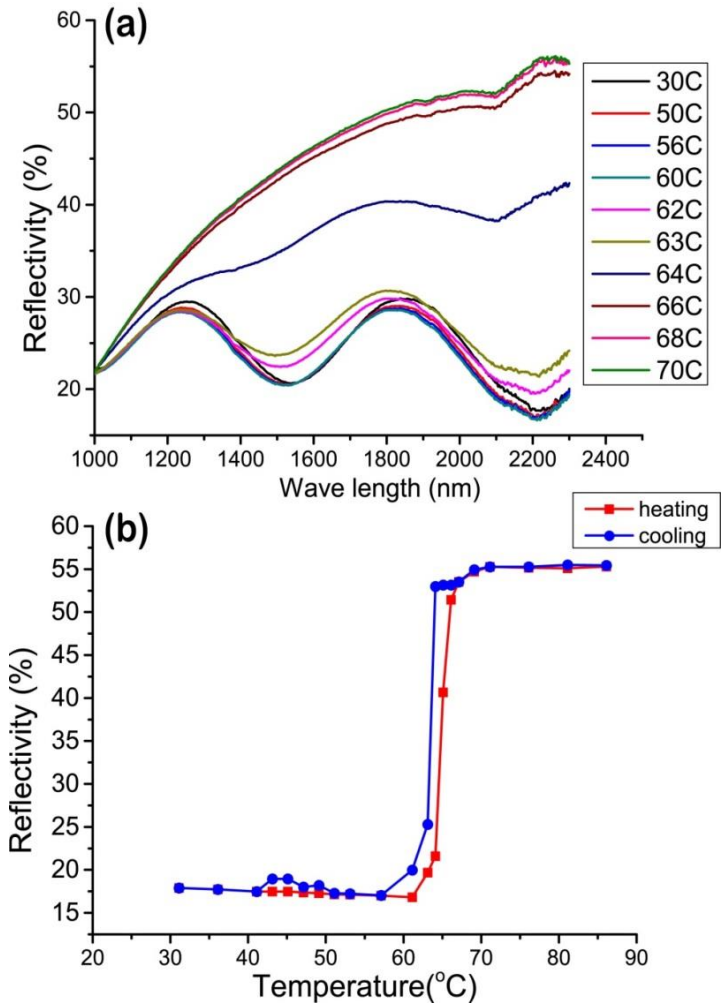

Figure 4. Temperature-dependent infrared reflectivity in the NIR region: Reflection spectra in the NIR upon heating (a) and the variation in reflection across the transition temperature (b) displayed for the arbitrary selected wavelength λ=2300 nm.

notice a difference of ΔT=1-2K between the heating and cooling stages, which confirms the small width of the hysteresis curve. The fraction and distribution of the metallic domains at 67-67.5°C during the heating stage are equivalent to these at 66-66.5°C in the cooling stage.

In a finite range of temperature, both semiconducting and metallic phases co-exist. These two phases with contrasting electrical and optical properties form the so-called "strongly correlated metal" or "disordered metamaterial".[35,36] The dominance of the metallic phase, figure 5(a), at 66.5°C contrasts greatly between the heating and cooling stages.

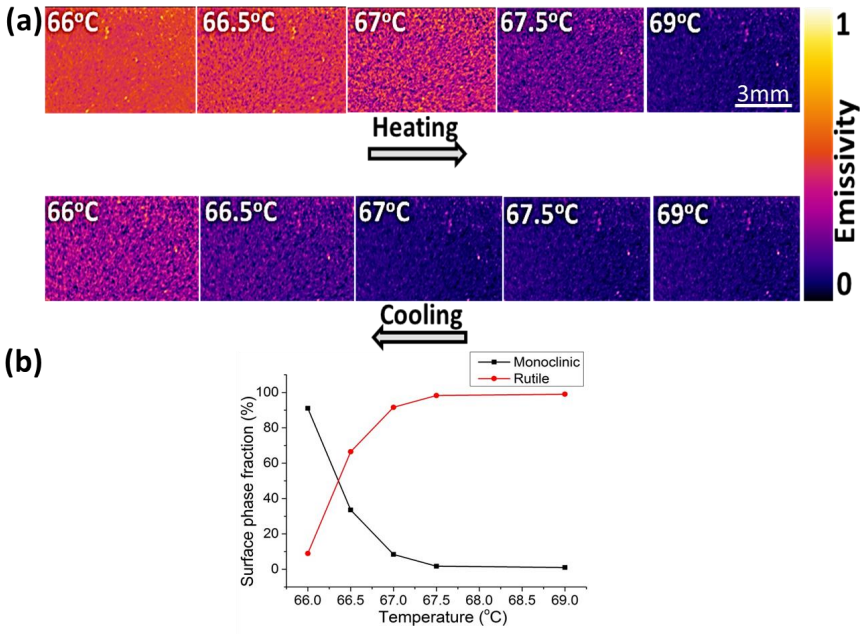

Figure 5. (a) Thermal imaging of VO2 film near the phase transition showing the formation of small metallic clusters as purple spots that grow in size with temperature. (b) The fraction of monoclinic and rutile phases calculated from the change of colour in the thermal images during the cooling stage.

Upon heating, the film is overwhelmingly composed of monoclinic semiconducting phase, whereas, it shows mainly a rutile metallic phase upon cooling. Hence, the self-assembled “disordered metamaterial” in this temperature range features appealing modular optical properties with high thermal sensitivity. The persisting small bright spots in the IR images correspond to surface defects as heterogeneities in surface topography (roughness, micron and submicron thickness, to name some) that influences the IR emissivity. [37]

The fraction of each phase changes abruptly, **figure 5b**, and the rutile domains grow in size and coalesce to form the majority phase at the transition temperature. The semiconducting and metallic domains co-exist and a small thermal excitation can result in large changes in terms of the self-assembly and the dominance of one phase over the other. The major change occurs essentially in a temperature window of ΔT = 1K. On reaching up to 69°C the R phase completely dominates the film, but there is still a tiny fraction of M phase.

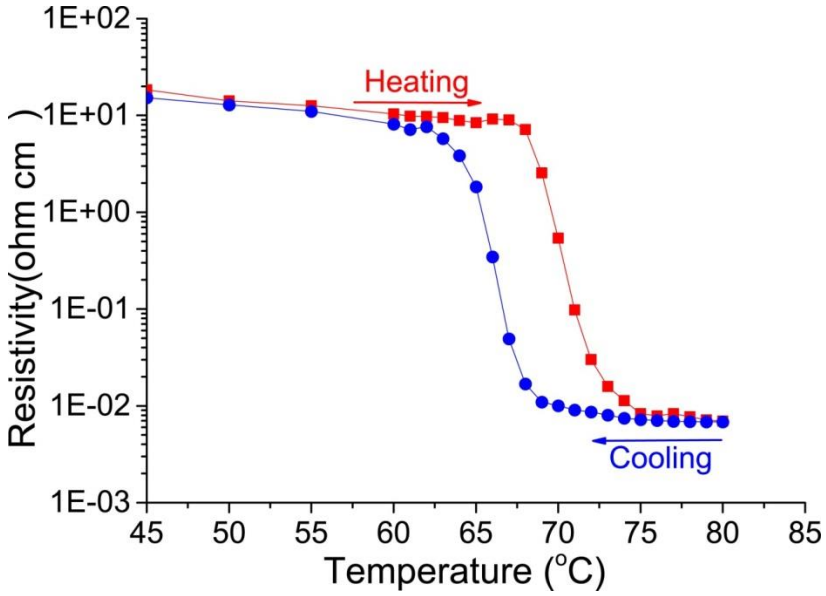

Figure 6. Change in electrical resistivity with temperature in heating and cooling cycles

Electrical resistivity was measured as a function of temperature, **figure 6**, for a 500 nm thick film on a Si substrate with its native oxide. The SMT induces an electrical resistivity change exceeding 3 orders of magnitude in the temperature range from 60 to 75°C. If we consider the ratio of sheet resistances R(30°C)/R(100°C) 5 orders of magnitude change can be deduced (see **figure 7**). The SMT occurs at 67°C in the heating cycle and the reverse phase transition occurs at 64°C indicating a hysteresis width of 3K.

Electrical resistance of the film is a macroscopic property that essentially takes into account the percolation between the metallic domains or the kinetics of their formation, growth and coalescence. The collective behavior of the film is therefore not representative of the intrinsic microscopic SMT. In the microscopic regime, isolated metallic domains appear almost instantaneously throughout the film at a much lower temperature (a video is provided as supplementary materials). Beside the formation of new rutile nuclei upon the increase of temperature, the existing domains grow and coalesce,[38] forming electrically conductive paths by percolation. It is worth to note that the resistivity of VO_2 depends on the coalescence of the metallic domains rather than their apparition. Therefore, the observed hysteresis for the electrical resistivity should be related to the temperature-dependent kinetics of coalescence or confinement of the

metallic domains. The here observed hysteresis width, ΔT = 3K, contrasts with the obtained width, ΔT = 1-2K, from XRD **(figure 3)**, IR reflection **(figure 4)** and thermal imaging **(figure 5)** measurements. The hysteresis in the last cases reflects rather the phase predominance and not the coalescence of the metallic rutile domains.

Further expanding on the electrical properties of the film, we can distinguish the electrical behaviour of VO_2 into two states, namely a high resistance semiconducting and low resistance metallic region at low and high temperatures respectively. **Figure 7a** exhibits the expected semiconducting behavior observed below 65°C where the electrical resistivity decreases with temperature due to the thermal activation of charge carriers. The deduced temperature coefficient of resistance (TCR) calculated in the semiconducting region, -2.6% K^{-1}, agrees with values reported for VO_x films.[39,40] A linear increase of the electrical resistance, **figure 7b**, is observed with temperature above 120°C indicating the metallic nature with a TCR of +0.17% K^{-1} that concurs with the reported values of common metals and alloys.[41] Interestingly films feature a metal behavior with positive TCR only starting at 120°C, which is far above the SMT temperature.

The electrical resistance continues to decrease above the SMT with the temperature, as displayed in figure 7b, hinting at the persistence of a semiconducting-like behavior. The occurrence of this behavior equally during the heating and the cooling stages, figure 7b, indicates its intrinsic nature. This has been noticed by Zhang et al[42] upon the investigation of the electrical properties of single VO_2 nanobeam within the 70-110°C temperature range. Authors could evidence the coexistence of M2 and R phases in this temperature range, and show their comparable electrical resistivity.[43] Although it seems to be overlooked, the negative TCR above SMT is visible in results displayed in several reports.[28,38,43] Jones et al [44] have reported the potential presence of M2 phase along with R at temperatures significantly higher than the SMT.

Regarding the M2 phase of VO_2, Ji et al[45] have reported its presence in epitaxial VO_2 and noticed a remarkable impact of the films' strain on its dominance and stabilization temperature. Kim et al have interestingly concluded that VO_2

undergoes a two-step (M1-M2-R) conversion during the electrically driven transition,[46] which is in line with static lattice calculations that predict an intermediate phase with a Peierls distortion when approaching the phase transition between M1 and the rutile phases.[47,48] A strong surface-induced stress stabilizes the M2 phase, which is assumed to mediate the transition.[42,49]

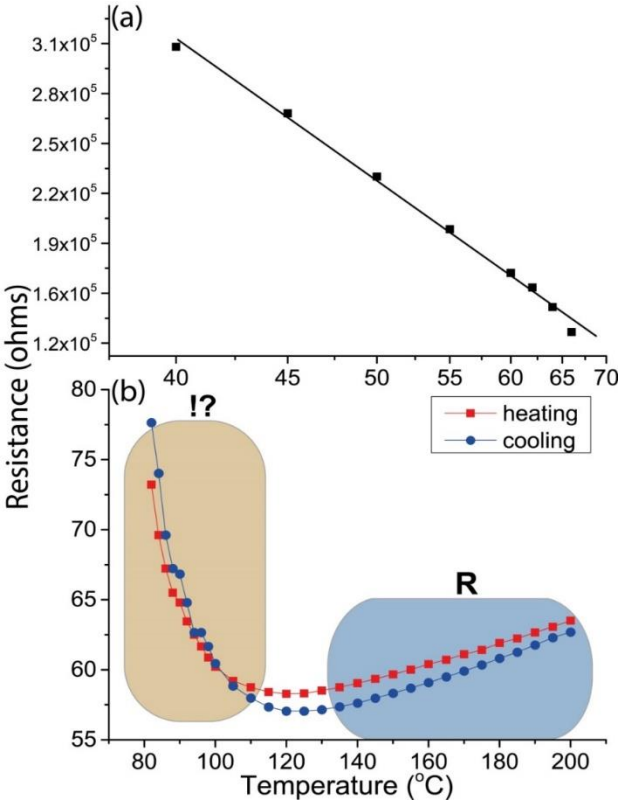

Figure 7. Electrical resistance in semiconducting monoclinic (M) and metallic rutile (R) phases of the VO_2 film in the temperature ranges: (a) 40 -65°C and (b) 80 -200°C. Notice the further decrease in resistance long after the SMT with temperature in the cooling and heating stages.

The presence of M2 would indeed clarify the observed metallic behavior with positive TCR only above 120°C. Thermal imaging, **figure 5**, does not allow distinguishing M1 from M2 phase because of their presumably similar emissivity values. Raman scattering, however, enables distinguishing these two phases via a significant A_g band shift from 620 cm^{-1} in M1 to 650 cm^{-1} in M2[46]. The Raman spectrum of the rutile metallic phase is devoid of any peaks. Temperature-programmed Raman spectroscopy was implemented to investigate the eventual

formation of the M2 phase through the SMT. As displayed in the supplementary information document, figure s3, the M2 phase could be detected as intermediate, but not systematically even at micrometer distances on the same sample. This seemingly unreliable detection of the M2 phase hints at its localized formation. This observation would agree with the assumption of Ji et al [45] that the formation of M2 phase is likely related to the presence of tensile stress. Unlike nanobeams, such a stress might be randomly localized in polycrystalline films. Not detecting the M2 phase with XRD (figure 3), where the signal is averaged over an area of several square millimeters, indicates that M2 is a minor phase in the entire investigated temperature range.

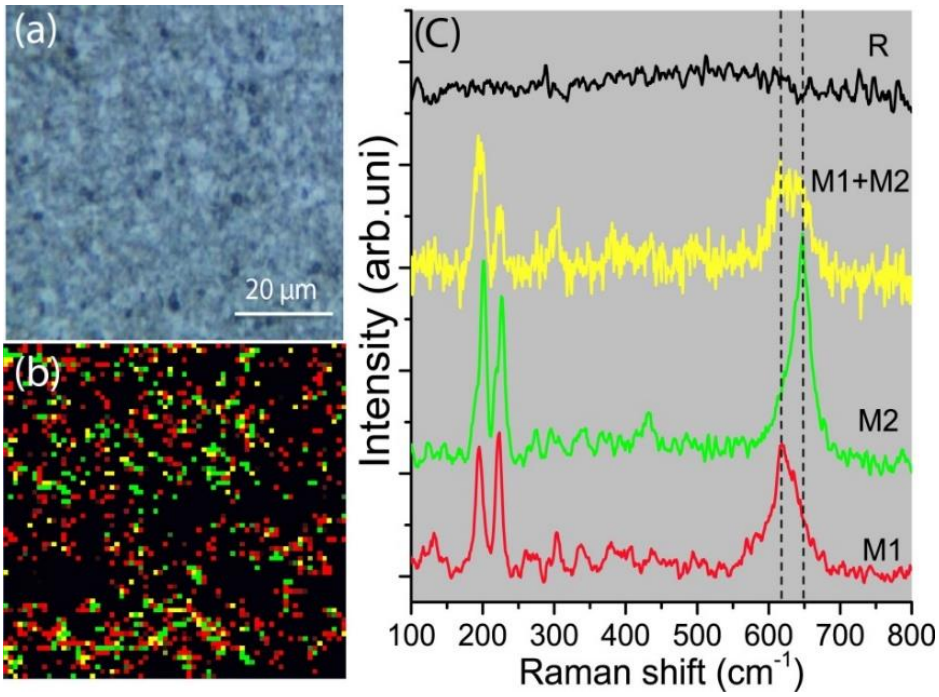

Figure 8. (a) Surface optical micrograph of a 500 nm thick VO_2 film. (b) Raman surface mapping of the M1, M2, M1+M2 and R phases as measured at 67.5°C (each dot correspond to 1x1 µm² analysis area) and (c) Raman spectra corresponding to the colour-coded used in the mapping.

Therefore, Raman mapping was performed at 67.5°C for both wavenumbers (M2:650 cm^{-1} and M1:620 cm^{-1}), **figure 8** (b), to spatially localize the distribution of M1, M2, M1+M2 and R phases. Each pixel corresponds to a 1x1 □m^2 analysis area. The red dots in figures 8b represent M1 phase, whereas the green and

yellow dots represent M2 and M1+M2 domains respectively. The black background illustrates the presence of the R phase of VO_2. The spectra of the aforementioned coloured points in the Raman map are displayed in figure 9c. Hence, Raman mapping evidences clearly the self-assembly of a disordered M1-M2-R metamaterial at the transition temperature. It is worth mentioning that the presence of M2 phase was not evidenced above 70°C, which is likely due to the excessive dominance of the metallic rutile phase.

Based on the Raman mapping recorded at 67.5°C, figure 8b, and the temperature-programmed Raman measurement, figure S3 in the supplementary information, it could be shown that thermally driven phase transition in polycrystalline VO_2 film involves indeed the formation of the M2 phase but in confined locations. It is assumed that the strain in these confined areas meets conditions where M2 significantly forms as intermediate phase.

It is noteworthy that the film was maintained at this state at 67.5 °C in air for extended periods (100 hrs) without any apparent degradation or drift of one state to another. Therefore, the disordered VO_2-metamaterial phase is quite stable and robust, which is an asset to its potential implementation in practical applications.

Vanadium oxide film as a thermally controlled electrical switch

As noticed during the investigation of the spatial phase distribution within VO_2, the metamaterial phase is surprisingly stable over long periods. Therefore, it is virtually possible to stabilize the system at any point within the hysteresis curve by adjusting the temperature. A practical application of this feature could be a thermally activated electrical switch, which might operate by the supply of short heating and cooling pulses with small amplitudes ΔT. These pulses bring the metamaterial to cycle between resistive “Off” and conductive “On” states while keeping the same background temperature around the SMT value.

Experimental thermal switching behaviour of VO_2 is displayed in **figure 9**. At the background temperature 67^oC the VO_2 films feature the disordered metamaterial structure. This temperature is applied using a heating stage while monitoring the electrical resistance. The highly resistive semiconducting state is considered as

an “off” state. A 3 seconds heating pulse ΔT drives the coalescence of the metallic rutile domains in the metamaterial, a state that is retained after the back stabilization of the temperature at 67°C. This behaviour originates from the difference between the forward and backward transition temperatures due to hysteresis width as illustrated schematically in **figure 10**. To get the metamaterial back to the “off” state, a cooling pulse for a short duration induces the shrinkage and confinement of the metallic domains. Consequently, the metamaterial features a resistive semiconducting behaviour even when it stabilized back at 67°C. Hence, short thermal activation pulses are reliably implemented for abrupt manipulation of the electrical properties of VO_2 in the metamaterial state. The amplitude of the thermal pulse activation has a direct impact on the response of VO_2 metamaterial as shown in figure 9 and 10.

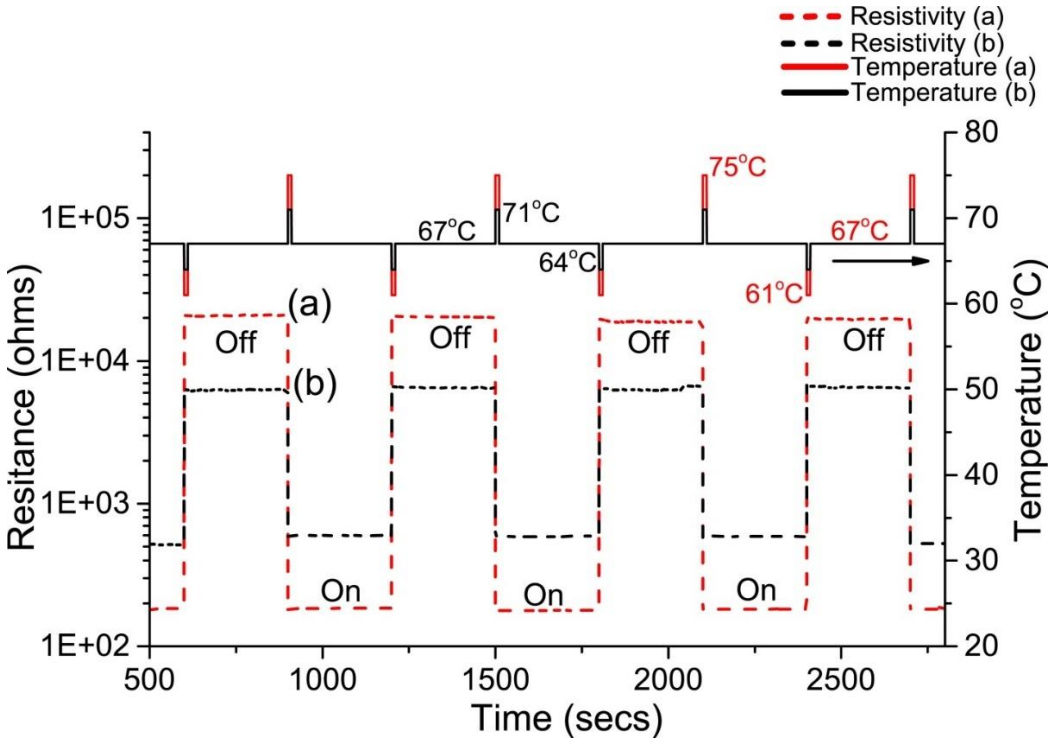

Figure 9. Thermal switching behaviour of the VO_2 disordered metamaterial. The “off” and “on” states are determined by the sudden drop or increase in electrical resistance because of small changes in the temperature given in the form of thermal activation pulses.

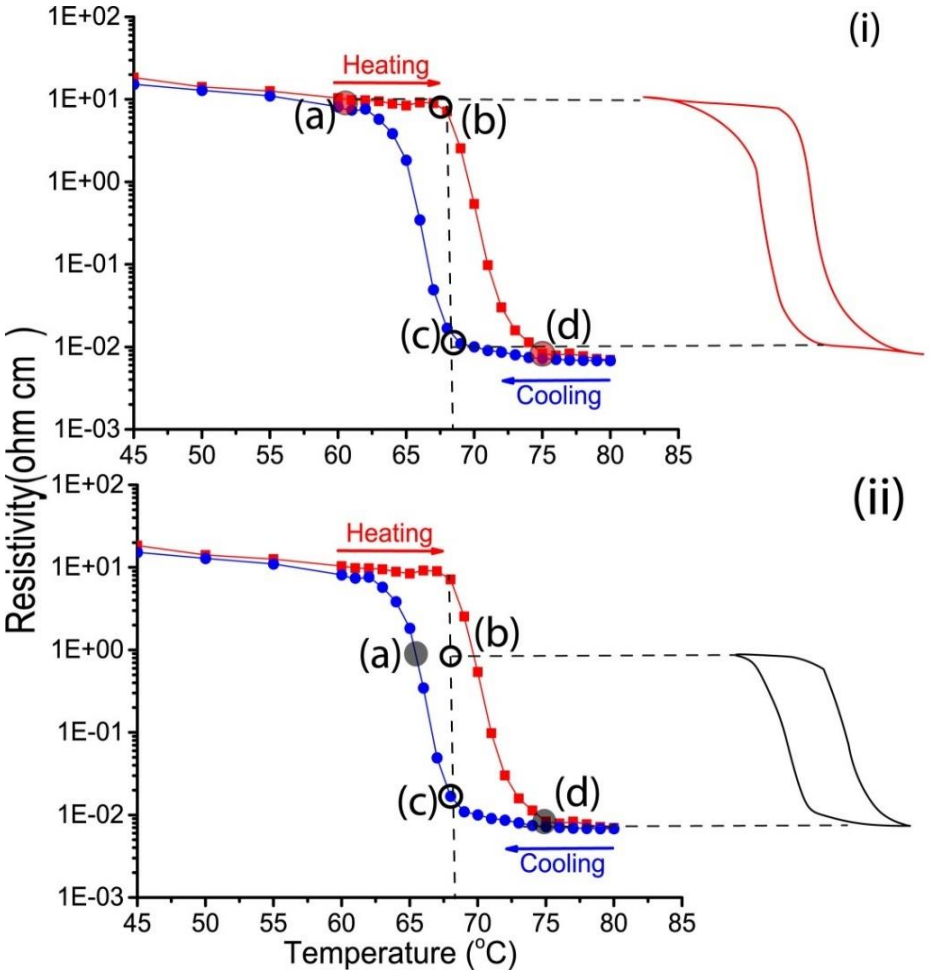

Figure 10. Schematic representation of the thermal switching process based on the hysteresis curve. The impact of adopting two different amplitudes of the thermal activation is illustrated in (i) and (ii). c→a→b: cooling pulse; b→d→c: heating pulse.

Using high strength of the thermal activation pulse as shown in fig 10 (i) allows the “on” and “off” states of the system at points (b) and (d) respectively, thus taking a high benefit of the resistivity change. Whereas a weaker thermal activation pulse as shown in fig 10 (ii) restricts the amplitude of switching. This enables programing the metamaterial to follow virtually any particular switching pattern. Few such examples are experimentally performed and the results are displayed in figure 11. Adjusting the strength of the heating and/or cooling pulses allows manipulating the resistance-switching pattern. This degree of flexibility proves the robustness and reliability of this thermally triggered VO_2 electrical switching metamaterial.

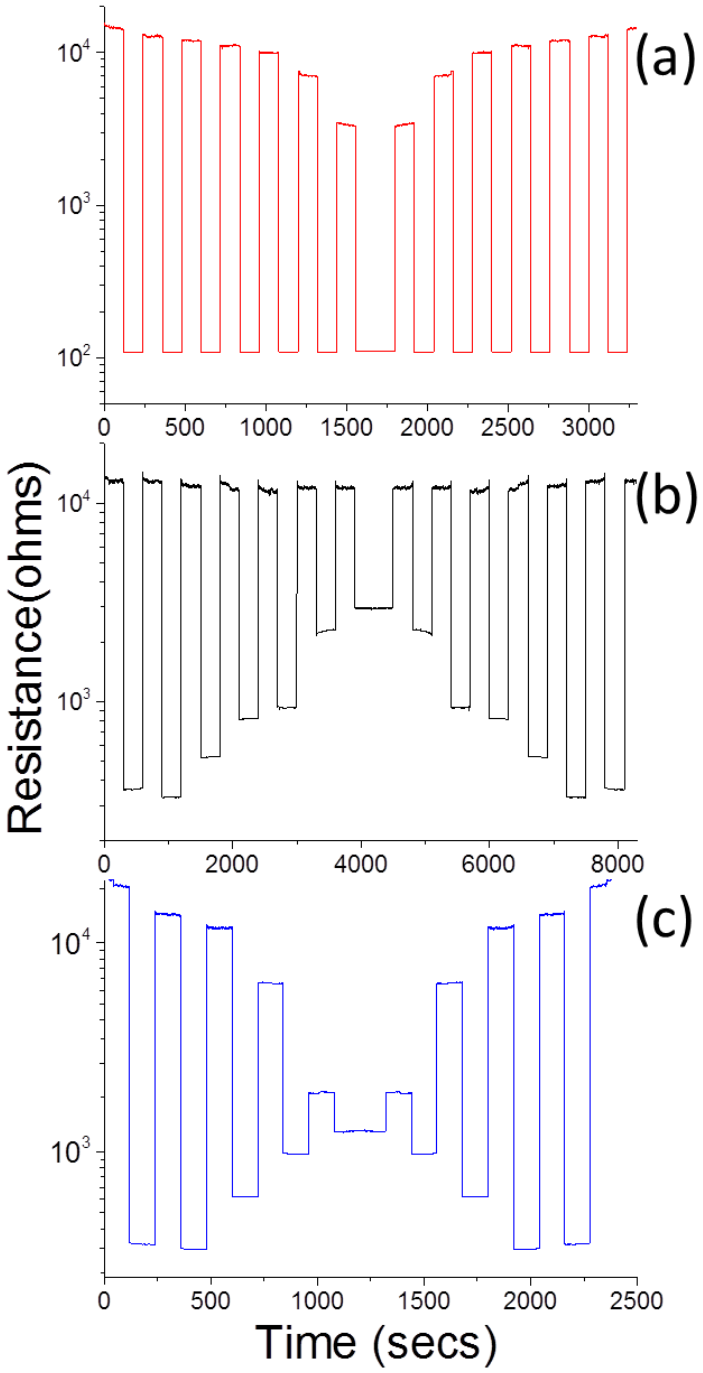

Figure 11. Temperature-programed resistance switching of the metamaterial via the adjustment of heating (a), cooling (b) or both heating and cooling (c) activation pulses.

It is worth noting that attaining high switching amplitude while implementing a small thermal activation requires a sharp transition with a minimal hysteresis width. The narrow hysteresis, $\Delta T = 3K$, obtained in this study is equivalent to single crystal or epitaxial films and is ideal for high performance applications.[24,26] The self-assembled VO_2 disordered metamaterial films operate optimally even after extensive and extended use, which makes it an attractive candidate for highly demanding applications. The attractiveness of such metamaterial will substantially enhance, provided a reliable approach is developed for the tuning of the SMT temperature without scarifying its quality in terms of amplitude, sharpness, and hysteresis width.

Conclusions

Spatially resolved phase analysis within the transition regime reveals the self-assembly of VO_2 disordered metamaterial that exhibit an outstanding long-term stability. The disordered metamaterial was thermally triggered to tune the degree of coalescence/confinement of the metallic domains with high precision. Such a control enables a highly accurate and tunable thermally controlled electrical switching. Oxidative sintering approach was implemented in this study to induce an efficient densification of MOCVD obtained VO_2. The resulting films feature SMT characteristics that match those of epitaxial or bulk VO_2 in terms of sharpness and width of the hysteresis.

Methods

Films of vanadium oxide were deposited on silicon substrates using direct liquid injection MOCVD (MC200 from AnnealSys), which is a stagnation point-flow warm-walled reactor. Cyclohexane solution containing $5x10^{-3}$ mol/l of vanadium (V) oxy-tri-isopropoxide was used as a single-source precursor, which was maintained under nitrogen atmosphere at room temperature before its injection into the evaporation chamber at a frequency of 2 Hz and an adjusted opening time to reach a feeding rate of 1 g/min. The pressure and temperature of the

evaporation chamber were maintained at 0.6 mbar and 200°C during deposition respectively, whereas the walls of the reactor were maintained at 200°C. During the growth, 500 sccm of nitrogen carrier gas was introduced alongside the precursor injection and the total pressure of the reactor was automatically regulated at 0.6 mbar. The substrate is maintained at 600°C during the 2 hours of deposition and the subsequent heat treatments.

In a second step, an hour long annealing was performed at 600°C right after the deposition under oxygen partial pressure of $1x10^{-2}$ mbar. The sample is then further subjected to annealing at the same temperature under vacuum (~ 0.6 mbar) acting as a reducing atmosphere for 4 hours, after which the chamber is allowed to cool down. All depositions were carried out on 4-inch silicon wafers without removing the upper native oxide layer that might act as a barrier. Samples were later cut into smaller pieces for analysis purposes. Uniform, high quality VO_2 films were observed throughout the wafers in a homogeneous manner.

Characterization

X-ray diffraction (XRD), Bruker D8, with CuKα as the X-ray source, was used to identify the crystalline phases of vanadium oxide. Data were collected in the θ-2θ (locked couple) mode from 2θ of 20 ^{o} to 60 ^{o} with a step size of 0.02^{o}.

Film thickness was measured using an Alpha step d-500 profilometer from KLA-Tencor and FEI Helios Nanolab 650™, Scanning Electron Microscope (SEM). Surface morphology was inspected by SEM at a working distance of 4 mm with an operating voltage of 25 kV.

Raman spectroscopy was performed using an InVia Raman spectrometer from Renishaw with a 532 nm laser. In situ temperature-dependent Raman measurements were performed at ambient air with a Linkam TMS heating stage using fixed heating and cooling ramp at 5°C/min.

The electrical resistivity was measured using four-point probe measurements in Van der Pauw configuration. Infrared image analysis was conducted using the

FLIR X6580SC thermal camera operating in the 1.5-5.1 µm spectral range with an accurate recording at a frequency of 355 Hz in a full 640 x 512 resolution. Temperature-dependent measurements were performed by placing the sample on a heating stage and cycling the temperature form 40°C to 80°C while a thermocouple was placed on the sample to measure the surface temperature. The ramp was fixed at 5°C/min in the transition range.

Acknowledgements

The authors would like to acknowledge Luxembourg Institute of Science and Technology (LIST) for providing the financial support for this work.

References

1. Morin. Oxides Which Show a Metal-to-Insulator Transition at the Neel Temperature. *Physical Review Letters* **3,** 34–36 (1959).
2. Nag, J. & Jr, R. Synthesis of vanadium dioxide thin films and nanoparticles. *J Phys Condens Matter* **20,** 264016 (2008).
3. Vernardou, D., Pemble, M. & Sheel, D. Vanadium oxides prepared by liquid injection MOCVD using vanadyl acetylacetonate. *Surface and Coatings Technology* **188-189,** 250254 (2004).
4. Lee, S., Meyer, T., Park, S., Egami, T. & Lee, H. Growth control of the oxidation state in vanadium oxide thin films. *Appl Phys Lett* **105,** 223515 (2014).
5. Liu, D., Zheng, W., Cheng, H. & Liu, H. Thermochromic VO2 Thin Film Prepared by Post Annealing Treatment of V2O5 Thin Film. Adv Mat Res **79-82,** 747–750 (2009).
6. Liu, D., Cheng, H., Zheng, W. & Zhang, C. Infrared thermochromic properties of VO2 thin films prepared through aqueous sol-gel process. *J Wuhan Univ Technology-mater Sci Ed* **27,** 861–865 (2012).

7. Castro, M., Ferreira, C. & Avillez, R. Vanadium oxide thin films produced by magnetron sputtering from a V2O5 target at room temperature. *Infrared Phys Techn* **60,** 103–107 (2013).
8. Vernardou, D. *et al.* A study of the electrochemical performance of vanadium oxide thin films grown by atmospheric pressure chemical vapour deposition. *Sol Energ Mat Sol C* **95,** 2842–2847 (2011).
9. Kam, K. & Cheetham, A. Thermochromic VO2 nanorods and other vanadium oxides nanostructures. *Mater Res Bull* **41,** 1015–1021 (2006).
10. Batista, C., Ribeiro, R. & Teixeira, V. Synthesis and characterization of VO2-based thermochromic thin films for energy-efficient windows. *Nanoscale Res Lett* **6,** 301 (2011).
11. Saeli, M., Piccirillo, C., Parkin, I., Ridley, I. & Binions, R. Nano-composite thermochromic thin films and their application in energy-efficient glazing. *Solar Energy Materials and Solar Cells* **94,** 141–151 (2010).
12. Kamalisarvestani, Saidur, Mekhilef & Javadi, F. S. Performance, materials and coating technologies of thermochromic thin films on smart windows. *Renewable and Sustainable Energy Reviews* **26,** 353–364 (2013).
13. Zhang, Z. *et al.* Thermochromic VO2 thin films: solution-based processing, improved optical properties, and lowered phase transformation temperature. *Langmuir Acs J Surfaces Colloids* **26,** 10738–44 (2010).
14. Perucchi, Baldassarre, Postorino & Lupi. Optical properties across the insulator to metal transitions in vanadium oxide compounds. *Journal of Physics: Condensed Matter* **21,** 323202 (2009).
15. Chain, E. Optical properties of vanadium dioxide and vanadium pentoxide thin films. *Appl Optics* **30,** 2782 (1991).
16. Bahlawane, N. & Lenoble, D. Vanadium Oxide Compounds: Structure, Properties, and Growth from the Gas Phase. *Chemical Vapor Deposition* **20,** 299–311 (2014).
17. Guzman, G., Morineau, R. & Livage, J. Synthesis of vanadium dioxide thin films from vanadium alkoxides. *Mater Res Bull* **29,** 509–515 (1994).

18. Gao, W, Wang, CM, Wang, HQ, Henrich, VE & Altman, EI. Growth and surface structure of vanadium oxide on anatase (001). *Surface science* (2004).
19. Peter, A. *et al.* Metal Insulator Transition in ALD VO2 Ultrathin Films and Nanoparticles: Morphological Control. *Adv Funct Mater* **25,** 679–686 (2015).
20. Cazzanelli, E, Mariotto, G, Passerini, S & Smyrl, WH. Raman and XPS characterization of vanadium oxide thin films deposited by reactive RF sputtering. *Solar energy materials …* (1999).
21. Mantoux, A., Groult, H., Balnois, E., Doppelt, P. & Gueroudji, L. Vanadium Oxide Films Synthesized by CVD and Used as Positive Electrodes in Secondary Lithium Batteries. *J Electrochem Soc* **151,** A368 (2004).
22. Crociani, L., Carta, G., Natali, M., Rigato, V. & Rossetto, G. MOCVD of Vanadium Oxide Films with a Novel Vanadium(III) Precursor. *Chem Vapor Depos* **17,** 6–8 (2011).
23. Kumar, S., Lenoble, D., Maury, F. & Bahlawane, N. Synthesis of vanadium oxide films with controlled morphologies: Impact on the metal–insulator transition behaviour. *Phys Status Solidi* **212,** 1582–1587 (2015).
24. Martens, K., Aetukuri, N., Jeong, J., Samant, M. & Parkin, S. Improved metal-insulator-transition characteristics of ultrathin VO2 epitaxial films by optimized surface preparation of rutile TiO2 substrates. *Appl Phys Lett* **104,** 081918 (2014).
25. Ji, YD, Pan, TS, Bi, Z, Liang, WZ & Zhang, Y. Epitaxial growth and metal-insulator transition of vanadium oxide thin films with controllable phases. Appl. Phys. Lett. **101**, 071902 (2012).
26. Muraoka & Hiroi. Metal-insulator transition of VO2 thin films grown on TiO2 (001) and (110) substrates. (2002).
27. Mansingh, A, Singh, R & Krupanidhi, SB. Electrical switching in single crystal VO 2. *Solid-State Electronics* (1980)
28. Klimov, VA, Timofeeva, IO, Khanin, SD & Shadrin, EB. Hysteresis loop construction for the metal-semiconductor phase transition in vanadium dioxide films. *Technical Physics* (2002).

29. Rampelberg, G. *et al.* In situ X-ray diffraction study of the controlled oxidation and reduction in the V–O system for the synthesis of VO 2 and V 2 O 3 thin films. *Journal of Materials Chemistry C* **3,** (2015).
30. Dreizin, EL, Allen, DJ & Glumac, NG. Depression of melting point for protective aluminum oxide films. *Chemical Physics Letters* **618,** 63–65 (2015).
31. Billaud, F, Duret, M & Elyahyaoui, K. Survey of recent cyclohexane pyrolysis literature and stoichiometric analysis of cyclohexane decomposition. *Industrial & Engineering …* (1991).
32. Barnard, JA & Hughes, H. The pyrolysis of ethanol. *Transactions of the Faraday Society* (1960).
33. Su, DS & Schlögl, R. Thermal decomposition of divanadium pentoxide V2O5: Towards a nanocrystalline V2O3 phase. *Catalysis letters* (2002).
34. Seeboth, A, Schneider, J & Patzak, A. Materials for intelligent sun protecting glazing. *Solar energy materials and solar cells* (2000).
35. Parkin, IP & Manning, TD. Intelligent thermochromic windows. *Journal of chemical education* (2006).
36. Qazilbash, M. *et al.* Mott Transition in VO2 Revealed by Infrared Spectroscopy and Nano-Imaging. *Science* **318,** 1750–1753 (2007).
37. Kats, Blanchard, Zhang, Genevet & Ko. Vanadium dioxide as a natural disordered metamaterial: perfect thermal emission and large broadband negative differential thermal emittance. (2013).
38. Maury, F & Duminica, FD. Diagnostic in TCOs CVD processes by IR pyrometry. *Thin Solid Films* (2007).
39. Madan, H., Jerry, M., Pogrebnyakov, A., Mayer, T. & Datta, S. Quantitative Mapping of Phase Coexistence in Mott-Peierls Insulator during Electronic and Thermally Driven Phase Transition. *Acs Nano* **9,** 2009–2017 (2015).
40. Venkatasubramanian, C., Horn, M. W. & Ashok, S. Ion implantation studies on VOx films prepared by pulsed dc reactive sputtering. *Nuclear Instruments and Methods in Physics Research Section B: Beam Interactions with Materials and Atoms* **267,** 1476–1479 (2009).

41. Han, YH *et al.* Fabrication of vanadium oxide thin film with high-temperature coefficient of resistance using V 2 O 5/V/V 2 O 5 multi-layers for uncooled microbolometers. *Thin Solid Films* (2003).
42. Weast, R. C. Handbook of chemistry and physics. *The American Journal of the Medical Sciences* **257,** 423 (1969).
43. Zhang, S., Chou, J. & Lauhon, L. Direct correlation of structural domain formation with the metal insulator transition in a VO2 nanobeam. *Nano Lett* **9,** 4527–32 (2009).
44. Zhang, H.-T. *et al.* Wafer-scale growth of VO2 thin films using a combinatorial approach. *Nature Communications* **6,** 8475 (2015).
45. Jones, A., Berweger, S., Wei, J., Cobden, D. & Raschke, M. Nano-optical investigations of the metal-insulator phase behavior of individual VO(2) microcrystals. *Nano letters* **10,** 1574–81 (2010).
46. Ji, Y. *et al.* Role of microstructures on the M1-M2 phase transition in epitaxial VO2 thin films. *Scientific reports* **4,** (2014).
47. Kim, B.-J. *et al.* Micrometer x-ray diffraction study ofVO2films: Separation between metal-insulator transition and structural phase transition. *Phys Rev B* **77,** (2008).
48. Pouget, JP, Launois, H, Rice, TM, Dernier, P & Gossard, A. Dimerization of a linear Heisenberg chain in the insulating phases of V 1− x Cr x O 2. *Physical Review B* (1974).
49. Whittaker, L., Patridge, C. & Banerjee, S. Microscopic and Nanoscale Perspective of the Metal−Insulator Phase Transitions of VO2: Some New Twists to an Old Tale. *J Phys Chem Lett* **2,** 745–758 (2011).
50. Sohn, J. I. *et al.* Surface-stress-induced Mott transition and nature of associated spatial phase transition in single crystalline VO2 nanowires. *Nano Lett.* **9,** 3392–7 (2009).

Supplementary Information

Sunil Kumar [1], Francis Maury [2], Naoufal Bahlawane [1].

[1]Luxembourg Institute of Science and Technology (LIST), 5 avenue des Hauts-Fourneaux L-4362 Esch-sur-Alzette Luxembourg.

[2]CIRIMAT, ENSIACET-4 allée E. Monso, 31030 Toulouse, France

The oxidation of the as-grown VO_2 to form V_2O_5 occurs already after short heating at 400°C. The increase of the diffraction peaks intensity and their narrowing highlight the considerable improvement of the V_2O_5 crystallinity with the increase of the temperature.

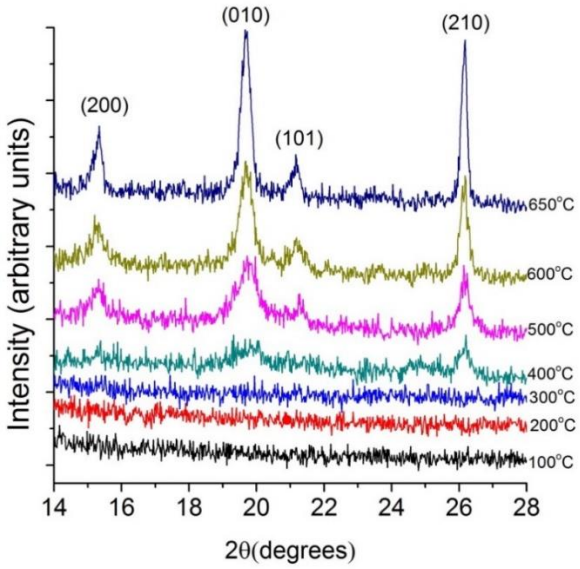

Figure S1. XRD patterns showing the oxidative conversion of the as-grown amorphous VO2 into crystalline V2O5 (PDF no 750457) as a function of temperature.

Structural phase transition is studied by tracking the changes in peak position from X-ray diffraction data as shown in figure S2. It is interesting to notice an apparent peak shift from monoclininc to rutile occurring abruptly over a narrow temperature range. However, no trace of M2 phase was detected (mains peaks expected at 27.4° and 28.3° after PDF 01-076-0673), which might be due to the small fraction of M2 when compared to M1. In this condition, it is likely that the implemented XRD technique is not able to capture the weak M2 signal.

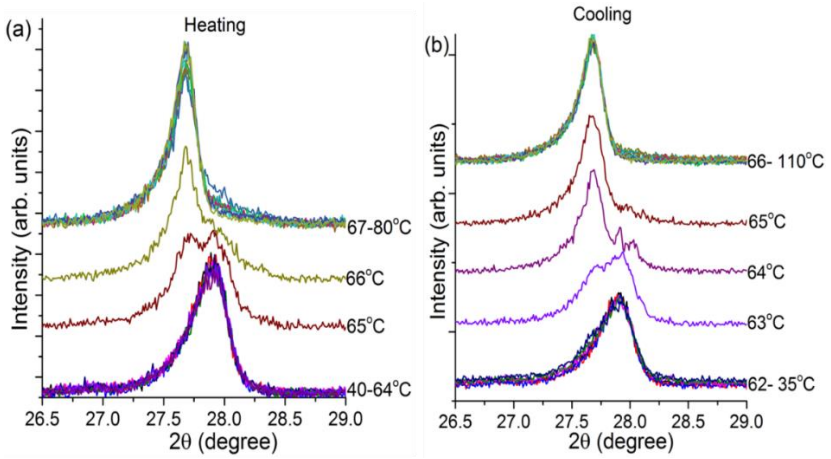

Figure S2. XRD patterns showing the peak shift from monoclinic to rutile and vice versa by (a) heating and (b) cooling the sample. Notice the change in the peak position from 27.9o to 27.6o before and after transition from monoclinic to Rutile phase.

The presence of the M2 phase could be captured using Raman spectroscopy as shown in figure S3. Although the overall Raman signature seems similar between the M1 and M2 phases, a shift of several peaks can be highlighted. The most prominent shift is observed for the peak at 620-650 cm^{-1}. On the same surface and at a distance some micrometres, it is possible to identify spots where the SMT occurs directly from the M1 to the R phase and others where the transition is mediated by the M2 phase.

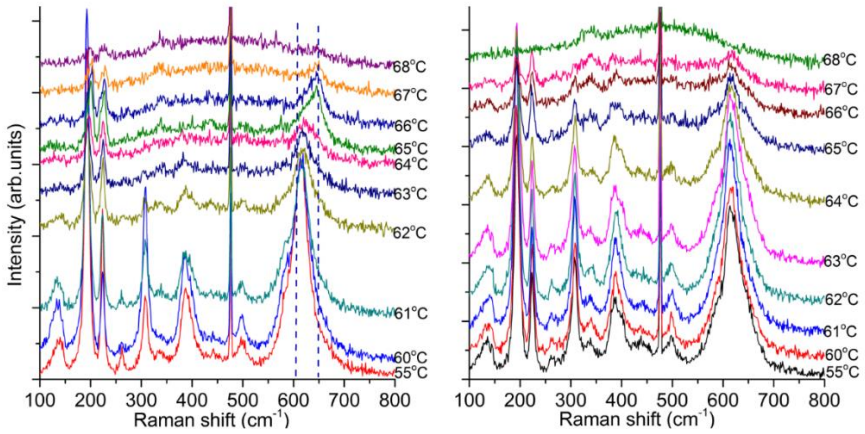

Figure S3. Temperature-programmed Raman analysis during the cooling stage in two close positions on the surface of VO2 film. The left-hand panel represents data from an analysis spot that shows an M1-M2-R transition path, whereas the right-hand panel shows a neighbouring position on the same sample that shows an M1-R transition.

4.3 Light Modulation in Smart Cermet Based on Phase Change Disordered Metamaterial.

Keywords – Metamaterial; smart cermet; Vanadium oxide; MOCVD; Emissivity control; solar selective coatings; Semiconductor-metal transition**.**

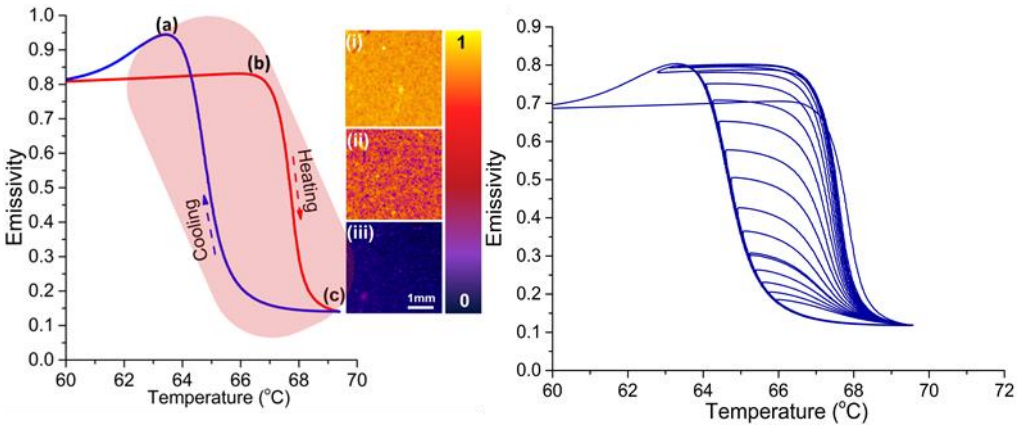

VO_2 in the metamaterial state is regarded as a highly responsive mixed phase system comprising of metallic inclusions in a semiconducting matrix. Emissivity of VO2 films reach that of a blackbody in a narrow window of temperature during the cooling cycle. Through accurate temperature control, variable emissivity states are achieved.

Submitted as Kumar, S., Maury, F. and Bahlawane, N. Light Modulation in Smart Cermet Based on Phase Change Disordered Metamaterial. 2017 *(Submitted)*

Abstract

Cermet coatings are popular solar selective absorbers as they capture most of the solar energy while minimising radiative losses. Embedded metallic nanoparticles in dielectric matrices promote multiple internal reflection of light resulting in its complete absorption. The metallic nature of the inclusions provides however an overall low emissivity. VO_2 in the metamaterial state is regarded in this study as a responsive mixed phase comprising metallic inclusions in semiconducting phase mimicking cermet. The smart cermet responds to thermal stimulus by modulating the size of the metallic inclusions and thereby enabling the manipulation of the interaction with light. The highly reliable and reproducible response of the smart cermet corroborates with the recently reported ramp reversal memory effect in VO_2. We demonstrate a thermally controlled 85% emissivity switch taking advantage of the narrow hysteresis and tuning abilities of the disordered metamaterial.

Introduction

Cermets are metal-dielectric composites in which metal particles are embedded in dielectric matrices as displayed in figure 1. Cermet based coatings are used as effective spectrally-selective absorbers due to their high solar absorbance and low thermal emittance. [1,2] The properties of the cermet strongly depend on the volume fraction of the metal inclusions in addition to their chemical nature, size, shape and dispersion within the matrix.[3] Nevertheless, the properties of the cermet coatings are frozen upon synthesis as the parameters influencing the optical properties can no more be altered. Therefore, the development of traditional cermet materials for light modulation sounds compromised.

One of the most popular and well-studied mechanisms for light modulation relies on materials with engineered structures to influence the nature of light. These materials are known as metamaterials and the phenomenon of light modulation through engineered surface modifications is termed as optical topological transition. [4,5] Perfect solar absorbers based on metamaterial were demonstrated

by fabricating specific shapes and configurations of metallic structures on dielectric matrix. By varying the size and configuration, the range of the perfect absorption window is adjusted. [6,7]

Relevant research was reported on emissivity control devices for their implementation in space applications. Programmable emissivity switching is crucial for spacecraft and satellite surfaces, but their implementation often includes tedious fabrication process comprising bulky and energy inefficient mechanisms. [8–11] Therefore, an ideal candidate for such application would be a coating material that switches reliably between distinct values of emissivity, and which is simple to fabricate and integrate, while consuming fraction of the power needed for existing technologies.

Vanadium dioxide is a strongly correlated material featuring a semiconducting-to-metal transition (SMT) near room temperature. In contrast to the metallic phase, the low temperature semiconducting phase features high infrared transmission and high thermal emissivity. The transition occurs with a narrow hysteresis, revealing a temperature range (64-68°C) where vanadium oxide features the coexistence of the metallic and semiconducting phases. This, so called disordered VO_2 metamaterial is analogous to cermet. Upon the increase of temperature, metallic inclusions nucleate and grow throughout the semiconducting phase.[12] In this article we introduce the concept of “smart cermet” material with tuneable optical properties based on disordered VO_2 metamaterial. The concept of tunability is addressed by temperature-enabled control of the size and density of metallic particles in the dielectric matrix. The unique feature of VO_2 based smart cermet is that, both dielectric matrix and metallic particles are one and the same material at different phases. Therefore, a single layer of VO_2 can be manipulated to feature (i) a fully dielectric state, (ii) a variable state with metallic inclusions embedded in the dielectric matrix, or (iii) a fully metallic state, by controlling the temperature at which it is operated. Such kind of characteristics is unheard of in the field of conventional cermet coatings. Moreover, existing cermet coatings require complex synthesis techniques to achieve the right size and density of metal volume fraction, and offer limited to no flexibility or tunability in terms of light modulation.

Emissivity returns to 0.8 from 0.1 upon cooling, however a hysteretic delay of ΔT = 2°C is observed. This hysteresis is intrinsic to VO_2 films and such a narrow hysteresis of approximately 2°C is observed for single crystal and epitaxial film, and is considered as a sign of high quality.[14]

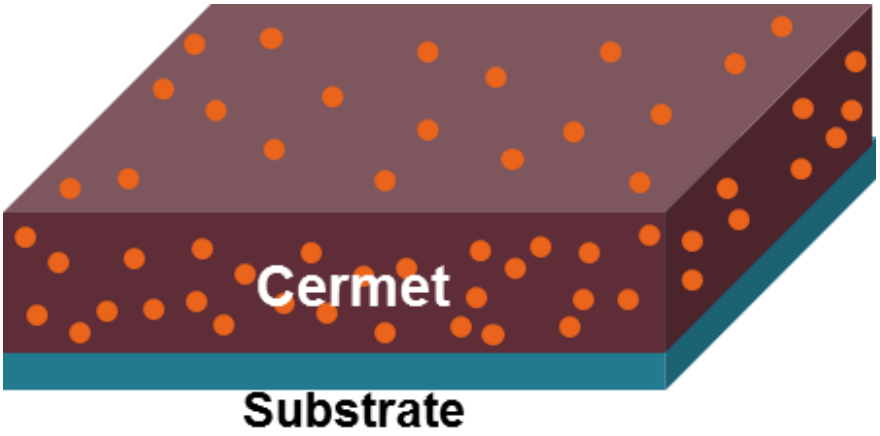

Figure 1: Schematic presentation of cermet coating.

Results and Discussion

Upon increasing temperature across 67.5°C, VO_2 undergoes a phase transition from semiconducting monoclinic phase to the metallic rutile. As the metallic phase features low thermal emittance, the surface appears colder when imaged with a thermal camera. This phenomenon is termed as negative differential thermal emittance.[13]

The VO_2 emissivity versus temperature upon cycling between 60 and 70°C, figure 2, features three distinct regions marked (a), (b) and (c). During heating stage, the system undergoes an abrupt semiconductor to metal transition (SMT) at 67.5°C resulting in an emissivity drop of 0.8 to 0.1 within a ΔT of 2°C. The infrared images in Figure 2 (i), (ii) and (iii) provide a visual representation of the material undergoing SMT, by formation of metallic puddles in the semiconducting phase, which grow in number and coalesce, thus making the whole layer metallic. These metallic puddles reflect Infra-red radiation and have a lower emissivity. [12–14]

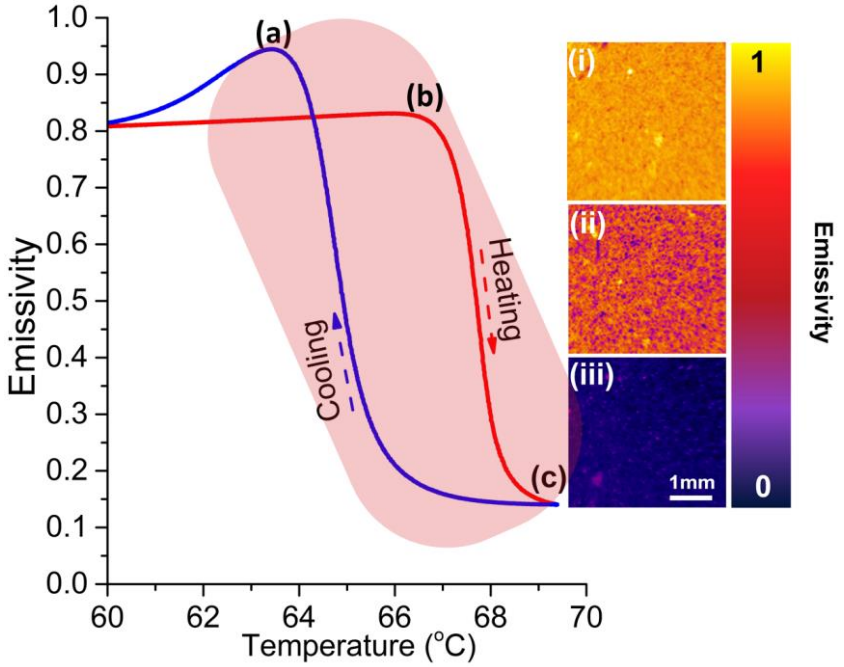

Figure 2: Temperature-dependent emissivity of VO_2 across the SMT and the infrared images of three selected regions (a, b and c) on the hysteresis curve. Metamaterial region is shown as a shaded area on the hysteresis curve.

In the cooling stage, emissivity features a transient peaking up to 0.94 at 63.5°C marked as (b) in figure 2. This peculiar peak of emissivity is highly reproducible and is systematically observed for all performed coatings. It should be noted that we observe this peak exclusively in the cooling stage, whereas other authors observed it in both heating and cooling stages. [13,15] This contrasting behaviour can be attributed to the difference in the synthesis method and the memory effect of VO_2. The peak in the emissivity curve is attributed to the formation upon cooling of nanoscale metallic inclusions in an arrangement that maximizes light absorption. At 63.5°C the density and size of the metallic inclusions align in such a way that a near perfect thermal emittance is reached.

Perfectly reversible and reliable emissivity transition is recorded for VO_2 films during extended thermal cycling tests. Furthermore, the transition characteristics were shown to be insensitive to the cycling rate. The stability of the metamaterial state is demonstrated in a previous work, where Raman mapping of the mixed

phase region was reported over 100 h to obtain a spatial mapping of the metallic inclusions in the semiconducting matrix.[14]

The metallic inclusions nucleate and grow upon heating, and shrink to disappear in the cooling stage. During a subsequent cycle, IR imaging reveals the nucleation of the metallic phase exactly at the same positions and confirms its systematic growth in an identical manner as the preceding heating cycle. Naor et al.[16] termed this phenomenon as a ramp reversal memory effect, implying that metallic inclusions form and vanish at the exact same position, and their grown/shrinkage occurs in an identical manner during consecutive thermal cycles. This behaviour is of paramount importance for a tuneable and reliable light modulation. The memory effect enables in our study adjusting and maintaining the system at specific values of emissivity. Therefore the temperature is a reliable parameter to precisely control the overall cermet architecture.

VO_2 metamaterial coatings offer a superior flexibility compared to traditional cermet coatings which feature fixed distribution and density of metal particles. Guo et al.[17] described how metallic inclusions can be engineered to tailor matter-light interaction. They reviewed the applications of metallic nanostructures for light trapping in solar energy-harvesting structures and devices from thin film photovoltaic cells to solar thermal structures and devices.[17] Therefore, by controlling the size, shape and density of metallic inclusions, VO_2 coatings clearly place themselves as an attractive and versatile all-oxide alternative. Tuneable emissivity provides a fertile ground for the design and integration of innovative smart light modulation functionalities in existing technologies.

Significant research has been done in the field of thermal management for spacecraft and satellites, due to varying exposure to sun illumination. Variable heat rejection surfaces are used to control the heat dissipation mechanisms. One of the earliest techniques of thermal management of spacecraft is by the use of mechanical or electric louvers, where actuating the louvers exposes or conceals a section of surface with a contrasting emissivity, thereby reflecting the IR radiation on demand. Electric louvers based on micro-electro-mechanical systems (MEMS) were introduced to further improve the same mechanism and

miniaturise the package.[9] Here micro-sized windows open and close on demand to reject IR radiation. An advantage of MEMS based louvers over the bulk mechanical counterparts is the possibility to achieve partial IR rejection by actuating part of the micro-louvers.[9] Electrochromic devices that rely on chemical changes to vary the emissivity of the surface are investigated as alternative solutions to change the optical properties of the radiating surface. An electrically triggered redox reaction on conductive polymers leads to a change of emissivity ($\Delta\varepsilon$). The absence of moving parts is advantageous in terms of cost of production, reliability and integration.[10] Nevertheless, slower switching times; high input power and the relatively low $\Delta\mathcal{E}$ remain clear drawbacks. This strengthens the need of developing variable emissivity coatings that offer large amplitude of emissivity change, with negligible switching delay and low actuation power. The coating should also have virtually no loss in performance over a longer time period and resist environmental degradation. Therefore inorganic metal oxide coatings with intrinsic phase transition behaviour are an appealing alternative. Ideally the phase transition occurs instantaneously between two strongly contrasting emissivity states without involving any chemical change. A change in emissivity form 0.8 to 0.1 is very considerable ($\Delta\mathcal{E}$ = 0.7), but an even higher change from 0.94 to 0.1($\Delta\mathcal{E}$ = 0.84), demonstrated here using VO_2 coatings, is unprecedented with conventional variable emissivity coatings that are primarily used in space applications.[18,19]

Figure 3 demonstrates emissivity tuning by adjusting the cooling and heating cycles in the metamaterial region. By limiting the extent of cooling to the temperature enabling the maximal emissivity (marked by a blue circle in figure 3b) and beginning the heating stage in the subsequent cycle (figure 3c), it is possible to take benefit of the observed emissivity spike to further enhance the amplitude of the emissivity change. The described control of temperature ramp yields tuneable emissivity of VO_2 metamaterial between 0.94 and 0.1. Figures 3d, 3e and 3f highlight the possibility to adjust the emissivity between 0.1 and virtually any intermediate value, ≤0.94, by appropriately selecting the minimal cooling temperature. Similar approach can be implemented to enable emissivity change between 0.94 and virtually any intermediate value, ≥0.1, by appropriately

selecting the maximal heating temperature. Other heating-cooling cycles can be conveniently designed to adjust both the minimal and maximal emissivity values within the 0.1- 0.94 range. As the semiconductor to metal transition of VO_2 occurs in picosecond time scale, [20,21] a high-speed light modulator can be designed.

Thermally controlled switching of emissivity in VO_2 films is demonstrated in figure 4(a). Initially VO_2 films are stabilized at a steady state temperature of 68^oC in the metallic state with low emissivity. A cooling pulse of $\Delta T=1.5^oC$ dips the temperature of the system to 66.5^oC, driving the system to switch from a low emissivity state at $\varepsilon = 0.1$ to a high emissivity state at $\varepsilon = 0.94$. A heating pulse of similar amplitude drives the system back to the low emissivity state. This way, VO_2 in the disordered metamaterial state can be used as an optical switch with controlled emissivity that correlates directly with the infrared reflection. Therefore, the smart cermets can be explored for applications as a shutter and IR light modulation. Stable emissivity switching behaviour for a prolonged duration, is also demonstrated in figure 4(b). By maintaining the system at a steady state temperature in the middle of the hysteresis loop, emissivity switching is achieved by providing tiny temperature pulses in either direction. Small energy inputs like temperature pulses lead to large changes in emissivity, thereby making them highly efficient and low power consuming alternatives to existing emissivity control devices.

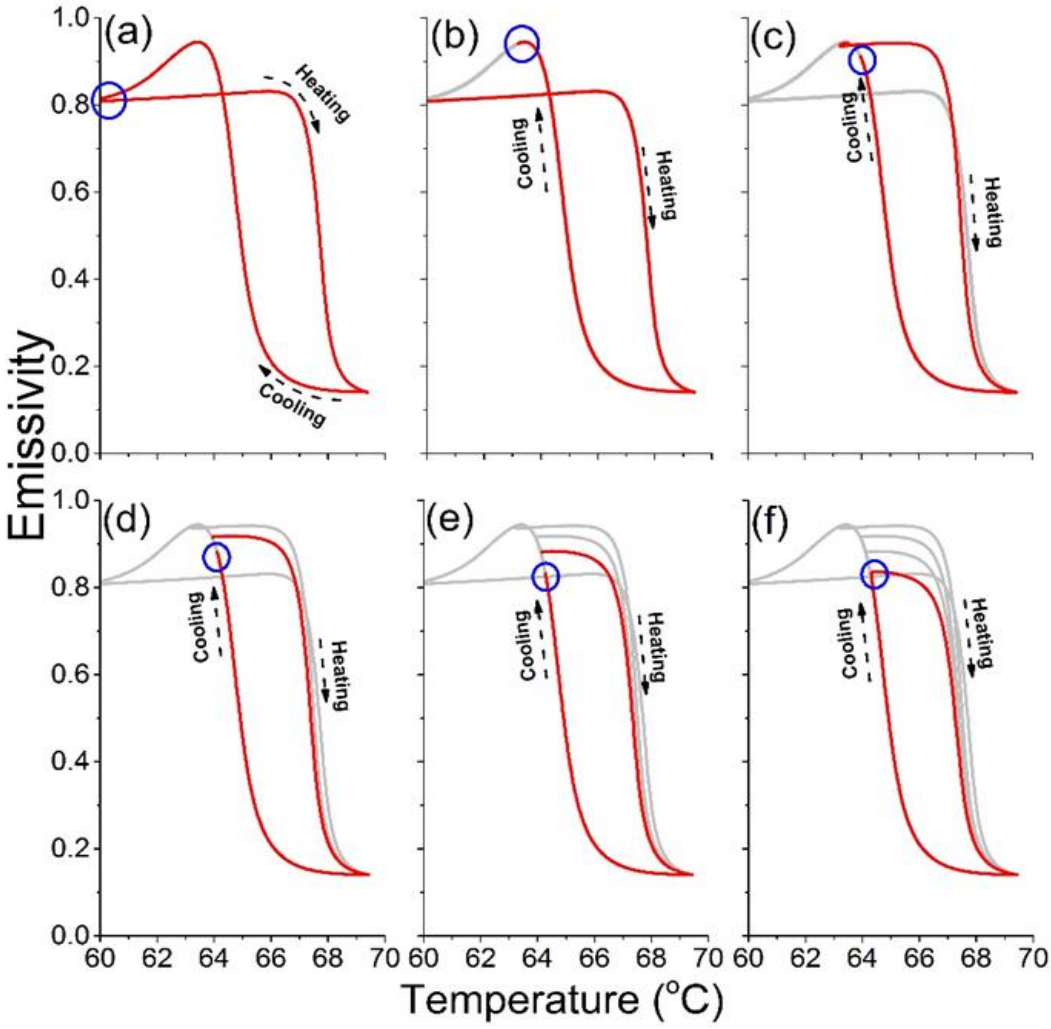

Figure 3: Variable emissivity as shown from (a) to (f) is achieved by adjusting the minimal temperature of cooling cycle, and beginning the heating cycle immediately. Precise emissivity state can be reached by manipulating the cooling and heating temperatures.

Coatings, exhibiting emissivity control and infrared modulation require micro fabrication and additional processing challenges like multilayer deposition, MEMS fabrication and patterning, [8,11,22–24] all of which increase the complexity and cost of the end product. Due to the intrinsic nature of VO_2 coatings, no additional processing or patterning steps are required to achieve light modulation. High $\Delta\varepsilon$ is achieved by providing small temperature pulses. These changes in emissivity are in fact a direct consequence of the variation in the topography of metallic inclusions in VO_2 metamaterial state. Hence a modular and tuneable emissivity

state is reached by changing the size, shape and density of metal inclusions into a semiconducting matrix thus functioning as a smart cermet. We believe it is the first time VO_2 films are suggested to act as smart cermet.

In conclusion, smart cermet concept was introduced using VO_2 films in the metamaterial temperature range. VO_2 and correlated oxides with SMT in general, can be ideal candidates for future light modulation, infrared reflectivity and thermal emissivity to name a few. Hereby, the optical modulation in VO_2 is thermally triggered. Electrical field [25] or mechanical stress [26] can also be implemented for the actuation of the SMT in VO_2. Combining this strongly responsive material property with existing and upcoming technologies opens up countless possibilities to integrate innovative functionalities in light modulation and solar energy harvesting.

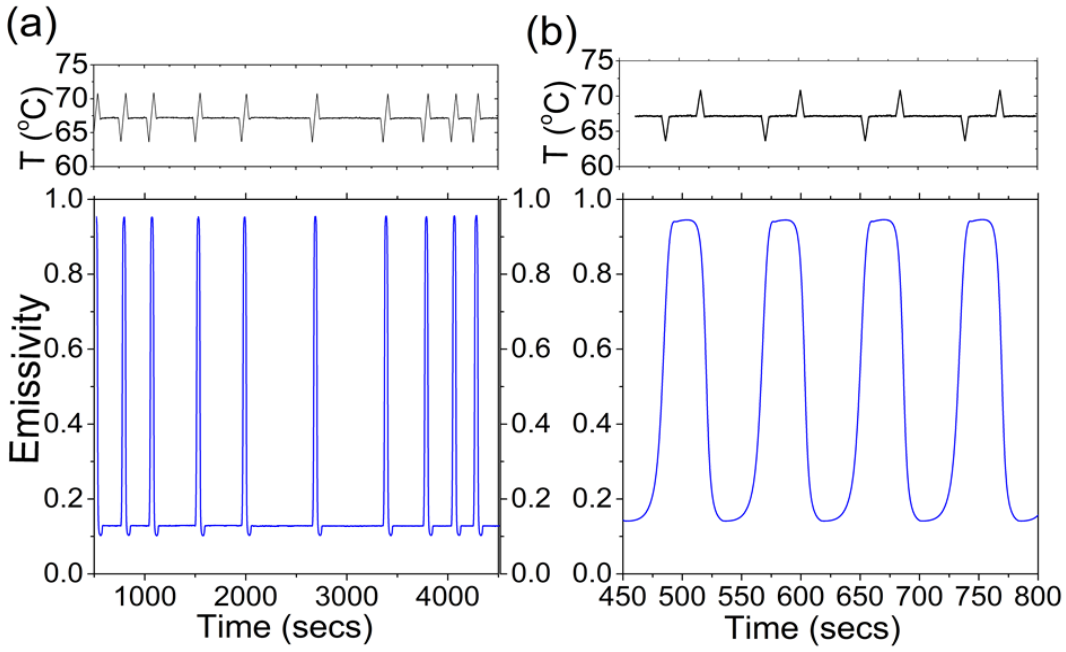

Figure 4 (a) Thermally controlled emissivity switch activated by minute temperature instantaneous (a) or sequential (b) double pulses with the amplitude of ±1.5oC.

Methods

VO_2 films were deposited on silicon substrates using direct liquid injection MOCVD (MC200 from Anneal Sys), which is a stagnation point-flow warm-walled reactor. Cyclohexane solution containing $5x10^{-3}$ mol/l of vanadium (IV) oxy-tri-isopropoxide is used as a single-source precursor which was maintained under nitrogen atmosphere at room temperature before its injection into the evaporation chamber at a frequency of 2 Hz and a feeding rate of 1 g/min. The pressure and temperature of the evaporation chamber were maintained at 0.6 mbar and 200°C during deposition respectively. The substrate is maintained at 600^0C during the 2 hours of deposition and the subsequent heat treatments.

An hour-long annealing was performed right after the deposition under oxygen partial pressure of $1x10^{-2}$ mbar. The sample is then further subjected to annealing under vacuum acting as a reducing atmosphere for 4 hours. The chamber is allowed to cool down to withdraw the sample. All depositions were carried out on 4-inch silicon wafers with an upper native oxide layer. Uniform and high quality VO_2 films were observed throughout the wafers with excellent homogeneity.

Characterization - Film thickness was measured using an Alpha step d-500 profilometer from KLA-Tencor. Infrared image analysis was conducted using the FLIR X6580SC thermal camera operating in the spectral range of 1.5 - 5.1 µm. A CNT based black coating was used as a reference black body for accurate determination of emissivity and temperature of VO_2 films. Precise temperature control was achieved through a Linkam TMS heating stage with programmable heating and cooling ramps.

References

1. Cao F, McEnaney K, Chen G, Ren Z. A review of cermet-based spectrally selective solar absorbers. *Energy Environ Sci* 2014; **7,** 1615–1627.
2. Moon J, Kim TK, VanSaders B, Choi C, Liu Z, Jin S, Chen R. Black oxide nanoparticles as durable solar absorbing material for high-temperature concentrating solar power system. *Sol. Energ. Mat. Sol C* 2015; **134,** 417–424.
3. Arancibia-Bulnes CA, Estrada CA, Ruiz-Suárez JC. Solar absorptance and thermal emittance of cermets with large particles. *Journal of Physics D: Applied Physics* 2000*;* **33,** 2489–2496.
4. Krishnamoorthy H, Jacob Z, Narimanov E, Kretzschmar I, Menon, V. Topological Transitions in Metamaterials. *Science* 2012*;* **336,** 205–209
5. Zhou J, Chen X, Guo J. Efficient Thermal-Light Interconversions Based on Optical Topological Transition in the Metal-Dielectric Multilayered Metamaterials. *Adv. Mater.* 2016*;* **28,** 3017–3023.
6. Wang H, Wang L. Perfect selective metamaterial solar absorbers. Optics express. 2013; **21(106)**, 1078-1093.
7. Liu X, Tyler T, Starr T, Starr AF, Jokerst NM, Padilla WJ. Taming the Blackbody with Infrared Metamaterials as Selective Thermal Emitters. *Phys Rev Lett* 2011; **107,** 045901
8. Swanson TD. MEMS device for spacecraft thermal control applications. United States patent US 6,538,796. 2003 .
9. Meseguer J, Pérez-Grande I, Sanz-Andrés A. Spacecraft thermal control. Elsevier; 2012 .
10. Hengeveld D, Mathison M, Braun J, Groll E, Williams A. Review of Modern Spacecraft Thermal Control Technologies. *HVAC&R Research* 2010*;* **16,** 189–220.
11. Demiryont H, Moorehead D. Electrochromic emissivity modulator for spacecraft thermal management. *Sol. Energ. Mat. Sol C* 2009*;* **93,** 2075–2078
12. Qazilbash MM, Brehm M, Chae BG, Ho PC, Andreev GO, Kim BJ, Yun SJ, Balatsky AV, Maple MB, Keilmann F, Kim HT. Mott Transition in VO_2

Revealed by Infrared Spectroscopy and Nano-Imaging. *Science* 2007*;* **318,** 1750–1753

13. Kats MA, Blanchard R, Zhang S, Genevet P, Ko C, Ramanathan S, Capasso F. Vanadium Dioxide as a Natural Disordered Metamaterial: Perfect Thermal Emission and Large Broadband Negative Differential Thermal Emittance. *Phys Rev X* 2013; **3,** 041004
14. Kumar S, Maury F, Bahlawane N. Electrical Switching in Semiconductor-Metal Self-Assembled VO_2 Disordered Metamaterial Coatings. *Sci. Rep.* 2016*;* **6,** 37699
15. Leahu G, Voti R, Sibilia C, Bertolotti M. Anomalous optical switching and thermal hysteresis during semiconductor-metal phase transition of VO_2 films on Si substrate. *Appl Phys Lett* 2013*;* **103,** 231114
16. Vardi N, Anouchi E, Yamin T, Middey S, Kareev M, Chakhalian J, Dubi Y, Sharoni A. Ramp-Reversal Memory and Phase-Boundary Scarring in Transition Metal Oxides. *Adv Mater* 2017; **29(21)** 1605029
17. Guo CF, Sun T, Cao F, Liu Q, Ren Z. Metallic nanostructures for light trapping in energy-harvesting devices. Light: Sci. Appl. 2014 ;**3(4)**: e161.
18. Demiryont H, Moorehead D. Electrochromic emissivity modulator for spacecraft thermal management. Sol. Energy Mater. Sol. Cells. 2009; **93(12)**, 2075-2078.
19. Douglas DM, Swanson T, Osiander R, Champion J, Darrin AG, Biter W, Chandrasekhar P. Development of the variable emittance thermal suite for the space technology 5 microsatellite. AIP Conference Proceedings 2002; **608**, 204-210
20. Zhai Z, Li Z, Xiao Y, Shi Q, Zhu L, Huang W, Peng Q. Ultrafast THz modulation characteristics of photo-induced metal-insulator transition of W-doped VO_2 film, 40th International Conference on Infrared, Millimeter, and Terahertz waves (IRMMW-THz), 2015; 1-1.
21. Muskens OL, Bergamini L, Wang Y, Gaskell JM, Zabala N, De Groot CH, Sheel DW, Aizpurua J. Antenna-assisted picosecond control of nanoscale phase transition in vanadium dioxide. *Light: Sci. Appl.* 2016*;* **5,** e16173

22. Rensberg J, Zhang S, Zhou Y, McLeod AS, Schwarz C, Goldflam M, Liu M, Kerbusch J, Nawrodt R, Ramanathan S, Basov DN. Active Optical Metasurfaces Based on Defect-Engineered Phase-Transition Materials. *Nano Lett* 2016*;* **16,** 1050–1055
23. Kocer H, Butun S, Palacios E, Liu Z, Tongay S, Fu D, Wang K, Wu J, Aydin K. Intensity tunable infrared broadband absorbers based on VO_2 phase transition using planar layered thin films. *Sci Reports* 2015*;* **5,** 13384
24. Demiryont H. Emissivity-modulating electrochromic device for satellite thermal control. SPIE News-room 2008; **10**, 1-2
25. Crunteanu A, Fabert M, Cornette J, Colas M, Orlianges JC, Bessaudou A, Cosset F. Electric field-assisted metal insulator transition in vanadium dioxide thin films: optical switching behavior and anomalous far-infrared emissivity variation Proc. SPIE 2015; 93640J
26. Sohn JI, Joo HJ, Ahn D, Lee HH, Porter AE, Kim K, Kang DJ, Welland ME. Surface-stress-induced Mott transition and nature of associated spatial phase transition in single crystalline VO_2 nanowires. *Nano Lett.*2009*;* **9,** 3392–3397.

4.4 An infrared blackboard based on the disordered metamaterial state of Vanadium oxide.

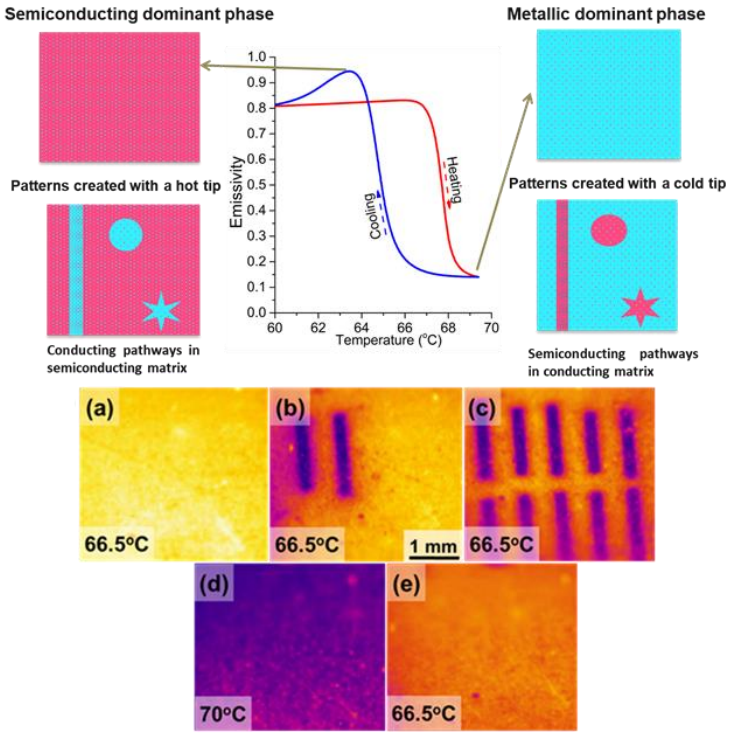

Electrically and optically contrasting patterns can be created on VO_2 films by localised laser heating which is visible in the NIR region. The patterns thus created are stable as long as the temperature is maintained and erased upon temperature cycling.

(In preparation)

Introduction

Reversible phase transitions [1–4] and rewritable patterning [5–7] are amongst the most sought-after properties in the current generation of memory storage and high density optical storage media. Conventional Lithography techniques are often irreversible and offer no flexible way of editing the pattern once it has been made. An ideal material would therefore allow patterning with ease, and allow to reconfigure with ease or erase, and rewrite without involving significant process steps. It would also be incredibly useful if the patterns created can offer additional functionalities other than just a visual information.

The current state of the art regarding reversible patterning mainly involves organic polymer materials which change the configuration by photosensitization, [8,9] change in pH, [10,11] thermochemical nanolithography [12] and electrical potential induced redox reaction. [13,14] Inorganic phase change materials are prototype candidates for such application. In this article, we present vanadium oxide as an ideal candidate to achieve such reversible and reversible patterning by utilizing its SMT property.

Vanadium oxide undergoes a first order phase transition from a semiconducting monoclinic phase to a metallic rutile structure at 68°C. Along with the electrical transition, VO_2 undergoes a change from an Infrared transparent, to reflective material when heated above the transition temperature. [15] Infrared images of VO_2 film obtained from thermal camera near the phase transition reveals an abrupt drop in the emissivity at SMT. Reduced emissivity due to the reflection of IR radiation is reversible with a narrow hysteresis of 3K. At this transition, semiconducting monoclinic phase is converted to a conducting rutile phase. Optically, the monoclinic phase has a higher emissivity in respect to the rutile phase [16]. During the SMT in VO_2, small puddles of rutile metallic start forming from 66°C and continue to coalesce as the

temperature rises. [17,18] The phase fraction of Monoclinic to rutile can be controlled by deliberately maintaining the system at adjusted temperature.

In a previously reported article [16] it was mentioned that at 67°C and 66°C in the heating and cooling cycles respectively, we essentially have the film stabilised with both M and R phase. Therefore, there exists an intermediate state in a narrow temperature range of 66- 69°C with two optically and electrically contrasting characteristics of the same material at one temperature point. This state of the material can be termed as a "naturally disordered metamaterial". [16,19]

Emissivity vs temperature curve shown in figure 1 when heating from 60 to 70°C shows an abrupt decrease in the emissivity from 0.83 to 0.1 during the heating cycle, but a very interesting phenomenon is observed in the cooling cycle. The emissivity while going back to the cold state rises abruptly and briefly exceeds to 0.94 in a narrow temperature window before reaching a steady state value of 0.8. The only existing report of such behaviour is by Kats et al. [19] where the authors show this spike of emissivity in both heating and cooling stages. This spike in emissivity is attributed to the specific arrangement of the metallic puddles during their shrinkage dynamics. This results in the peaking of emissivity in short temperature intervals.

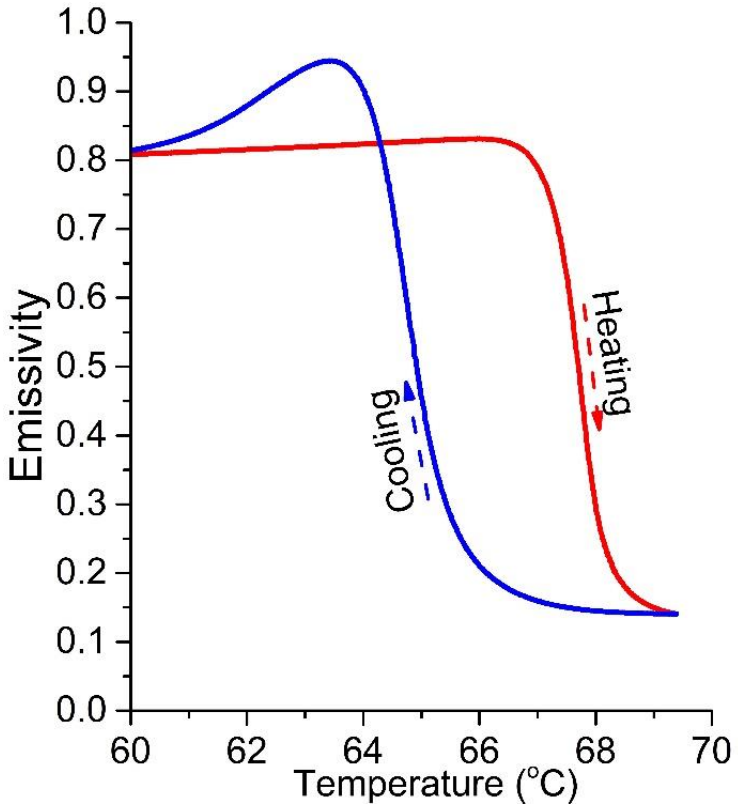

Figure 1: Integrated emissivity of VO_2 film as a function of temperature during heating and cooling cycle.

The spike in emissivity can however be accessed by making sure that during the cooling cycle the temperature is set to stabilize at the point where the emissivity is maximal. By controlling the upper and lower limit of the temperature cycle, one can dictate the system to stabilize at the desired emissivity between 0.1 to 0.9. The narrow hysteresis width of 3K provides the ability to cycle between the low and high emissivity states by quick heating or cooling pulses. By keeping the system at a steady state temperature of 67°C the material can be operated in its metamaterial region where a dynamic coexistence of the semiconducting and metallic phases of VO_2 occurs. Quick heating or cooling pulses will force the system to either switch to high or low emissivity state, which persists when the films returns to the steady state temperature.

Dynamic control of VO_2 metamaterial

After establishing the fact that VO_2 films operating in the narrow range of temperature around the transition temperature (T_C) behaves as a disordered metamaterial, film properties like emissivity, reflectivity, and resistivity can be manipulated to exhibit contrasting behaviours by choosing the state at which VO_2 metamaterial can be stabilized, simply by controlling the temperature. Figure 2 shows a schematic of these three states namely a high emissivity state at 66°C, a modular emissivity state between 66-69°C and low emissivity state above 69°C.

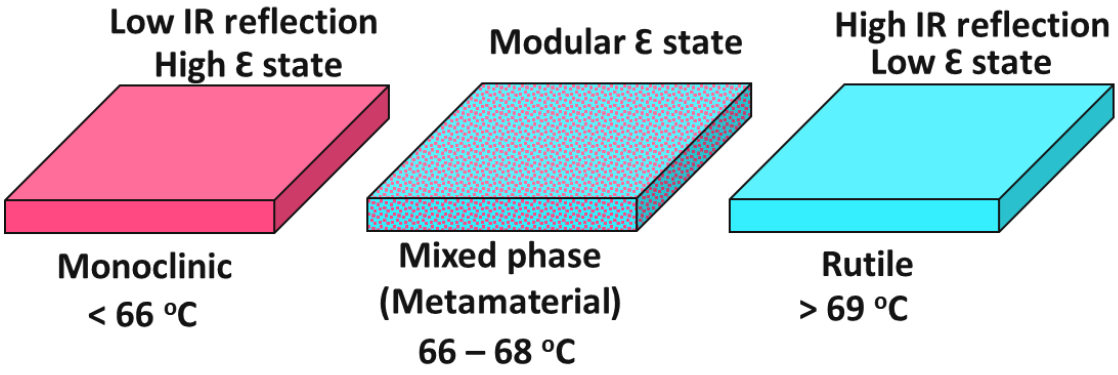

Figure 2. Schematic representation of different states of VO_2 in three different temperature ranges.

Since the metamaterial can be maintained as long as it is kept at the required temperature, it's possible to locally change the phase of the material to either M or R depending on the type of temperature impulse. Such localized triggering of phase transition can be observed very clearly with an IR camera due to the large variations of emissivity and reflectivity values for the M and R phases. In theory, the metamaterial can be controlled to have localized phase transformations by introducing precise temperature changes in the region of interest as shown in figure 3.

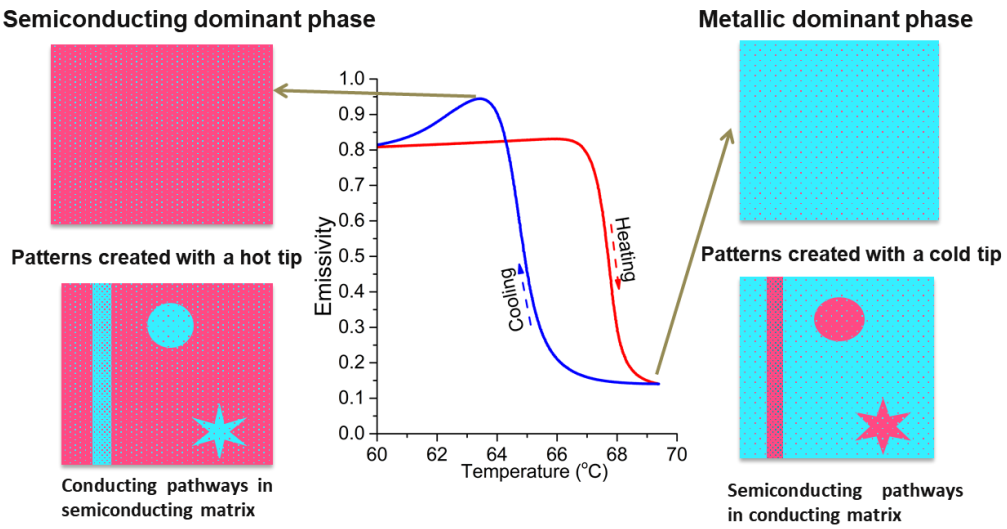

Figure 3 modulating the metamaterial region either in hot or cold state by locally triggering the phase transition.

Several ways can be hypothesised to induce a localized phase transition in vanadium oxide. However, for the sake of simplicity, in this study we restrict ourselves to operations that directly result in localised temperature changes that can induce phase transition in VO_2 at the point of contact. The following techniques are employed for the localized modification of metamaterial.

Imprinting by contact

Point to point modification of phase from semiconducting to metallic nature can be done by localized heating. Here the film is maintained at a fixed temperature of 67°C and local heating is introduced by a pointed tip (Hot Tip) which is at least 4-5°C higher than the fixed temperature. As soon as the “hot-tip” touches the surface, it forces the point of contact to undergo a phase transition. Since the point of contact is very small and the phase transition occurs instantaneously, we can just tap the “hot tip” on the surface and form dots of metallic nature with lower emissivity on a semiconducting matrix having higher emissivity. Thereby creating an

electrically and optically contrasting medium at the same temperature. Figure 4 shows a simple schematic creating metallic low emissivity dots by contact imprinting using a “Hot-Tip”.

Using this technique, one can also drag the hot tip along the surface to make lines or any other patterns. Which gives rise to the formation of reversible dynamic conducting pathways in semiconducting matrix? Another way of modifying the phase is by using a “cold tip”. In this approach, we maintain the film in the metallic state having low emissivity and by make the point of contact by a tip which is at least 5°C colder, we can induce a phase transition in the opposite direction to semiconducting region with higher emissivity. Therefore, allowing the possibility of patterning resistive semiconducting pathways having higher emissivity in a low emissive metallic matrix.

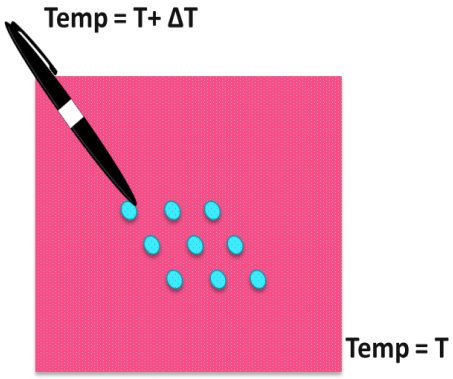

Figure 4: Schematic of localized phase transition induced by contact imprinting by a "Hot-Tip"

Pattern transfer by Stamping.

A precast stamp of certain shape could be used to instantaneously transfer the shape or pattern over a large area. The stamp when maintained at 72°C can be made to come in direct contact with the metamaterial, thereby facilitating a phase transition. Hot and cold stamp can be realised.

Imprinting by electric field

It is well known that SMT can be triggered in VO_2 by applying an electrical potential.[20] Hence a novel way to induce a localized phase transition would be to use electrical bias and a contact tip with an appropriate potential.

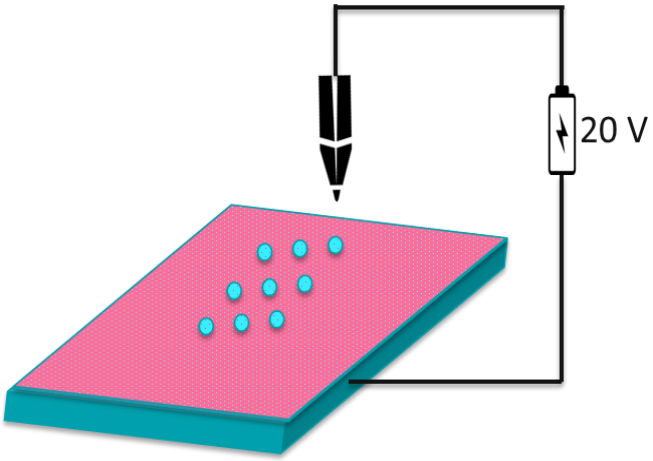

Figure 5: A schematic of localized triggering of SMT by applying an electrical potential.

VO_2 can be maintained at a steady state of 67°C on a conducting substrate. Voltage bias when applied through a tip by contact allows the creation of metallic structures in the semiconducting VO_2 matrix. Just by reversing the polarity, we can either erase the patterns or perform corrections to existing patterns. This procedure can be thought as analogous to traditional ion beam lithography where we create patterns by charged particles as depicted in figure 5.

Pattern transfer by photolithography.

Another way to achieve this localized phase transition is with the use of a high intensity light. Just like photolithography a mask placed on top of the metamaterial is illuminated by a high intensity light in short bursts to heat up the surface on exposure and transfer the pattern as shown in figure 6.

This technique can enable fast and large area patterning. Just by cooling down we can erase the whole pattern and re-use the same VO_2 substrate for a different design later.

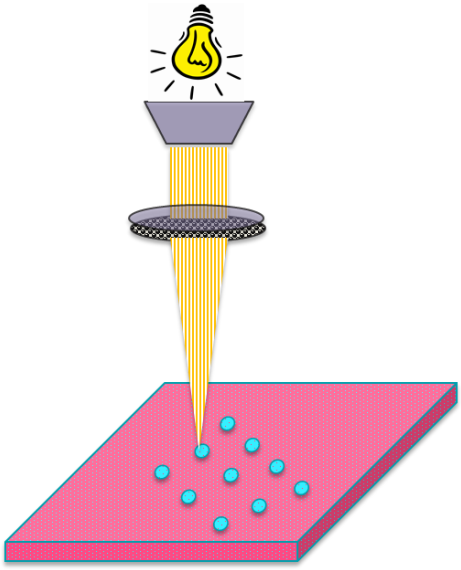

Figure 6: Transferring pattern through an optical mask and inducing SMT by high intensity light.

Reversible patterning by localized laser heating.

A laser offers a contactless method to locally heat the surface of the metamaterial. Laser heating enables a non-invasive way of patterning and by adjusting the laser power and focus to appropriately heat the target, this technique is most convenient. It also allows better resolution when compared to physical contact by a pointed tip. Figure 7 shows a schematic of how a laser of appropriate wavelength and power when focused on the VO_2 metamaterial state can locally heat up and induce a phase change. Figure 8 shows how patterns can be made by simply moving the laser across the metastable state just as described in the schematic of figure 7. The patterns although are invisible to naked eye, are clearly visible under infrared imaging.

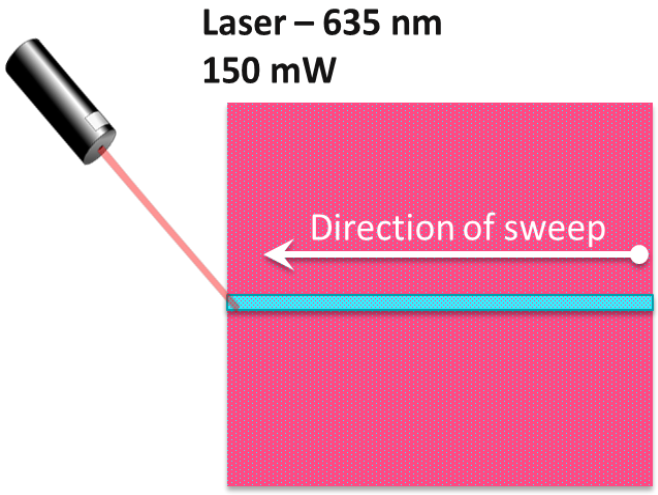

Figure 7: Schematic of a laser induced phase transition and formation of conducting pathways in semiconducting film

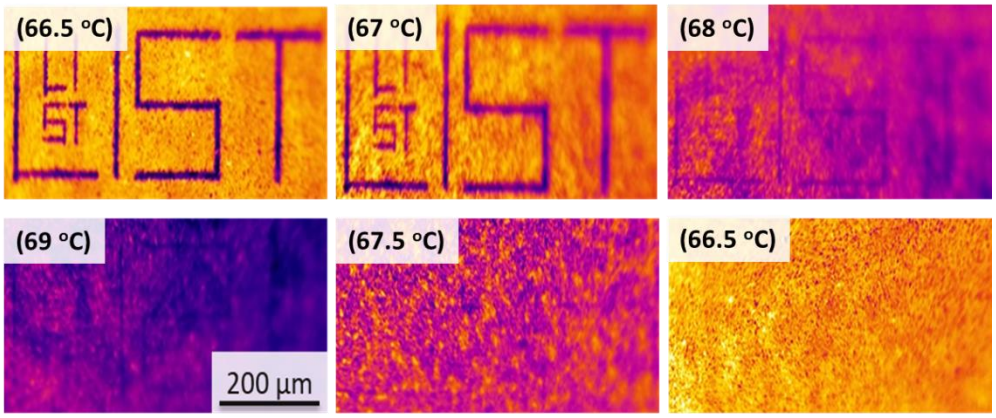

Figure 8: Thermal images from an IR camera showing the laser written pattern (LIST) undergoing the display erase and reset process, controlled by temperature cycling. The pattern slowly disappears as the steady state temperature is increased to 69°C. Lowering the temperature back to 66.0°C resets the system for new a pattern.

The laser, when focused through a 5x optical objective narrows the beam and helps to focus the beam efficiently. This results in an improved resolution of the patterns. Furthermore, a 20x objective lens enables patterning of even smaller features as shown in figure 9. We believe this is the first ever report on evidencing such kind of reversible, rewritable IR visible patterning of the VO_2 metamaterial state.

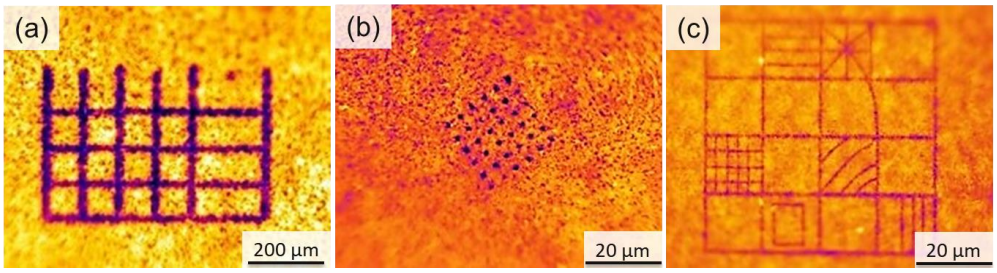

Figure 9: Patterns of grids (a), dots (b) and complex matrixes (c) can be easily drawn.

In conclusion, we have discussed different concepts of achieving localised phase transition in VO_2 metamaterial, relying on its phase transition. Creating patterns with contrasting optical and electrical features on the same surface and maintaining them at the same temperature we open numerous possibilities for next generation Opto-electronic devices which rely on fast and reliable switching mechanisms and finds use in infrared camouflage, thermal regulation, and IR tagging and other applications.

Experimental section

Sample preparation

Films of vanadium oxide were deposited on silicon substrates using direct liquid injection MOCVD (MC200 from AnnealSys), which is a stagnation point-flow warm-walled reactor. Cyclohexane solution containing $5x10^{-3}$ mol/l of vanadium (V) oxy-tri-isopropoxide was used as a single-source precursor, which was maintained under nitrogen atmosphere at room temperature before its injection into the evaporation chamber at a frequency of 2 Hz and an adjusted opening time to reach a feeding rate of 1 g/min. The pressure and temperature of the evaporation chamber were maintained at 0.6 mbar and 200°C during deposition respectively, whereas the walls of the reactor were maintained at 200°C. During the growth, 500 sccm of nitrogen carrier gas was introduced alongside the precursor

injection and the total pressure of the reactor was automatically regulated at 0.6 mbar. The substrate is maintained at 600°C during the 2 hours of deposition and the subsequent heat treatments.

In a second step, an hour-long annealing was performed at 600°C right after the deposition under oxygen partial pressure of 1x10^{-2} mbar. The sample is then further subjected to annealing at the same temperature under vacuum (~ 0.6 mbar) acting as a reducing atmosphere for 4 hours, after which the chamber is allowed to cool down. All depositions were carried out on 4-inch silicon wafers without removing the upper native oxide layer that might act as a barrier. Samples were later cut into smaller pieces for analysis purposes. Uniform, high quality VO_2 films were observed throughout the wafers in a homogeneous manner.

Laser patterns were drawn over the surface by placing the sample over the linkam heat stage set to maintain the temperature at 66.5^{o}C, and passing the laser beam over the surface. Infrared image analysis was conducted using the FLIR X6580SC thermal camera operating in the 1.5-5.1 µm spectral range with an accurate recording at a frequency of 355 Hz in a full 640 x 512 resolution. Temperature-dependent measurements were performed by placing the sample on a heating stage and cycling the temperature form 40°C to 80°C while a thermocouple was placed on the sample to measure the surface temperature. The ramp was fixed at 5°C/min in the transition range.

Acknowledgements

The authors would like to acknowledge Luxembourg Institute of science and Technology (LIST) for providing the financial support for this work.

References:

(1) Wuttig, M. Phase-Change Materials: Towards a Universal Memory? *Nature materials* **2005**, 265–6.

(2) Wuttig, M.; Yamada, N. Phase-Change Materials for Rewriteable Data Storage. *Nature Materials* **2007**, 1004–1004.

(3) Lencer, D.; Salinga, M.; Wuttig, M. Design Rules for Phase-Change Materials in Data Storage Applications. *Advanced materials (Deerfield Beach, Fla.)* **2011**, 2030–58.

(4) Shi; Chong. Nanophase Change for Data Storage Applications. *Journal of nanoscience and nanotechnology* **2007**, 65–93.

(5) Lu, Z.; Liu, Y.; Hu, W.; Lou, X.; Li, C. Rewritable Multicolour Fluorescent Patterns for Multistate Memory Devices with High Data Storage Capacity. *Chemical communications (Cambridge, England)* **2011**, 9609–11.

(6) Ma; Liu; Yang. Organic Electrical Bistable Devices and Rewritable Memory Cells. *Applied Physics Letters* **2002**, 2997–2999.

(7) Gindre, D.; Boeglin, A.; Fort, A.; Mager, L.; Dorkenoo, K. Rewritable Optical Data Storage in Azobenzene Copolymers. *Optics express* **2006**, 9896–901.

(8) Müller, V.; Hungerland, T.; Baljozovic, M.; Jung, T.; Spencer, N. D.; Eghlidi, H.; Payamyar, P.; Schlüter, D. A. Ink-Free Reversible Optical Writing in Monolayers by Polymerization of a Trifunctional Monomer: Toward Rewritable "Molecular Paper."*Advanced Materials 29* (27), 1701220.

(9) Fudickar, W.; Fery, A.; Linker, T. Reversible Light and Air-Driven Lithography by Singlet Oxygen. *J Am Chem Soc* **2005**, *127* (26), 9386–9387.

(10) Ionov, L.; Minko, S.; Stamm, M.; Gohy, J.-F.; Jérôme, R.; Scholl, A. Reversible Chemical Patterning on Stimuli-Responsive Polymer Film: Environment-Responsive Lithography. *J Am Chem Soc* **2003**, *125* (27), 8302–8306.

(11) Sun, W.; Zhou, S.; You, B.; Wu, L. Polymer Brush-Functionalized Surfaces with Reversible, Precisely Controllable Two-Way Responsive Wettability. *Macromolecules* **2013**, *46* (17), 7018–7026.

(12) Wang; Szoszkiewicz; Lucas; Riedo; Okada; Jones; Marder; Lee; King. Local Wettability Modification by Thermochemical Nanolithography with Write-Read-Overwrite Capability. *Applied Physics Letters* **2007**, *91* (24), 243104.

(13) Liu, H.; Hoeppener, S.; Schubert, U. Reversible Nanopatterning on Polypyrrole Films by Atomic Force Microscope Electrochemical Lithography. *Advanced Functional Materials* **2016**, *26* (4), 614–619.

(14) Wang, L.; Peng, B.; Su, Z. Tunable Wettability and Rewritable Wettability Gradient from Superhydrophilicity to Superhydrophobicity. *Langmuir* **2010**, *26* (14), 12203–12208.

(15) Morin. Oxides of the 3d Transition Metals*. *Bell System Technical Journal* **1958**, 1047–1084.

(16) Kumar, S; Maury, F; Bahlawane, N. Electrical Switching in Semiconductor-Metal Self-Assembled VO2 Disordered Metamaterial Coatings. *Scientific reports* **2016**.

(17) Qazilbash, MM; Brehm, M; Andreev, GO; Frenzel, A. Infrared Spectroscopy and Nano-Imaging of the Insulator-to-Metal Transition in Vanadium Dioxide. *Physical Review B* **2009**.

(18) Qazilbash, M. M.; Brehm, M.; Chae, B.-G.; Ho, P.-C.; Andreev, G. O.; Kim, B.-J.; Yun, S.; Balatsky, AV; Maple, MB; Keilmann, F. Mott Transition in VO2 Revealed by Infrared Spectroscopy and Nano-Imaging. *Science* **2007**, *318* (5857), 1750–1753.

(19) Kats, MA; Blanchard, R; Zhang, S; Genevet, P; Ko, C. Vanadium Dioxide as a Natural Disordered Metamaterial: Perfect Thermal Emission and Large Broadband Negative Differential Thermal Emittance. *Physical Review X* **2013**.

(20) Madan H, Jerry M, Pogrebnyakov A, Mayer T, Datta S. Quantitative mapping of phase coexistence in Mott-Peierls insulator during electronic and thermally driven phase transition. ACS nano. **2015**;9(2):2009-2017.

4.5 Visible thermochromism in Vanadium pentaoxide coatings

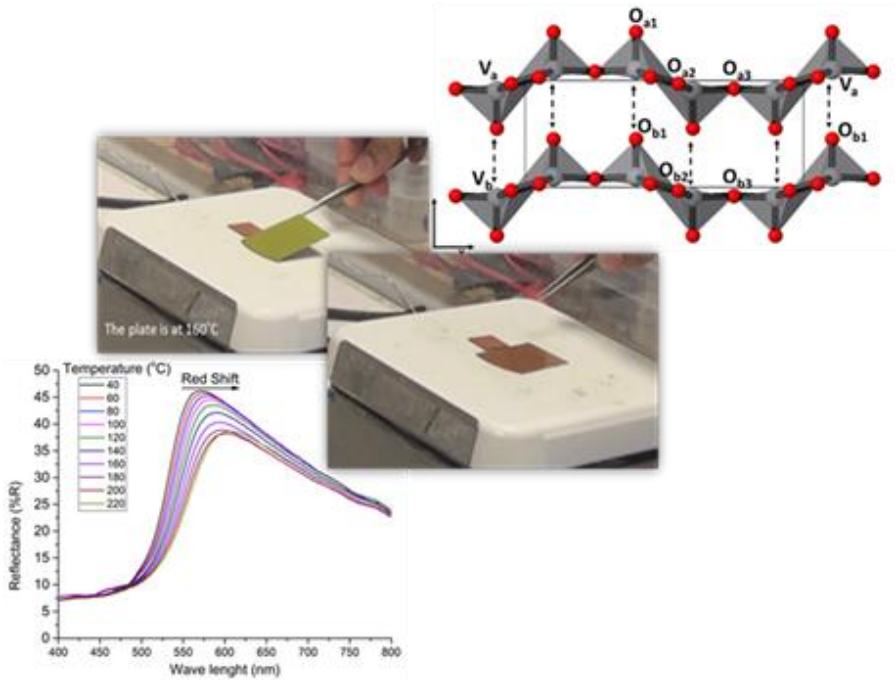

Vanadium pentaoxide (V_2O_5) coatings grown by MOCVD display visible range thermochromism form pale yellow at room temperature to deep orange at elevated temperatures. The red shift in the reflectance spectra and variation in optical band gap is linked to expansion of V_2O_5 lattice and the increasing inter planar distance between two adjacent sheets of V_2O_5

Published as Kumar, S., Maury, F. and Bahlawane, N. Visible thermochromism in Vanadium pentoxide coatings. *ACS Applied Materials and Interfaces* 9 (25), pp 21447–21456 (2017).

Abstract

Although di-vanadium pentoxide (V_2O_5) has been a candidate of extensive research for over half a century, its intrinsic thermochromism has not been reported so far. Films of V_2O_5 grown on silicon, glass and metal substrates by MOCVD in this study, exhibit a thermally induced perceptible colour change from bright yellow to deep orange. Temperature-dependent UV-Vis spectroscopy and XRD allow the correlation between the reversible continuous red shift of the absorption and the anisotropic thermal expansion along the (001) direction, *i.e.* perpendicular to the sheets constituting the layered structure. Furthermore, the possibility of tuning the thermochromic behaviour was demonstrated via a chemical doping with chromium.

Introduction

Thermochromism is a perceptible phenomenon, in many materials and compounds,[1] in which a change in colour is observed as a response to a variation of temperature over a small or large range. This process involves thermally induced lattice expansion or change in ligands, molecular structure or coordination number. [2,3] Thermochromic materials find application in a variety of fields ranging from simple decorative show pieces or toys to potentially breakthrough technological applications including comfort, lifesaving and safety devices as smart windows, sensors. [4,5]

Thermochromism might be reversible [6–9] or irreversible [10,11]. Reversible thermochromic materials, which restore their original colour once the temperature stimulus is withdrawn, are useful temperature indicators. Everyday' products, such as cooking pan, can be coated with a thermochromic paint to indicate the attainment of the cooking temperature by visual cues. [12,13] Change in optical properties, if occurring in the visible spectral range, offers a considerable

advantage and ease of detection. Reversible thermochromism can be further classified into two types that contrast in the accuracy of determining the temperature:

(a) Continuous thermochromism [14] takes place over a relatively wide range of temperature. The change of the optical properties is then attributed to a gradual structural modification in the solid.

(b) Discontinuous thermochromism [15] occurs abruptly and corresponds to a change in structure, *e. g.* consequence of a ring opening and closing mechanism in polymer chains at a specific temperature. [16]

The colour transitions in irreversible thermochromic materials, typically results from decomposition, phase transition or phase separation. [17] [11] Irreversible thermochromism is useful in situations where it is necessary to keep trace of the change in temperature even after the temperature stimulus has been withdrawn. Few examples include packaging labels of temperature sensitive drugs or perishable food items which indicate if e.g. the cold chain integrity was compromised. [18–20] The irreversibility in thermochromism can either be attributed to thermodynamic or kinetic hindrance of the transformation.

Table 1 illustrates the different material groups that feature thermochromic behavior along with the transition temperature, the mechanism which leads to thermochromism and the extent of reversibility. Thermochromic materials can be broadly categorized as organic and inorganic compounds.

Organic thermochromic compounds include, ***Conjugated Polymers*** [21] – where thermochromism arises due to the conformational change, which influences the effective conjugation length of the polymer backbone. Slight change in the structure usually leads to a significant colour shift. Some examples for each category are discussed hereafter:

Bianthrones [1] – With the increase in temperature; the central double bond expands and weakens, allowing the two non-coplanar anthrone moieties to rotate in their planes. Thus, enabling stereo isomerism with a consequent thermochromism.

Schiff bases [6,22] – Proton transfer is the basis of thermochromic behavior in many metal Schiff's base complexes. The shift in the keto-enol equilibrium, brought by the thermally influenced pH change is the fundamental aspect of colour change.

Spiropryans and Spirooxazines [16,23] **–** Thermally induced molecular rearrangements lead to the change of Spiro carbon hybridization from sp^3 to sp^2. This change is accompanied by a large delocalization of the electron density, giving rise to electron transitions which fall in visible region of the spectrum thus producing colour and colour change.

Leuco dyes and liquid crystals [12,24,25] - In a cholesteric liquid crystal, changes in temperature result in thermal expansion, which leads to a change in layer spacing and angle of rotation with a consequent colour change. Since the pitch varies continuously as the temperature changes a continuous thermochromism is expected in such compounds. Liquid crystals and leuco dyes have to be micro encapsulated for them to be used for colouration. This includes embedding them in a shell material.

Inorganic thermochromic compounds consist of ***metal salts and metal oxides.*** The mechanisms of colour change include temperature-dependent changes in ligand geometry, change in metal coordination, variation of band-gap energy, the arrangement and distribution of defects in the crystalline solid, and most importantly through phase transitions occurring in the material. [3,15]

Among the plethora of thermochromic materials, inorganic compounds provide the advantage of being stable at high temperatures when compared to their organic counterparts. Since inorganic materials are generally much more resistant to photo-induced decomposition than organic counterparts, they feature a substantially extended lifetimes. Furthermore, the preparation of powders, pigments or films based on inorganic compounds is more convenient owing to their ease of handling and robustness. As most inorganic thermochromism results from lattice expansion, perceptible change in colour can be observed even at elevated temperatures. [26]

	Type	Mechanism of Thermochromism	Temperature range of operation	Nature of transition	Decomposition temperature	Examples	References
Organic Compounds	Liquid Crystals	Variation in the crystal field and braggs reflection	-30 - 120 °C	Reversible	130 – 150 °C	Cholesterol esters	[12, 24, 25]
	Leuco dyes	Change of molecular structure	-100 - 200 °C	Reversible	> 200 °C	Fluorans or crystal violet lactone, spiropyrans, or fulgides	
	Conjugated polymers	Conformational change of polymer backbone	70 - 350 °C	Both Reversible and irreversible	> 400 °C	Polydiacetylenes or Polythiophenes	[21]
	Bianthrones	Sterio-Isomerism	80 - 300 °C	Reversible	> 300 °C	Bianthrones and highly crowded ethlenes	[1]
	Schiff's base and acids	Hydrogen ion Transfer	60 - 300 °C	Both Reversible and irreversible	> 400 °C	Nickel(II) and copper(II) complexes of Schiff bases derived from 8-aminoquinoline	[6, 22]
Inorganic Compounds	Metal salts	Phase transition and change in ligand geometry or co-ordination	100 – 200 °C	Both Reversible and irreversible	>300 °C	Cu_2HgI_4, Ag_2HgI_4, and AgI	[3, 15]
	Metal oxides		50 - 800 °C	Reversible	>800 °C	TiO_2, VO_2, ZnO,WO_3, $NiCO_2$, NH_4VO_3 and $NiMoO_4$	

Table 1 An overview of various thermochromic materials with their working mechanisms and operation temperature.

Metal oxides act in general as semiconductors showing a decrease in electrical resistivity with temperature. Hence metal oxide compounds featuring a wide band gap semiconducting property, which also exhibits a continuous visible range thermochromism over a wide temperature window, could be ideal candidates for many thermo-electro-optical applications. In this context, Cunjiang Yu *et al* [27] developed an adaptive optoelectronic camouflage based on the integration of thermochromic dyes with arrays of actuators and photo-detectors laminated on transparent and flexible substrates. A second example is reported by Kim G *et al* [28] demonstrating the mechanism and performance of a resistive pressure sensor and its integration into a dynamic and interactive thermochromic panel.

Oxides of vanadium are very popular for their chromic behavior due to the numerous oxidation states of vanadium: +5, +4, +3, and +2, easily distinguishable by their contrasting optical properties. Vanadium pentoxide (V_2O_5) with an oxidation state of +5 is by far the most studied phase. [29–31] V_2O_5 has an orthorhombic layered structure that can host small guest molecules or ions. Due to this property V_2O_5 is intensively investigated as a catalyst for organic reactions,

[32]and also finds use in lithium ion batteries, [33] gas sensors, [34] electrochromism [35] and photochromism. [36] Nevertheless, there is a wide inconsistency when it comes to the description of the physical colour of V_2O_5 at room temperature. The reported colours of the compound range from yellow, yellow- to- red or rust brown or orange. [37–39]

Additionally, there seems to be no previous report on the thermochromic behavior of pure V_2O_5. Lataste *et al* reported the implementation of V_2O_5 as a mixture in pigments to alter the thermochromic behavior of barium carbonate. [40] In a study reporting the use of inorganic material blend to mimic the red to green transition by M. Gaudon *et al*, [41] V_2O_5 powder was blended with Cr_2O_3 to investigate the thermally induced colour change. Surprisingly the intrinsic thermochromic behavior of V_2O_5 seems to be overlooked. It should be cautiously noted that another oxide of vanadium, namely VO_2, is extensively studied for its thermochromic behavior in the infrared spectral range, [42] but we strictly restrict this study to V_2O_5 for all purposes. In this work, we shed light on the intrinsic visible thermochromism in pure and chemically doped vanadium pentoxide (V_2O_5) thin films at elevated temperatures.

Experimental

Deposition process

Thin films of vanadium oxide were deposited on silicon substrates by Direct Liquid Injection (DLI) Metal Organic Chemical Vapor Deposition (MOCVD) in a custom built warm wall vertical stagnation point flow reactor. Low concentration ($5x10^{-3}$M) ethanol solution of 99.9% pure Vanadium (V) oxy-tri-isopropoxide ([$VO(O^iPr)_3$] was used as the precursor feedstock. Liquid injection was performed in an evaporation tube maintained at 225°C to secure the quasi instantaneous vaporization of the precursor solution. The injection was maintained at 4 Hz with 4 ms opening time resulting in a liquid flow rate of 1.33 ml/min. Argon was used as the carrier gas at a flow rate of 50 cm^3/min while the chamber pressure was

adjusted to 10 mbar. Substrates were maintained at a constant temperature of 500°C during the four hours of deposition.

After deposition, the samples were allowed to cool to room temperature in argon atmosphere under low pressure before withdrawing from the chamber and further handling under ambient atmosphere. A post deposition anneal was performed under ambient air at 550°C.

A series of Cr-doped V_2O_5 thin films was also grown by the implementation of mixed precursor feedstock with adjusted Cr/V ratio. Doping V_2O_5 films with Cr was achieved by simply mixing at various dilutions a 5 mM ethanol solution of chromium acetylacetonate, $Cr(acac)_3$, into the vanadium precursor used for the MOCVD deposition.

Thin film characterization

X-ray diffraction (XRD) was used to characterize the films using the Bruker D8, with CuKα as the X-ray source. Data were collected in the θ-2θ (locked couple) mode from 2θ of 10° to 30° with a step size of 0.02°. Temperature-dependent XRD was performed using a heated stage with an integrated thermocouple and air cooling for temperature regulation. The film thickness was measured using an Alpha step d-500 Profilometer from KLA-Tencor and the cross-section inspection with FEI Helios Nanolab 650™ Scanning electron microscopy (SEM). Surface and cross-sectional morphologies were characterized by SEM at a working distance of 4 mm with an acceleration voltage of 25 kV.

Raman scattering was performed using an InVia Raman spectrometer from Renishaw with a 532 nm laser at 0.2 mW to avoid non-controlled surface heating. Optical reflectivity measurements were carried out on LAMBDA 1050 UV/Vis/NIR spectrophotometer from Perkin Elmer with a 100 mm integration sphere in the reflection configuration. Measurements were performed in the visible spectral range (400-800 nm). For both spectroscopies, in situ measurements at variable temperatures were carried out under ambient atmosphere. For technical reasons related to apparatus, we restrict the UV Vis measurements to a maximum temperature of 220°C.

Results and discussion

Undoped V_2O_5 thin films

The film deposition parameters, like temperature and pressure, were adjusted to achieve highly porous nanocrystalline films with mixed crystalline phases of vanadium oxide VO_x. Deposition conditions were chosen based on a previously reported systematic study. [43] With an average growth rate of 10 nm/min, a 4 h deposition yields 2.4 µm thick film (Figure 1).

Temperature-dependent XRD and Raman scattering provide evidence that annealing of the as-grown VO_x films under ambient air at 450 °C for 10 min allows the complete oxidative conversion of the films to pure V_2O_5. This is in good agreement with the temperature range of 450 - 550 °C previously reported to be optimal for this purpose.[44] The oxidation process requires an extended time of annealing at lower temperature. For example, 1 hour is needed at the annealing temperature is 300°C. The oxidation of vanadium occurs due to gas-solid reaction followed by oxygen diffusion into the film. It is worth mentioning that the porous structure of the film, Figure 1, has a clear advantage in this respect. The aforementioned post treatment results in the formation of a thermodynamically preferred phase, which is the layered orthorhombic V_2O_5 with the Pmmn space group. [45]

Figures 1(a) and (b) display the surface and cross section micrographs of as-deposited films which exhibit a highly nano-porous structure. Upon oxidation, grains coalesce, grow in size and exhibit apparent sheet like terraces. The porosity of the films is retained as shown in the surface and cross section micrographs in figures 1(c) and (d) respectively. The layered sheet like morphology of the grains shown in Figure 1(c) is characteristic of orthorhombic V_2O_5. [46,47]

X ray diffraction and Raman spectroscopy of the oxidized films, shown in figure 2, reveal the single phase pure V_2O_5 nature of the resulting films from the oxidative post annealing. The presence of all expected XRD peaks indicate the polycrystalline nature of the film. The comparison of the relative intensities with

that of randomly oriented V_2O_5 powder given by the PDF file 00-041-1426 does not reveal any apparent preferred orientation even if the (200) peak is slightly more intense than in the standard. The porous morphology of the coating favors the random orientation of the small crystallites. The average crystallite size calculated using the Scherrer's formula from the XRD spectra is approximately 50 nm. Raman vibrational peaks observed at 102, 197, 304, 404, 483, 526, and 994 cm^{-1} belong to A_g vibrational modes, whereas peaks observed at 145, 285 and 701 cm^{-1} belong to B_g modes of V_2O_5. [46, 48]

Two strategies were adopted to thermally oxidize the as-deposited films. Samples were either heated gradually from room temperature to 450°C using a heating ramp of 10°C/min then maintained at 450°C for 10 min (1st route), or were subjected to an instantaneous heat at 450°C in ambient air for 10 min (fast oxidation route). During the oxidation process, the colour of the VO_x films changed from dark grey to deep red-orange. No further perceptible change in colour was perceived even after extended periods, indicating the complete oxidation to V_2O_5. Both oxidation approaches yield XRD-pure V_2O_5 films that are orange at high temperature and yellow at room temperature. The gradually oxidized films feature a glossy appearance and resist scratching when compared to the matte films obtained through a fast oxidation. Therefore, the systematic investigation was limited to films obtained through gradual oxidation.

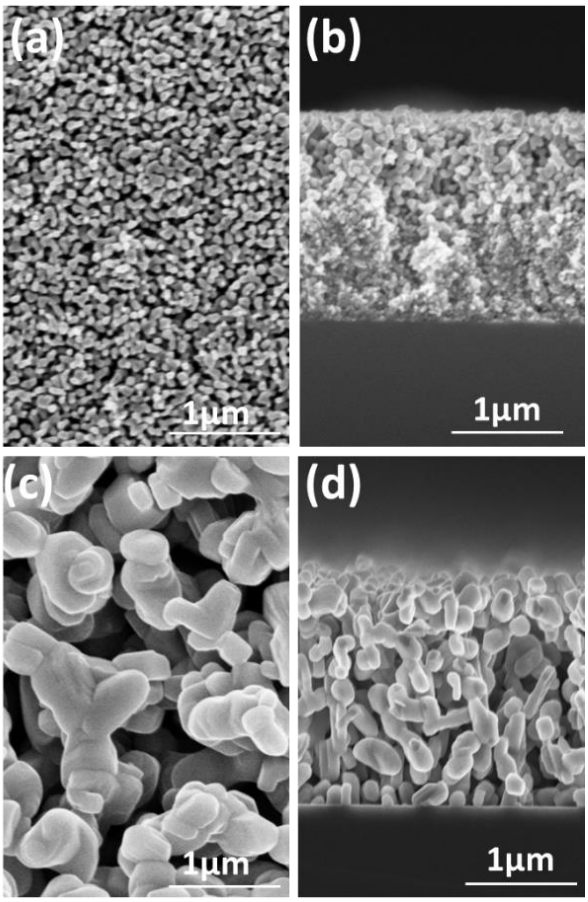

Figure 1: Surface (a/c) and corresponding cross-section (b/d) micrographs of as-deposited (VOx)/annealed (V_2O_5) films respectively.

Temperature-dependent XRD was performed under ambient atmosphere in the 25-300°C range. It is interesting to notice from figure 3 that, while peak positions and intensity remain constant, the peak corresponding to (001) orientation shows a regular and reversible shift towards low diffraction angles with increased temperature. This shift is a clear indication of the anisotropic expansion of the lattice along the 'c' direction.

The contour plots in figure 3(b) clearly show (001) peak shifting gradually toward low values of 2 theta upon heating while the (200) peak remains unaffected. On cooling to room temperature, the reverse shift occurs uniformly without any hysteresis effect as shown in figures 3(c) and (d). Figure 4 shows the variation in the calculated lattice parameters from the XRD data as a function of temperature.

While the lattice parameters “a” and “b” remain unchanged, the parameter (c) features a linear increase with the temperature.

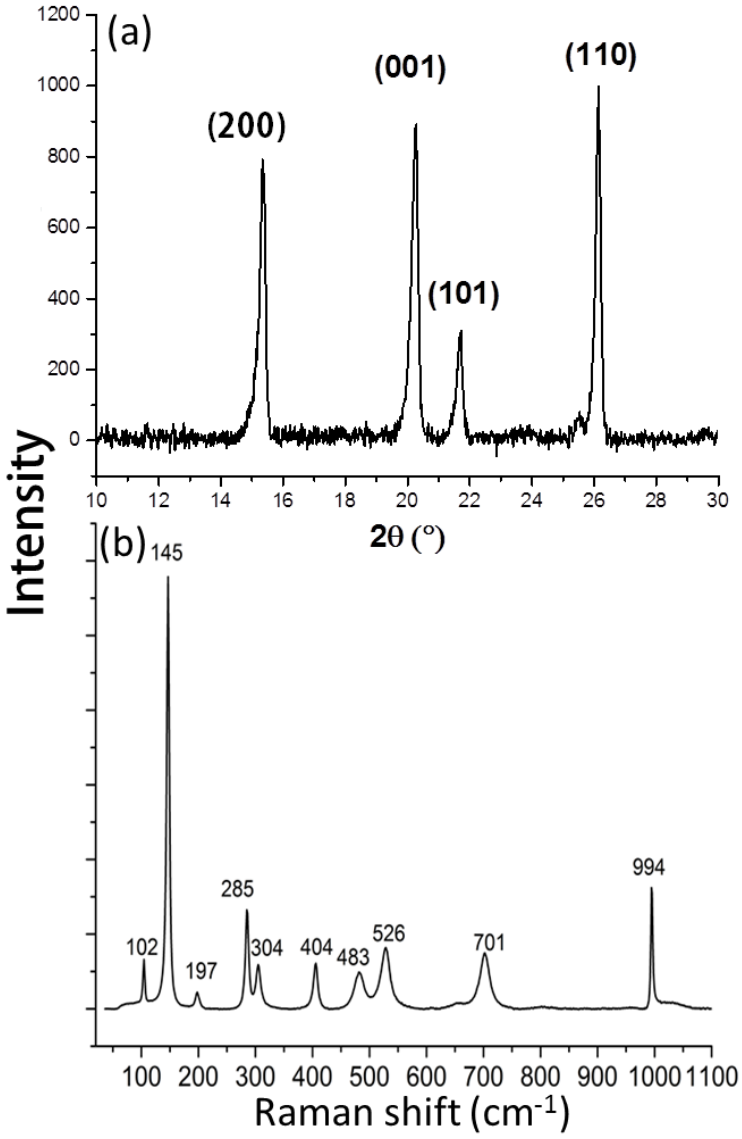

Figure 2: (a) X-ray diffractogram and (b) Raman spectrum of the oxidized films indicating the formation of single phase V_2O_5 film. Panel (a) corresponds to Miller indices of the diffraction peaks, attributed to the orthorhombic V_2O_5 per PDF no [00-041-1426]. Each indicated peak in the Raman spectrum corresponds to V_2O_5.

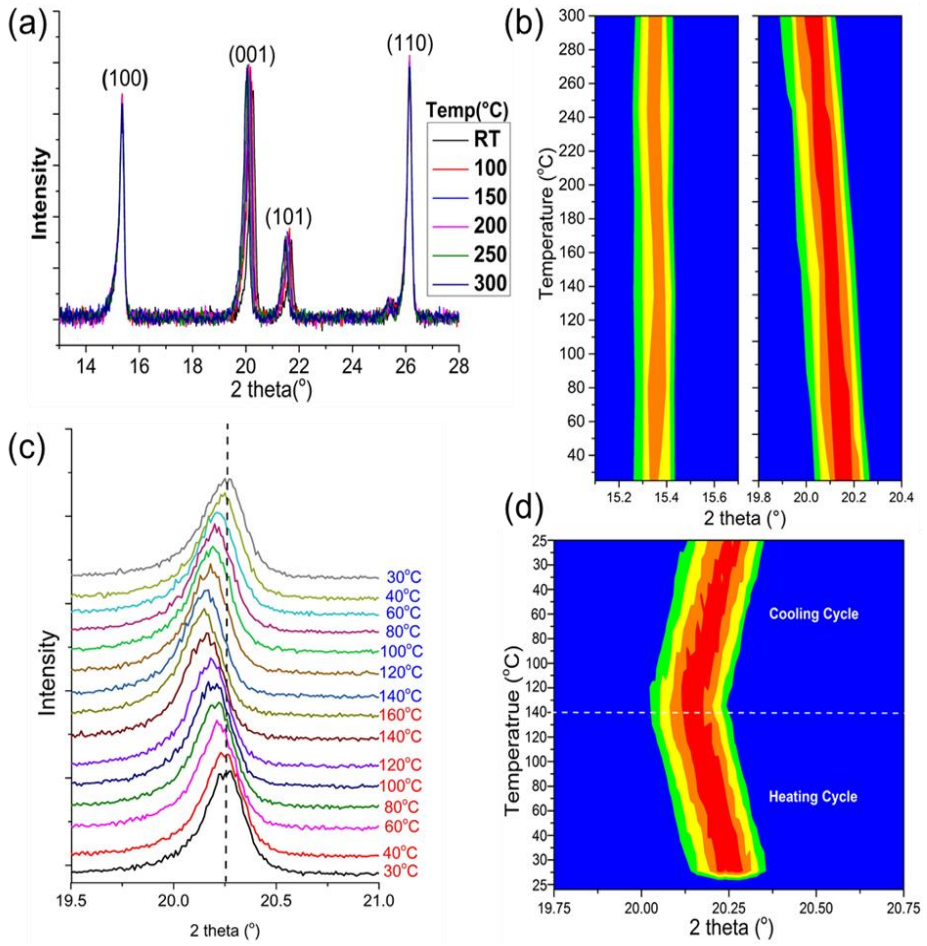

Figure 3: (a) Temperature-dependent X-ray diffraction of V_2O_5 film and (b) contour plot of the peaks corresponding to (200) and (001) reflexes. Notice the peak of (001) orientation shifting gradually with increasing temperature. Both contour plots correspond to a Δ(2θ) = 0.6°. The reversibility of the thermochromism is monitored in (c) and (d) by measuring the shift of the reflex (001) in the heating and cooling stages.

Some oxides of vanadium are well known for their semiconductor-metal transition (SMT), which the occurrence in V_2O_5 has been suggested by few authors. [49,50] Recent studies disagree however with this suggestion. [51,52] The change in electrical conductivity, interpreted as SMT, [49,50] was attributed to irreversible surface-limited reduction of V_2O_5 to V_6O_{13} due to the UHV conditions encountered for the analysis. [51,52] The rate of this reduction is further enhanced by electron beam or X ray irradiation. From both Raman and XRD analysis over a wide range

of temperatures, it is evident in our study, that V_2O_5 films remain pure under ambient air and show no signs of reduction at elevated temperatures.

Temperature-dependent Raman spectroscopy, displayed in figure 5(a), reveals a red shift of the Raman vibration modes due to thermal expansion. Relative frequency shift (w_0/w, where w_0 is the frequency at 30°C) for each vibrational mode is plotted as a function of temperature in figure 5(b). This shift shows which bonds undergo modifications due to thermal excitation.

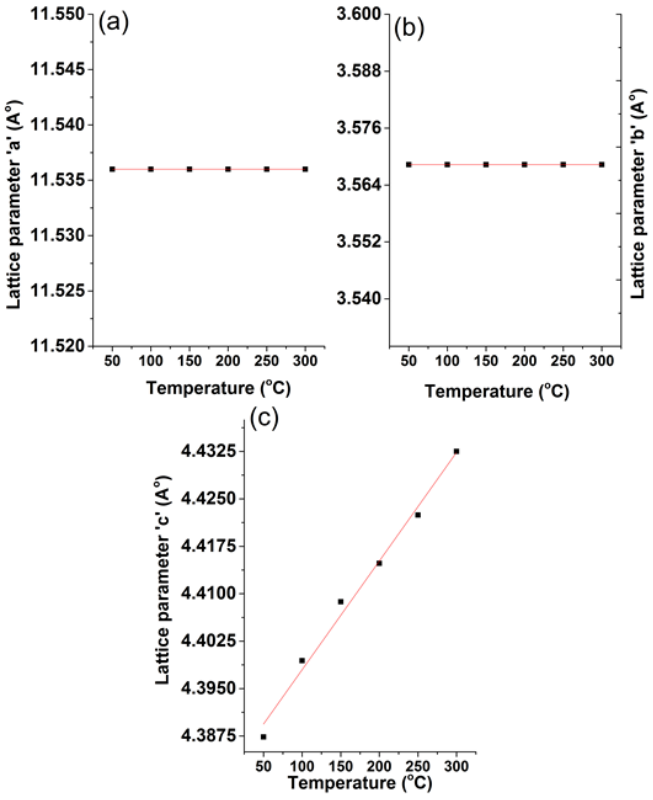

Figure 4: Variation of V2O5 lattice parameters 'a', 'b', and, 'c' with respect to temperature. Lattice parameters 'a' and 'b' are insensitive to the temperature, whereas the parameter 'c' features a linear increase with the temperature.

V_2O_5 has a layered structure, as illustrated in figure 6. For the sake of convenience, let us name the sheets shown as layer "A" and layer "B". The vanadium and oxygen atoms for sheet "A" are denoted as V_a and O_a and those of sheet "B" are V_b and O_b. Each unit cell comprises VO_5 square pyramids. These pyramids having O_{a1}/O_{b1} at their apexes and are connected through their bases

either by sharing edges, involving O_{a2}/O_{b2} oxygen ions, or vertices by involving O_{a3}/O_{b3} oxygen ions. The lattice parameter 'c' equals to the sum of the bond lengths V_a-O_{a1} and V_a-O_{b1}. Raman analysis with respect to temperature reveals no impact on the peak position at 994 cm^{-1}.

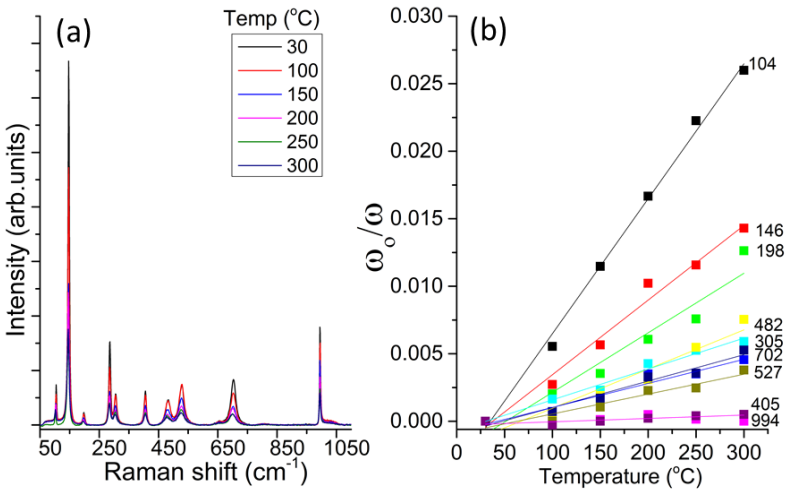

Figure 5 : (a) Temperature-dependent Raman scattering of pure V_2O_5 films. (b) Raman shift for each individual vibrational mode with respect to increasing temperature (w0 is the frequency at 30°C).

This corresponds to the stretching of V_a-O_{a1} or V_b-O_{b1} bonds. Hence, we can conclude that the bond length between V and O from the top of the pyramid does not change as the temperature increases. However, we do notice an increase in the lattice parameter 'c' from the XRD analysis. This means, while the bond length of V_a-O_{a1} remains constant, there is an increase in the bond length of V_a-O_{b1} and V_b-O_{a1} exclusively. Therefore, an expansion in the (001) direction can be visualized as if each individual sheet is moving apart from each other due to the elongation of the weak bonds holding the two sheets in place, thus expanding the interlayer space. This kind of anisotropic expansion enables the V_2O_5 lattice to host ions with important application in energy storage, sensing and electrochromism. [35]

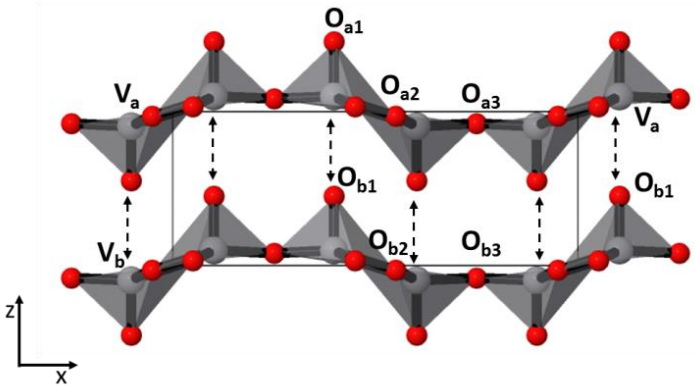

Figure 6: An illustration of V_2O_5 lattice showing the layered sheet like structure. Individual sheets are held together by the weak Va-Ob1 and Vb-Oa1 interactions.

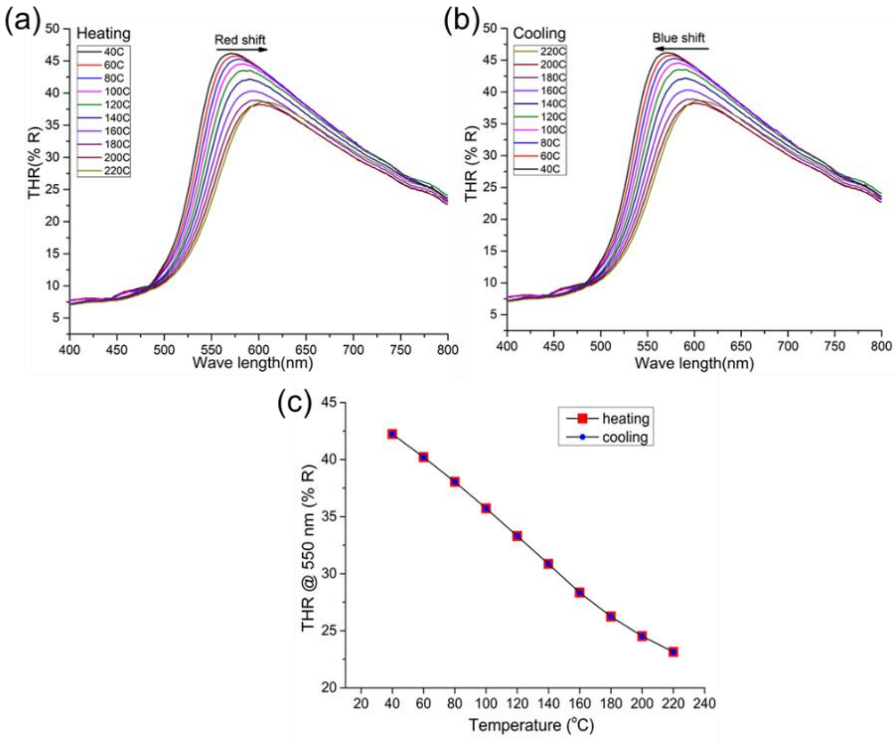

Figure 7: Temperature-dependent total hemispherical reflectance (THR in %) for V2O5 films under ambient atmosphere during (a) heating and (b) cooling stages. (c) THR at 550 nm plotted versus temperature during heating and cooling cycle.

The total hemispherical reflectance measured in the range from 400 to 800 nm as a function temperature, figure 7, indicates a thermochromic behavior of V_2O_5.

A clear red shift is witnessed with increasing temperature. This shift is also reversible over the entire range of temperature from 25 – 450 ^{o}C. The measured THR values during the heating and cooling stages coincide with differences in the third decimal. The film is a single phase crystalline V_2O_5 as confirmed by Raman and XRD analysis. Therefore, figure 7 represents the first demonstration of the visible gradual thermochromism in pure crystalline V_2O_5 films.

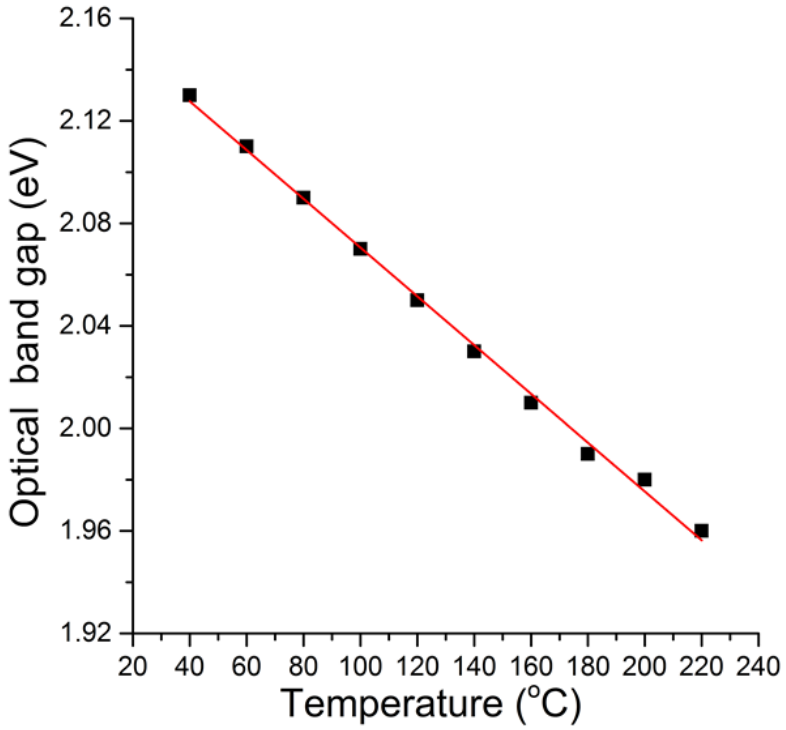

Figure 8: Optical energy band gap calculated as function of temperature from the reflectance spectra.

The optical band gap E_g was calculated as function of temperature using the temperature-dependent reflectance spectra, by Tauc's equation, $\alpha h\nu = B(h\nu - Eg)^r$. Where, α is absorption coefficient, Eg = the optical energy gap of the film, B = a constant, hv = the incident photon energy and r is a numeric value equal to 1/2 for allowed direct transitions and 2 for allowed indirect transitions. The optical energy gap is estimated by plotting $(\alpha h\nu)^{1/r}$ versus (hv), then interpolating the straight line to the photon energy axis at the value $(\alpha h\nu)^{1/r} = 0$. The obtained data

for vanadium pentoxide films were found to give a better fit for the exponent r = 1/2 confirming the direct allowed nature of the involved transition. The calculated optical band gap of 2.13 eV at RT is in good agreement with the values reported in the literature for allowed direct band gap excitations in V_2O_5. [53] A gradual decrease in the optical band gap is observed when V_2O_5 is heated, figure 8. This observation correlates with the lattice expansion in the (001) direction observed in the XRD analysis (Figure 4).

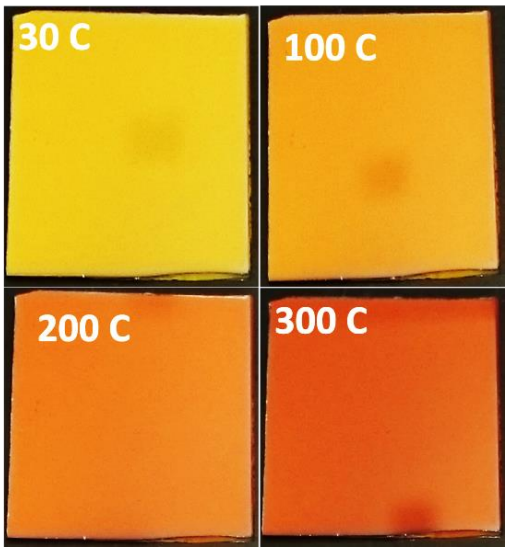

Figure 9: Photographs taken at different temperature intervals of coated silicon substrate with V_2O_5 films in ambient atmosphere.

Figure 9 evidences the thermochromism of V_2O_5 coated silicon substrates. A change of colour from bright yellow to deep orange is observed as the temperature increases under ambient air. This behavior is robust and highly reproducible. The V_2O_5 layers are highly stable and do not undergo reduction into other oxides of vanadium under ambient atmosphere at elevated temperatures. This high thermal stability of the thermochromic coating is noteworthy. This thermochromic behavior persists even when the V_2O_5 layer was encapsulated by a thin transparent layer of 20 nm Al_2O_3 to avoid the interaction with ambient air.

The thermochromic behavior of V_2O_5 films with various thicknesses was investigated to clarify the potential attribution of the thermochromism to the extreme surface state. The results displayed in figure 10(a) highlight various

aspects. The observed reflectance below □=500nm weakens for thicker films suggesting its association with the substrate behavior. The reflectance above this wavelength strengthens considerably with the increased V_2O_5 film thickens, which is a clear evidence of its attribution to the coating. Thermochromism of V_2O_5, red-shift of the film's reflection edge with increased temperature, is observed regardless of the film thickness. The amplitude of the red-shift remains unchanged as shown in figure 10(b), and the differential spectra show maxima at wavelengths that depend on the temperature and not the thickness of the film. The intensity of the differential spectra features a considerable enhancement with the thickness of the film, which hints at the contribution of the bulk of the film to the thermochromism of V_2O_5.

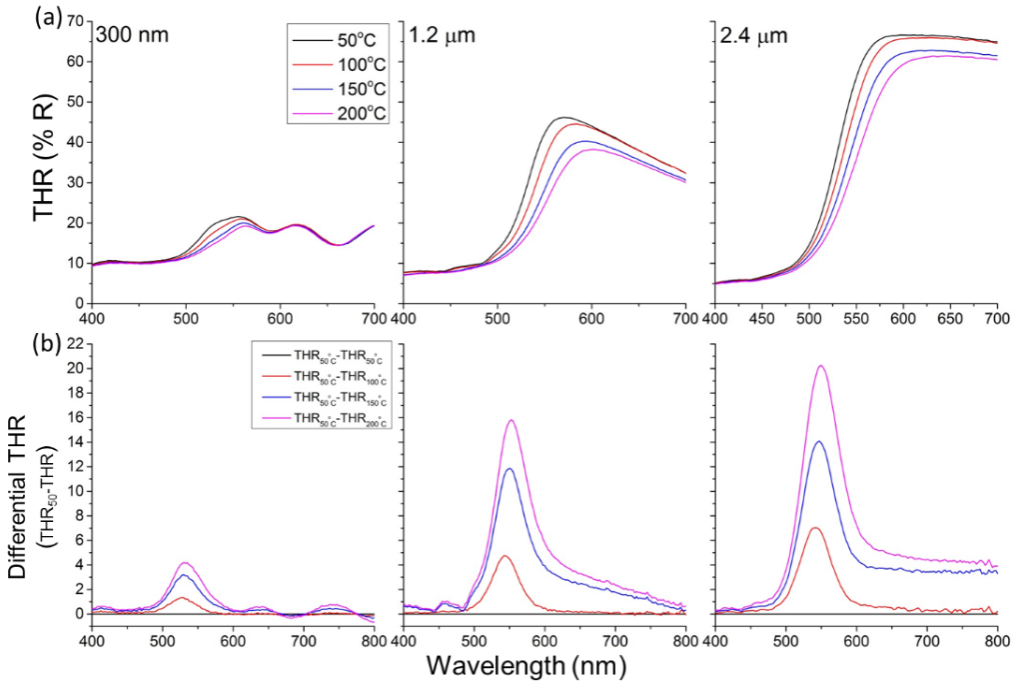

Figure 10: (a) Temperature-dependent THR for various thicknesses (0.3, 1.2 and 2.4 □m) of V_2O_5 films on silicon substrates and (b) the differential spectra referring to the obtained spectra at 50°C.

Cr-doped V_2O_5 thin films

The thermochromic nature is itself an appealing property for the already popular and multi-functional V_2O_5. Providing means to tune the optical properties of the

thermochromic V_2O_5 is advantageous to tailor the optical response to specific wavelengths or constrain to certain temperature windows. Chemical doping offers a convenient way to alter film properties. Initial demonstration was performed by chromium incorporation into the lattice.

Three different Cr doping levels were attained in the V_2O_5 films, having a Cr atomic concentration in the film of 0.21%, 2.41% and 4.23% respectively. A noticeable change in the perceived colour at room temperature results from the Cr-doping of V_2O_5. As shown in figure 11, films with Cr doping concentration of 0.21% appear very similar to non-doped film owing to the very low doping concentration. Nevertheless, as the doping level increases to 2.41% and 4.23% the colour of the films changes progressively to mustard yellow and olive green respectively as shown in figures 11(b) & (c).

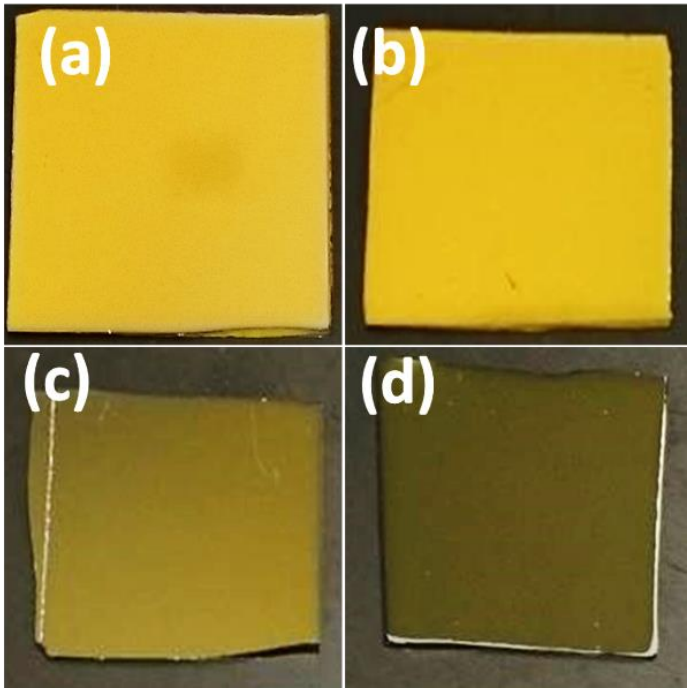

Figure 11 : Photographs of (a) un-doped V_2O_5, (b) 0.21%; (c) 2.41% and (d) 4.34% Cr doped V2O5 at room temperature.

The impact of temperature on the Cr- doped films is shown in figure 12(a) for the doping concentration of 4.34%. A clear perceptible colour change is observed. Although not as impressive as for non-doped V_2O_5, Cr-doped films feature a

thermochromism with colours that differ from those of the parent material. Higher concentration of doping has not resulted in any further perceptible colour change. Temperature-dependent THR and change of lattice parameter 'c', displayed in figure 12(b) and (c) respectively, reveal no abrupt changes in structure or optical properties.

The XRD patterns and Raman spectra of Cr doped films, not shown here, remain unchanged at room temperature. They look identical to pure V_2O_5 films, with no measurable alteration of the crystal structure as observed for undoped-V_2O_5 films.

Highly porous films comprising orthorhombic V_2O_5 hold the key for perceptible thermochromism. Chemical doping has clearly shown its impact on the tunability of this thermochromism. Other doping elements are expected to further extend the tunability of the optical properties in V_2O_5 films.

Conclusions

Pure single phase and polycrystalline films of vanadium pentoxide (V_2O_5) were synthesized by thermal oxidation of as grown VO_x films with DLI-MOCVD. The resulting films exhibit excellent reversible and continuous thermochromism from bright yellow at room temperature to deep orange at elevated temperatures. Although V_2O_5 functionality was evidenced for a wide variety of applications, thermochromism has never been reported till date. Temperature-dependent XRD and Raman confirm the absence of any kind of abrupt changes or phase transitions, and the bulk of the film was shown to contribute to the observed thermochromism. A regular anisotropic thermal expansion of the lattice along the (001) direction was observed *i.e.* perpendicular to the sheets constituting the structure and correlated with the observed thermochromism. Tuning the thermochromic behavior was also investigated. Cr doping was successively used to alter the perceived colour of V_2O_5 at ambient and elevated temperatures. This study opens additional opportunities and application possibilities with V_2O_5 as a thermochromic material.

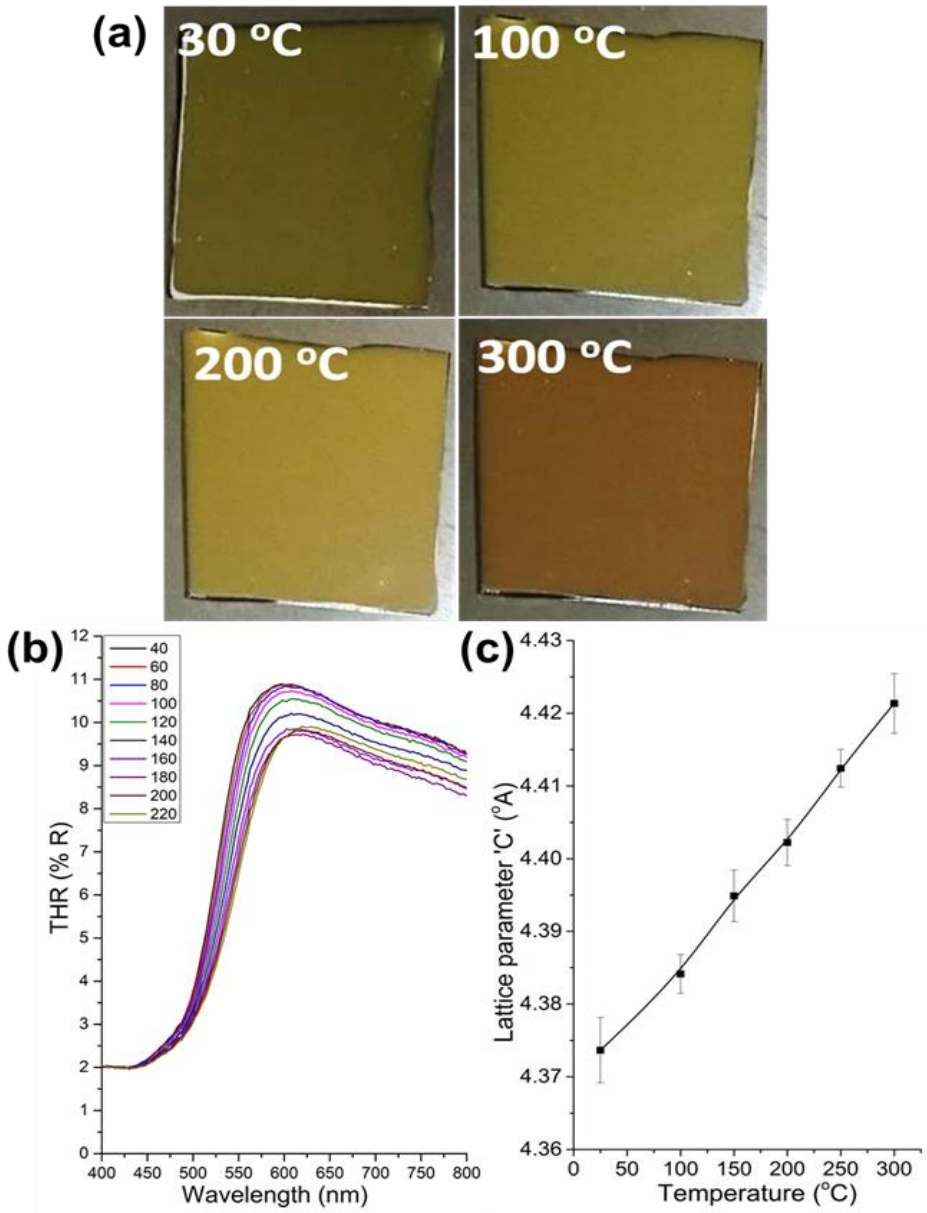

Figure 12 : (a) Photographs of Cr-doped, 4.34%, V2O5 at different temperatures, (b) the temperature-dependent THR and (c) lattice parameter 'c'.

References

1. Day, Jesse H. Thermochromism. Chem. Rev., 1963, 1, 65-80.
2. Samat, André, and Vladimir Lokshin, Thermochromism of Organic Compounds, In Organic Photochromic and Thermochromic Compounds, Springer US, 2002, 2, 415-466.
3. Day, Jesse H. Thermochromism of Inorganic Compounds, Chem. Rev., 1968, 6, 649-657.
4. Blaney, T. Sink and Bath Plugs. U.S. Patent US6105618 A. 2000
5. Lerner, William. Method of Warning Individuals About Hot Surfaces on Stoves Including Cooktops. U.S. Patent Application 10/658,214, 2003.
6. Grzybowski, Marek, and Daniel T. Gryko. Diketopyrrolopyrroles: Synthesis, Reactivity, And Optical Properties. Adv. Opt. Mater. 2015, 3, 280-320.
7. Guo, Hui, Jinming Zhang, David Porter, Huisheng Peng, Dennis WPM Löwik, Yu Wang, Zhidong Zhang, Xin Chen, and Zhengzhong Shao. Ultrafast and Reversible Thermochromism of a Conjugated Polymer Material Based on The Assembly of Peptide Amphiphiles. Chem. Sci., 2014, 11, 4189-4195.
8. Wei, Ruirui, Panshu Song, And Aijun Tong. Reversible Thermochromism of Aggregation-Induced Emission-Active Benzophenone Azine Based on Polymorph-Dependent Excited-State Intramolecular Proton Transfer Fluorescence. J. Phys. Chem. C, 2013, 117, 3467-3474.
9. Gaudon M, Deniard P, Demourgues A, Thiry AE, Carbonera C, Le Nestour A, Largeteau A, Létard JF, Jobic S. Unprecedented “One-Finger-Push” -Induced Phase Transition with A Drastic Colour Change in An Inorganic Material. Adv Mat. 2007, 19(21), 3517-3519.
10. Koshihara SY, Tokura Y, Takeda K, Koda T, Kobayashi A. Reversible and Irreversible Thermochromic Phase Transitions in Single Crystals Of Polydiacetylenes Substituted With Alkyl-Urethanes J. Chem. Phys. 1990, 92(12), 7581-7588.
11. Rougeau L, Picq D, Rastello M, Frantz Y. New Irreversible Thermochromic Polydiacetylenes. Tetrahedron, 2008, 64(40), 9430-9346.
12. Lazaroff, William, And Alfred Raschdorf. "Thermochromic Cookware." U.S. Patent Application 10/965,317. 2004.

13. Pimia, Juha. Temperature Indicator for Temperature Changing Material or Means and Method for Its Preparation. U.S. Patent Application 13/637,097, 2011.
14. Petruševski, V. M., Miha Bukleski, And M. Monkoviж. "The Economic Demonstrator: Prepare It Once, Use It Many Times. II. Continuous Thermochromism In Aqueous Solutions Of Transition Metal Chlorides. Chemistry, 2007, 16, 20-26.
15. Petruševski VM, Bukleski M. The Economic Demonstrator: Prepare It Once, Use It Many Times. III. Phenomena of Discontinuous Thermochromism. Chemistry, 2008, 17(2).
16. Dorogan, I.; Minkin, V. Theoretical Modeling of Electrocyclic 2H-Pyran and 2H-1,4-Oxazine Ring Opening Reactions in Photo- And Thermochromic Spiropyrans And Spirooxazines. Chem. Heterocycl. Compd. 2016, 52, 730–735
17. Tian G, Xu W, Meng L. Reversible and Irreversible Thermochromism Of Some Schiff Base Metal Complex. Chin. J. Chem. Eng. 2008, 59(4), 1032.
18. Parker, Robert. Time-Temperature Indicator. U.S. Patent 4,805,188, 1989.
19. Parker, Robert. Expiration Indicator. U.S. Patent 7,188,996, 2007.
20. Galliani D, Mascheroni L, Sassi M, Turrisi R, Lorenzi R, Scaccabarozzi A, Stingelin N, Beverina L. Thermochromic Latent-Pigment-Based Time–Temperature Indicators for Perishable Goods. Adv. Opt. Mater. 2015, 3(9), 1164-1168.
21. Yoon SJ, Kim JH, Kim KS, Chung JW, Heinrich B, Mathevet F, Kim P, Donnio B, Attias AJ, Kim D, Park SY. Mesomorphic Organization and Thermochromic Luminescence of Dicyanodistyrylbenzene-Based Phasmidic Molecular Disks: Uniaxially Aligned Hexagonal Columnar Liquid Crystals at Room Temperature with Enhanced Fluorescence Emission and Semiconductivity. Adv. Funct. Mater, 2012, 22(1), 61-69.
22. Donia AM, El-Boraey HA. Reversible and Irreversible Thermochromism Of Some Schiff Base Metal Complexes. Transition Met. Chem. 1993, 18(3), 315-318.

23. Bourque, Alexander. Investigations of Reversible Thermochromism in Three-Component Systems, Ph.D. Thesis, Dalhousie University, Canada, 2014.
24. Sage I. Thermochromic Liquid Crystals in Devices. Liq. Cryst. 1992, 3, 301-343.
25. White MA, Leblanc M. Thermochromism in Commercial Products. J. Chem. Educ. 1999, 76(9), 1201
26. Poole, C. P. The Optical Spectra and Colour of Chromium Containing Solids. J. Phys. Chem. Solids, 1964, 11, 1169-1182.
27. Yu C, Li Y, Zhang X, Huang X, Malyarchuk V, Wang S, Shi Y, Gao L, Su Y, Zhang Y, Xu H. Adaptive Optoelectronic Camouflage Systems with Designs Inspired by Cephalopod Skins. Proc. Natl. Acad. Sci. 2014, 111(36), 12998-13003.
28. Kim G, Cho S, Chang K, Kim WS, Kang H, Ryu SP, Myoung J, Park J, Park C, Shim W. Spatially Pressure-Mapped Thermochromic Interactive Sensor. Adv. Mat. 2017, 29(13).
29. Beke, S. A Review of The Growth of V_2O_5 Films From 1885 To 2010. Thin Solid Films 2011, 519, 1761–1771.
30. Liu, S.; Tong, Z.; Zhao, J.; Liu, X.; Wang, J.; Ma, X.; Chi, C.; Yang, Y.; Liu, X.; Li, Y. Rational Selection of Amorphous or Crystalline V_2O_5 Cathode for Sodium-Ion Batteries. Phys Chem Chem Phys 2016, 18, 25645–25654.
31. Wang, Q.; Hung, P. C.; Lu, S.; Chang, M. B. Catalytic Decomposition of Gaseous PCDD/Fs Over V_2O_5/Tio_2-Cnts Catalyst: Effect Of NO And NH_3 Addition. Chemosphere 2016, 159, 132–137.
32. Erdohelyi A, Solymosi F. Partial Oxidation of Ethane Over Supported Vanadium Pentoxide Catalysts. Journal of Catalysis. 1990, 123(1), 31-42.
33. Wang, Ying, Katsunori Takahashi, Kyoungho H. Lee, And G. Z. Cao. Nanostructured Vanadium Oxide Electrodes for Enhanced Lithium-Ion Intercalation. Adv. Funct. Mater 2006, 9, 1133-1144.
34. Raj, A. Dhayal, T. Pazhanivel, P. Suresh Kumar, D. Mangalaraj, D. Nataraj, And N. Ponpandian. Self-Assembled V2O5 Nanorods For Gas Sensors. Curr. Appl. Phys. 2010, 2, 531-537.

35. Ottaviano, L., A. Pennisi, F. Simone, And A. M. Salvi. RF Sputtered Electro Chromic V2O5 Films. Opt. Mater. 2004, 27, 307-313.
36. Liu, Zuli, Guojia Fang, Youqing Wang, Yandong Bai, And Kai-Lun Yao. "Laser-Induced Colouration of V_2O_5. J. Phys. D: Appl. Phys. 2000,18, 23-27.
37. Benmouss, M., A. Outzourhit, R. Jourdani, A. Bennouna, And E. L. Ameziane. Structural, Optical and Electrochromic Properties of Sol–Gel V_2O_5 Thin Films. Act. Passive Electron. Compon. 2003, 26(4), 245-256.
38. Le HA, Chin S, Park E, Bae G, Jurng J. Chemical Vapor Synthesis and Physico-Chemical Properties of V_2O_5 Nanoparticles. Chem. Vap. Deposition 2012, 18(1-3) 6-9.
39. Liu DQ, Zheng WW, Cheng HF, Liu HT. Thermochromic VO_2 Thin Film Prepared by Post Annealing Treatment Of V_2O_5 Thin Film. Adv. Mater. Res 2009, 79,747-750
40. Lataste E, Demourgues A, Salmi J, Naporea C, Gaudon M. Thermochromic Behavior (400< T° C< 1200° C) Of Barium Carbonate/Binary Metal Oxide Mixtures. Dyes Pigm. 2011, 91(3), 396-403.
41. Gaudon M, Deniard P, Voisin L, Lacombe G, Darnat F, Demourgues A, Perillon JL, Jobic S. How to Mimic the Thermo-Induced Red to Green Transition of Ruby with Control of The Temperature Via the Use of An Inorganic Materials Blend? Dyes Pigm. 2012, 95(2), 344-350.
42. Kumar, S.; Maury, F.; Bahlawane, N. Electrical Switching in Semiconductor-Metal Self-Assembled VO_2 Disordered Metamaterial Coatings. Sci Rep 2016, 6, 37699.
43. Kumar, S.; Lenoble, D.; Maury, F.; Bahlawane, N. Synthesis of Vanadium Oxide Films with Controlled Morphologies: Impact on The Metal–Insulator Transition Behavior. Phys Status Solidi 2015, 212, 1582–1587.
44. Rampelberg, G.; Schutter, B.; Devulder, W.; Martens, K.; Radu, I.; Detavernier, C. In Situ X-Ray Diffraction Study of The Controlled Oxidation and Reduction in the V–O System for The Synthesis Of VO2 And V_2O_3 Thin Films. J Mater Chem C 2015, 3, 11357–11365.

45. Bahlawane, N.; Lenoble, D. Vanadium Oxide Compounds: Structure, Properties, And Growth from The Gas Phase. Chem. Vap. Deposition 2014, 20, 299–311.
46. Su; Liu; Ma; Guo; Wang Raman Spectroscopic Characterization of The Microstructure of V_2O_5 Films. J. Solid State Electrochem. 2008, 12, 919–923.
47. Haber J, Witko M, Tokarz R. Vanadium Pentoxide I. Structures and Properties. Appl. Catal., A . 1997, 157(1-2), 3-22.
48. Zhou, Bo, And Deyan He. Raman Spectrum of Vanadium Pentoxide from Density-Functional Perturbation Theory. J. Raman Spectrosc. 2008, 39 (10), 1475-1481.
49. Kang, M.; Kim, I.; Kim, S.; Ryu, J.-W.; Park, H. Metal-Insulator Transition Without Structural Phase Transition in V_2O_5 Film. Appl. Phys. Lett. 2011, 98, 131907.
50. Blum, R.; Niehus, H.; Hucho, C.; Fortrie, R.; Ganduglia-Pirovano, M.; Sauer, J.; Shaikhutdinov, S.; Freund, H. Surface Metal-Insulator Transition on A Vanadium Pentoxide (001) Single Crystal. Phys Rev Lett 2007, 99, 226103.
51. Fisher; Genossar; Patlagan; Chashka; Reisner Electric-Field-Induced Semiconductor–Semiconductor Transition in V_2O_5. Appl. Phys. A: Solids Surf. 2015, 120, 435–442
52. Pergament, A. L., G. B. Stefanovich, N. A. Kuldin, And A. A. Velichko. On the Problem of Metal-Insulator Transitions in Vanadium Oxides. ISRN Condensed Matter Physics 2013.
53. Aita, C.; Liu, Y.-L.; Kao, M.; Hansen, S. Optical Behavior of Sputter-Deposited Vanadium Pentoxide. J. Appl. Phys. 1986, 60, 749–753.

4.6 Tunable thermochromic properties of V_2O_5 coatings

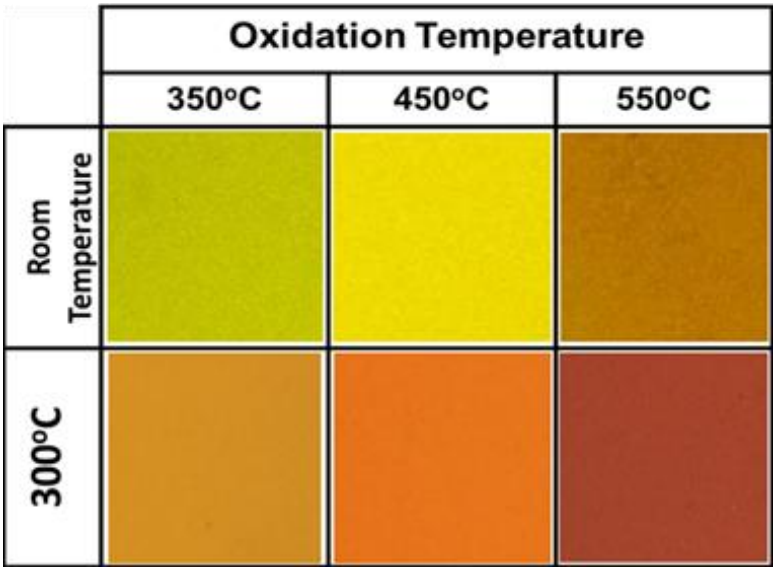

Thermochromic V_2O_5 coatings obtained by oxidation in air at different temperatures, exhibit a variety of colours at room temperature and upon heating. Oxygen vacancy is directly linked to the appearance of such a wide gamut of colours. Therefore, tunable thermochromic V_2O_5 coatings are obtained by controlled oxidative annealing. The illustration displays cropped photographic image of the actual coated substrates.

Published as Kumar, S., Maury, F., and Bahlawane, N. Tunable thermochromic properties of V_2O_5 coatings, Materials *today physics* (2) pp 1-5; (2017).

Abstract

Thermochromic Di vanadium pentoxide (V_2O_5) coatings displaying a variety of colours were synthesised. Tuning of thermochromic behaviour was achieved via a controlled oxidative annealing under ambient air of the as-grown VO_x films. Adjusting the oxygen deficiency in V_2O_5, allows tuning the colour of the films and as a consequence its thermochromic behaviour. Non-oxygen deficient V_2O_5 did not feature any measurable thermochromism.

Introduction

Thermochromic materials display a perceptible change in colour upon temperature variations. [1–3] This behaviour is observed in several types of compounds, ranging from organic molecules, [4,5] inorganic compounds, [6,7] organometallic, [8,9] and transition metal oxides. [10–12] Due to the simplistic nature of temperature dependent colour changing ability, they are utilized in several devices like temperature sensor, [13–15] information display, [16,17] safety devices and food packaging. [18,19] Nevertheless, there has been a considerable interest in obtaining compounds with a control over the colour of the thermochromic materials. In terms of the temperature at which thermochromic transition occurs, as well as the colours they exhibit during transition. [20–23] Hence, tunable thermochromic compounds are expected to widen their scope of applications.

Tuning of thermochromic behaviour can be implemented by several mechanisms. Physical mixing of two or more thermochromic pigments was used to adjust the perceived colour. [24,25] In chemical pathways, the constituents are modified to alter the optical properties and produce the desired colour. In Leuco dyes, changing the alkyl chain lengths in developer or solvent impacts the thermochromic nature of the dye. [26,27] In transition metal oxides (TMO) tuning of optical properties and thermochromism is achieved by the help of chemical doping. [28,29] Dopants fill the interstices or replace the host atom to modify the

band gap by forming additional donor or acceptor levels, which facilitate inter band transitions.

In addition to conventional doping methods, creating oxygen vacancies emerges as an efficient technique to alter the optical properties. [30,31] The obtained optical properties are stable as far as the oxygen vacancy level is maintained. Generating oxygen vacancies is in fact analogous to self-doping. In case of tungsten oxide, [32] it has been demonstrated that vacuum annealing leads to loss of oxygen with a consequent impact on the optical properties. Chromium oxide (Cr_2O_3), a widely studied TMO for its chromic properties, shows a variation in optical properties after annealing at adjusted oxygen partial pressures. [11] Although the control of oxygen vacancies in TMO can significantly impact their optical properties, it has not been proposed as an approach to adjust their thermochromic behaviour.

There have been several studies correlating the oxygen vacancies in V_2O_5 to variation in electro-chemical and optical properties. However, thermochromic tuning linked to the adjusted sub-stoichiometry has not been reported so far. The present study deals with the tuning of thermochromic properties of V_2O_5 coatings, to achieve fine control over the perceived colour and thermally induced colour change.

Experimental

Preparation of V_2O_5 coatings

Thin films of vanadium oxide were deposited on silicon substrates by Direct Liquid Injection (DLI) Metal Organic Chemical Vapour Deposition (MOCVD), the details of which are reported elsewhere. [33,34] Argon was used as the carrier gas at a flow rate of 50 sccm while the chamber pressure was adjusted to 10 mbar. Substrates were maintained at a constant temperature of 500°C during the four hours of deposition.

After deposition, samples were allowed to cool till room temperature in argon atmosphere at low pressure before withdrawing from the chamber. Further handling of the samples was carried out under ambient atmosphere. Post deposition annealing was performed under ambient air at 300-580°C. The annealing time was adjusted to allow a complete oxidation from VO_x to V_2O_5. While 10 min were sufficient for oxidation at 550°C, significantly longer times were required at lower temperatures; this can be explained by simple temperature dependent oxidation kinetics.

To isolate V_2O_5 coatings form atmospheric gas phase interactions, Atomic layer deposition (ALD) of Al_2O_3 was performed using the sequential introduction of Trimethylaluminium (TMA) and water. The pulse times for each reactant were adjusted to 40 ms with a 15 s purge in between each pulse. The rather large pulse and purge times were chosen to achieve complete conformal coverage over the film. ALD was carried out at 120° C under partial pressure of 2 mbar and Argon was used as the carrier gas at a flow rate of 50 sccm.

Film characterization

Total hemispherical reflection (THR) measurements were carried out on LAMBDA 1050 UV/Vis/NIR spectrophotometer from Perkin Elmer with a 150 mm integration sphere in the reflection configuration. Measurements, which correspond to the sum of specular and diffuse reflections, were performed in the visible spectral range (400-800 nm). Temperature-dependent measurements were carried out with the help of a custom made sample holder with an integrated heating element. Temperature control was achieved by a Horst HT 60 temperature controller coupled to a K-type thermocouple.

The film thickness and roughness were measured using an Alpha step d-500 Profilometer from KLA-Tencor and the cross-section inspection with FEI Helios Nanolab 650™ Scanning electron microscopy (SEM). Surface morphology was characterized by SEM at a working distance of 4 mm with an acceleration voltage of 5 kV. X-ray diffraction (XRD) was used to characterize the films using the Bruker D8, with CuKα as the X-ray source. Data were collected in the θ-2θ (locked couple) mode from 2θ of 10° to 30° with a step size of 0.02°.

Results and discussion

The as-deposited VO_x films feature a dark grey colour. A relatively high growth rate of 37.5 nm/min was recorded. VO_x films were oxidised under ambient air at various temperatures ranging from 350 – 580 ^oC until the films displayed a complete oxidation. This time was adjusted between 60 min at 350^oC to 10 min at 580^oC. Films changed from dark grey to bright orange or crimson red indicating successful oxidation to V_2O_5.

V_2O_5 films obtained by oxidative annealing at 350^oC- 400^oC feature a lime green colour at room temperature. Coatings obtained at oxidation temperature of 450^oC - 475^oC were bright yellow in colour. Whereas, coatings oxidised at 500^oC - 550^oC appeared honey yellow and coatings oxidised at 580^oC appear metallic grey.

It is worth noting that V_2O_5 colours ranging from green to honey yellow was reported earlier by Aita et al. [35] The authors associated the colour of sputter deposited V_2O_5 films with different oxygen partial pressures. It was observed that films deposited with low O_2 partial pressures appeared green, whereas films with higher O_2 partial pressure were yellow. The change of colour from green to honey yellow is attributed to decreased oxygen deficiency and is in line with our observation.

X ray diffraction patterns of films oxidised at various temperatures, shown in figure 1(a), indicate the formation of pure phase polycrystalline V_2O_5 throughout the range of oxidation temperature. The peaks at 2θ = 15.3, 20.3, 21.8 and 26.1 are assigned to the (200), (001), (101) and (110) lattice planes of orthorhombic structure of V_2O_5 (PDF- 000411426). Higher oxidation temperatures (500^oC) improved the crystallinity and resulted in strongly ‘c’- oriented films. This is attributed to the increased coalescence to form larger crystallites as shown in figure 1(b). No measurable variation in the lattice parameters could be observed.

Films feature a highly porous morphology at the oxidation temperatures of 350^oC and gradually transform to large crystallites at 550^oC with reduced porosity. The average crystallite size, calculated using the Scherrer’s equation increased from 130 nm for films oxidised at 350^oC to about 800 nm for films that have undergone

oxidation at 550°C. Alongside the increase in crystallite size, the surface roughness of the coatings increased linearly with oxidation temperature as shown in Figure S1 of the supplementary information.

In order to distinguish the optical properties of V_2O_5 coatings obtained at different oxidation temperatures, optical spectroscopy was performed on individual samples at room temperature. THR spectra shown **figure 2** (a) indicate that the oxidation temperature has a significant impact on the wavelength at which a reflection plateau is observed. An apparent red shift is observed with the increased in oxidation temperatures. This observation concurs with the variation in colours noticed after the post oxidative treatments.

The brightness of the coating can be defined as the total integrated THR (area under the curve) over the full range of visible spectrum (400-800 nm). Therefore, from figure 2 (a) we observe that V_2O_5 coatings obtained by oxidation at 450°C are brighter compared to the films oxidised at 350°C and 550°C. The graph showing the variation of brightness with respect to oxidation temperature is show in figure S2 of the supplementary information. Figure 2(b) correlates the brightness of the films to their texture. It is evidenced that brightness varies linearly with $I_{(200)}/I_{(001)}$, indicating that coatings that are highly oriented to (001) direction exhibit lower brightness compared to polycrystalline samples. No obvious explanation could be postulated for this un-doubtful brightness to texture correlation.

V_2O_5 has a layered structure with a large affinity towards accommodating guest molecules between the interlayer spaces. This property of V_2O_5 has made it an ideal candidate for many applications like gas and humidity sensing, [36] energy storage [37] and catalysis. [38] In order to prove that thermochromism in V_2O_5 is an intrinsic property, and that it does not depend on the atmospheric conditions, we isolated the coatings from ambient atmosphere. The passivation was performed using the established Atomic Layer Deposition (ALD) of Al2O3. [39,40] ALD coatings offer superior advantages compared to other deposition techniques by allowing low temperature of deposition and a conformal coating characteristics. All the samples were coated with a 20 nm of Al_2O_3 oxide. In addition to

encapsulation, Al_2O_3 would also act as a protection layer by making V_2O_5 scratch resistant and prevent from aging via a change of the oxygen deficiency.

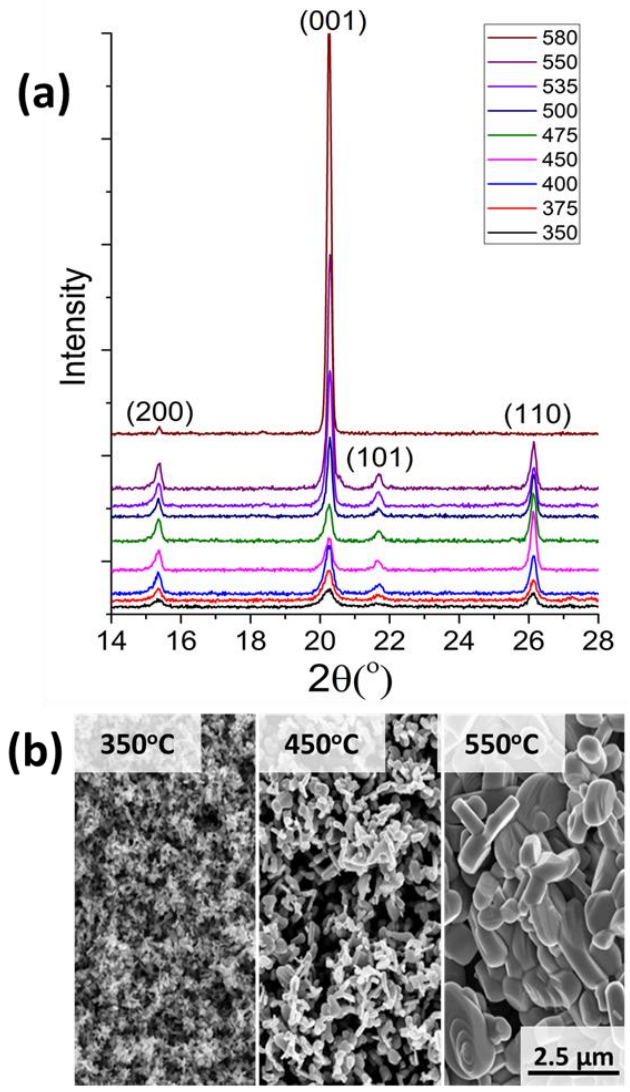

Figure 1: (a) X-Ray diffractograms of V_2O_5 films oxidised at different temperatures reveal formation of pure, single phase orthorhombic structure as per PDF no [000411426] and (b) surface scanning electron micrographs of the oxidised films at 350°C, 450°C and 550°C.

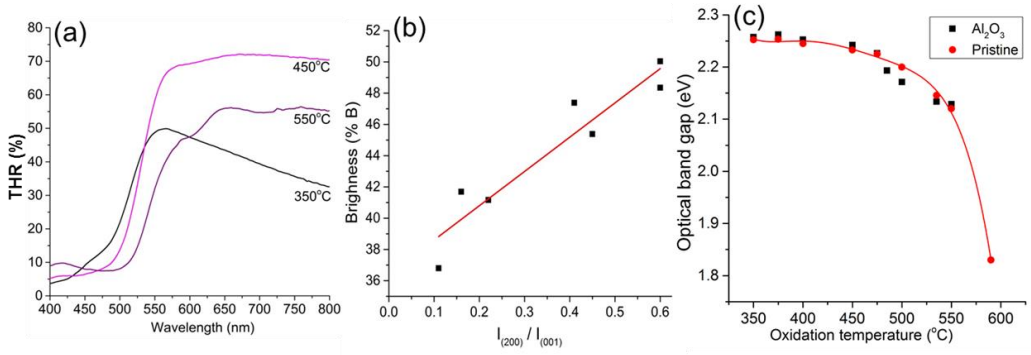

Figure 2. (a) Room temperature THR spectra of samples oxidised at 350, 450 and 550oC. (b) Dependence of the brightness of the coatings with the ratio of XRD intensity I200/I001 and (c) the variation of optical energy band gap as a function of oxidation temperature for both pristine V_2O_5 as well as Al_2O_3 coated V_2O_5.

The optical band gap E_g was calculated as a function of temperature using the temperature dependent THR spectra, by Tauc's equation, $\alpha hv = B(hv–E_g)^r$. Where, α is absorption coefficient, E_g = the optical energy gap of the film, B = a constant, hv = the incident photon energy and r is a numeric value equal to 1/2 for allowed direct transitions and 2 for allowed indirect transitions. The optical energy gap is estimated by plotting $(\alpha hv)^{1/r}$ versus (hv), then interpolating the straight line to the photon energy axis at the value $(\alpha hv)^{1/r} = 0$. The optical data for vanadium pentaoxide films were found to give a better fit for the exponent r = 1/2 confirming the direct allowed nature of the involved transition. **Figure 2c** shows the variation of the optical band gap at room temperature with respect to the oxidation temperature for both pristine and Al_2O_3 deposited V_2O_5 coatings. Similar to the THR, Al_2O_3 deposition has no significant impact in the band gap values. The optical band gap decreases from 2.26 to 1.8 by increasing the oxidation temperature. The reason for this variation can be associated with the oxygen deficiency in the film.

Optical properties of Al_2O_3 coated samples showed no significant deviation from those of pure coatings. Therefore those results are not presented here. Henceforth all the data reported in this article correspond to V_2O_5 coatings with an Al_2O_3 encapsulation. V_2O_5 coatings oxidised 350°C-550°C exhibited visible range thermochromism. Whereas coatings oxidised at 580°C do not show any

sign of thermochromism. The brightness and the extent of red shift vary considerably depending on the temperature at which post deposition oxidative annealing was performed. First derivative curves of temperature-dependent optical spectra of samples oxidised at 350°C, 450°C and 550°C are shown in **figure 3 (a), (b) and (c)** respectively. On heating the samples from RT to 250 ^{o}C, a red shift is observed with a slight decrease in the brightness of the coatings. The insets in each panel of figure 3 show the photographic images of V_2O_5 coatings at RT and at elevated temperature respectively. Figure S3 in the supplementary information show the temperature dependent optical spectra of V_2O_5 coatings oxidised at various temperatures.

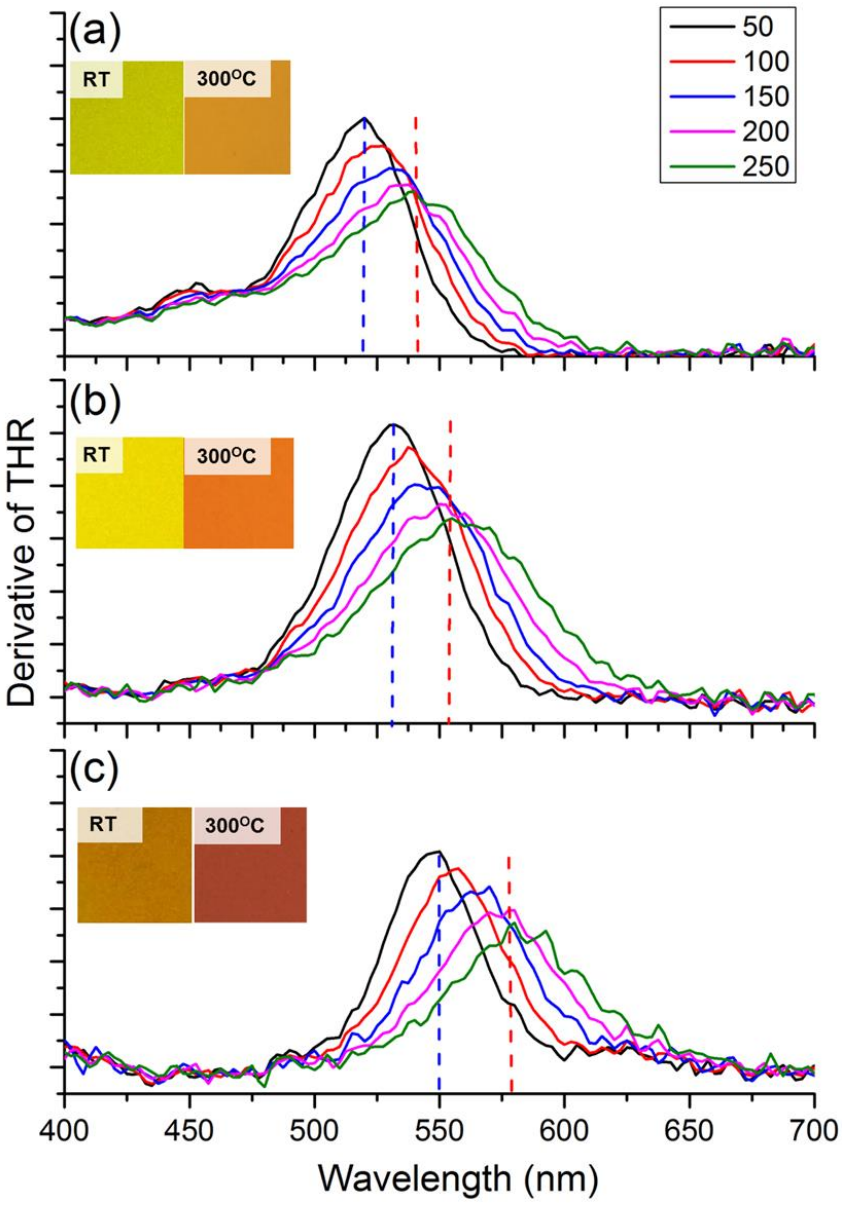

Figure 3: Temperature- dependent $\frac{d(THR)}{d\lambda}$, demonstrating thermochromic behaviour of samples oxidised at (a) 350 oC, (b) 450 oC and (c) 550 oC respectively. Inset for each panel displays the photographic image of V_2O_5 coatings at room temperature and 300oC respective to each oxidation temperature.

The colour of V_2O_5 returned to its room temperature state on cooling, evidencing a perfectly reversible nature of this thermochromism. It should be noted that thermochromism under ambient air is measured at temperatures that are significantly lower than the respective oxidation temperatures. Blue and red

vertical dotted lines in figure 3 provide a visual guide to inform about the spectral range concerned by thermochromism for each sample.

Besides the thermochromism that occurs with an impressive change in colour, total brightness of the sample, which can be described as the integrated reflection over the whole range of visible spectrum, decreases as a function of temperature. The rate of decrease in brightness can be equated to the sensitivity of V_2O_5 to temperature changes. Figure 4 shows the variation of brightness with increasing oxidation temperature for the three samples. We observe a linear decrease in the brightness for all samples.

The sensitivity of the thermochromic coating is defined here as the slope of the linear fitting of the brightness versus temperature curve. From figure 4, slope of V_2O_5 coatings obtained by oxidation at 350°C, 450°C and 550°C is 0.018, 0.033 and 0.032 Δ%R/^{o}C. Hence samples obtained by oxidation at 450°C and 550°C feature a similar sensitivity and are almost twice as much sensitive to temperature changes compared to the one obtained by oxidation at 350°C. Since the sensitivity is measured taking into account the variation in brightness, the quantified sensitivity value are quite low as brightness is calculated over the full visible spectrum. However, if the sensitivity is measured as the variation in THR for a particular wavelength (e.g. λ = 535, 555 and 575 nm) as shown figure S4, we notice a one order of magnitude higher thermochromic sensitivity.

With the ability to showcase precise and accurate changes in optical properties, which respond to temperature changes, these thermochromic V_2O_5 coatings could be ideal candidates to operate as a contactless optical temperature sensor. The range and variation of colours observed further strengthen the versatility and tunability aspects of these V_2O_5 coatings. Through controlled oxidative annealing we obtain thermochromic coatings with adjusted colours and varying sensitivity to the temperature stimulus.

The high susceptibility of V_2O_5 to undergo reduction under ultra-high vacuum with X–rays or electron beam exposure complicates its quantitative analysis. [43,44] Therefore analysis conditions as those encountered in EDX and XPS, reduce

V_2O_5 to immediate lower oxides of vanadium such as V_6O_{13} [45] creating hurdles in accurate determination of vanadium and oxygen ratios.

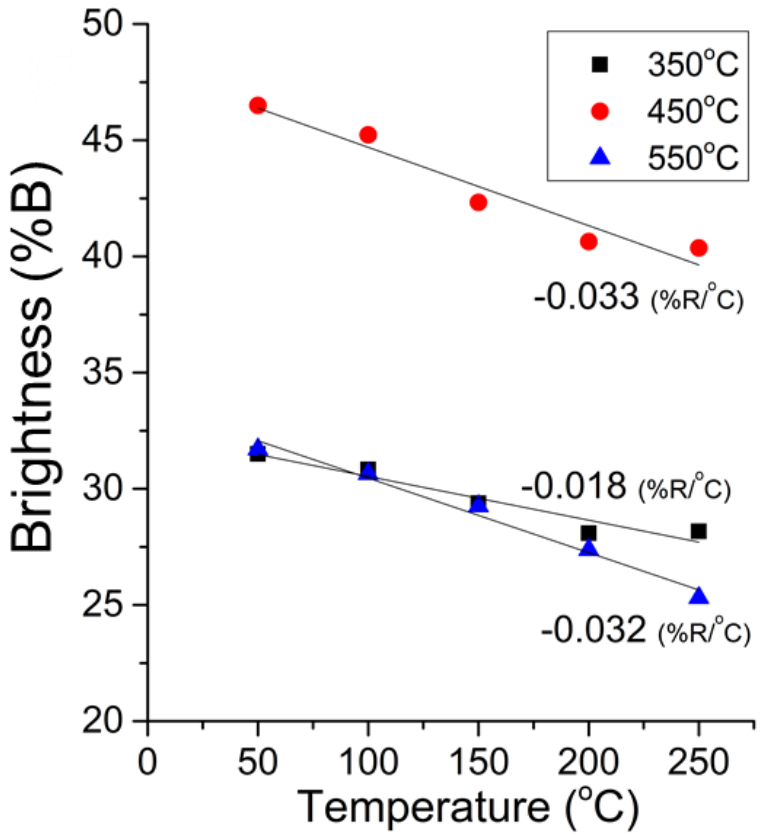

Figure 4: Variation of brightness as a function of temperature for V_2O_5 obtained by oxidation at 350 °C, 450 °C and 550 °C .

Controlled oxidation of as-grown films to V_2O_5 is accepted to yield films with various oxygen deficiencies. [41,42] These oxygen deficiencies are assumed to be responsible for the wide range of reported optical band gaps [46] and perceived colours.[35] We present tunable thermochromic V_2O_5 coatings, achieved by controlled oxidative annealing. In addition, Al_2O_3 encapsulation prevents change of the oxygen vacancies in the film during extended periods of operation at elevated temperatures, without impacting the thermochromic properties.

Conclusions

Pure single phase V_2O_5 coatings were obtained by controlled oxidation of VO_x films deposited using DLI MOCVD. Reversible visible thermochromism was observed upon heating under ambient atmosphere. The colour of thermochromic V_2O_5 could be adjusted by controlling the synthesis conditions. XRD reveals a pure phase polycrystalline nature of the coatings. Temperature-dependent optical spectroscopy for samples obtained by oxidation at 350°C, 450°C and 550°C confirm that each sample has a different window of thermochromic transition. Therefore, tuning the thermochromic behaviour is effectively achieved by controlling the oxidative annealing that enables adjusting the oxygen deficiency. Films oxidised at 580°C were not thermochromic, indicating that thermochromism is directly related to the oxygen deficiency. Hence it was shown that controlled oxygen vacancy plays a key role in expressing new functionalities of transitional metal oxides and V_2O_5 in particular.

References

1. Lötzsch, D.; Eberhardt, V.; Rabe, C. Ullmann's Encyclopedia of Industrial Chemistry; **2000**.
2. White, M.; LeBlanc, M. Thermochromism in Commercial Products. J Chem Educ **1999**, 76, 1201.
3. Chowdhury MA, Joshi M, Butola BS. Photochromic and thermochromic colourants in textile applications. Journal of Engineered Fibers and Fabrics. **2014** Jan 1;9(1):107-23.
4. Samat A, Lokshin V. Thermochromism of organic compounds. In Organic photochromic and thermochromic compounds **2002** (pp. 415-466). Springer US..
5. Day, J. Thermochromism. Chem Rev **1963**, 63, 65–80.
6. Sone, K; Fukuda, Y Inorganic Thermochromism.**1987**.
7. Day, J. Thermochromism of Inorganic Compounds. Chem Rev **1968**, 68, 649–657.

8. Hanhong X, Chuanfang Z. Reversible Thermochromism of Schiff Bases and Schiff Base Metal Complexes [J]. CHEMISTRY. **2000**;8:002..
9. Seeboth, A; Lötzsch, D Thermochromic and Thermotropic Materials. **2013**.
10. Babulanam, S. M.; Eriksson, T. S.; Niklasson, G. A.; Granqvist, C. G. Thermochromic VO2 Films for Energy-Efficient Windows. Sol Energy Mater **1987**, 16, 347–363.
11. Al-Kuhaili, M. F.; Durrani, S. M. A. Optical Properties of Chromium Oxide Thin Films Deposited by Electron-Beam Evaporation. Opt Mater **2007**, 29, 709–713.
12. Fine, G.; Cavanagh, L.; Afonja, A.; Binion, R. Metal Oxide Semi-Conductor Gas Sensors in Environmental Monitoring. Sensors Basel Switz **2010**, 10, 5469–502.
13. Lazaroff, W; Raschdorf, A Thermochromic Cookware. US Patent App. 10/965 **2004**.
14. Kuswandi, B.; Wicaksono, Y.; Abdullah, A.; Heng, L.; Ahmad, M. Smart Packaging: Sensors for Monitoring of Food Quality and Safety. Sensing and Instrumentation for Food Quality and Safety **2011**, 5, 137–146.
15. Pimia, J Temperature Indicator for Temperature Changing Material or Means and Method for Its Preparation. US Patent App. 13/637 **2011**.
16. Heo, K.; Sohn, Y.; Yi, J.; Kwon, J.; Gwag, J. Flexible Reflective Colour Displays Using Thermochromic Pigments. J Opt Soc Korea **2013**, 17, 428–432.
17. Heo, K. C.; Sohn, Y.; Yi, J.; Kwon, J. H.; Son, P. K.; Gwag, J. S. Reflective Colour Display Using Thermochromic Pigments. Appl Opt **2012**, 51, 4246–9.
18. Parker, R Expiration Indicator. US Patent 7 **2007**.
19. Parker, R Time-Temperature Indicator. US Patent 4 **1989**.
20. Varughese, S. Non-Covalent Routes to Tune the Optical Properties of Molecular Materials. J Mater Chem C **2014**, 2, 3499–3516.
21. Schäfer, C.; Lederle, C.; Zentel, K.; Stühn, B.; Gallei, M. Utilizing Stretch-Tunable Thermochromic Elastomeric Opal Films as Novel Reversible

Switchable Photonic Materials. Macromol Rapid Comm **2014**, 35, 1852–1860.

22. Wacharasindhu, S.; Montha, S.; Boonyiseng, J.; Potisatityuenyong, A.; Phollookin, C.; Tumcharern, G.; Sukwattanasinitt, M. Tuning of Thermochromic Properties of Polydiacetylene toward Universal Temperature Sensing Materials through Amido Hydrogen Bonding. Macromolecules **2010**, 43, 716–724.
23. Okaniwa, M.; Oaki, Y.; Imai, H. Intercalation-Induced Tunable Stimuli-Responsive Colour-Change Properties of Crystalline Organic Layered Compound. Adv Funct Mater **2016**, 26, 3463–3471.
24. Gaudon; Deniard; Voisin; Lacombe; Darnat; Demourgues; Perillon, J.-L.; Jobic How to Mimic the Thermo-Induced Red to Green Transition of Ruby with Control of the Temperature via the Use of an Inorganic Materials Blend? Dyes and Pigments **2012**, 95, 344–350.
25. Lataste; Demourgues; Salmi; Naporea; Gaudon Thermochromic Behavior (400<T°C<1200°C) of Barium Carbonate/binary Metal Oxide Mixtures. Dyes and Pigments **2011**, 91, 396–403.
26. MacLaren DC, White MA. Design rules for reversible thermochromic mixtures. Journal of materials science. **2005** Feb 1;40(3):669-76..
27. MacLaren DC, White MA. Competition between dye–developer and solvent–developer interactions in a reversible thermochromic system. Journal of Materials Chemistry. **2003**;13(7):1701-4.
28. Wild RL, Rockar EM, Smith JC. Thermochromism and Electrical Conductivity in Doped SrTiO3. Physical Review B. **1973** Oct 15;8(8):3828.
29. Salek; Demourgues; Jubera; Garcia; Gaudon Mn2+ Doped Zn3(PO4)2 Phosphors: Irreversible Thermochromic Materials Useful as Thermal Sensors. Opt Mater **2015**, 47, 323–327.
30. Dong L, Jia R, Xin B, Peng B, Zhang Y. Effects of oxygen vacancies on the structural and optical properties of β-Ga2O3. Scientific Reports. **2017** Jan 9;7:40160.
31. Wang, L.; Dash, S.; Chang, L.; You, L.; Feng, Y.; He, X.; Jin, K. J.; Zhou, Y.; Ong, H. G.; Ren, P.; Oxygen Vacancy Induced Room-Temperature

Metal-Insulator Transition in Nickelate Films and Its Potential Application in Photovoltaics. ACS Appl Mater Interfaces **2016**, 8, 9769–76.

32. Durrani, S. M. A.; Khawaja, E. E.; Salim, M. A.; Al-Kuhaili, M. F.; Al-Shukri, A. M. Effect of Preparation Conditions on the Optical and Thermochromic Properties of Thin Films of Tungsten Oxide. Sol Energ Mat Sol C **2002**, 71, 313–325.
33. Kumar, S.; Lenoble, D.; Maury, F.; Bahlawane, N. Synthesis of Vanadium Oxide Films with Controlled Morphologies: Impact on the Metal–insulator Transition Behaviour. Phys Status Solidi **2015**, 212, 1582–1587.
34. Kumar, S.; Maury, F.; Bahlawane, N. Electrical Switching in Semiconductor-Metal Self-Assembled VO2 Disordered Metamaterial Coatings. Sci Rep **2016**, 6, 37699.
35. Aita, C.; Liu, Y.-L.; Kao, M.; Hansen, S. Optical Behavior of Sputter-Deposited Vanadium Pentoxide. J Appl Phys **1986**, 60, 749–753.
36. Sreedhara, M. B.; Ghatak, J.; Bharath, B.; Rao, C. N. Atomic Layer Deposition of Ultrathin Crystalline Epitaxial Films of V2O5. ACS Appl Mater Interfaces **2017**, 9, 3178–3185.
37. Mattelaer, F.; Geryl, K.; Rampelberg, G.; Dendooven, J.; Detavernier, C. Amorphous and Crystalline Vanadium Oxides as High-Energy and High-Power Cathodes for Three-Dimensional Thin-Film Lithium Ion Batteries. ACS Appl Mater Interfaces **2017**.
38. Nicholas NJ, da Silva G, Kentish S, Stevens GW. Use of Vanadium (V) Oxide as a Catalyst for CO2 Hydration in Potassium Carbonate Systems. Industrial & Engineering Chemistry Research. **2014** Feb 18;53(8):3029-39.
39. Wan Z, Zhang TF, Lee HB, Yang JH, Choi WC, Han B, Kim KH, Kwon SH. Improved Corrosion Resistance and Mechanical Properties of CrN Hard Coatings with an Atomic Layer Deposited Al2O3 Interlayer. ACS applied materials & interfaces. **2015** Nov 23;7(48):26716-25
40. Baraldi G, Carrada M, Toudert J, Ferrer FJ, Arbouet A, Paillard V, Gonzalo J. Preventing the degradation of Ag nanoparticles using an

ultrathin a-Al2O3 layer as protective barrier. The Journal of Physical Chemistry C. **2013** Apr 30;117(18):9431-9.

41. Ramana; Smith; Hussain; Chusuei; Julien Correlation between Growth Conditions, Microstructure, and Optical Properties in Pulsed-Laser-Deposited V2O5 Thin Films. Chem Mater **2005**, 17, 1213–1219.
42. Ramana, C.; Hussain, O. Optical Absorption Behaviour of Vanadium Pentoxide Thin Films. Adv Mater Opt Electr **1997**, 7, 225–231.
43. Chenakin, S. P.; Prada Silvy, R.; Kruse, N. Effect of X-Rays on the Surface Chemical State of Al2O3, V2O5, and Aluminovanadate Oxide. J Phys Chem B **2005**, 109, 14611–8.
44. Silversmit, G.; Depla, D.; Poelman, H.; Marin, G. B.; Gryse, R. An XPS Study on the Surface Reduction of V 2 O 5 (001) Induced by Ar+ Ion Bombardment. Surface science **2006**, 600, 3512–3517.
45. Bahlawane, N.; Lenoble, D. Vanadium Oxide Compounds: Structure, Properties, and Growth from the Gas Phase. Chemical Vapour Deposition **2014**, 20, 299–311.
46. Krishna, G.; Bhattacharya, A. K. Effect of Thickness on the Optical Absorption Edge of Sputtered Vanadium Oxide Films. Materials Science and Engineering: B **1997**, 49, 166–171.

4.7 Optical and morphological properties of thermochromic V_2O_5 coatings

Abstract

We present optical and morphological characterizations performed on thermochromic V_2O_5 coatings. V_2O_5 coatings were obtained by oxidation of as-deposited VO_x films. Comparisons were made among coatings oxidized at various temperatures. Photographic evidence is also shown to provide the reader a clear visual description of the colour change that occurs during thermochromic process.

Published as Kumar S, Maury F, Bahlawane N. Optical and morphological properties of thermochromic V_2O_5 coatings. Data in Brief. (2017)

1. Data

V_2O_5 coatings show a linear increase in the surface roughness with temperature. Fig. 1(i) shows the plot of surface roughness versus oxidation temperature and Fig. 1 (ii) shows the roughness profile of the coatings obtained by oxidation at (a) 350 °C, (b) 450 °C and (c) 550°C over a scanning distance of 0.8 mm. The brightness of the coatings is defined as the total area under the curve over the full range of visible spectrum (400–800 nm). The curve plotted with brightness versus oxidation temperature shown in Fig. 2 has a bell curve profile with maximum at 450 °C and a brightness of 50%. Temperature-dependent optical spectra in the visible region are shown in Fig. 3 for coatings obtained by oxidation at (a) 350°C, and (b) 450°C and (c) 550°C respectively. THR at specific wavelengths like 535 nm, 555 nm and 575 nm was compared among the films obtained by oxidation at 350°C, 450°C and 550°C in Fig. 4. Lastly Fig. 5 shows the photographic images of thermochromic V_2O_5 coatings at both room temperature and 300°C.

2. Experimental design, materials, and methods

2.1. Preparation of V_2O_5 coatings

Thin films of vanadium oxide were deposited on silicon substrates by Direct Liquid Injection (DLI) Metal Organic Chemical Vapor Deposition (MOCVD), the details of which are reported elsewhere [1,2]. Argon was used as the carrier gas at a flow rate of 50 sccm while the chamber pressure was adjusted to 10 mbar. Substrates were maintained at a constant temperature of 500 °C during the four hours of deposition.

After deposition, samples were allowed to cool till room temperature in argon atmosphere at low pressure before withdrawing from the chamber under ambient atmosphere. Post deposition annealing was performed under ambient air at 300–580 ° C. The annealing time was adjusted to allow a complete oxidation from VO_x to V_2O_5. While 10 min were sufficient for oxidation at 550 °C, significantly longer

times were required at lower temperatures; this can be explained by simple temperature dependent oxidation kinetics. To isolate V_2O_5 coatings from atmospheric gas phase interactions, ALD of Al_2O_3 was performed using the sequential introduction of Trimethylaluminium (TMA) and water. The pulse times for each reactant were adjusted to 40 ms with a 15 s purge in between each pulse. The rather large pulse and purge times were chosen to achieve complete conformal coverage over the film.

2.2. Film characterization

Total hemispherical reflection (THR) measurements were carried out on LAMBDA 1050 UV/Vis/NIR spectrophotometer from Perkin Elmer with a 150 mm integration sphere in the reflection configuration. Measurements, which correspond to the sum of specular and diffuse reflections, were performed in the visible spectral range (400–800 nm). Temperature-dependent measurements were carried out with the help of a custom made sample holder with an integrated heating element. Temperature control was achieved by a Horst HT 60 temperature controller coupled to a K-type thermocouple. The film thickness and roughness were measured using an Alpha step d-500 Profilometer from KLA-Tencor

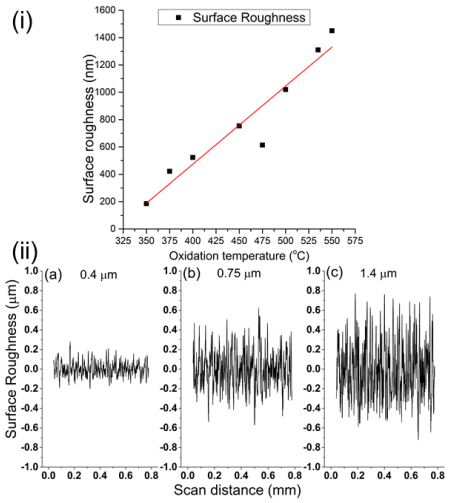

Figure S1: (i) Surface roughness increases linearly with oxidation temperature. (ii) Roughness profile of coatings oxidised at (a) 350°C, (b) 450°C and (c) 550°C measured using a profilometer tip dragging across the surface with a scan distance of 0.8 mm.

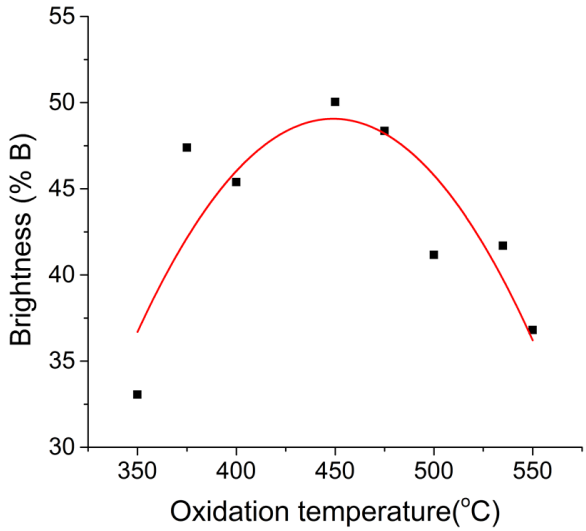

Figure S2: Brightness versus oxidation temperature curve indicates a maximum brightness at 450°C. It is noteworthy that sample colour is bright yellow at this oxidation temperature.

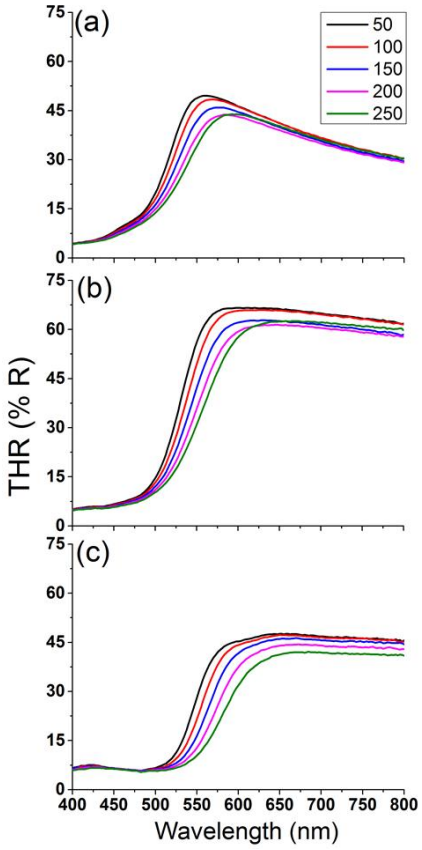

Figure S3: Temperature dependent optical spectra of coatings obtained by oxidation at (a) 350°C, (b) 450°C and (c) 550°C respectively.

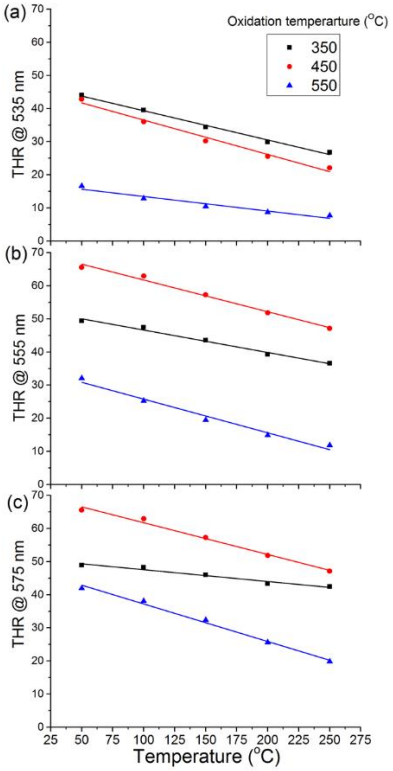

Figure S4: Plot of THR at (a) 535 nm, (b) 555 nm and (c) 575 nm versus temperature for V_2O_5 coatings annealed at 350°C, 450°C and 550°C respectively.

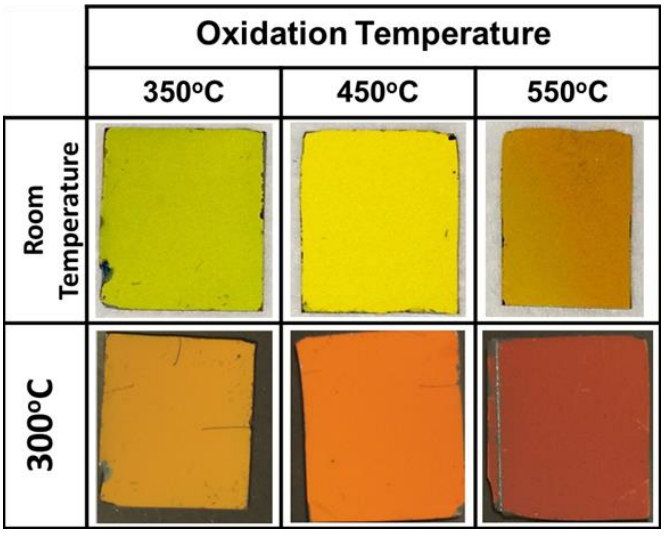

Figure S5: Photographs of V_2O_5 coatings on silicon wafer, obtained by oxidation at different temperatures. Thermochromic colour change for each film is shown upon heating the films from room temperature (1st row) till 300°C (2nd row)

References

1. Kumar, S., Maury, F. and Bahlawane, N. Visible thermochromism in Vanadium pentoxide coatings. *ACS Applied Materials and Interfaces* 9 (25), pp 21447–21456 (2017).
2. Kumar, S., Maury, F., and Bahlawane, N. Tunable thermochromic properties of V_2O_5 coatings, Materials *today physics* (2) pp 1-5; (2017)

5. Conclusions and Future Work

In this thesis, gas phase synthesis of VO_2 and V_2O_5 films by metal organic chemical are reported, along with the characterisation of semiconductor to metal transition in VO_2 and the thermochromic properties of both VO_2 and V_2O_5.

The effect of various CVD parameters on the morphology and its impact on the SMT was reported, which in turn encouraged us to growing VO_2 films of the highest quality. With the help on an indigenous one pot three step oxidation reduction processes near epitaxial films of VO_2 were grown. Fundamental understanding of the phase change characteristics of VO_2 were explained with the help of temperature dependent XRD, Raman and Infrared thermal imaging respectively.

The presence of a semiconducting metal M2 (phase) intermediate was evidenced with the help of temperature dependent resistivity measurements and Raman spatial mapping in the hysteresis region of VO_2. It was concluded that this M2 phase is the consequence of the strain on the film. Later the nature of phase transition was explained visually with the help of infrared imaging, where the electrical and optical changes occurring in VO_2 upon heating are evidenced to the direct consequence of the confinement and coalescence of the metallic puddles that form upon heating and disappear once the temperature is sufficiently low.

Investigations of thermochromic properties through infrared images of VO_2 reveal anomalous emissivity changes in the disordered metamaterial region. During the temperature cycling VO_2 undergoes massive emissivity change from 0.95 in the semiconducting phase to 0.1 in the metallic state.

In case of V_2O_5 visible range thermochromism was discovered, where the colour of V_2O_5 coatings would change from yellow to orange when subjected to elevated temperature. It was the first time that thermochromism was reported for V_2O_5 which was until now only been regarded as a high TCR material and studied for its catalytic properties. Interlayer expansion of individual layers of V_2O_5 was

proved to be reason for this colour changing behaviour. Change in optical band gap as a function of temperature confirms with the findings.

In terms of applications VO_2 coatings were demonstrated to act as a thermally controlled electrically switch. By controlling the metamaterial state of VO_2 by short and quick temperature pulses, electrical resistivity changed more than three orders of magnitude. In similar fashion, a temperature controlled emissivity switch was also demonstrated. Furthermore, temperature induced localised phase change was demonstrated to highlight the VO_2 metamaterial as an on-demand Infrared visible reversible, rewritable slate. IR visible patterns were created by locally changing the phase of the material from semiconducting to insulating having a large variation in their emissivity. Such patterns would stay stable as long as the steady state temperature was maintained, and once the temperature cycling has been done the patterns would disappear and the VO_2 metamaterial state would be ready for another pattern.

After explaining the origin of visible thermochromism in V_2O_5, tuning the window of thermochromic transition was successfully demonstrated by simply varying the oxygen vacancy in the film. Therefore, by annealing the as deposited VO_x films at different temperatures, V_2O_5 films with varying oxygen deficiency were obtained, each of which having a different window of thermochromic transition.

Regarding the future work, VO_2 metamaterial characteristics open a whole new world for studying them for nonlinear optics, flat lenses, thermal IR camouflages, emissivity control in space applications and for energy harvesting applications and terahertz radio frequency tuning. Combining the host of properties that VO_2 has to offer, it's only limited by the imagination of the researchers to utilize VO_2 in unique ways. Future work on thermochromic V_2O_5 can be concentrated on exploring the selective oxidation of VO_x films by creating different thermochromic regions with fixed window of transition on the same sample. V_2O_5 coatings obtained by the current method proved to highly pure and feature a porous morphology. Along with a tremendous growth rate and the ability to deposit over a wide variety of substrates, it can be an ideal way to employ them as future battery and energy storage applications.

In conclusion, new and unique properties of these highly researched and industrially relevant materials were investigated and several technologically relevant application concepts were demonstrated. Through this thesis and from the results published in the form of journal publications, I hope to inspire future researchers to further investigate these fascinating and ultra-responsive oxide systems to incorporate their functionality into existing and future applications that are yet to be discovered.

Annexe 1

Extended summary in French

I- Introduction – Etat de l'art

Les oxydes fortement corrélés sont largement étudiés pour de nombreuses applications dans des composants exploitant par exemple la supraconductivité à haute température, la magnéto-résistance colossale, La sensibilité au champ magnétique. Les oxydes de métaux de transition constituent la majorité des systèmes d'oxydes fortement corrélés, incluant donc des oxydes de vanadium, en particulier VO_2 et V_2O_5 qui sont les deux phases les plus étudiées pour diverses applications, notamment en raison d'une transition semiconducteur-métal (SMT) à basse température pour VO_2.

Dans cette thèse, la croissance et la caractérisation de films minces VO_2 et V_2O_5 sont décrites et discutées avec un focus particulier sur l'impact des conditions de dépôt sur la qualité de la SMT de VO_2 et sur les propriétés optiques, notamment les propriétés thermochromiques dans le cas de V_2O_5.

Traditionnellement, le comportement de la SMT [1-4] était vu comme une transition abrupte de résistivité et de réflectivité [5-7] et ce n'est que récemment que VO_2 est traité comme un système beaucoup plus complexe qui présente les caractéristiques d'un **métamatériau naturellement désordonné** avec, à proximité de la transition de phase, la coexistence d'une phase semi-conductrice (M, monoclinique) et d'une autre métallique (R, rutile).[8-12] Étant donné que chaque phase de VO_2 a des propriétés optiques et électriques distinctes, le contrôle de l'étendue de la transition de phase par modulation fine de la température permet l'exploitation de nouvelles propriétés, telles que la modulation de l'émissivité dans la région du proche infrarouge (NIR) et la création de systèmes modèles expérimentaux, réversibles et réinscriptibles, avec potentiellement des applications dans des composants optoélectroniques ou l'invisibilité en IR.

V_2O_5 est usuellement considéré comme un matériau à haut coefficient de température, TCR [13,14], qualifiant sa résistance à une propriété physique, et également comme un matériau de choix pour des applications allant de la catalyse, [15,16] aux capteurs de gaz [17,18] et aux batteries au lithium.[19,20] Dans ce mémoire, nous nous concentrons sur les propriétés optiques du matériau, en particulier l'effet thermochromique dans le visible des revêtements V_2O_5 synthétisés par MOCVD suivi d'un recuit oxydant. L'impact du dopage et de la production sélective et contrôlée de déficits en oxygène sur la propriété thermochromique est discuté.

II- Croissance MOCVD de VO_2

II.1- Cas I : réacteur « Spoutnik »

Des films minces de VO_2 ont été déposés sur des substrats en Si par DLI-MOCVD dans un réacteur vertical à jet frappant et à paroi tiède fait « maison » (Spoutnik). De faibles concentrations (5 mM) de solutions d'éthanol (pureté initiale 99,9%) de vanadium(V) oxy-tri-isopropoxyde [$VO(O^iPr)_3$] ont été utilisées en tant que précurseur. L'injection de la solution liquide a été réalisée dans un tube d'évaporation maintenue à 200°C pour garantir une vaporisation quasi instantanée de la solution de précurseur. Les substrats ont été maintenus à une température constante dans la gamme 400-600°C. Au cours du dépôt, l'injection de précurseur a été maintenue à 4 Hz avec 2 ms de temps d'ouverture produisant un débit de liquide de 2.5 ml.min^{-1}. L'azote a été utilisé comme gaz porteur avec un débit de 40 sccm, la pression de la chambre était ajustée entre 3 et 9 mbar et le temps de dépôt a été varié entre 15 et 180 min pour contrôler différentes épaisseurs. Une fois recouverts, les substrats ont été refroidis à température ambiante à basse pression sous atmosphère d'azote avant d'être retirés de la chambre. Aucun recuit de post-dépôt n'a été effectué. Tous les échantillons ont été manipulés à l'air après dépôt.

II.2- Cas II : réacteur « MC200 »

Des films d'oxyde de vanadium ont également été déposés sur des substrats de Si en utilisant un réacteur commercial MOCVD de plus grande capacité (MC200, AnnealSys). C'est un réacteur à paroi tiède équipé d'un système à injection

liquide directe et qui a également une géométrie à jet frappant. Des solutions de cyclohexane contenant 5 mM de vanadium(V) oxy-tri-isopropoxyde ont été utilisées comme source unique de vanadium et oxygène. La solution était maintenue sous atmosphère N_2 à la température ambiante avant son injection dans la chambre d'évaporation, puis elle était injectée à une fréquence de 2 Hz avec un temps d'ouverture ajusté pour atteindre un débit d'alimentation de 1 g / min. La pression et la température de la chambre d'évaporation ont été maintenues à 0,6 mbar et 200°C respectivement pendant le dépôt, tandis que les parois du réacteur ont été thermostatées à 200°C. Au cours de la croissance, 500 sccm de N_2 ont été introduits comme gaz porteur du précurseur et la pression totale du réacteur a été automatiquement réglée à 0,6 mbar. Le substrat était maintenu à 600 C pendant les 2 h de dépôt et les traitements thermiques ultérieurs.

Un recuit oxydant d'une heure a été réalisé à 600°C juste après le dépôt sous une pression partielle d'oxygène de $1x10^{-2}$ mbar. L'échantillon est ensuite soumis à un recuit à la même température sous vide (~ 0,6 mbar) agissant comme atmosphère réductrice pendant 4 h, après quoi la température de chambre était ramenée à l'ambiante. Tous les dépôts ont été effectués sur des plaquettes de Si de 4'' sans enlever la couche d'oxyde natif qui constitue une barrière de diffusion. Les échantillons ont ensuite été coupés en petits morceaux à des fins d'analyse. La grande homogénéité des films VO_2 a été observées sur l'ensemble des plaquettes.

Les films déposés à l'aide de cyclohexane en tant que solvant sont amorphes aux RX, ce qui contraste avec les films polycristallins obtenus avec une solution d'éthanol dans la même plage de température.[21] La raison vient de la plus grande stabilité thermique du cyclohexane à 600°C. Par exemple, la pyrolyse de l'éthanol dans la gamme 576-624°C produit essentiellement des composés contenant du méthane, de l'hydrogène et surtout de l'oxygène comme l'acétaldéhyde et le CO. Contrairement au cyclohexane, l'éthanol peut donc participer à la chimie des dépôts comme source potentielle d'oxygène. Il est à noter que les films qui sont donc amorphes aux RX présentent la signature Raman caractéristique de VO_2, mais ne comportent aucun changement soudain

de résistivité électrique lors du chauffage au niveau de la SMT. Il fut donc nécessaire d'appliquer des post-traitements pour améliorer la cristallinité de ces films VO_2 et diminuer ainsi la densité des joints de grains.

II.3- Processus d'oxydation-réduction des films VO_x

Deux approches ont été mises en œuvre pour induire le frittage des films VO_2. Le recuit sous vide en l'absence d'oxygène a été effectué à 600°C directement dans la chambre de dépôt. Comme cette température est bien au-dessous du point de fusion (1970°C) de VO_2, aucun frittage significatif n'a eu lieu. La deuxième approche implique la conversion préalable de VO_2 en V_2O_5, cette dernière phase présentant un point de fusion plus bas (690°C) le frittage doit en être favorisé. Cette approche fut réussie. La conversion de VO_2 à V_2O_5 a été effectuée sous la pression partielle d'O_2 de 0,01 mbar. La température a été fixée à 600°C pour induire un frittage efficace sur une période de courte durée (1 h) et simplifier ce procédé en plusieurs étapes en maintenant constante la température du substrat.

Les films V_2O_5 frittés subissent ensuite une réduction en VO_2 à la même température (600°C) en l'absence d'oxygène. La morphologie observée dans les micrographies de surface de la figure 1 montre l'évolution de la microstructure du film à différentes étapes du procédé, de grains nano poreux à de grands domaines bien formés. Au moment de la réduction sous vide, V_2O_5 libère de l'oxygène sans affecter de manière significative la morphologie dense obtenue. Un traitement prolongé dans ces conditions donnerait V_2O_3 mais ce n'était pas le but. L'étape de frittage par oxydation donne bien la phase orthorhombique V_2O_5 qui se transforme en VO_2 monoclinique (M_1) après recuit sous vide.

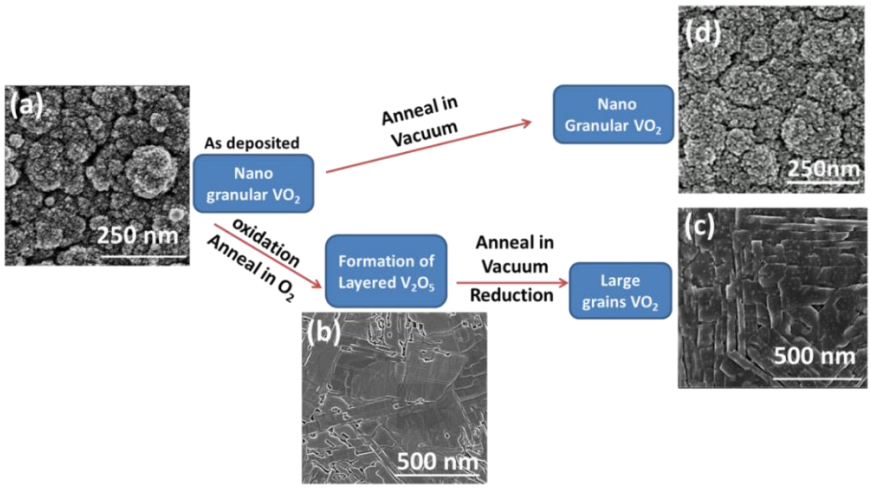

Figure 1: Etapes d'oxydation et de réduction des films d'oxyde de vanadium élaborés dans le réacteur MC200.

III- Impact de la morphologie sur la SMT de films VO_2

Un contrôle précis de la croissance de films VO_2 avec une large gamme de morphologie a été obtenu en faisant varier les paramètres de dépôt dans le procédé DLI-MOCVD telles que la température, la pression, la concentration du précurseur et le temps de dépôt. Dans cette série, une transition typique métal-semiconducteur (SMT) $t_c = 52^{\circ}C$ a été mesurée. La variation des paramètres de dépôt a permis la croissance de films nanocristallins très poreux et d'autres plus denses, avec des tailles de cristallite contrôlées jusqu'à plusieurs centaines de nanomètres. L'oxy tri-isopropoxyde de vanadium (V) a été utilisé dans cette étude en tant que précurseur source unique. Les films poreux présentent un changement de résistivité diffus à travers la température de transition tandis que les films cristallins ont une variation abrupte et importante de résistivité. Cela a permis de corréler le comportement de la SMT aux différentes morphologies. Les figures 2 et 3 montrent les micrographies de films VO_2 avec des morphologies et épaisseurs différentes. La figure 4 montre le comportement SMT des films à haute porosité par rapport aux films compacts.

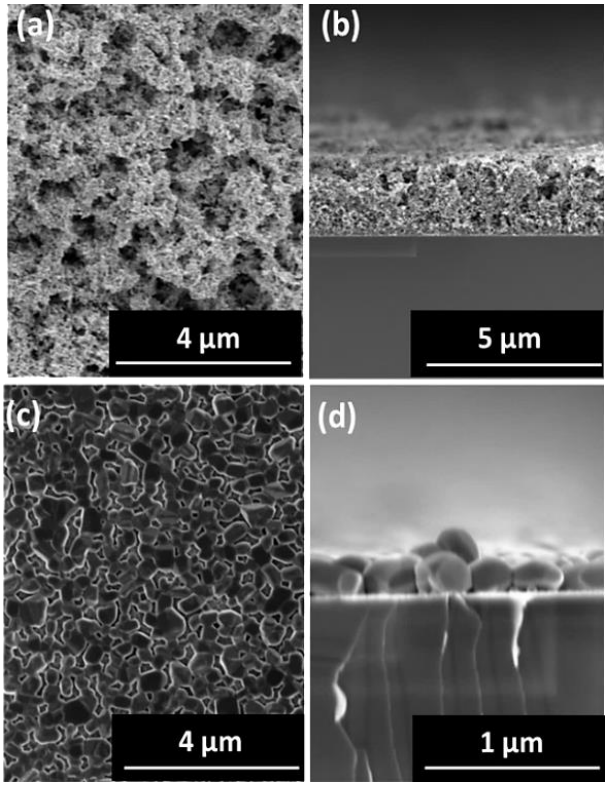

Figure 2: (a, c) micrographies MEB de surface et (b, d) de section transversale de films VO_2 déposés à 500°C avec 5 (a, b) et 2,5 mM (c, d) de concentration de précurseur et une pression totale de 9 mbar.

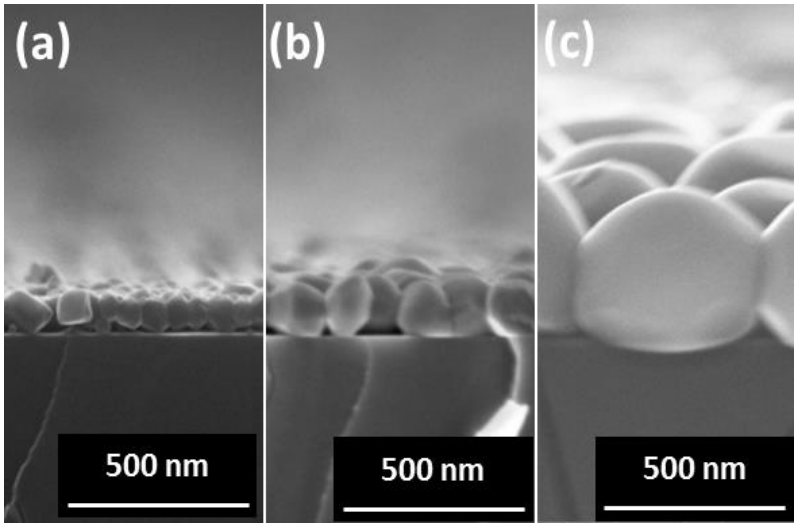

Figure 3: Micrographies MEB de section transversale de films VO_2 déposés à 575°C pour une durée de (a) 15, (b) 30 et (c) 120 min.

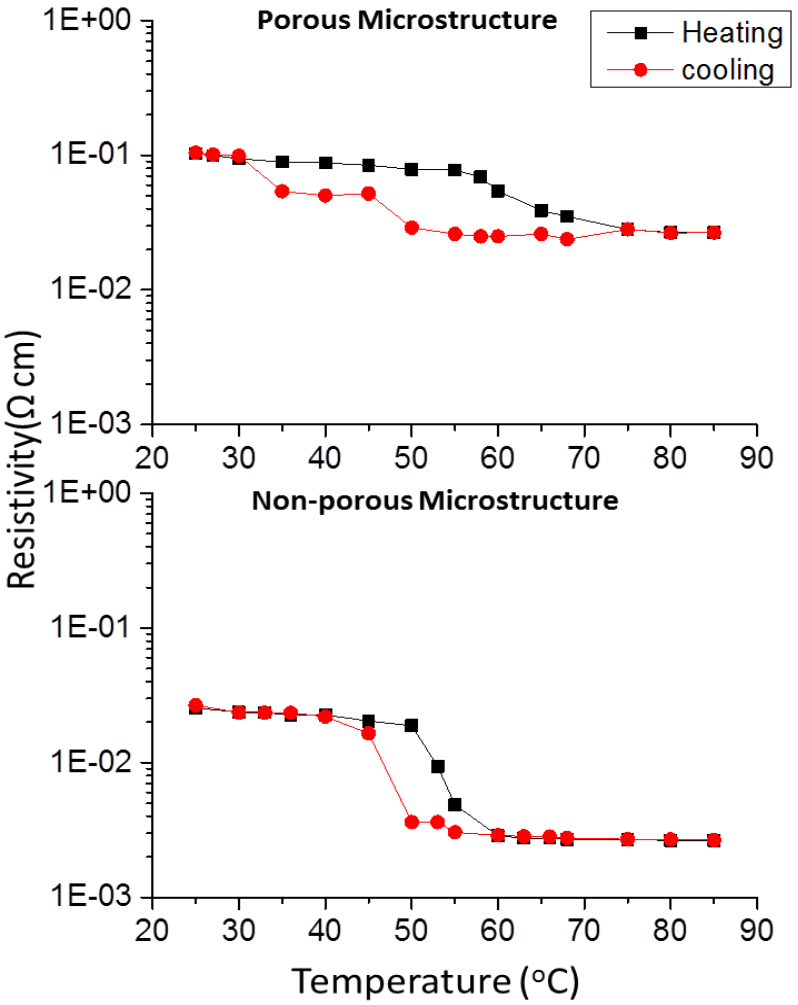

Figure 4: Comparaison du comportement SMT de films VO_2 avec une microstructure poreuse (haut) et compacte (bas) pour une épaisseur de 1,4 µm chacun.

Conclusion de ce chapitre. Par MOCVD à partir de $[VO(O^iPr)_3]$ on a fait croître des couches minces de VO_2 avec différentes microstructures et morphologies. Ce procédé a été utilisé pour produire des films d'épaisseur allant de 90 nm à 3 µm avec un contrôle fin de la porosité, la cristallinité et la taille des grains. Cette étude révèle que la morphologie joue un rôle de premier plan sur le comportement de la SMT. L'épaisseur du film, la granulométrie, la porosité, la cristallinité et la forme des cristallites ont tous un impact sur les ΔT, différence de résistivité électrique (Δρ) et Température de transition (Tc). Fort de ces constats, nous avons la liberté et la capacité d'affiner la croissance des films et la SMT selon l'application souhaitée.

IV- VO_2 comme un métamatériau naturellement désordonné

En tant qu'oxyde fortement corrélés, VO_2 inspire plusieurs applications de haute technologie. La synthèse de plaquettes Si recouvertes de VO_2 de haute qualité cristalline a été démontrée à l'échelle fiable de 4". La transition SMT se produit alors comme prévu à 67°C à partir de la phase monoclinique pure, M1, pour produire une phase rutile pure (R). Cette transition comprend un changement de résistivité électrique brusque de plus de 3 ordres de grandeur et une hystérésis étroite, 3K, (figure 5). Ce comportement est comparable à celui des dépôts épitaxiques. Les analyses IR et Raman résolues spatialement ont mis en évidence les domaines de l'auto-assemblage de VO_2 caractéristiques d'un métamatériau désordonné, avec la coexistence de phases monocliniques (M1 et M2) et rutile (R) dans la région de la SMT. La phase M2 suit la transition M1/R dans les zones restreintes. Des impulsions de chauffage ou de refroidissement courtes induisent de manière fiable la coalescence / confinement des domaines métalliques dans le métamatériau stable dans le temps. Le degré de coalescence a été déclenché thermiquement avec une grande précision pour fournir une commutation électrique fiable avec amplitude et profil réglables.

L'imagerie IR avec une caméra thermique révèle le mécanisme de la SMT dans les films VO_2. Comme le montre la figure 6, de petits domaines métalliques se forment et se développent à mesure que la température augmente jusqu'à la coalescence et la percolation, couvrant ainsi à la fin toute la surface. Cette coexistence de régions de phase intermédiaire est appelée métamatériau naturellement désordonné.

Le métamatériau désordonné a été déclenché thermiquement pour régler le degré de coalescence / confinement des domaines métalliques avec une grande précision compatible avec celle d'un commutateur électrique thermiquement contrôlé, comme montré sur la figure 7. Ce comportement d'hystérésis réglable montré à la figure 8 est obtenu par modulation de la température dans la région du métamatériau VO_2.

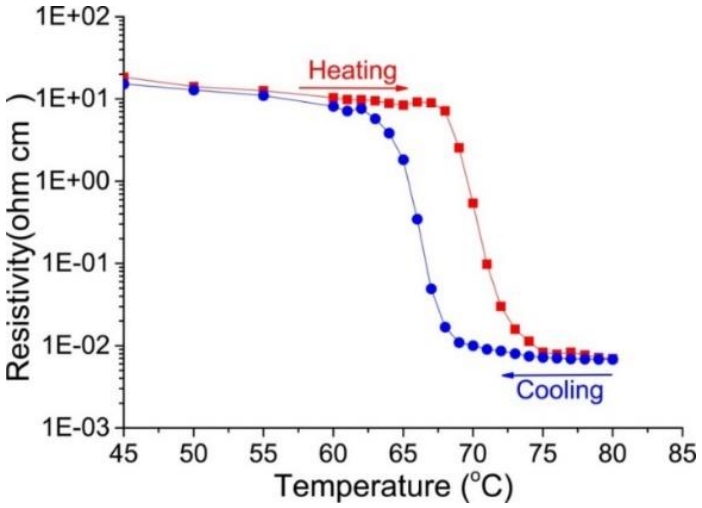

Figure 5: Variation de la résistivité électrique d'un film VO_2 avec la température lors des cycles de chauffage et de refroidissement.

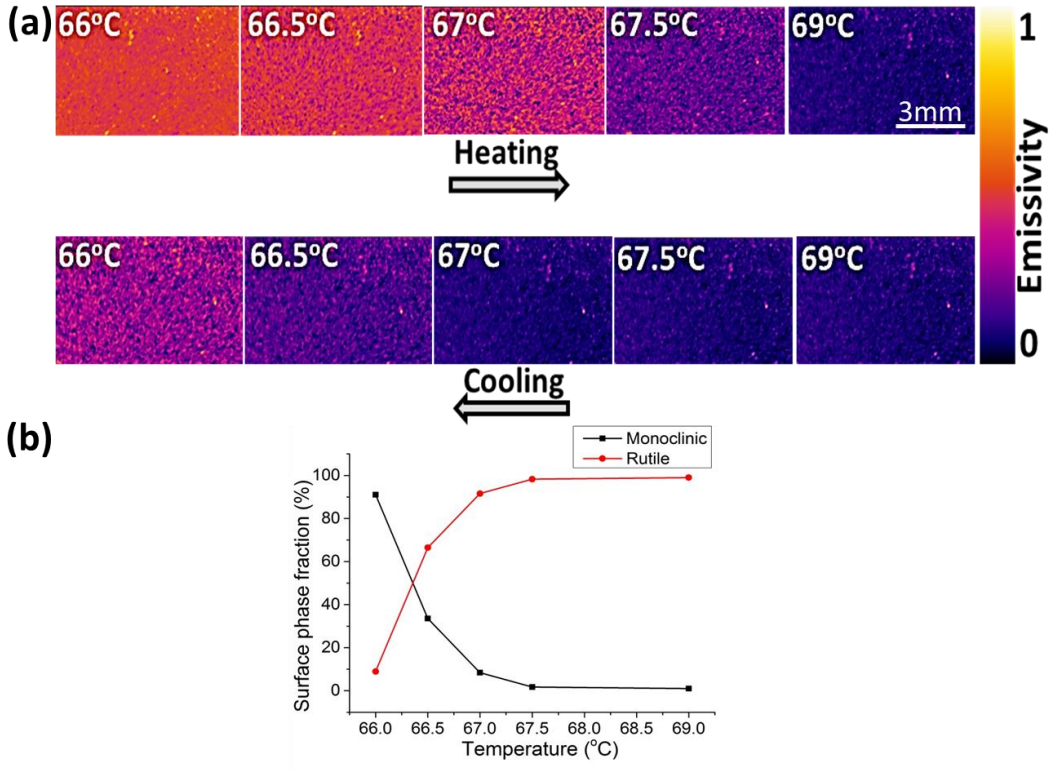

Figure 6: (a) Imagerie thermique du film VO_2 près de la SMT montrant la formation de petits domaines métalliques comme taches violettes qui croissent avec la température. (b) Variation de la fraction des phases monoclinique et rutile calculée à partir du changement de couleur dans les images thermiques pendant l'étape de refroidissement.

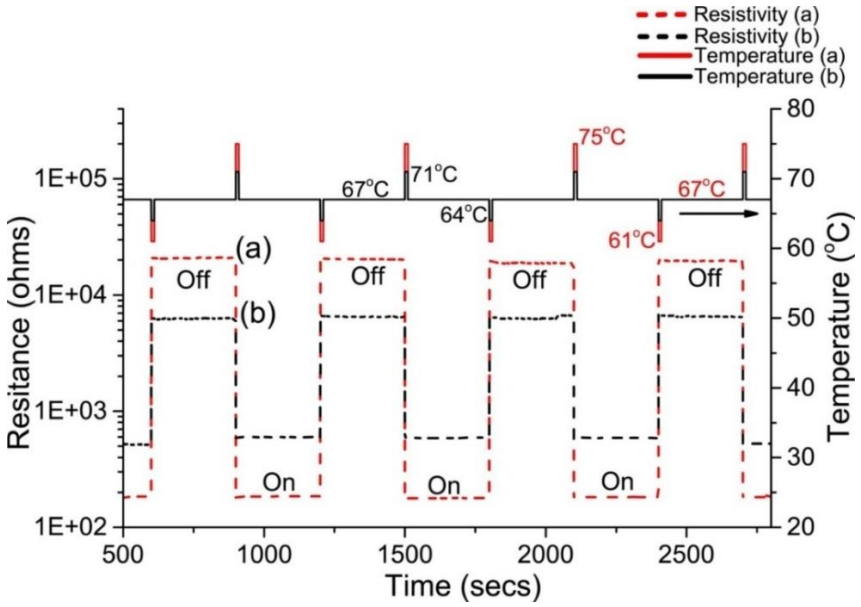

Figure 7: Comportement de commutation thermique du métamatériau désordonné VO_2. Les états "off" et "on" sont déterminés par la chute soudaine ou l'augmentation de la résistance électrique en raison de petits changements de température donnés sous forme d'impulsions d'activation thermique.

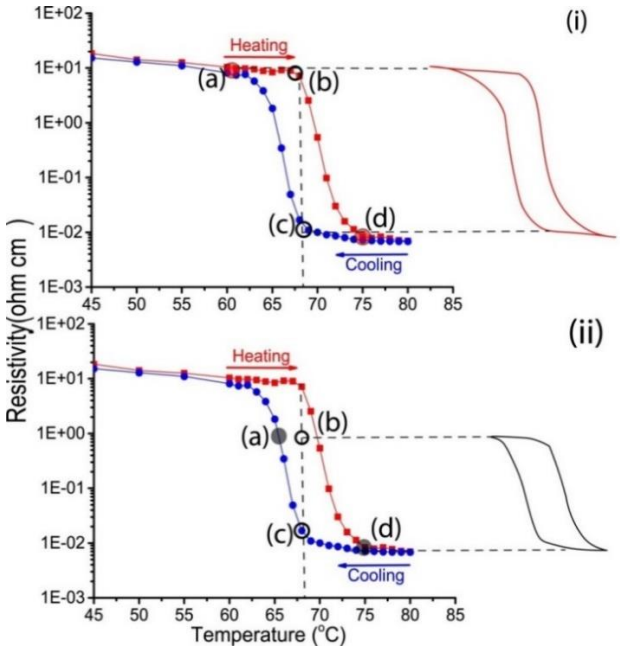

Figure 8: Représentation schématique du processus de commutation thermique à partir de la courbe d'hystérésis. L'impact de l'adoption de 2 amplitudes différentes de l'activation thermique est illustré en (i) et (ii). c → a → b: impulsion de refroidissement; b → d → c: impulsion de chauffage.

V- Modulation de la lumière par des films VO_2

Les revêtements Cermet sont des absorbeurs sélectifs solaires populaires car ils captent la majeure partie de l'énergie solaire tout en minimisant les pertes radiatives. Les nanoparticules métalliques intégrées dans les matrices diélectriques favorisent une réflexion interne multiple de la lumière, ce qui entraîne son absorption complète. La nature métallique des inclusions offre cependant une faible émissivité globale. VO_2 à l'état métamatériau est considéré dans cette étude comme une phase mixte sensible comprenant des inclusions métalliques dans une phase semi-conductrice imitant un cermet. Le cermet intelligent répond aux stimuli thermiques en modulant la taille des inclusions métalliques et permettant ainsi la manipulation de l'interaction avec la lumière. La réponse très fiable et reproductible du cermet intelligent vient corroborer la mémoire d'inversion récemment rapporté pour VO_2. Nous démontrons un commutateur d'émissivité à 85% commandé thermiquement en profitant de l'hystérésis étroite et des capacités de réglage du métamatériau désordonné.

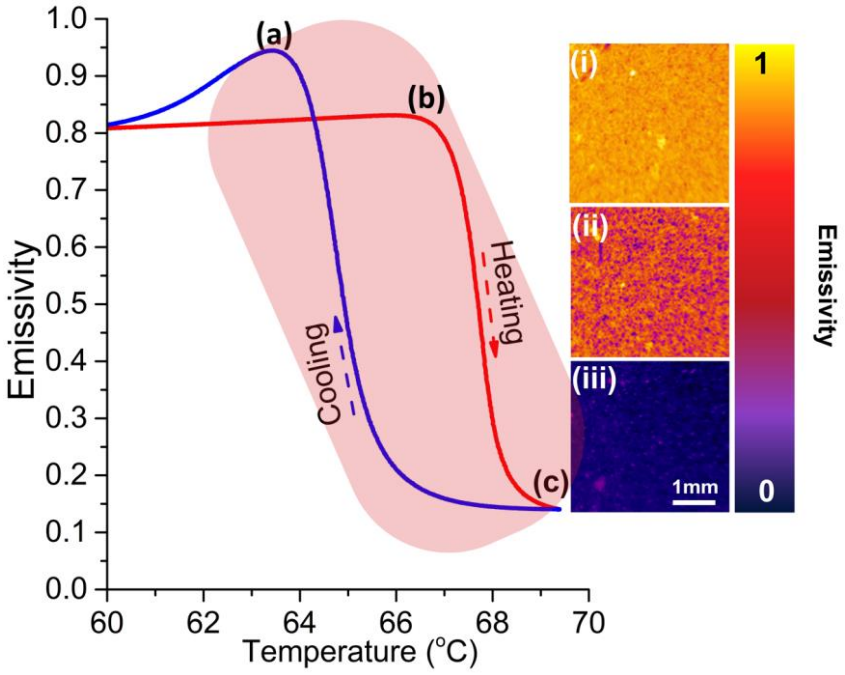

Figure 9: émissivité dépendant de la température de VO_2 à travers la SMT et images IR de 3 régions sélectionnées (a, b, c) sur la courbe d'hystérésis. La région métamatériau est représentée par une zone colorée sur la courbe d'hystérésis.

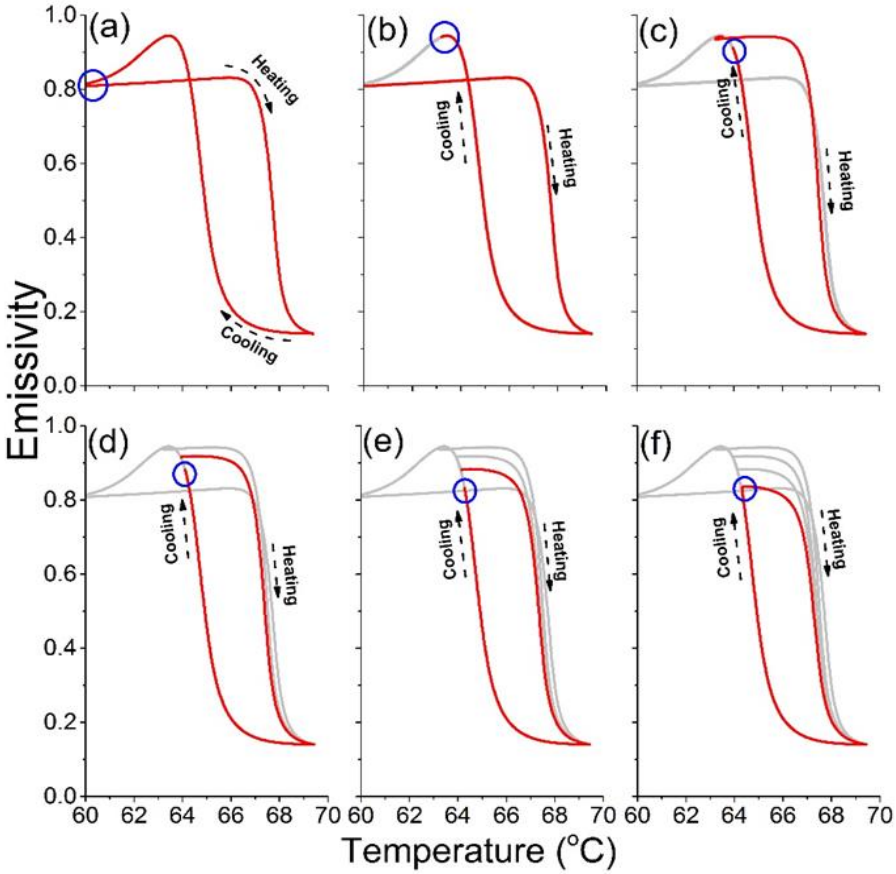

Figure 10: L'émissivité variable telle qu'indiquée de (a) à (f) est obtenue en ajustant la température minimale du cycle de refroidissement et en commençant immédiatement le cycle de chauffage. On peut atteindre un état d'émissivité précis en ajustant les températures de refroidissement et de chauffage.

Conclusion de ce chapitre : le concept de cermet intelligent a été introduit en utilisant des films de VO_2 dans la plage de température de l'état métamatériau. VO_2 et les oxydes corrélés avec SMT en général, peuvent être des candidats idéaux à l'avenir pour la modulation de la lumière, la réflectivité IR et l'émissivité thermique pour ne citer que quelque uns. Nous avons montré que la modulation optique de VO_2 est déclenchée thermiquement.[25] Un champ électrique ou une contrainte mécanique [26] peuvent également être mis en œuvre pour actionner la SMT de VO_2. La combinaison de cette propriété des matériaux fortement sensible avec les technologies existantes et à venir ouvre d'innombrables possibilités pour intégrer des fonctionnalités innovantes dans la modulation de la lumière et la collecte de l'énergie solaire.

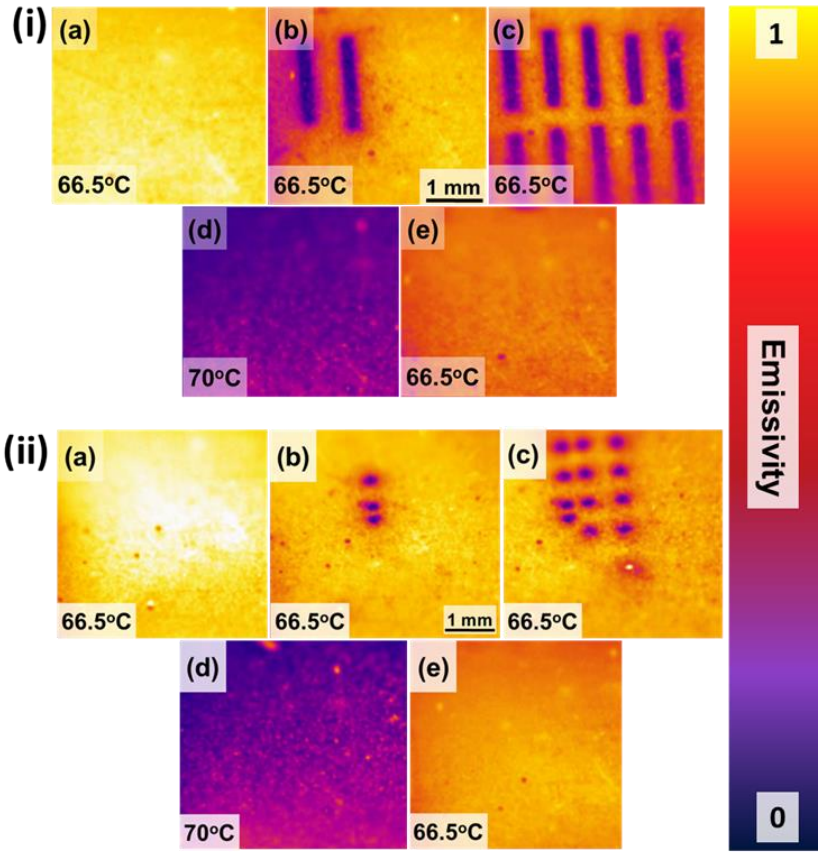

Figure 11: les images IR à partir d'une caméra thermique montrent un motif réversible sur une surface VO_2 à l'aide d'un laser pour tracer des lignes (i) et (ii) des points. (a) un film VO_2 est maintenu à une température stable de 66.5 C, lors d'une irradiation laser, la température est instantanément augmentée dans la zone d'interaction d'environ 4-5°C provoquant un changement de phase localisée d'un état émissif élevé à un état émissif bas (b) (c). En raison du comportement d'hystérésis intrinsèque de VO_2, les motifs restent sans aucune dégradation. L'augmentation de la température de l'ensemble du film et son retour à l'état d'équilibre (d) et (e) efface et remet à zéro l'état du film VO_2.

Une autre utilisation très intéressante et unique de l'état métamatériau de VO_2 est illustrée à la figure 11, où une ardoise IR est démontrée. En induisant un changement de phase localisé par irradiation laser, nous pouvons modifier l'émissivité de la région exposée tout en conservant le reste du fond continu intact. En raison de la grande différence dans la valeur d'émissivité, une caméra thermique affichera des couleurs contrastées pour les deux régions d'émissivité différentes. Tant que la température est maintenue constante, les motifs restent

intacts sans disparition ou dégradation. Une simple opération sur le cycle de température efface et réinitialise la surface.

VI- Synthèse de films V_2O_5

VI.1- DLI-MOCVD

Des films minces d'oxyde de vanadium ont été déposés sur des substrats de Si par DLI-MOCVD dans un réacteur vertical à jet frappant et à paroi tiède. Une faible concentration de vanadium(V) oxy-tri-isopropoxyde (5 mM) dans une solution d'éthanol à 99,9% a été utilisée comme précurseur. Son injection liquide a été réalisée dans un tube d'évaporation maintenue à 225°C pour obtenir une vaporisation quasi instantanée. L'injection de précurseur a été faite à 4 Hz avec un temps d'ouverture de 4 ms résultant en un débit de liquide de 1,33 ml / min. L'argon a été utilisé comme gaz porteur avec un débit de 50 sccm tandis que la pression de la chambre a été ajustée à 10 mbar. Les substrats ont été maintenus à une température constante de 450°C pendant les 4 h de dépôt.

Une série de films de Cr-dopés V_2O_5 a également été réalisée avec une solution mixte de précurseurs caractérisée par un rapport Cr/V ajusté. Le dopage a été réalisée par simple mélange à diverses dilutions d'une solution d'éthanol à 5 mM de l'acétylacétonate de chrome, $Cr(acac)_3$, dans le précurseur de vanadium.

VI.2- Traitement thermique post-dépôt

Après le dépôt MOCVD, les échantillons ont été laissés se refroidir jusqu'à la température ambiante dans une atmosphère Ar à basse pression avant d'être sortis de la chambre. Ils ont ensuite subi un recuit dans l'air ambiant à 300-580°C. Le temps de recuit a été ajusté pour permettre une oxydation complète de VO_x à V_2O_5. Alors que 10 min ont été suffisantes pour l'oxydation à 550°C, des temps beaucoup plus longs ont été nécessaires à des températures plus basses. Cela s'explique par la cinétique d'oxydation qui dépend de la température.

VI.3- Dépôt de couches atomiques de Al_2O_3 sur V_2O_5

V_2O_5 a une structure cristalline en couches avec une grande affinité pour accueillir des molécules entre les espaces interfoliaires. Cette propriété de V_2O_5

en fait un candidat idéal pour de nombreuses applications telles que la détection de gaz et de l'humidité, le stockage d'énergie et la catalyse. Afin de prouver que le thermochromisme de V_2O_5 est une propriété intrinsèque, et qu'elle ne dépend pas des conditions ambiantes, on a isolé les couches VO_2 de l'atmosphère ambiante. La passivation a été réalisée avec un dépôt ALD de Al_2O_3. L'ALD offrent des avantages supérieurs par rapport à d'autres techniques de dépôt en permettant une faible température de dépôt, de très fines épaisseurs et des caractéristiques de revêtement conformes. Tous les échantillons ont été revêtus de 20 nm de Al_2O_3. En plus de l'encapsulation, Al_2O_3 agit également en tant que couche de protection car il est plus résistant aux rayures ce qui permet de prévenir le vieillissement dû à une variation du déficit en oxygène.

Le dépôt ALD d'Al_2O_3 a été effectué en introduisant séquentiellement du triméthylaluminium (TMA) et de la vapeur d'eau. Les temps d'impulsion pour chaque réactif ont été ajustés à 40 ms avec une purge de 15 s entre chaque impulsion. Des temps de purge assez importants ont été choisis pour obtenir une couverture conforme et complète sur le film. L'ALD a été effectuée à 120°C sous une pression partielle de 2 mbar et 50 sccm d'Ar ont été utilisé comme gaz porteur.

VII- Revêtements thermochromiques V_2O_5

Bien que V_2O_5 soit l'objet de recherches approfondies depuis plus d'un demi-siècle, son thermochromisme intrinsèque n'a pas été signalée jusqu'à présent. Les films de V_2O_5 déposés par MOCVD sur Si, verre et substrats métalliques dans cette étude, présentent un changement de couleur perceptible induite par la chaleur allant du jaune vif à l'orange foncé.[22,23] Les analyses UV-Vis et la diffraction RX en fonction de la température permettent de corréler le décalage continu et réversible de l'absorption vers le rouge avec la dilatation thermique anisotrope le long de la direction cristallographique (001), soit perpendiculaire aux feuillets constituant la structure lamellaire de l'oxyde.

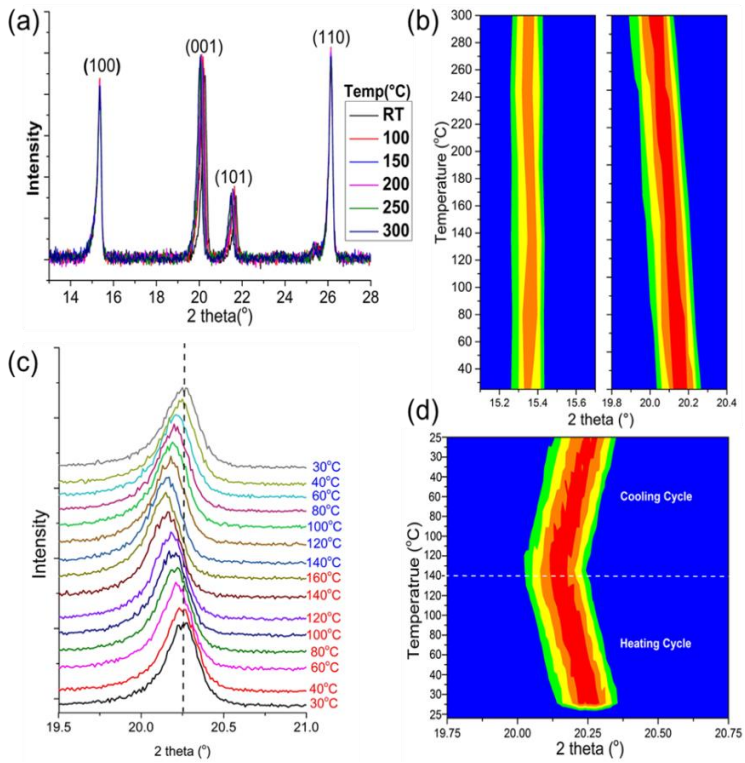

Figure 12 (a) Diffraction des RX vs la température du film V_2O_5 et (b) trame de contour des pics correspondant aux réflexions (200) et (001). Notez le déplacement progressif du pic (001) avec l'augmentation de la température. Les 2 parties du contour correspondent à un Δ(2θ) = 0.6°. La réversibilité du thermochromisme est vérifiée en (c) et (d) en mesurant le décalage de la réflexion (001) lors du chauffage et du refroidissement.

L'absence d'une transition abrupte représentée sur les figures 12 et 13 montre que thermochromisme de V_2O_5 est un phénomène continu et ne résulte pas d'un phénomène de transition de phase.

La figure 14 montre le schéma de la structure en couches de V_2O_5 avec les différentes liaisons V-O et qui permettent de distinguer clairement celles qui sont responsables de l'expansion du réseau. La figure 15 montre les photographies de films V_2O_5 en transition thermochromique du jaune à l'orange lors du chauffage.

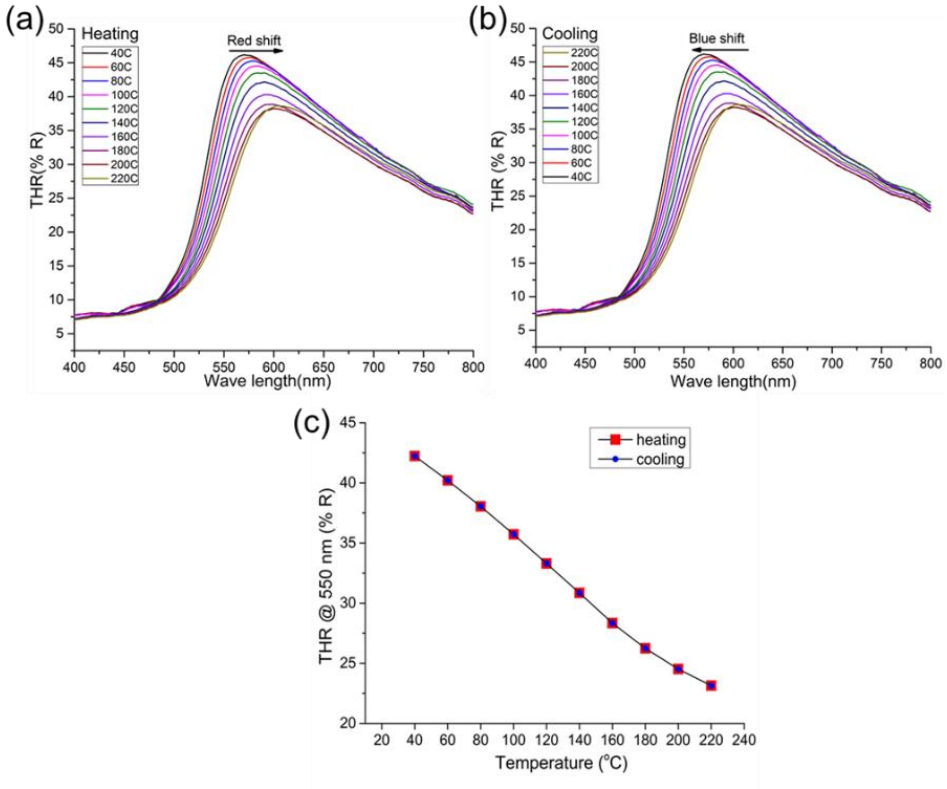

Figure 13: Réflectance totale hémisphérique (THR en%) vs la température pour V_2O_5 sous atmosphère ambiante pendant (a) le chauffage et (b) le refroidissement. (c) THR à 550 nm par rapport à la température pendant le cycle de chauffage et de refroidissement.

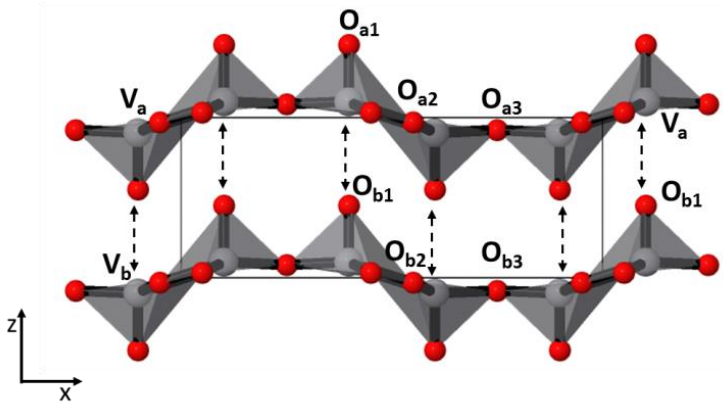

Figure 14: Illustration des feuillets de V_2O_5 montrant qu'ils sont retenus entre eux par les interactions faibles de V_a-O_{b1} et V_b-O_{a1}.

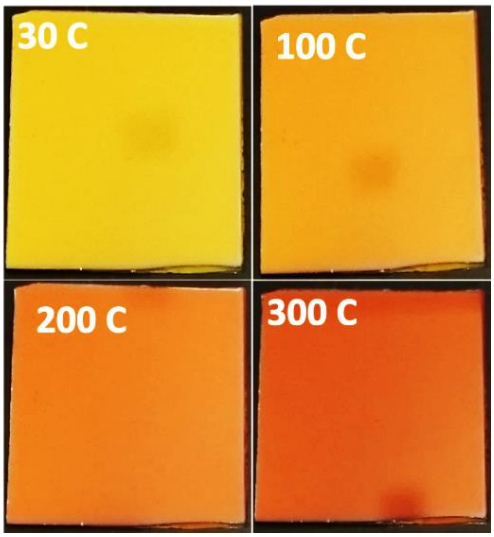

Figure 15: Photographies prises à différentes températures du substrat de silicium revêtu avec des films V_2O_5 dans l'atmosphère ambiante.

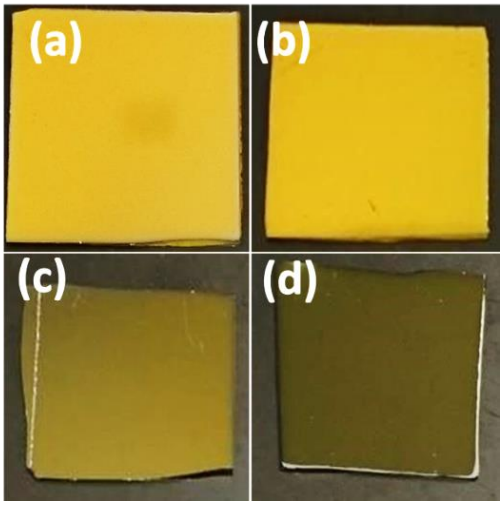

Figure 16: Photographies à la température ambiante (a) de films V_2O_5 non dopé, et de V_2O_5 dopé au Cr avec des niveaux de dopant de (b) 0,21%; (c) 2,41% et (d) 4,34%.

Conclusion de ce chapitre. Des films polycristallins et monophasés de V_2O_5 ont été synthétisés par DLI-MOCVD suivi d'une oxydation thermique des films VO_X tels que déposés. Les films résultants présentent un excellent thermochromisme réversible et continu, du jaune vif à la température ambiante à l'orange profond à des températures supérieures. Bien que des fonctionnalités de V_2O_5 aient été mises en évidence pour une grande variété d'applications, le thermochromisme n'a jamais été signalé jusqu'à ce jour. La diffraction RX et le Raman en fonction

de la température confirment l'absence de tout type de changements abrupts ou de transition de phase, et l'ensemble du film a contribué au thermochromisme observé. Une dilatation thermique anisotrope régulière du réseau V_2O_5 selon la direction (001) a été observée, c'est-à-dire perpendiculaire aux feuillets constituant la structure lamellaire de cet oxyde et elle a été corrélée au thermochromisme observé.

En outre, la possibilité de régler le comportement thermochromique a été démontrée par un dopage chimique avec du Cr. L'ajustement du comportement thermochromique a également été étudié. Le dopage au Cr a été successivement utilisé pour modifier la couleur perçue de V_2O_5 à des températures ambiantes et élevées. La figure 16 montre des photographies de films V_2O_5 dopé Cr par rapport aux films les plus purs non dopés.

VIII- <u>Réglage du comportement thermochromique de films V_2O_5</u>

Le thermochromisme de V_2O_5 conduit à une variété de couleurs. Le réglage du comportement thermochromique a été réalisé au moyen d'un recuit d'oxydation contrôlé dans l'air ambiant des dépôts MOCVD de VO_x. Ce post-traitement corrige le déficit en oxygène de V_2O_5 et permet un ajustement de la couleur des films, et par conséquent de leur comportement thermochromique. Des films V_2O_5 stœchiométriques en oxygène ne présentent pas de thermochromisme.

Une seule phase pure V_2O_5 a été obtenue par post-oxydation contrôlée des films VO_x déposés par DLI-MOCVD. Un thermochromisme dans le visible, et réversible, a été observé lors du chauffage sous atmosphère ambiante. La couleur induite par le thermochromisme de V_2O_5 peut être ajustée en contrôlant les conditions de synthèse. L'analyse RX confirme la nature polycristalline et pure de la phase V_2O_5 obtenue. La spectroscopie optique en fonction de la température faite sur des échantillons obtenus par post-oxydation à 350°C, 450°C et 550°C confirme que chaque échantillon a une fenêtre de transition thermochromique différente. Par conséquent, le réglage du comportement thermochromique est effectivement réalisé en contrôlant le recuit oxydant qui permet d'ajuster le déficit en oxygène. Les films oxydés à 580°C ne sont pas thermochromiques, ce qui indique que le thermochromisme est directement lié

au déficit en oxygène. Par conséquent, il a été montré que ce déficit joue un rôle clé dans l'expression de nouvelles fonctionnalités d'oxydes de métaux de transition, et en particulier de V_2O_5.

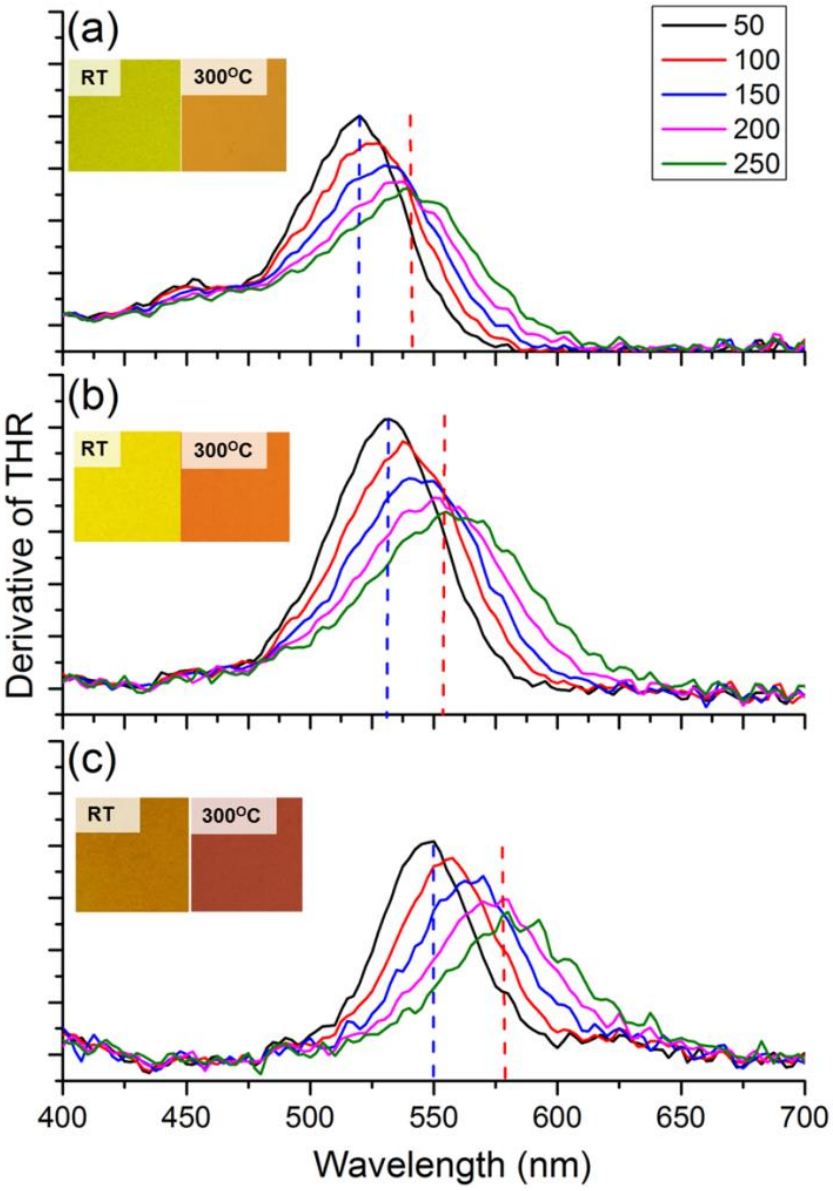

Figure 17: dépendance de la dérivée de la THR ($\frac{d(THR)}{d\lambda}$) vs la température montrant un comportement thermochromique d'échantillons oxydés à (a) 350°C, (b) 450°C et (c) 550°C respectivement. Pour chaque température de post-oxydation, l'image photographique insérée montre l'aspect des revêtements V_2O_5 à température ambiante et à 300°C.[24]

Références

1. Oka, Y.; Ohtani, T.; Yamamoto, N.; Takada, T. Phase Transition and Electrical Properties of VO_2 (A). *J. Ceramic Society Japan* **1989**, 1134–1137.

2. Khan; Khan, R. Preparation and Properties of Vanadium Dioxide Thermochromic Thin Films. *Pramana* **1992**, 389–396.

3. Kang, M.; Kim, S.; Ryu, J.-W.; Noh, T. Optical Properties for the Mott Transition in VO2. *AIP Advances* **2012**, 012168.

4. Zhou; Li; Cao; Bao; Jin. Optical and Electrical Properties of Thermochromic VO_2 Thin Films on Pt Layers. *Mater. Res. Innovations* **2015**, S246–S250.

5. Guinneton, F.; Sauques, L.; Valmalette, J.-C.; Cros, F.; Gavarri, J.-R. Role of Surface Defects and Microstructure in Infrared Optical Properties of Thermochromic VO_2 Mater. *J. Physics and Chem. Solids* **2005**, 63–73.

6. Richardson, M.; Coath, J. Infrared Optical Modulators for Missile Testing. *Optics & Laser Technology* **1998**, 137–140.

7. Gonçalves; Resende; Marques, A. C.; Pinto, J. V.; Nunes; Marie; Goncalves; Pereira; Martins; Fortunato. Smart Optically Active VO_2 Nanostructured Layers Applied in Roof-Type Ceramic Tiles for Energy Efficiency. *Solar Energy Materials and Solar Cells* **2016**, 1–9.

8. Prayakarao; Mendoza; Devine; Kyaw; van Dover; Liberman; Noginov. Tunable VO_2/Au Hyperbolic Metamaterial. *Appl. Phys. Lett.* **2016**, 061105.

9. Wang, S.; Kang, L.; Werner, D. Hybrid Resonators and Highly Tunable Terahertz Metamaterials Enabled by Vanadium Dioxide (VO_2). *Scientific Reports* **2017**, 4326.

10. Liang, J.; Song, X.; Li, J.; Lan, K.; Li, P. A Visible-near Infrared Wavelength-Tunable Metamaterial Absorber Based on the Structure of Au Triangle Arrays Embedded in VO_2 Thin Film. *J. Alloys and Compounds* **2017**, 999–1007.

11. Kats, M.; Blanchard, R.; Zhang, S.; Genevet, P.; Ko, C.; Ramanathan, S.; Capasso, F. Vanadium Dioxide as a Natural Disordered Metamaterial: Perfect Thermal Emission and Large Broadband Negative Differential Thermal Emittance. *Physical Review X* **2013**, 041004.

12. Kumar, S; Maury, F; Bahlawane, N. Electrical Switching in Semiconductor-Metal Self-Assembled VO_2 Disordered Metamaterial Coatings. *Scientific reports* **2016**.

13. Goltvyanskyi, Y.; Khatsevych, I.; Kuchuk, A.; Kladko, V.; Melnik, V.; Lytvyn, P.; Nikirin, V.; Romanyuk, B. Structural Transformation and Functional

Properties of Vanadium Oxide Films after Low-Temperature Annealing. *Thin Solid Films* **2014**, *564*, 179–185.

14. Lv, Y.; Hu, M.; Wu, M.; Liu, Z. Preparation of Vanadium Oxide Thin Films with High Temperature Coefficient of Resistance by Facing Targets D.C. Reactive Sputtering and Annealing Process. *Surf. Coat. Technol.* **2007**, 4969–4972.

15. Zhu, Z.; Niu, H.; Liu, Z.; Liu, S. Decomposition and Reactivity of NH_4HSO_4 on V_2O_5/AC Catalysts Used for NO Reduction with Ammonia. *J. Catalysis* **2000**, 268–278.

16. Satsuma, A.; Nakata, M.; Iwasaki, S.; Hattori, T.; Murakami, Y. Studies in Surface Science and Catalysis. *New Aspects of the Mechanism and Surface Keactivity of Selective Oxidation Catalysts* **1990**, 789–796.

17. Kodu, M.; Berholts, A.; Kahro, T.; Kook, M.; Ritslaid, P.; Seemen, H.; Avarmaa, T.; Alles, H.; Jaaniso, R. Graphene Functionalised by Laser-Ablated V_2O_5 for a Highly Sensitive NH3 Sensor. *Beilstein journal of nanotechnology* **2017**, 571–578.

18. Wang, Y.; Zhou, Y.; Meng, C.; Gao, Z.; Cao, X.; Li, X.; Xu, L.; Zhu, W.; Peng, X.; Zhang, B.; Lin, Y.; Liu, L. A High-Response Ethanol Gas Sensor Based on One-Dimensional TiO_2/V_2O_5 Branched Nanoheterostructures. *Nanotechnology* **2016**, 425503.

19. Wang, H.; Bai, Y.; Chen, S.; Luo, X.; Wu, C.; Wu, F.; Lu, J.; Amine, K. Binder-Free V_2O_5 Cathode for Greener Rechargeable Aluminum Battery. *ACS Applied materials & interfaces* **2014**, 80–4.

20. Afyon, S.; Krumeich, F.; Mensing, C.; Borgschulte, A.; Nesper, R. New High Capacity Cathode Materials for Rechargeable Li-on Batteries: Vanadate-Borate Glasses. *Scientific reports* **2014**, 7113.

21. Kumar, S.; Lenoble, D.; Maury, F.; Bahlawane, N. Synthesis of Vanadium Oxide Films with Controlled Morphologies: Impact on the Metal-Insulator Transition Behaviour. *Physica Status Solidi (a)* **2015**, 1582–1587.

22. Kumar, S.; Maury, F.; Bahlawane, N. Optical and Morphological Properties of Thermochromic V_2O_5 Coatings. *Data in Brief* **2017**, 6 pages; http://dx.doi.org/10.1016/j.dib.2017.07.028.

23. Kumar, S.; Qadir, A.; Maury, F.; Bahlawane, N. Visible Thermochromism in Vanadium Pentoxide Coatings. *ACS applied materials & interfaces* **2017**, 21447–21456.

24. Kumar, S.; Maury, F.; Bahlawane, N. Tunable Thermochromic Properties of V_2O_5 Coatings. *Materials Today Physics* **2017**, 1–5.